Magnetic Semiconductors for Spin Electronics

Jonathan Alaria
Department of Physics
University of Dublin

A thesis submitted for the degree of
Doctor of Philosophy

October 2009

DECLARATION

This thesis is submitted by the undersigned for examination for the degree Doctor of Philosophy at the University of Dublin. It has not been submitted as an exercise for a degree at any other University or other degree-giving institution.

This thesis, apart from the advice, assistance and joint effort mentioned in the acknowledgements and in the text, is entirely my own work.

I agree, that the Library may lend or copy this thesis freely upon request.

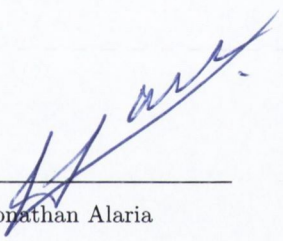

Jonathan Alaria

I would like to dedicate this thesis to my loving parents ...

Acknowledgements

Firstly, I would like to thank my co-supervisors Prof. J.M.D. Coey and Prof. J.G. Lunney for giving me the opportunity to come to Ireland and to study in Trinity all those years ago. I am very grateful for the support, both financial and academic, that they have both readily proffered over the past four years. Sincere thanks goes to Prof. Coey in particular, for the freedom (and belief) he gave me in my research activities throughout this term.

Secondly, I would like to acknowledge Dr. P. Stamenov, without whose wisdom and constant council this thesis would not be possible. I am indebted to him for his instruction and his friendship. I would also like to thank his infinitely patient wife and son, Maria and Stani, and to apologise for always delaying them and for depriving them of so much of his time. I equally wish to thank Dr. M. Venkatesan... or is that Dr. Ó Venkatesan? I want you to know that I appreciate those countless hours we spent discussing controversial magnetic theories, but I would probably appreciate them a little more now as I struggle to finish this dissertation before the deadline.

Many results presented in this thesis are the result of collaboration with international laboratory. I would like to acknowledge Pr. D. N. Basov and all his students to welcome me in his lab for a week. Special thanks to Andrew LaForge and Alex Schafgan who helped me during my stay. The determination of the crystal structure of $CuCr_2Se_3Br$ start to be a long story (still not finished) and several persons have seen the crystal in their hands, namely Dr. T. McCabe (TCD), Pr. A. Slawin (University of St. Andrews), and finally Dr. F. Porcher. During the course of this work I had the opportunity to go twice in the LLB (CEA Saclay) and I would like to thank Dr. F. Bourée, Dr. G. André, Dr. F. Porcher, and Bernard Rieu for their help during the experiment and for the interpretation of the data.

I would like to thank Zhu and Peter for their constant programming-babble in the lab. It is incumbent upon me to point out that you are both extremely powerful. I

want to thank Fowley for his crash-course in being Irish many pints ago. Thanks too to Fiona (who had to suffer -in the morning- the nasty rotten egg smells), Lorena and Karl who make the SNIAMS lab even better. A debt of gratitude is owed to Robbie, Lucio and Karsten, most of whom have moved on now, for imparting their interesting adaptations of PLD and XRD. Thanks to Tony and Enrique in the laser lab for teaching me all I know about Langmuir probes. And thanks to all members of Group D (including the summer students) past and present.

Now that I have completed my studentship I would like to thank Mlle. Lespinasse, Dr. S. Colis, and Pr. A. Dinia for their encouragement. Thanks to my parents Claude and Djémila for their unwavering support.

Thanks to Marita - who sits beside me for absolutely everything.

Abstract

The development of the relatively new field of spin electronics is based on the possibility of manipulating the spin of the electron through a structure. If one aspect is to develop new device architecture to inject, transmit, and detect spin polarised current, the materials involved in the fabrication of these structures plays a major role. In fact, if most of the standard electronic devices have been successfully translated in spin-based electronic devices, the magnetic bipolar transistor has not been demonstrated. The major obstacle for the construction of such device is the lack of a ferromagnetic semiconductor that can be bipolar. Other materials such as half metals have been studied extensively as potential spin polariser.

The experiments described in this thesis are aimed to synthesise and characterise compounds that have a strong potential to be integrated in spin electronic structures. It includes materials with a high Curie temperature, metallic conduction and a relatively high spin polarisation and ferromagnetic semiconductor. The fundamental properties of these materials have been studied thoroughly as well as the magnetic properties of diluted magnetic oxide.

The second chapter is a literature review on the chalcochromite spinels, a class of material that was studied extensively in the 70's. It focuses on three particular composition that have been chosen for their potential useful physical properties in the spin electronics field. A discussion on a fundamental problem that puzzles the material sciences community is given and the justification of a modern study on these materials is proposed.

In the third chapter, the synthesis of polycrystalline $CuCr_2Se_4$, its solid solution with $CuCr_2Se_3Br$, $CdCr_2Se_4$, and $HgCr_2Se_4$ are described and the structural and magnetic characterisation of these system has been carried out. Powder neutron diffraction was carried out on $CuCr_2Se_4$, $CuCr_2Se_3Br$ and some intermediate compositions. The magnetic structure of $CuCr_2Se_3Br$ has been determined for

the first time and a transition from ferromagnetic for $CuCr_2Se_4$ to ferrimagnetic is observed. The powder neutron diffraction on $CdCr_2Se_4$ was also performed for the first time confirming the accepted ferromagnetic structure. Zero field susceptibility measurements on $CuCr_2Se_4$ revealed a Curie temperature 20 K higher than the one reported in the literature.

In the fourth chapter, the synthesis of $CuCr_2Se_3Br$, $CdCr_2Se_4$, and for the first time $CuCr_2Se_4$ is described. The structural characterisation revealed that the Br doped samples present some disorder on the Cu atoms. Susceptibility, and the first torque measurement have revealed some anomalies around 100 K and 200 K. Infrared spectroscopy was measured for the first time, and the plasma frequency of the system was determined. The heat capacity, torque and low temperature magnetotransport measurement were performed for the first time on $CdCr_2Se_4$. The magnetotransport on pure $CuCr_2Se_4$ was measured for the first time and two carriers (majority and minority holes) were identified.

In the fifth chapter, an attempt in the synthesis of $CuCr_2Se_4$ thin films by pulsed laser deposition and selenisation of metallic precursors is described. The structural and magnetic properties of the synthesised films were measured. The films obtained by conventional pulsed laser deposition were Se deficient and a second step was necessary to obtain the right phase. Nevertheless no single phase films were prepared.

In the sixth chapter the synthesis of ZnO nanoparticles doped with various transition metal is presented showing that when an homogeneous sample is prepared no ferromagnetism is observed. Hexagonal CoO was prepared for the first time by pulsed laser deposition and its magnetic properties studied showing that it is an antiferromagnet.

In view of keeping the text free from heavy description of preparation and characterisation procedure, appendices with relevant information on the experiments carried out during this thesis are provided.

Contents

List of Figures

List of Tables

LIST OF TABLES

Nomenclature

Roman Symbols

a, b, c	lattice constants
B_{iso}	Isotropic atomic thermal parameter
C_p	Heat capacity
D	spin-wave stiffness constant
$d(A-X)$	bond length between atom A and X
e	elementary charge $(1.602176487(40) \cdot 10^{-19}\mathrm{C})$
E_F	Fermi energy
E_g	main energy gap
g	Lande g factor
H	magnetic field
J	effective exchange integral
k	Boltzmann constant
k_F	Fermi wave vector
k_m	magnetic propagation vector
K	equilibrium constant
L	torque amplitude
L_{mag}	magnetic correlation length

M	magnetisation
m	magnetic moment
m_e	electron mass $(9.10938215(45) \cdot 10^{-31}\text{kg})$
m^*	effective mass
n	carrier density
N_A	Avogadro number
P	spin polarisation
R	molar gas constant
R_Bragg	Bragg agreement factor
R_{mag}	magnetic agreement factor
R_p	conventional agreement factor
R_{wp}	weighted agreement factor
s	refined atomic stoichiometry
$\mathbf{S}_i$	spin vector on the ion i
T	temperature
T_C	Curie temperature
T_C	Curie temperature
T_D	Debye temperature
u	spinel deformation parameter
U_{eq}	Equivalent atomic thermal displacement
Z	effective barrier

Greek Symbols

χ	volume magnetic susceptibility

χ'	real part of the volume magnetic susceptibility
χ''	imaginary part of the volume magnetic susceptibility
Δ_1	Niobium superconducting gap
Δ_2	Refined superconducting gap in the proximity region
ΔG	free Gibbs energy
Δ	$= 10Dq$ crystal field splitting
ϵ_0	permittivity of free space ($8.854187817 \cdot 10^{-12}$F/m)
γ	damping factor
λ	degree of inversion in a spinel
μ	linear absorption coefficient
μ_B	Bohr magneton
μ_0	permeability of free space ($4\pi 10^{-7}$H/m)
ν_0	Lorentz oscillator frequency
ω_p	plasma frequency
ρ_{xx}	longitudinal component of the resistivity tensor
ρ_{xy}	transverse component of the resistivity tensor
σ	magnetic moment per unit mass
τ	scattering time
θ	scattering angle

Superscripts

HS	high-spin electronic configuration
LS	low-spin electronic configuration

Subscripts

o octahedral symmetry

t tetrahedral symmetry

Acronyms

AMR anisotropic magnetoresistance

CFSE crystal field stabilisation energy

CMR colossal magnetoresistance

CMS concentrated magnetic semiconductor

CVD chemical vapour deposition

CVT chemical vapour transport

DMO diluted magnetic oxide

IMM inhomogeneous magnetic materials

DMS diluted magnetic semiconductor

FMS ferromagnetic semiconductor

FWHM full width half maximum

HTS high temperature solution growth

PCAR point contact Andreev reflection

PLD pulsed laser deposition

RHEED reflection high-energy electron diffraction

SMS semi magnetic semiconductor

TM transition metals

XRD x-ray diffraction

Chapter 1

Introduction

The magnetic and electrical properties of transition metal (and rare earth) inorganic compounds have been the subject of intensive study in the field of solid state science from both academic and practical viewpoints. Many properties of solids can be understood through the analysis of their electronic band structure [1].

The free electron model, in which the electrostatic interaction between the electron and the periodic array of nuclei is neglected, gives a continuous quadratic energy dispersion. This first approximation does not explain the behaviour of some solids in which a periodic potential has to be taken into consideration. This periodic potential leads to the appearance of forbidden energy bands at the edge of the Brillouin zone.

The way in which the bands are filled with the electrons of the system illustrates the main differences in electrical conduction of solids and allows them to be classified in two main categories:

- Metals, which are described by the free electron model or by a non-zero electron population at the Fermi level E_F [2] (by direct filling of the bands or by band overlap). In this case, the application of an electric field allows carriers to gain energy and contribute to electrical conduction. We can distinguish two kinds of carrier, electrons and holes, the latter being an unoccupied state in the valence band.

- Insulators, in which one or more bands, i.e. the conduction band or the valence band, are filled leaving the other empty. The highest filled (valence) band and the lowest unoccupied

[1] This is true for weak potential, ionic solids cannot be treated in a band view
[2] The notation is explained in the nomenclature section.

(conduction) band are separated by an energy gap E_g. In this case, there are no carriers in the conduction band.

A special case of insulator occurs when the band gap is small enough that some carriers can be thermally activated around room temperature[1]. The solids presenting this feature are classified as semiconductors.

A perfectly pure (intrinsic) semiconductor, at absolute zero, is an insulator since no carrier can be moved into the conduction band. With increasing temperature, the probability of having carriers in the conduction band increases. The carrier concentration increases exponentially with the temperature and the Fermi energy is near the middle of the energy gap.

One peculiarity of semiconductor materials, and perhaps the reason for their industrial success, is the possibility of tailoring electrical properties by controlled addition of impurities to the material. This process, called doping, involves replacing an element of the crystal by a foreign element possessing a different valence. The doped semiconductor is called an extrinsic semiconductor.

The substitution of some atoms in the host material with impurities that have a higher valence creates a donor level below the conduction band. This leads to an excess of mobile electrons, and the material is referred to as n-type. Conversely, acceptor impurities have a lower valence than the host which leads to incomplete atomic bonding in the lattice. This creates an acceptor level above the valence band supplying holes to the valence band (i.e. the acceptor centres become negatively charged), and the semiconductor is referred to as p-type.

In an extrinsic semiconductor, electrons are majority carriers and holes are minority carriers in an n-type semiconductor. In a p-type material, electrons are minority carriers and holes are majority carriers. When similar concentrations of shallow donors and acceptors are present in the semiconductor, one type of impurity will cancel out the effect of the other, and the semiconductor is referred to as compensated.

If the impurity concentration reaches the same magnitude as the effective density of states, the Fermi energy will be shifted into the valence band (for p-type) or into the conduction band (for n-type), the semiconductor is referred to as a degenerate semiconductor. As a direct result of this heavy doping, the carrier concentration is high (although lower than in a normal metal) and almost independent of the temperature. The conductivity of such materials is therefore mobility controlled, the mobility being quite low due to the high probability of scattering from these impurities.

[1] At room temperature the thermal energy is 0.026 eV.

1. Introduction

Semiconductor based devices have been studied for more than a century and this still produces new technological advances. Since the explosion of microelectronics with the discovery of the bipolar transistor, we have witnessed, more recently, the appearance of "spinelectronics" a new technology where magnetism and electronics are combined. The first generation of such devices used the giant magnetoresistance effect, where only metals are involved. They are already widely applied in magnetic sensors. The next step is to introduce logic devices using spin polarised current. To achieve this, new materials have to be found and characterized for integration in devices such as spin injectors, transmitters, and detectors. In recent years there has been a huge effort from the scientific community in the development of ferromagnetic semiconductors (FMS) . Antiferromagnetic semiconductors have been known for a long time, and they are very numerous. However, not a single ferromagnetic semiconductor had been discovered; indeed, an opinion had been voiced that ferromagnetic and semiconducting properties were incompatible Zener (1951) until the first FMS $CrBr_3$ was synthesised in 1960 Tsubokawa (1960). This answered the question of the compatibility of the two properties.

Nonmetallic magnetic materials have been known for a long time, magnetic oxides such as the ferrites and garnets are outstanding examples. One might ask why these materials are not considered magnetic semiconductors. It was thought that in these materials any electrical conduction should be due to the motion of magnetic d electrons. Analysis of electrical data indicated that these d electrons are well localised at the magnetic atoms, and that the motion of the charge carriers under the action of an applied electric field occurs by a thermally activated hopping process. The mobilities are very low and increase strongly with temperature. Thus the conduction mechanism in the magnetic oxides appears to be quite different from that in semiconductors, where the mobile charge carriers occupy states in a broad energy band.

Although it is hard to find a genuine ferromagnetic semiconductor, possible candidates can be classified in different groups [1] :

Concentrated Magnetic Semiconductors (CMS) Concentrated magnetic semiconductors are compounds in which the magnetic ions have their own magnetic sub lattices. Examples of such crystals are : europium chalcogenides, chromium chalcogenide spinels, and a number of transition metal oxides (manganites) and pnictides[2]. Despite the fact that CMS possess a number of interesting spin related properties, these materials did not,

[1] A review for each class is provided as an example reference, an extended database on magnetic semiconductors is maintained at http://unix12.fzu.cz/ms.

[2] Compounds of phosphorus, arsenic, antimony, and bismuth.

heretofore, meet requirements (purification and perfection of the crystal) imposed by semiconductor engineering. A more detailed literature review on chalcogenide spinels is given in Chapter 2.

Semi Magnetic Semiconductors (SMS) Ramdas & Alawadhi (1998) Semiconductors based on type $A^{II}B^{VI}$ and $A^{IV}B^{VI}$ ($A^{II} = Zn, Cd, Hg$; $A^{IV} = Pb, Sn$; $B^{VI} = S, Se, Te$) matrices, in which the transition metal ions Fe^{2+}, Co^{2+}, or Mn^{2+} randomly replace the A elements in the lattice sites are called Semi Magnetic Semiconductors because their magnetisation can be readily changed by applying external magnetic fields but the materials retain the characteristics of the semiconductor matrix. The $3d$ dopants are paramagnetic, but a strong exchange interaction is observed between the $3d$ states and the carriers. Indeed, an external magnetic field polarises the $3d$ spins, the intrinsic magnetic field of the dopant spins causes a giant spin splitting. This class of material presents a combination of strong exchange interaction between the $3d$ states and the carriers in the semiconductor matrix with very low or even absent ordering temperatures of magnetic phase transitions, which makes semi magnetic semiconductors based on type $II-VI$ and $IV-VI$ matrices very interesting objects, suitable for studies of exchange interactions. This class of materials is also appropriate for fabrication of spin injection devices.

Diluted Magnetic Semiconductors (DMS) Jungwirth *et al.* (2006) Following the CMS, semimetals, half metals, and semi magnetic semiconductors, the DMS synthesised in the 1990s serve as the basis for next generation spintronic materials. In these compounds certain atoms of Group III elements of the semiconductor matrix ($InAs$, InP, $GaAs$, GaP or GaN) are randomly replaced by transition metal (TM) atoms with unfilled $3d$ electron shells (Mn or Cr). It is important that DMS retain the crystal structure of the semiconductor matrix, being isoelectronic to silicon. A distinctive feature of this class of magnetic semiconductors is that their Curie temperatures and other magnetic properties depend on the dopant concentration or current carrier density. The first DMS, $Mn : InAs$, had a Curie temperature of 7K. Since then the most successful material has been $Mn : GaAs$ where the Curie point has been increased from 60K to about 170K. The main drawback of the DMS is their Curie temperature, which is much too small for room temperature applications. Their "bad metal" electrical behaviour and the necessity of expensive facilities to grow high quality thin films also presents difficulties.

Diluted Magnetic Oxides (DMO) Coey (2006) Apparently similar to DMS, this class of material is based on wide band gap semiconductor (TiO_2, ZnO and In_2O_3) as host matrix and various TM (V, Cr, Fe, Co, Ni). Although the origin of the magnetic interaction in DMS is qualitatively understood, the high temperature ferromagnetism[1] observed in these systems has led to the development of controversial models to explain its origin. To date, there have been no reports of useful properties for spintronic applications.

Inhomogeneous Magnetic Materials (IMM) Since the first report of a high temperature ferromagnetic diluted magnetic oxide Matsumoto *et al.* (2001), a vast number of experimental reports claimed the synthesis of a new DMO. Soon after, contradicting reports appeared in the literature, leading to the conclusion that inter- and even intra-laboratory reproducibility of the properties of these new materials proves difficult. A careful analysis of the first claim showed the presence of metallic Co in the films Murakami *et al.* (2004). The experience of our group has been that many oxide compounds can be made conducting by doping. The insertion of magnetic TM in the matrix under certain conditions results in the appearance of high temperature ferromagnetism Gunning (2006). Nevertheless, a detailed study of the electrical properties of these materials shows that some of them contains metallic precipitate and that the material can not be classified as a FMS Stamenov (2007). In others, the ferromagnetism may be associated with a small fraction of the sample volume(possibly grain boundaries). Some aspects of the magnetic properties of such materials are addressed in Chapter 6.

It is becoming increasingly evident, from the somewhat random manner in which new FMS compounds are continuously being discovered (Fig.1.1), that there is no precise way of tailoring the properties of materials to make them both ferromagnetic and semiconducting.

Detailed characterisation studies of each of these materials are needed to envisage their integration into devices. The spin diode would be the first building block of bipolar spinelectronics. One of the first experiments demonstrating spin injection in an all semiconductor device [2] was realised with a paramagnetic $II-VI$ based semiconductor in the form of a spin-LED Fiederling *et al.* (1999); Jonker *et al.* (2000). Spin polarisation of the carriers is obtained at low temperatures and in intense magnetic fields. The recombination of spin-polarised electrons with non polarised holes gives circularly polarised light emission. The efficiency of the spin injection was

[1] A Curie temperature well above room temperature.
[2] For a complete review on spin electronic based devices see Zutic *et al.* (2004).

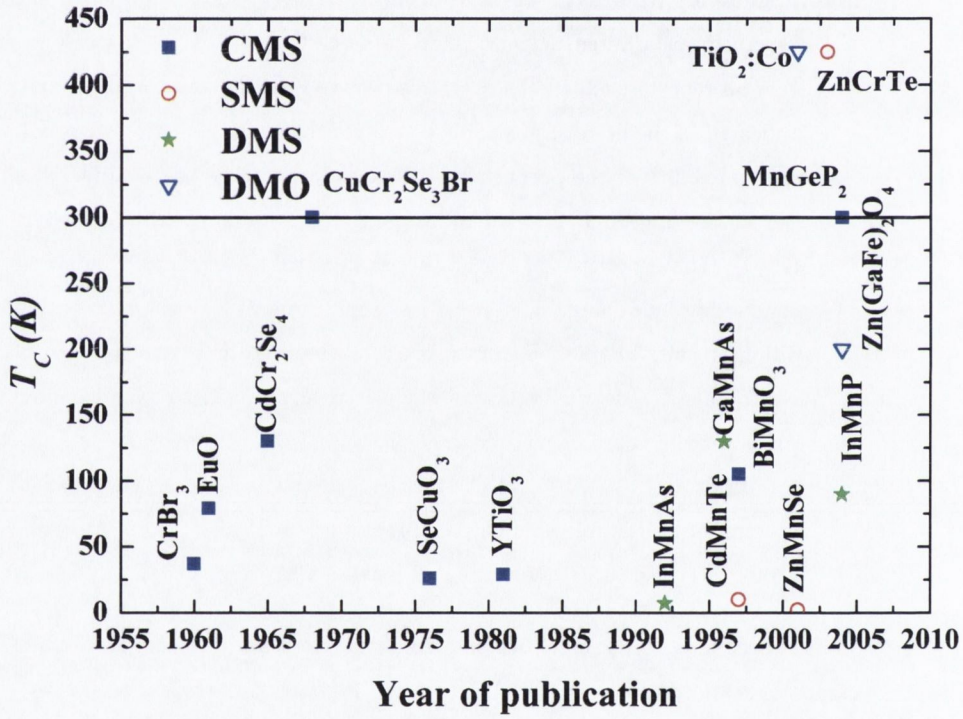

Figure 1.1: Magnetic Semiconductor by year of discovery, Curie temperature (T_C) and type. The blue squares represent Concentrated Magnetic Semiconductor (CMS), the hollow red circles represent SemiMagnetic Semiconductor (SMS), the green stars represent Diluted Magnetic Semiconductor (DMS) and the hollow blue triangles represent Diluted Magnetic Oxide (DMO). The black line represents the room temperature limit. Baltzer *et al.* (1965); Chiba *et al.* (1997); Cho *et al.* (2004); Gaj *et al.* (1978); Garrett *et al.* (1981); Kohn *et al.* (1976); Komarov *et al.* (1980); Matsumoto *et al.* (2001); Matthias *et al.* (1961); Munekata *et al.* (1989); Ohno *et al.* (1996); Risbud *et al.* (2005a); Robbins *et al.* (1968); Saito *et al.* (2003); Shon *et al.* (2004); Tsubokawa (1960)

found to be close to 90% Jonker *et al.* (2001). With the development of the ferromagnetic diluted semiconductor, spin injection in a semiconductor without an external magnetic field was demonstrated in a similar heterostructure Ohno *et al.* (1999). They demonstrated that the holes could be transported across a distance of the order of 200 nm. A second approach, inspired by the first generation of spin electronic devices, led to the development of magnetic tunnelling diodes from a ferromagnetic to a nonmagnetic semiconductor Johnston-Halperin *et al.* (2002). Nevertheless, one device that has not been demonstrated is the magnetic bipolar diode, even though a magnetic $p - n$ junction has been fabricated Wen *et al.* (1968).

The chalcochromite spinels seem to be perfect candidates for the demonstration of a magnetic bipolar diode, even though the earlier studies on spin injection in semiconductors appear to have been ignored Nagaev (1983). A comprehensive study has been caried out to develop the growth and understand the physical properties of such materials. The results are presented in Chapters 3, 4, and 5.

Chapter 2

Chalcochromites a family of magnetic semiconductors

2.1 Taxonomy of chalcogenide spinels

The development of CMS in the 70's was led by the potential application of such semiconductors in optoelectronics. With the renewed interest in magnetic semiconductor research, a modern study of these materials could be beneficial. One family that presents a rich physico-chemistry is the chalcogenide spinels.

We present, in Table 2.1, selected chalcospinel phases with their notable properties. A relatively wide range of properties is observed in these materials. Metals, semiconductors, and insulators are represented, along with more rare occurrences of superconductivity and metal-insulator transitions. The full spectrum of magnetic properties is also in evidence.

Phase	Selected Properties	a_0 (Å)	References
$ZnAl_2S_4$	paramagnetic insulator	10.009	Mazurak *et al.* (2000)
$CuCo_2S_4$	superconductor, antiferromagnetic metal	9.462	Sugita *et al.* (2000)
$NiCo_2S_4$	paramagnetic metal	9.384	Bouchard *et al.* (1965)
$CdCr_2S_4$	ferromagnetic semiconductor	10.24	Lehmann & Robbins (1966)
$CuCr_2S_4$	metallic, ferromagnetic	9.814	Lotgering & van Stapele (1967)
$FeCr_2S_4$	ferrimagnetic semiconductor, CMR	9.995	Yang (2004)
$HgCr_2S_4$	metamagnetic, CMR	10.206	Weber *et al.* (2006)
$ZnCr_2S_4$	antiferromagnetic insulator	9.986	Hemberger *et al.* (2006)
$CdCr_2Se_4$	ferromagnetic semiconductor	10.721	Lehmann & Robbins (1966)
$CuCr_2Se_4$	ferromagnetic metal	10.336	Lotgering & van Stapele (1967)
$HgCr_2Se_4$	ferromagnetic semiconductor	10.74	Selmi *et al.* (1986)
$CuIr_2S_4$	metal-insulation transition	9.959	Nagata *et al.* (1994)
CuV_2S_4	charge density wave	9.809	Fleming *et al.* (1981)

Continued on next page ···

Phase Continued ···	Selected Properties	a_0 (Å)	References
$CuRh_2S_4$	superconductor	9.76	Hagino *et al.* (1995)
$CuTi_2S_4$	metallic, Pauli paramagnetism	9.99	Okada *et al.* (2005)
$Ga_{2/3}Cr_2Se_4$	spin glass	9.936	Novotortsev *et al.* (2005)

Table 2.1: Survey of the main physical properties of selected chalcospinels.

2.2 The spinel structure

Since all the compounds cited above adopt a spinel structure, we will now describe its crystallographic properties.

2.2.1 Description of the crystal structure

The spinel structure, named for the mineral spinel $MgAl_2O_4$, is based on a face-centred cubic (fcc) network of anions. The unit cell used to describe spinels contains two lattices of fcc anion (and therefore contains eight fcc cubes). The cell is composed of a cubic close-packed array of anions which possess two types of interstice, one formed by four anions at the vertices of a tetrahedron, and the other by six anions at the vertices of an octahedron. These interstices are commonly called the tetrahedral (A-sites) and the octahedral (B-sites) respectively. A unit cell of a general spinel with the chemical formula AB_2X_4 is represented along two high symmetry directions shown in Fig.2.1.

Depending on the valence of the cations, two different types of spinel can be differentiated. The 2-3 spinel contains divalent and trivalent cations and the 4-2 spinel contains tetravalent and divalent cations.

The space group of the spinel structure is $Fd\bar{3}m$ with the number 227 in the *International Tables for Crystallography* Hahn (1996). It should be noted that for this space group two possible equi-points with point symmetry $\bar{4}3m$ (origin choice 1) and $\bar{3}m$ (origin choice 2) can be chosen for the unit-cell origin (see Table 2.2).

The conventional unit cell contains 56 atoms: 8 A-atoms, 16 B-atoms and 32 X-anions. Half of the octahedral interstices are occupied with cations of element B, forming a BX_2 (atacamite) lattice. The B-centred octahedra are arranged into edge-sharing chains parallel to the cubic (110) planes. The atacamite structure becomes the spinel structure with the insertion of additional cations into the lattice. One eighth of the tetrahedral interstices are occupied by cations, A, such that the AX_4 tetrahedra complete the tetrahedral coordination of each anion.

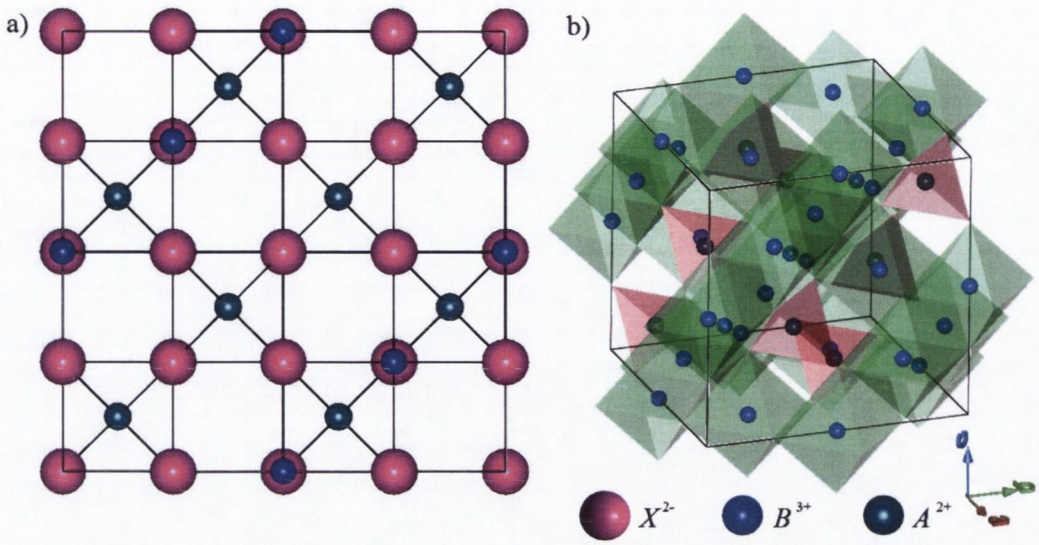

Figure 2.1: Representation of one spinel unit cell along (a) [001] direction and (b) [111] direction.

Multiplicity	Wyckoff letter	Site symmetry	Coordinates	
			Origin choice 1	
$8A$	a	$\bar{4}3m$	$(0,0,0),(3/4,1/4,3/4)$	
$16B$	d	$\bar{3}m$	$(5/8,5/8,5/8),(3/8,7/8,1/8),(7/8,1/8,3/8),(1/8,3/8,7/8)$	
$32C$	e	$3m$	(x,x,x),	$(x+3/4,x+1/4,-x+3/4)$,
			$(-x,-x+1/2,x+1/2)$,	$(-x+1/4,-x+1/4,-x+1/4)$,
			$(-x+1/2,x+1/2,-x)$,	$(x+1/4,-x+3/4,x+3/4)$,
			$(x+1/2,-x,-x+1/2)$,	$(-x+3/4,x+3/4,x+1/4)$,
			Origin choice 2	
$8A$	a	$\bar{4}3m$	$(1/8,1/8,1/8),(7/8,3/8,3/8)$	
$16B$	d	$\bar{3}m$	$(1/2,1/2,1/2),(1/4,3/4,0),(3/4,0,1/4)(0,1/4,3/4)$	
$32C$	e	$3m$	(x,x,x),	$(x+3/4,x+1/4,-x+1/2)$,
			$(-x+3/4,-x+1/4,x+1/2)$,	$(-x,-x,-x)$,
			$(-x+1/4,x+1/2,-x+3/4)$,	$(x+1/4,-x+1/2,x+3/4)$,
			$(x+1/2,-x+3/4,-x+1/4)$,	$(-x+1/2,x+3/4,x+1/4)$,

Table 2.2: Wyckoff positions for the space group $Fd\bar{3}m$ (SG 227). Hahn (1996)

These A-centred tetrahedra are isolated from one another, but the anion at each of the four vertices is also shared by two edge-sharing B-centred octahedra. As a result, each anion X occupies the centre of a tetrahedron of the form XAB_3. The coordination environment of the cations A, B, and anion X of a perfect spinel is represented in Fig.2.2.

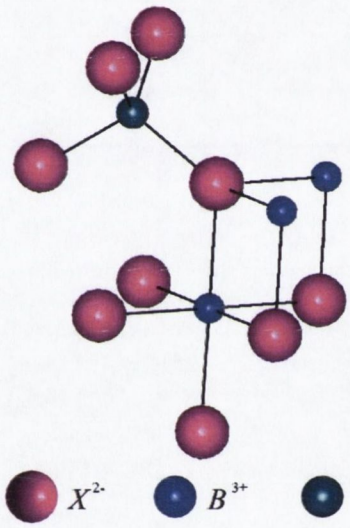

Figure 2.2: Coordination environments of the cations A, B and anion X. B cations are octahedrally coordinated by X. A cations are tetrahedrally coordinated by X. X anions are in the centre of a tetrahedron with one A and three B cations.

2.2.1.1 Normal spinel

When each type of cation fully occupies one site, *i.e.*, all cations A are in tetrahedral sites, and all B cations are in octahedral sites, the spinel is called normal, and the only set of parameters needed to describe the structure are the lattice constant a and the deformation parameter u. The deformation parameter describes the displacement of anions along one of the body diagonals of the cubic cell. Ideally, $u_0 = 3/8$ ($u = x = y = z$) (origin choice 1)[1] corresponds to perfect close-packing of the anions with an exact fcc arrangement. For real substances, however, $u > u_0$ and the anions are shifted along the body diagonals away from the A-cations (see Fig.2.3). The tetrahedrons, therefore, become enlarged while maintaining their overall $\bar{4}3m$ point symmetry, whereas the octahedrons become distorted and assume $\bar{3}m$ symmetry.

[1] In the case of origin choice 2, $u_0 = 1/4$.

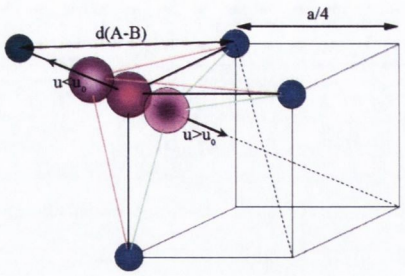

Figure 2.3: Portion of the spinel structure with different values of the anion parameter u.

The essential symmetry of the structure is more easily distinguished merely by the part of the spinel cell along the body diagonal <111> (Fig.2.4). The small cubes of dimension $a/4$ illustrate the tetrahedral coordination of the A-atoms (centres of selected cubes) and the octahedral coordination of the B-atoms (corners of some cubes).

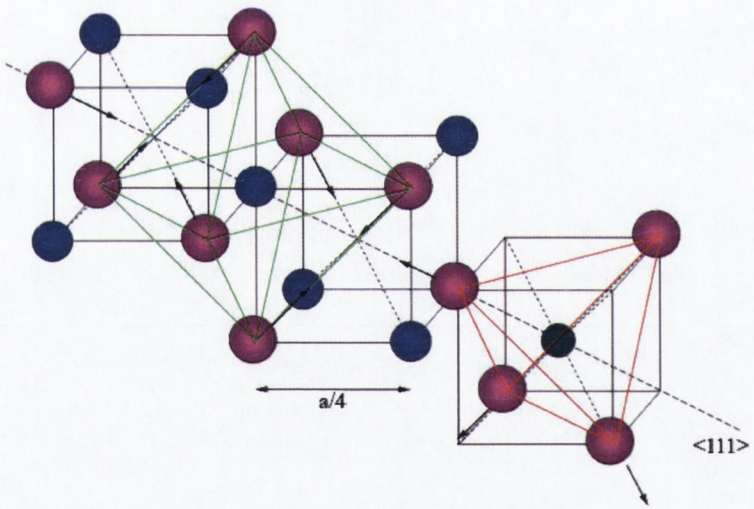

Figure 2.4: The part of the spinel unit cell near the body diagonal <111> showing the essential symmetry properties of the structure. The $A-$ and $B-$atoms with framing exhibit the tetrahedral (red tetrahedron) and octahedral (green octahedron) coordination of the anions. In the case of $u > 1/4$ the anions are shifted along the body diagonals of the small cubes in the direction of the arrows.

2.2.1.2 Inverse and mixed spinel

A different arrangement of the cations is possible when the tetrahedral sites are occupied by trivalent ions and the octahedral sites by a random arrangement of divalent and trivalent ions, the structure is said to be *inverse*. Intermediate arrangements are also possible and the general form of the structural formula may be represented as $(A_{1-\lambda}B_{\lambda})[A_{\lambda}B_{2-\lambda}]C_4$, where λ is the degree of inversion, equal to zero and unity for the normal and inverse structure respectively.

2.2.1.3 Algebraic description of the spinel structure

Although the spinel crystal structure is relatively complex, only a few parameters are needed to describe the system. From the portion of the spinel represented in Fig.2.3, the two nearest neighbour distances can be obtained from the following relations :

$$\begin{cases} d(A-X) = a\sqrt{3}\left(\frac{1}{8}+\delta\right) \\ d(B-X) = a\sqrt{\frac{1}{16}-\frac{\delta}{2}+3\delta^2} \end{cases} \tag{2.1}$$

where $\delta = u - u_0$.

Assuming that $d(A-X) = r_A + r_X$ and $d(B-X) = r_B + r_X$, one can deduce the lattice parameter and the anionic displacement using the ionic radii r_A, r_B, and r_X.

The angle $A-X-A$ is independent of the anion parameter but the angles $B-X-B$ and $B-X-A$ are only a function of u. We observe that $B-X-B$ increases with increasing value of δ while $B-X-A$ decreases. These dependences can be expressed algebraically if we observe that the distance $d(A-B)$ depends only on the lattice parameter a. The evolution of these two angles is represented in Fig.2.5.

2.2.2 Prediction of the spinel type

Determination of the site preference in spinels is a delicate problem and several methods have been developed to predict whether the structure will be more stable in a normal or inverse configuration. We can categorise them in three different classes, the first one treats the distribution of the cation thermodynamically Navrotsky & Kleppa (1967), the second discusses the change in internal energy upon disordering the cations (based on crystal field theory or electrostatic energy), and the last method resorts to structural sorting maps. We will present the last two methods and apply them to the material of our interest where one of the cations is Cr[1].

[1] All of these methods assume an ionic crystal.

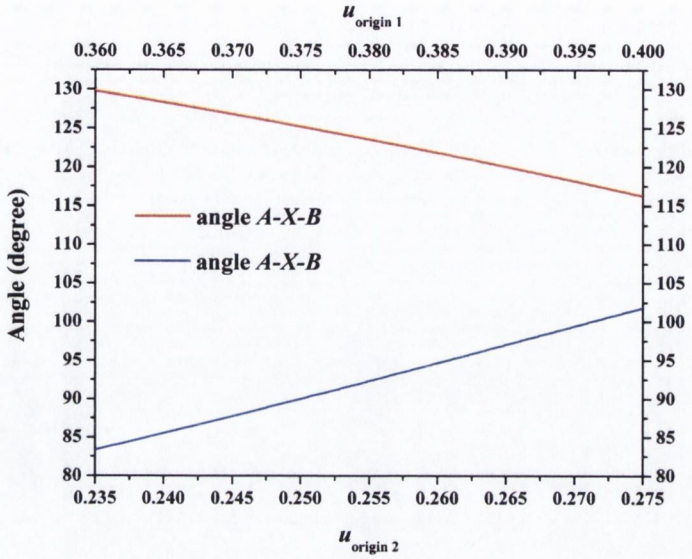

Figure 2.5: Interbond angles as a function of the anion parameter u. Bond angles are independant of a.

2.2.2.1 Crystal field stabilisation energy

When the cation A or B is a TM, the traditional approach is to consider the crystal field stabilisation energy Dunitz & Orgel (1957). We will briefly describe the basic principles of this method.

The five d orbitals are constructed as follows:

$$d_{3z^2-r^2} \sim f(r) \cdot Y_2^0(\theta, \phi)$$

$$d_{3z^2-y^2} \sim f(r) \cdot \frac{Y_2^2(\theta, \phi) + Y_2^{-2}(\theta, \phi)}{\sqrt{2}}$$

$$d_{xz} \sim f(r) \cdot \frac{Y_2^1(\theta, \phi) + Y_2^{-1}(\theta, \phi)}{\sqrt{2}}$$

$$d_{yz} \sim f(r) \cdot \frac{Y_2^1(\theta, \phi) - Y_2^{-1}(\theta, \phi)}{\sqrt{2}}$$

$$d_{xy} \sim f(r) \cdot \frac{Y_2^2(\theta, \phi) - Y_2^{-2}(\theta, \phi)}{\sqrt{2}}$$

where $f(r)$ is the radial function for the principal quantum number and $Y_l^m(\theta, \phi)$ are the spherical harmonics. The five orbitals are represented in Fig.2.6.

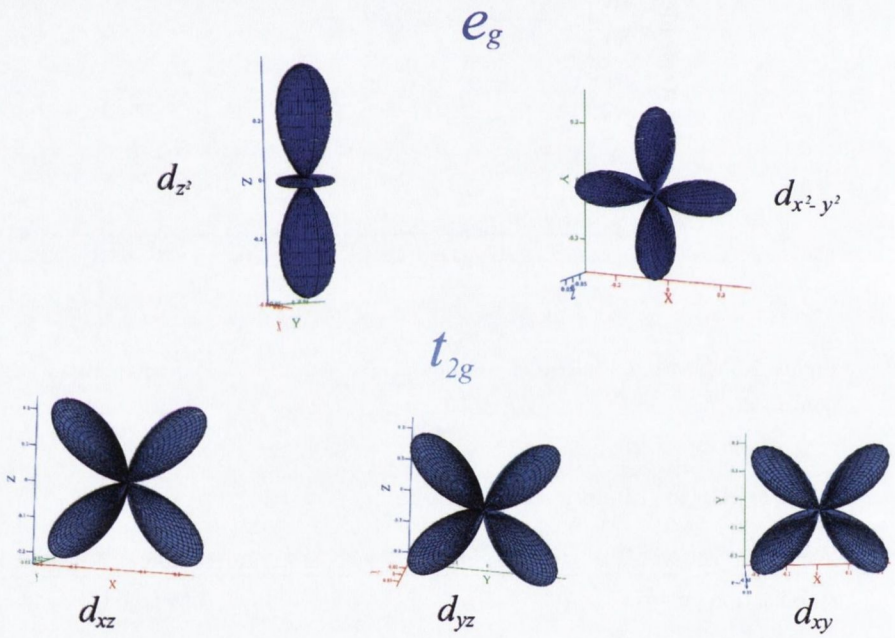

Figure 2.6: Representation of the angular electronic density of the d orbitals with their symmetry. The x, y, and z axis are represented in red, green, and blue respectively.

The five degenerate $3d$ orbitals may be divided into two groups according to their respective symmetry properties. Three of the orbitals, d_{xy}, d_{yz}, and d_{xz}, have lobes projecting between the Cartesian axes. This group is designated t_{2g}. The two other orbitals, $d_{x^2-y^2}$ and d_{z^2}, have lobes directed along the Cartesian axes, and they are designated e_g[1].

When the ligand anions are placed in the centre of the cube face *i.e.* at the vertices of an octahedron (or B site of a spinel) on the x, y, z coordinate axes, electrons in all five $3d$ orbitals experience a repulsive Coulombic interaction due to the negatively charged surrounding p anion orbitals, and the overall energy of the degenerate orbitals is raised. Moreover, since the lobes of the e_g orbitals are aligned with the anion, the repulsive interaction is much stronger than that of the t_{2g} orbitals. The energy separation between the t_{2g} and e_g levels is called octahedral crystal field splitting and is designated by Δ_0 or $10Dq$.

[1] An alternative designation for the two groups of d orbitals is sometimes used: d_ϵ and $d\gamma$ for the e_g and t_{2g}.

In the case of tetrahedral coordination, the symmetry is the same as in a cubic environment without the inversion centre. According to group theory nomenclature the two groups of orbitals are designated t_2 (for d_{xy}, d_{yz}, and d_{xz}) and e ($d_{x^2-y^2}$ and d_{z^2}). Nevertheless, the splitting of the d orbitals in a tetrahedral coordination will be similar, since all the d orbitals are even with respect to the inversion. The anion orbitals are at the vertices of the cube, and therefore the electrons of the t_2 orbitals are now repelled by the ligand to a greater extent than the e orbitals. The separation between the e and t_2 orbitals is denoted by the tetrahedral crystal field splitting Δ_t [1]. The relative crystal field splitting is represented schematically in Fig.2.7.

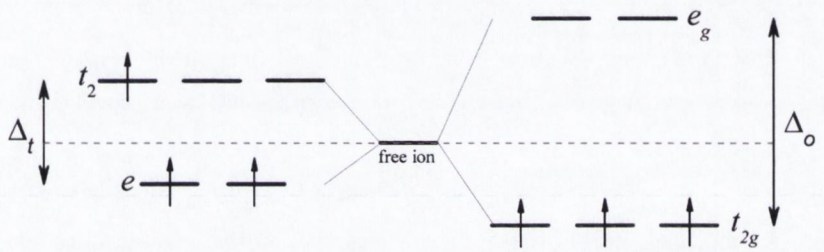

Figure 2.7: The crystal field for a Cr^{3+} ion in an tetrahedral (left) and octahedral (right) environment.

From a simple centre of gravity argument, each electron stabilises a TM ion by $0.4\Delta_0$ in an octahedral coordination for a t_{2g} orbital, and by $0.6\Delta_t$ in a tetrahedral coordination for an e orbital. On the other hand, every electron in an e orbital or a t_2 orbital will destabilise the TM ion by $0.6\Delta_0$ and $0.4\Delta_t$ respectively. The resultant net stabilisation energy is called the crystal field stabilisation energy (CFSE).

Because of the splitting of the d orbitals in a crystal field, the filling of electrons is done by taking into account two opposite phenomena. Firstly, the electrons follow Hund's first rule, placing them in as many different d orbitals with parallel spins as possible. Secondly, the crystal field stabilisation of some orbitals causes electrons to populate the d orbitals having the lowest energy. These two opposing tendencies lead to high-spin (filling dominated by Hund's first rule) and low-spin (filling dominated by crystal field stabilisation) electronic configurations in certain TM. In the case of tetrahedral coordination, low-spin electronic configurations are unlikely because of the smaller value of Δ_t.

[1] When cations, ligands, and metal-ligand distances are identical in the two coordinations, it may be shown that $\Delta_t = -\frac{4}{9}\Delta_o$, the negative sign shows the reversal of the stabilisation of the orbitals.

2.2.2.2 Lattice electrostatic energy

In the method presented previously, the change in lattice energy was neglected. However it has been shown that the electrostatic part of the lattice energy with disordering is likely to be much greater than the CFSE Glidewell (1976). The electrostatic energy in a crystal can be written as :

$$U_E = \frac{Ne^2M}{4\pi\epsilon_0 a} = 1389\frac{M}{a}\text{kJ/mol}$$

where M is the Madelung constant, which depends on the crystal structure and the charge of each ion. A general formulation for the spinel has been provided by Thompson & Grimes (1977):

$$M(u) = \alpha_1 Z_o^2 + \alpha_2 Z_o Z_t + \alpha_3 Z_t^2 + \alpha_4(u) Z_o Z_X \alpha_5(u) Z_X^2 + \alpha_6(u) Z_t Z_X$$

where Z_o, Z_t and Z_X are the average charges on the octahedral, tetrahedral and anion sites. The coefficients α_i are computed using the Ewald transformation. The calculated Madelung constants for different cation distributions are plotted against u on Fig.2.8[1]. In the case of

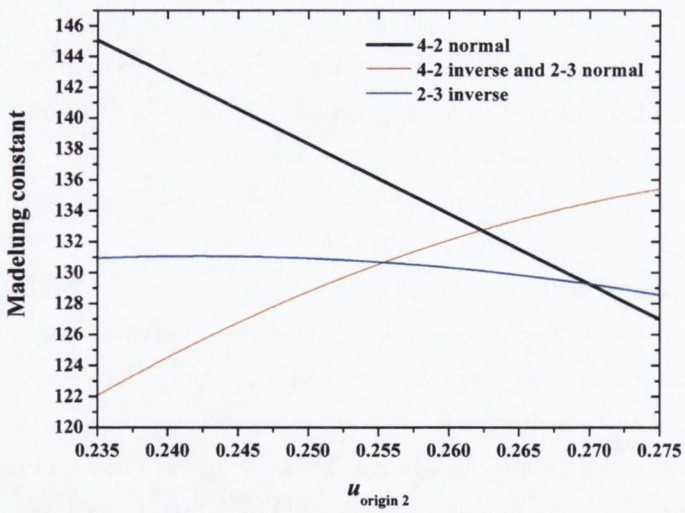

Figure 2.8: Madelung constant versus the anion parameter for normal and inverse 2-3 spinels and normal 4-2 spinels.

2-3 spinel, for $u < 0.2555$, the inverse distribution is favoured. In the case of 4-2 spinel, for $u < 0.2625$, the normal distribution is favoured.

[1]Since an inverse 4-2 spinel has the same average charges in each site as a normal 2-3 spinel, it will also have the same Madelung constant.

2.2.2.3 Structural sorting maps

To predict the structure of inorganic compounds, an alternative method has been developed in a Mendelevyan approach. It involves finding a set of coordinates where well defined regions can be distinguished. This method has been applied to the cation distribution in spinels by plotting the orbital radii r_σ^A and r_σ^B of each cation Burdett *et al.* (1982). Such a diagram is represented in Fig.2.9 for selected chalcogenide spinels. We have not included any mixed spinels in the diagram and the orbital radii have been taken from Zunger (1980).

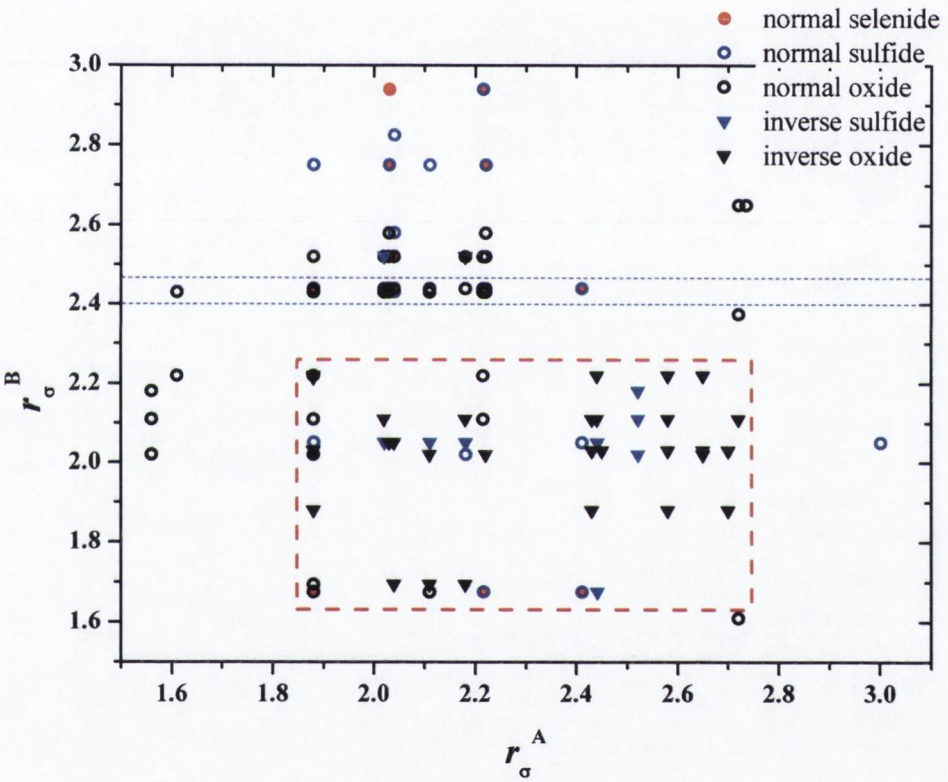

Figure 2.9: Structural sorting map for AB_2X_4 spinels. Normal spinels are represented by a circle and inverse spinels by a triangle. Oxides are in black, sulfides in blue, and selenides in red. The red square represents the region where the inverse spinel structure is more stable. The blue stripe represents the region where all the chromites are situated.

This method relies on the prior knowledge of the cation distribution of some compounds to define the region where normal and inverse spinels are. A zone where inverse spinels are

expected is shaded on the sorting map. All the chromites lie in the blue stripe and they are all normal spinels. It can be noted that all spinels containing Cr as the A cation are inverse confirming the strong preference of Cr for the octahedral sites.

2.2.2.4 Application to the chromate case

In the case of the materials of our research, the B-cation is Cr^{3+}. The Cr^{3+} ion has the electronic configuration $[Ar], 3d^3$ [1] and is subject to an octahedral environment. When a free TM ion is placed in a crystal field, the five degenerate d levels split. In fact, the electrostatic energy of an orbital is different whether or not it is in the direction of a neighbouring ion due to its symmetry.

The electronic configuration of Cr^{3+} is represented for the octahedral and tetrahedral configuration in Fig.2.7.

Only three electrons have to be distributed in the orbitals, therefore it can only have one electronic configuration in the octahedral coordination: t_{2g}^3. In the case of tetrahedral symmetry, two electronic configurations are theoretically possible, the high-spin state e^2, t_2^1 and the low-spin configuration e^3. The crystal field stabilisation energies for each of these electronic configurations are :

- $\text{CFSE}_o = \frac{6}{5}\Delta_o$
- $\text{CFSE}_t^{HS} = \frac{4}{5}\Delta_t = \frac{16}{45}\Delta_o$

Since $\text{CFSE}_o > \text{CFSE}_t^{HS}$, the crystal field theory predicts that Cr^{3+} has a strong preference for octahedral coordination site.

From the electrostatic lattice energy prediction, a threshold value for the size of the A cation can be obtained. The assumptions are that:

- the lattice can be described as an ionic compound
- the ionic radius of Cr^{3+} is 0.615Å

The threshold value for the size of the A cation to have a normal spinel in a 2-3 spinel is found to be $r_{ionic}(A) > 0.451$Å.

The sorting map shows clearly that all chromium containing spinels are normal. Therefore all spinels studied in subsequent sections will be treated as normal spinels.

[1] $[Ar]$ is the argon core : $1s^2\ 2s^2\ 2p^6\ 3s^2\ 3p^6$.

2.3 Magnetic interactions in spinels

In general, the chalcospinels with unpaired electrons on the TM ions tend to be ferrimagnetic [1]. To understand the magnetic properties of the chalcospinel, it is important to review the different microscopic mechanisms responsible for the exchange interactions in the spinel structure.

2.3.1 Ionic model

The magnetic interaction of neighbouring spins (or moment) in an ionic solid can be described bythe Heisenberg exchange Hamiltonian [2]:

$$\mathcal{H}_{\text{Heis}} = -\sum_{i,j} J_{i,j}\, \mathbf{S}_i \cdot \mathbf{S}_j$$

where $J_{i,j}$ is the effective exchange integral between atom i and j (when J is positive, the exchange energy favours electrons with parallel spins, when J is negative, the interaction favours electrons with antiparallel spins) having total spin $\mathbf{S}_j$. The sign and the strength of $J_{i,j}$ will determine the magnetic ground state of the compound. For an ionic or semi-covalent compound there are, in general, three types of interactions: cation-cation (direct exchange) or cation-anion-cation (superexchange and double exchange).

2.3.1.1 Direct exchange interactions

The direct exchange arises from the overlap of the wave functions of two neighbouring atoms and, in a simple case, its value corresponds to the Coulomb interaction between the electrons situated on the neighbouring atoms. If we consider two different orbitals $|\varphi_i\rangle$ and $|\varphi_j\rangle$ centred on two different atoms and two electrons, the resulting wave function $|\psi_i\rangle$ must be symmetric or antisymmetric according to the exclusion principle :

$$\psi(\mathbf{r}_1, \mathbf{r}_2) = \frac{1}{\sqrt{2}}[\varphi_i(\mathbf{r}_1)\varphi_j(\mathbf{r}_2) \pm \varphi_i(\mathbf{r}_2)\varphi_j(\mathbf{r}_1)]$$

The average Coulomb energy can be expressed by the relation :

$$\left\langle \psi \left| \frac{e^2}{4\pi\epsilon_0 |\mathbf{r}_1 - \mathbf{r}_2|} \right| \psi \right\rangle = J \pm K$$

[1] A ferrimagnetic material is one in which the magnetic moment of the atoms on different sub-lattices are opposed, as in antiferromagnetism; however, in ferrimagnetic materials, the opposing moments are unequal and a spontaneous magnetisation remains.

[2] The factor two is omitted because the summation includes each pair twice.

where J represents the exchange integral between the two electrons over the two orbitals. In an ionic crystal, if the electrons on the magnetic ions can be considered as localised, they are separated by an anion. Therefore the magnitude of the direct exchange is negligible since its magnitude will decrease inversely with $|\mathbf{r}_1 - \mathbf{r}_2|$. Another mechanism is, therefore, required to explain the magnetism in transition metal compounds.

2.3.1.2 Superexchange interactions

Kramers suggested that the strong exchange interaction between the magnetic atoms observed experimentally is due to the presence of nonmagnetic atoms Kramers (1934). Qualitatively, this indirect exchange, known as superexchange, is caused by the generation of virtual conduction electrons and holes as a result of their exchange interaction with another magnetic atom. Anderson formulated this phenomenon and concluded that superexchange interactions lead to antiferromagnetism Anderson (1950, 1959). Later on, Goodenough and Kanamori formulated semi-empirical rules to determine the sign of the magnetic interaction by the analysis of the symmetry of overlapping cation and anion orbitals Goodenough (1955, 1963); Kanamori (1959).

Assuming that the overlap between the d orbital of a cation M^{m+} and p orbital of an anion X^{2-} is ϵ, Anderson showed that the one electron Wannier functions for the cation at the position n can be written as:

$$|f_n\rangle \cong |\psi_d(M_n^{m+})\rangle - \epsilon\,|\psi_p(X^{2-})\rangle$$

Choosing the axes as presented in Fig.2.10, the effective transfer integral $b_{i,j}$ is:

$$b_{i,j} = \langle f_i\,|V|\,f_j\rangle \approx \epsilon^2 T$$

where T is the kinetic energy of the unpaired electrons, and V the electron-cores potential energy. This transfer integral represents the correlation of the virtual hopping of the electron between ligands with the average repulsive Coulomb interaction U between electrons on the same complex Anderson (1959). Three different couplings must be discussed Anderson (1959); Goodenough (1963):

Coupling between two half filled d orbitals In this case Anderson showed that the superexchange comes from a second order perturbation development and deduced that the cation-cation contribution is given by:

$$J_{i,j} = -\frac{2b_{i,j}^2}{U}$$

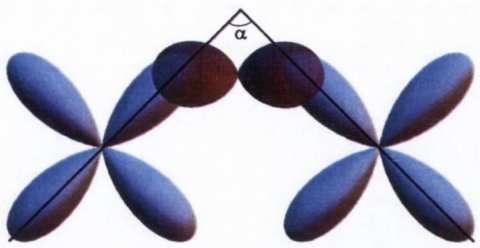

Figure 2.10: Geometry of the cation-anion-cation bond in the general case.

This contribution is always antiferromagnetic.

Coupling between a half filled and an empty orbital In this case, the direct exchange has to be considered and a third order perturbation interaction and an effective exchange contribution is given by :

$$J_{i,j} = +\frac{2b_{i,j}^2 J_{direct}}{4U^2}$$

This interaction is ferromagnetic and weaker than the previous one.

Coupling between a half full and a full orbital This case is similar to the previous one if we consider holes instead of electrons. It leads to the same ferromagnetic interaction.

2.3.1.3 Goodenough-Kanamori rules

Determining the sign and the value of the exchange interaction is difficult because:

- All the orbitals (cation t_{2g}, e_g and ligand p_σ, p_π) and their symmetry must be considered
- the strength of the superexchange depends strongly on the bond angle

Two situations have been described qualitatively, the 180° case when the cations and ligands are aligned Goodenough (1955), and the 90° case Kanamori (1959). From these two cases, the Goodenough-Kanamori rules[1] have been formulated and extended for intermediate bond angles Goodenough (1963):

1. If two lobes of the magnetic cations are aligned and if the overlapping is significant, the exchange interaction is antiferromagnetic

[1] In the literature these are often also called Goodenough-Kanamori-Anderson (GKA) rules.

2. If the orbitals are in contact, but the overlapping is small (especially if it is null by symmetry), the exchange interaction is ferromagnetic

In the case of our structure, the cations in the octahedral interstices share an edge. The overlapping of the orbital is represented in Fig.2.11. The magnetic interactions for $Cr^{3+} - Cr^{3+}$ in the spinel structure are, following the Goodenough-Kanomori rules ferromagnetic and they are very sensitive to the anion-anion separation.

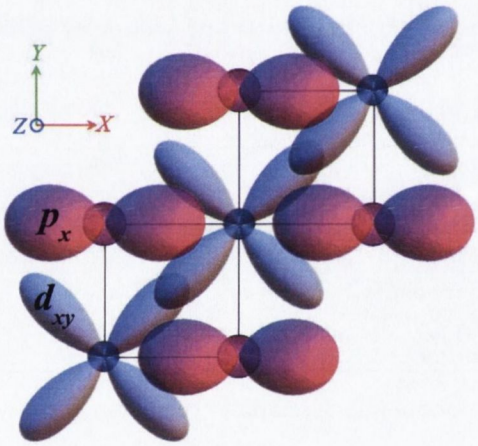

Figure 2.11: Orientation of the cation d_{xy} and anion p_x orbitals in the spinel structure.

2.3.2 Carrier-mediated magnetic interaction

All the exchange mechanisms described above have involved electrons that are contained within the cores of the atoms in solids. However, there are materials in which magnetism arises from conduction electrons. We will present three cases of carrier-mediated ferromagnetic interaction that may explain the ordering in magnetic semiconductors (MS):

2.3.2.1 Double exchange

The double exchange interaction can be interpreted as an extension of the ferromagnetic superexchange[1]. The fundamental difference between the two mechanisms is that in the superexchange, the ferro- or antiferro-magnetic alignment occurs between two cations with the same

[1]In ferromagnetic superexchange, the kinetic energy saved corresponds to a virtual hopping of the electron in an excited state, in the double exchange the kinetic energy saved corresponds to a gain in electron bandwidth.

or a different oxidation state, whereas in the double exchange, one of the two magnetic cations possess one additional electron. The term double exchange was introduced by Zener in an effort to explain the coexistence of conductivity and ferromagnetism in $(La_{1-x}Ca_x)(Mn^{3+}_{1-x}Mn^{4+}_x)O_3$ compounds[1] Zener (1951). It corresponds to two simultaneous electron transfers as represented on Fig.2.12. Anderson and Hasegawa analysed the mechanism of double exchange in the simple

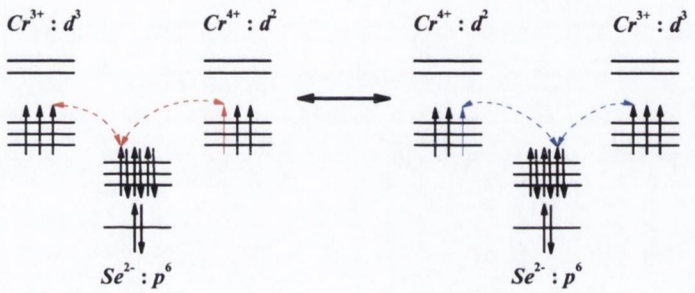

Figure 2.12: Representation of the double exchange mechanism between Cr^{3+} and Cr^{4+} with an intermediate Se^{2-} anion. The ferromagnetic state is stabilised because the p orbitals of Se^{2-} are full.

case of two magnetic ions with a spin S separated by a non magnetic anion X Anderson & Hasegawa (1955). They showed that if the intra-atomic exchange J is much greater than the transfer integral b, the lowest energy level is:

$$E \cong -JS \pm b\cos\left(\frac{\theta}{2}\right)$$

where θ is the angle between the cations' spins. For the case $\theta = 0$, the ferromagnetic ground state is favoured. De Gennes tried to generalise this result for the case of an arbitrary number of magnetic atoms and came to the conclusion that canted phases are stabilised DeGennes (1960). In the case of the double exchange, two differences are apparent compared to the other exchange interactions:

- it is linear in spin, instead of quadratic
- it involves $\theta/2$ instead of θ

Therefore, it is not possible to describe it in the form $-J\mathbf{S}_i \cdot \mathbf{S}_j$ and integrate it into the Heisenberg Hamiltonian.

[1]The end members of the solid solution are insulating and antiferomagnetic, the magnetic structure is described by superexchange.

2.3.2.2 $c-l$ model

The $c-l$ model was first introduced by Vonsovskii and Zener, it describes the coupling of electrons in the conduction band (c) with the lattice of localised magnetic moment (l). This exchange interaction is responsible for a spin density of free electrons at the site occupied by magnetic ions. It is often used as a starting point in the description of the properties of FMS. The general Hamiltonian is given by :

$$\mathcal{H} = \mathcal{H}_{\text{Heis}} + \mathcal{H}_e + \mathcal{H}_{c-l}$$

where the first term $\mathcal{H}_{\text{Heis}}$, is the Heisenberg Hamiltonian for the localised electrons. The second term $\mathcal{H}_e$ describes the conduction electrons, and the Hamiltonian $\mathcal{H}_{c-l}$ describes the exchange between the conduction electrons and the spins of magnetic ions. A more detailed explanation of the $c-l$ model can be found in Nagaev (1983).

2.3.2.3 RKKY interactions

Ruderman & Kittel originally described the interaction between two nuclear spins Ruderman & Kittel (1954), and later applied their model to the case of two magnetic moments Kasuya (1956); Yosida (1957). The interaction is treated as a second order perturbation of the $c-l$ model and is an indirect exchange between two spin impurities via an intervening electron gas. The electron gas responds to the first spin by spin density oscillation, whose period is set by the Fermi wave vector k_{F}. A second spin, at a distance r from the first, couples to the spin density wave. For a 3-dimensional free electron gas the asymptotic behaviour of the exchange integral ($k_{\text{F}} r \gg 1$) is given by :

$$J^{\text{3D}}_{\text{RKKY}}(r) = -\frac{1}{\pi} J^2 n_0(\epsilon_{\text{F}}) k_{\text{F}}^3 \frac{\cos(2k_{\text{F}} r)}{(2k_{\text{F}} r)^3}$$

Characteristic features of the RKKY interaction are its long range and oscillating sign. The effective exchange is quadratic in the intra-atomic coupling and thus does not depend on the sign of J.

2.3.3 Magnetically ordered chalcochromite spinels

In the case of spinels, the determination of the magnetic ground state is not straightforward due to the complex crystal structure and the coexistence of several exchange interactions.

Néel was the first to propose the magnetic structure of spinel ferrites and introduced the concept of ferrimagnetism Néel (1948). A review of the competing magnetic interactions in

oxyspinels can be found in Goodenough (1963). In the case of the chalcochromite spinel, we have shown that only one magnetic cation occupies the B sites, a diamagnetic cation occupies A sites, and the anion being X^{2-}. We will first discuss the magnetic exchange interaction in chalcochromite spinels described by the ionic model, in which the magnetic moments are considered to be localised. Let us consider a portion of a normal spinel as represented in Fig.2.13. Apart from the direct exchange J_0 interaction between two Cr atoms, we can distinguish several paths of magnetic interaction through superexchange :

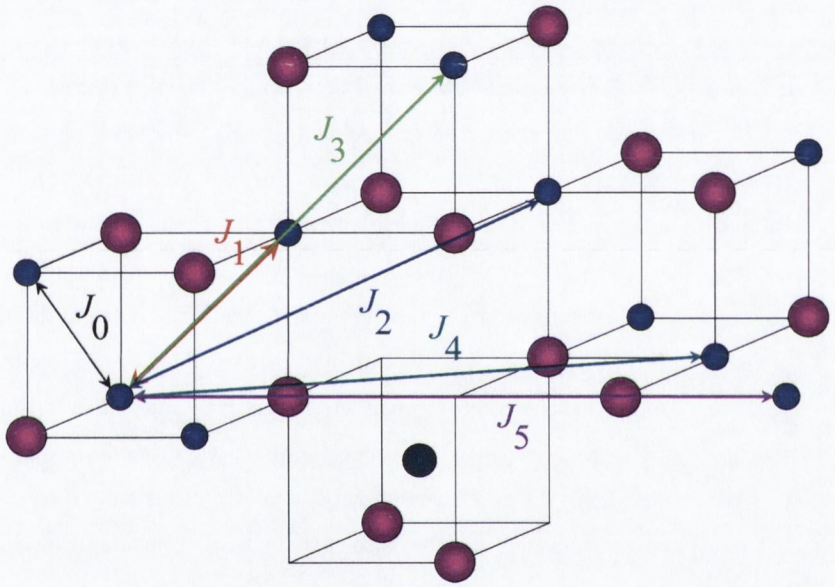

Figure 2.13: Different nearest neighbour magnetic interactions in the spinel structure.

- Nearest neighbour interaction J_1 following the path $Cr - X - Cr$ (red arrow).
- Second nearest neighbour interaction J_2 following paths $Cr - X - X - Cr$ and $Cr - X - A - X - Cr$ (blue arrow).
- Third nearest neighbour interaction J_3 following paths $Cr - X - X - Cr$ and $Cr - X - A - X - Cr$ (green arrow).
- Fourth nearest neighbour interaction J_4 following the path $Cr - X - A - X - Cr$ (dark cyan arrow).

- Fifth nearest neighbour interaction J_5 following paths $Cr - X - X - Cr$ and $Cr - X - A - X - Cr$ (violet arrow)

Following the rules described in the previous paragraph on the sign of the superexchange, J_1 and J_4 will be ferromagnetic, J_3 and J_5 antiferromagnetic, and the sign of J_2 is uncertain Dwight & Menyuk (1968). The relative strength of the exchange constants depends on the cation-cation and cation-anion distances, bond angles, and the degree of the ligand covalency. It has been shown that the ferromagnetic nearest neighbour exchange interaction increases as the anion is changed from $O^{2-} \rightarrow S^{2-} \rightarrow Se^{2-}$ Huang & Orbach (1968). This discussion is still valid even in the case of other exchange interaction mechanisms due to the polarisation of free carriers. The appearance of delocalised moments modifies the total magnetic interaction. The ground state is therefore determined by the magnitude of the different interactions. Calculation of the exchange integrals is difficult, but due to the wide range of materials available in this family, it is possible to extract approximate values from magnetisation measurements and to speculate some general rules to determine the magnetic ground state Lotgering (1971). The first report describing the exchange interactions in $CdCr_2Se_4$ and $HgCr_2Se_4$ showed that they had a ferromagnetic ground state but also that the antiferromagnetic interactions of the distant neighbours contribute to the establishment of the ground state Baltzer *et al.* (1966). Nevertheless their analysis cannot explain why $ZnCr_2Se_4$ is an antiferromagnet with a spiral ground state. An improved model was then developed, it included new exchange paths to establish the magnetic phase diagram for chalcogenide spinels Dwight & Menyuk (1967). Based on the analysis of the distant neighbours interactions, a simplified proposition was formulated based on the assumption that spinels can have a lower symmetry than expected Grimes & Isaac (1977). According to this model, biquadratic exchange interactions arise due to the Cr^{3+} displacement at low temperature which dominates the bilinear distant neighbours exchange interactions via the diamagnetic A cations. For systems with enough free carriers, it has been shown that the magnetic ground state can be determined from the analysis of the competition between direct intra-atomic exchange interactions and RKKY interactions Warczewski *et al.* (2002). The theoretical values of the exchange integrals have recently been calculated by *ab initio* calculations using the local density approximation (LDA) Saha-Dasgupta *et al.* (2007); Yaresko & Antonov (2007); Yaresko (2007). The calculated magnetic ground state is in agreement with qualitative analysis of the superexchange interactions in accordance with the Goodenough-Kanamori rules.

In the context of our study, we are interested in the ferromagnetic ground state, we will therefore focus on one particular family of chalcospinels, the selenochromates, which represent the richest population of magnetic semiconductors.

2.4 The selenochromate family

In the context of the chemical sorting map, it would be interesting to find some chemical parameter which can be used to establish a sorting map between magnetic and electrical properties. This diagram could be used as a guideline to select useful materials to study. The first diagram of this sort for normal spinels was proposed using the tetrahedral and octahedral ionic packing factor Satoh *et al.* (1974). In this diagram, a clear demarcation between insulators, semiconductors, and metals is established. The electrical properties seem to be strongly dependant on the ionic packing factor of the tetrahedral site. The border between ferromagnetism and antiferromagnetism is not as obvious. An improved version of this mapping used the ratio of the ionic radii for the two different sites Krok-Kowalski *et al.* (2001). In this diagram the ratio r_o/r_a is plotted against r_t/r_a where r_o, r_t, and r_a are the octahedral, tetrahedral, and anion ionic radii respectively. We have successfully reproduced such a diagram for selected compounds in Fig.2.14. The frontier between ferromagnetic and antiferromagnetic interactions extends across the diagram showing that both cations take part in the magnetic ground state. Compounds close to the border present complex magnetic structures such as spiral antiferromagnetism.

From this phase diagram, three selenochromates stand out for their properties in the context of our study: $CdCr_2Se_4$, $HgCr_2Se_4$, and $CuCr_2Se_4$. A particularly interesting case is the solid solution of $CuCr_2Se_4$ with the halogen Br since the change in conduction type and magnetic ground state was predicted by this model. These three compounds have been studied extensively in the 70's and a literature review for each of them is presented in detail in the subsequent sections. A summary of the interesting physico-chemical properties is presented in Table 2.4.

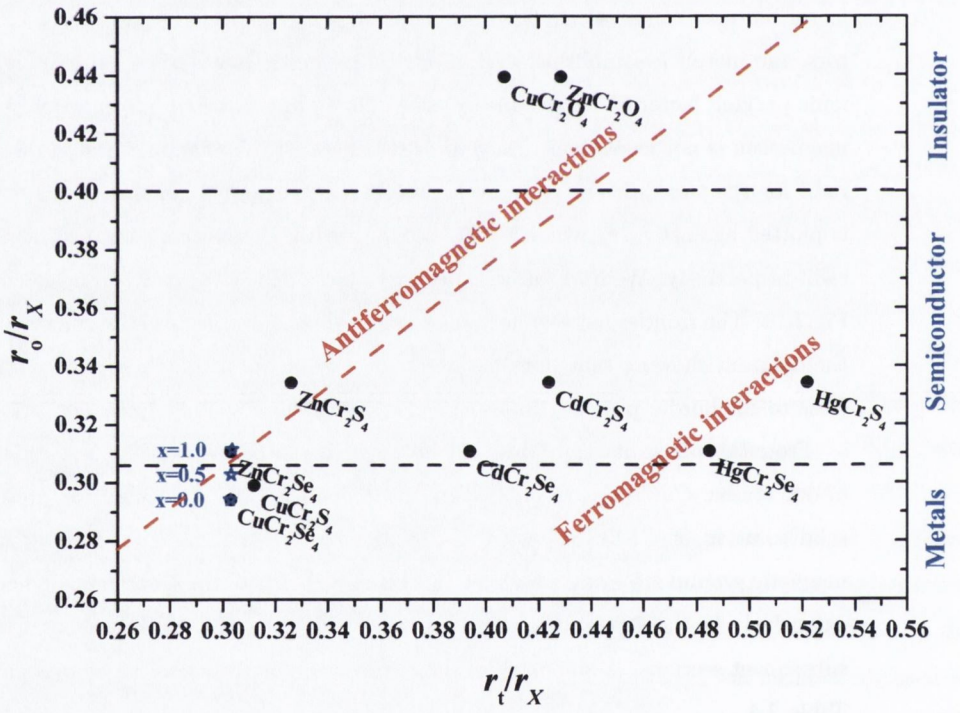

Figure 2.14: Diagram showing the correlation of the ionic radii ratio with the electrical and magnetic properties. The inset shows the evolution of the ratio for the solid solution $CuCr_2Se_4 - CuCr_2Se_3Br$. Adapted from Krok-Kowalski *et al.* (2001)

2.4.1 $CdCr_2Se_4$

The first report in the literature of $CdCr_2Se_4$ showed that this spinel behaves like a classical semiconductor in the paramagnetic and ferromagnetic states Baltzer *et al.* (1965). For a general review see Kalinnikov *et al.* (2003).

2.4.1.1 Synthesis

Several methods have been used to prepare $CdCr_2Se_4$ in polycrystalline, single crystal or thin film form.

The polycrystalline samples were prepared by solid state reaction. The earlier studies were dedicated to the study of the main physical properties Baltzer *et al.* (1965); Lehmann & Robbins (1966), while the later studies focused more on the establishment of the phase diagram Barraclough & Meyer (1973); Kiyosawa & Masumoto (1977) and the effect of non-stoichiometry Tret'yakov *et al.* (1972). Thin films of chalcogenide spinel were deposited by direct evaporation of the elements Berzhansky *et al.* (1989); Lubecka *et al.* (1989), by sputtering Sikora *et al.* (2004) and by molecular beam epitaxy Park *et al.* (2002). The single crystals have been prepared by different methods :

- Liquid transport Eastman & Shafer (1967); Philisborn (1967, 1969)
- Vapour-liquid transport Neida & Shick (1969)
- Flux growth using various salts Shabunina *et al.* (1981) and high temperature solution growth using $CrCl_3$ and $CdCl_2$ Berger & Pinch (1967); Harbeke & Pinch (1966); Larson & Sleight (1968); Wold & Rulff (1973)
- Vapour transport using $CrCl_3$, and $CdCl_2$ as transport agents Kolowos *et al.* (1974); Wehmeier (1969)
- Travelling heater method Hoschl *et al.* (1981); Okuda *et al.* (1980)

Solid solutions based on $CdCr_2Se_4$ have been studied with different cations substituting either at Cd or Cr sites, certain cases have not been fully resolved. Ag seems to incorporate into the lattice substituting at Cd sites with a solubility limit exceeding 10 at. %. The insertion of a cation with a higher oxidation number such as Ga or In leads to the possibility of substitution of both cations; the solubility limit in this case being much lower (about 3 at. % for In) Bel'skii *et al.* (1985); Merkulov *et al.* (1982). Studies showed that Ga substituted Cr only on the B site

Kozlowska *et al.* (2001) and for more than 5 % Ga concentration, a rhombohedral distortion in the crystal structure is observed Sagredo & de Chalbaud (2004).

2.4.1.2 Physical properties

Many physical properties of this system depend on the stoichiometry of the compound, the information given in the next paragraph is based, where possible, on measurements performed on single crystals.

$CdCr_2Se_4$ is a ferromagnet with a saturation moment close to $6\mu_B$/mol and a Curie temperature of 130 K Pinch & Berger (1968). The magnetic structure is assumed to be a collinear ferromagnet, with all the moment localised on the Cr^{3+} ions. The addition of Ag does not drastically change the magnetic properties, but an increase in the Curie temperature is observed Merkulov *et al.* (1982). In the case of In doping in thin films, the magnetic properties have been reported to exhibit a spin-glass behaviour for higher doping content Lubecka *et al.* (1990). Similar behaviour has been reported in polycrystalline samples Shabunina *et al.* (2003).

Undoped $CdCr_2Se_4$ is observed to be a p-type semiconductor with a room temperature resistivity of around $10^6 - 10^7 \Omega \cdot$ cm Hoschl *et al.* (1981). Small percentage substitution (on the order of 1 at. %) of monovalent elements, such as Ag for the Cd, increase the p-type conductivity, while similar substitutions of trivalent elements, such as In for the Cd, render the material n-type Lehmann (1967). The galvanomagnetic properties, however, are drastically different for the two different types. n-type $CdCr_2Se_4$ shows a sharp resistivity jump and a giant magnetoresistance near T_C, whereas p-type samples show no marked anomaly at T_C. The conductivity of Ag doped samples increases with doping and present a mobility of around 20 $\mathrm{cm}^2/\mathrm{V} \cdot \mathrm{s}$. The magnetoresistance is negative below the Curie temperature and becomes positive and quadratic at higher temperature Lehmann (1967). The temperature dependence of the resistivity in n-type samples is becomes increasingly complex with decreasing temperature. It increases exponentially initially and then drops suddenly by four orders of magnitude around the Curie temperature Aminov *et al.* (1980). The mobility in these samples is much lower ($\approx 0.1 \mathrm{cm}^2/\mathrm{V} \cdot \mathrm{s}$). A maximum of the magnetoresistance is observed at this inflection point of the resistivity. This behaviour, also observed in Gd-doped EuO, led to the development of several models Bongers *et al.* (1969); Kogan & Auslander (1988); Nagaev (1983). In contrast to the other well known FMS, $CdCr_2Se_4$ is the first Mott magnetic extrinsic semiconductor in which the $3d$ electrons are responsible for both transport and magnetism Héritier (1983).

Although the resistivity behaviour is striking in n-type FMS, the shift of the band edge has attracted more attention. The optical absorption edge of $CdCr_2Se_4$ has been investigated in transmission Harbeke & Pinch (1966) and in diffuse reflectance Busch *et al.* (1966). The room temperature absorption edge is found to be 1.35 eV, a small blue shift of 0.03 eV is observed upon lowering the temperature to 190 K. Lowering the temperature further gives rise to an opposite phenomenon, a red shift, in the absorption edge which reaches a value of 1.16 eV. A red shift is also observed upon applying an external magnetic field, the effect was greatest in the vicinity of the Curie point. The red shift is expected for holes moving over non-magnetic atoms Haas (1968); Nagaev (1983), the $c-l$ exchange interaction causes the conduction band to split below the Curie temperature, and therefore lower the main energy gap. The blue shift is explained with the same model proposed by Nagaev (1983) but the interband exchange is the dominant factor. This compound shows a large Faraday rotation, with a maximum of -9200 deg/cm at 1.17 μm just near the absorption edge Bongers & Zanmarchi (1968). Raman spectroscopy of $CdCr_2Se_4$ has been carried out Koshizuka *et al.* (1977), and two extra lines appeared below T_C due to scattering of light by magnons Almeida & Miranda (1978). Another peculiar property observed in FMS is photoferromagnetism, where the ferromagnetic properties are changed by the illumination of a sample. This phenomenon has been observed in undoped Nagaev (1983) and Ga-doped $CdCr_2Se_4$ [1] Lems *et al.* (1968).

2.4.1.3 Electronic structure

Goodenough was the first to qualitatively describe the band structure of $CdCr_2Se_4$ Goodenough (1969). In an attempt to interpret the observed blue and red shift of the main energy gap as a function of temperature, he concluded that the Cr^{3+} level was in the valence band and the excited Cr^{2+} state was just below the conduction band. Electronic band structure calculations have also been performed Kambara *et al.* (1980). They used extended Hückel method and found that in the case of $CdCr_2Se_4$ the highest valence band is formed mainly from the $4p$ orbitals of Se and that the lowest conduction band consists of the $4s$ orbitals of Cr strongly hybridised with the $5s$ of Cd. The main gap is found to be direct with a value of 1.91 eV and the crystal field splitting energy is evaluated to be about 0.6 eV. In the ferromagnetic state, the lowest conduction band is lowered and the features of the valence band and the d band do not change. They show that the fundamental band-to-band transition splits into two components:

[1] High purity crystals are required to observe photoferromagnetism, samples contaminated with impurities show no effect.

a red shift component for the majority spin and a weakly blue shift component for the minority spin. A further refinement of this calculation was done using discrete variational X_α method Oguchi *et al.* (1980). Results obtained by this method give similar conclusions with a slightly different value for the energy gap and width of the valence and conduction band. Photoemission and photoluminescence studies have been carried out on the system Miniscalco *et al.* (1982); Yao *et al.* (1981) and the experiments agree well with the calculations. To investigate and compare with the hybridisation of the $p-d$ orbitals described in the calculated band structure, resonant photoemission has been measured and agrees well with the calculations Taniguchi *et al.* (1989). First-principles calculations have been performed using full-potential linearised augmented plane wave method in the paramagnetic and ferromagnetic states to compare the density of states obtained by photoemission Continenza *et al.* (1994). To incorporate crystal orbit Hamilton population analysis the electronic structure of $CdCr_2Se_4$ was calculated using the linearised muffin-tin orbital method in the atomic-sphere-approximation Shanthi *et al.* (2000). The main conclusion was that the calculated exchange splitting is larger than the crystal field splitting leading to a strong spin polarisation of the bands. Similar results were obtained using ultra-soft pseudopotential method to explain the observed spin polarisation of the minority spin Kioseoglou *et al.* (2004).

2.4.1.4 Devices and applications

$CdCr_2Se_4$ has been considered one of the most promising CMS for applications. It was first considered for implementation in monolithic microwave integrated circuits where the magnetic and semiconducting properties would be used separately Wen *et al.* (1968). A number of possibilities have been discussed and are summarised in Wojtowicz (1969) The latest fundamental and interesting result obtained using this material has been the successful injection of spin-polarised electrons from a n-type FMS into a $GaAs$ based heterostructure device Kioseoglou *et al.* (2004).

2.4.2 $HgCr_2Se_4$

$HgCr_2Se_4$ was discovered at the same time as $CdCr_2Se_4$ Baltzer *et al.* (1965). In spite of its small band gap and high mobility, this compound has been studied very little. The properties are more complex and depend strongly on the Hg and Se vacancies.

2.4.2.1 Synthesis

The phase diagram and the preparation of polycrystalline $HgCr_2Se_4$ are not well documented, but the preparation of single crystals has been studied in detail Selmi *et al.* (1986). The main method used to prepare single crystals is chemical vapour transport. The first report used various transport agents such as $HgCl_2$, $CrCl_3$, Br_2, Cl_2 and CrO_2Cl_2 Lehmann & Emmenegger (1969). They observed that transport with Br_2 and $CrCl_3$ was inefficient and Cl_2 is not suitable for the growth of this compound. Nevertheless, high quality undoped Ag- and In-doped single crystals of millimetre size were obtained with a higher concentration of $CrCl_3$ Takahashi (1969). In substitutes Cr and the solubility limit is found to be around 20 mol% in polycrystalline forms and 5 mol% in the single crystals Takahashi *et al.* (1971). A complete thermodynamic and experimental study of the chemical transport with $AlCl_3$ was proposed and showed a high yield in the growth of bulk crystals Gibart (1978).

High temperature solution growth is another method suitable for the growth of $HgCr_2Se_4$. Several fluxes have been attempted, such as Se, $PbCl_2$, KCl, but the difficulty of extracting the crystals from the flux without damaging them is a major drawback. The use of $CdCl_2$ offers a solution to this technical problem, but a significant amount (5% in weight) of Cd is doped into the crystals Zhukov *et al.* (2006).

Thin films of $HgCr_2Se_4$ have been prepared by molecular beam epitaxy Masumoto *et al.* (1983).

2.4.2.2 Physical properties

The saturation magnetic moment of polycrystalline $HgCr_2Se_4$ has been reported to be $5.4\mu_B$ with a Curie temperature of 109 K. It possesses the same magnetic structure as $CdCr_2Se_4$ Baltzer *et al.* (1965). The incorporation of In in the lattice lowers the Curie temperature Takahashi *et al.* (1971)

Goldstein *et al.* studied the transport properties of $HgCr_2Se_4$ annealed in Se or Hg vapour Goldstein *et al.* (1978). They observed that Hg annealed samples are degenerate n-type semiconductors with a high mobility whereas selenium annealed samples are p-type at room temperature and become n-type at 4.2 K. They explained these features assuming a two-carrier conduction model. The map of the carrier density as a function of Hg and Se partial pressures has been investigated, and it shows the transition from n- to p-type conduction. The observation of CMR in n-type samples led to the development of several theories to explain this behaviour Kostylevb *et al.* (1990); Selmi *et al.* (1985); Solin *et al.* (2008); it is believed that a strong

electron-magnon interaction occurs. Recently Balaev *et al.* observed quantum oscillations in Hg annealed samples in both magnetisation and magnetoresistance Balaev *et al.* (1998). The absorption edge has been studied both in transmission and reflection and a similar behaviour to that of $CdCr_2Se_4$ is observed, namely, a red shift of the absorption edge upon lowering the temperature or in the presence of an applied field Selmi *et al.* (1986). The observed shift is an order of magnitude greater in the mercury compound. Raman spectroscopy measurements on $HgCr_2Se_4$ showed no additional lines below the magnetic ordering temperature Iliev *et al.* (1978).

2.4.2.3 Electronic structure

The electronic structure of $HgCr_2Se_4$ was calculated using the discrete variational X_α method Oguchi *et al.* (1981). They concluded that among the chalcochromite family it is the most covalent member based on the Mullinken charge population and the fact that a spin polarisation of the minority spin, opposite in sign to the moment localised on the Cr ions, appears on the Se $4p$. A model of the band structure based on the $c-l$ model was proposed to explain the anomalous transport properties observed in degenerate $HgCr_2Se_4$ Auslender & Bebenin (1989).

2.4.2.4 Device applications

Spin injection from the FMS to a non magnetic semiconductor has been observed in a diode heterostructure Osipov *et al.* (1998); Viglin *et al.* (1999).

2.4.3 $CuCr_2Se_4$ and its halogen derivative

The copper chalcochromites are anomalies among both the chalcochromites and the larger population of known chalcospinels. The phases $CuCr_2X_4$ with $X = S, Se, Te$ are all reported to be simultaneously metallic and ferromagnetic with a relatively high Curie temperature compared to the other family of compounds described earlier.

2.4.3.1 Synthesis

Hahn *et al.* first prepared polycrystalline samples by solid state reaction from the elements in 1956 and indexed the powder diffraction pattern on the basis of a face-centred cubic lattice with the spinel structure Hahn *et al.* (1956). Lotgering prepared samples by a similar method and measured ferromagnetism with a Curie temperature above room temperature and metallic conduction in all members of the $CuCr_2X_4$ family Lotgering (1964a). The phase diagram

of $CuCr_2Se_4$ was established by Chernitsyna *et al.* (1977). Solid state reaction has been used to prepare solid solutions with halogens such as Br and Cl from $CuBr$ and $CuCl$. The halogen anion substitutes at the Se site, the solubility limit being of the order of 25 mol%. The end member of the chloride solid solution was found to be highly hygroscopic Robbins *et al.* (1968). The stability of the halogeno-chalcogenide compounds in air has been a subject of controversy , the physico-chemical properties obtained varying widely depending on the preparation conditions Lotgering & van Stapele (1968); Miyatani *et al.* (1971); Robbins *et al.* (1968). A careful chemical analysis showed that the general formula for the bromine doped compound is better described by $Cu_yCr_2Se_{4-z}Br_x$ Pink *et al.* (1974a). They concluded that the Cu-rich spinel is unstable in air and decomposes through the reaction:

$$Cu_yCr_2Se_{4-z}Br_x + \frac{n}{2}O_2 \longrightarrow Cu_{y-n}Cr_2Se_{4-z}Br_x + nCuO$$

A method to obtain Cu-deficient spinel is to start from the cupric bromide $CuBr_2$ instead of the cuprous bromide $CuBr$. They also showed that spinels with x up to 2 could be stabilised in the form of single crystals from $CuBr$ flux. Another solid solution worthy of mention is the system $CuCr_2Se_4 - CuCrSe_2$, where a miscibility region has been found and the compound $Cu_{1+x}Cr_2Se_4$ is formed with x up to 15 mol% Babitsyna *et al.* (1980). Another way to insert Cu in the lattice is by electrochemical intercalation process Schollhorn & Payer (1986). Polycrystalline crystals of $CuCr_2Se_4$ have been obtained in a glass matrix using As_2Se_3 as the glass matrix Tver'yanovich *et al.* (2005).

There have been reports of the preparation of $CuCr_2Se_4$ single crystals by:

- vapour transport with I_2, $CuBr_2$, $CuBr$, $CuCl$, $CrCl_3$, $SeBr_4$ as transport agent Lotgering (1964a); Matsumoto & Nakatani (1976); Miyatani *et al.* (1968, 1971); Nakatani *et al.* (1977); Neulinger (2006); Radautsan (1983)

- flux growth from various salts $CdCl_2$, $NaCl$, $CaCl_2$, $PbCl_2$ and high temperature solution from $CrCl_3$, $CuBr$, and $CuBr_2$ Babitsyna *et al.* (1978); Chernitsyna *et al.* (1978); Pink *et al.* (1974a); Sleight & Jarrett (1967)

The main drawback of the above methods is the doping of halogens into the lattice. Although it has been reported that iodine does not substitute Se in $CuCr_2Se_4$, there is some evidence that a few at. % is diluted in the lattice Neulinger (2006).

Thin films of $CuCr_2Se_4$ have been prepared by thermal evaporation from individual elemental sources Berzhansky *et al.* (1989); Yamanaka *et al.* (1971) and by pulsed laser deposition Bettinger *et al.* (2008); Kim *et al.* (2008). The quality of the films is rather poor (polycrystalline, with the presence of a second phase) and subsequent annealing of the film is required to obtain some of the desired phase.

Nanoparticles of $CuCr_2Se_4$ have been prepared from solution using different solvents. The first report used the decomposition of metal stearates at 330°C Mitchell & Morgan (1974). Solvothermal method has been used to prepare sub-micron sized particles with a maximum size of 200 nm Ramesha & Seshadri (2004). A microwave assisted polyol decomposition was used to prepare nanocrystalline powder with an average particle size of 35 nm Kim *et al.* (2006); Rusnak *et al.* (2006). Recently, a method based on the decomposition of metal acetylacetonate in a boiling solvent, the choice of the solvent controlling the size of the particles from 15 to 30 nm Wang *et al.* (2007).

2.4.3.2 Physical properties

This material has attracted the material science and magnetism communities because of its high T_C and the tunability of its transport properties by doping with halogens. In fact, it has been reported that substitution of Se by Br changes the conduction from metallic to semiconducting Robbins *et al.* (1968).

The magnetic properties of $CuCr_2Se_4$ have been studied by magnetometry and neutron diffraction. The saturation magnetic moment is found to vary from 4.7 μ_B/mol Robbins *et al.* (1967) to 5.33 μ_B/mol Neulinger (2006). The Curie temperature is not well defined, several values can be found in the literature, ranging from 460 K Lotgering (1964a) to 430 K Nakatani *et al.* (1977) [1]. The magnetic structure was determined by neutron diffraction and the powder study assigned the value of 3 μ_B/Cr on the Cr ion Colominas (1967); Robbins *et al.* (1967). A more recent study proposed that the magnetic moment on the Cr ions is 2.8 μ_B/Cr, assuming a magnetic form factor for Cr^{3+}, and concluding that the calculated moment results from a mixture of Cr^{3+} and Cr^{4+} Rodic *et al.* (1998). A polarised neutron diffraction study showed that the magnetic moment on the Cr ions is 2.6 μ_B/Cr with a very small moment (-0.07 μ_B/Cu) on the Cu ion Yamashita *et al.* (1979a). The magnetic properties of the solid solution with Br and Cl have been extensively studied, and the diversity of the results is certainly due to

[1] The discrepancy of data obtained from single crystals grown with I_2 as transport agent might be due to the insertion of iodine in the lattice.

the sensitivity of the preparation conditions. Nevertheless a general trend can be pictured: the insertion of Br in the lattice increases the saturation magnetic moment to a value close to 6 μ_B/mol for the end member compound, and decreases the Curie temperature Lotgering & van Stapele (1968); Miyatani *et al.* (1968, 1971); Robbins *et al.* (1968); Sleight & Jarrett (1967); Yamashita *et al.* (1979b). In the case of Cl doping two trends are observed in the literature:

- in the first case the Curie temperature does not change consistently with the insertion of Cl and the saturation moment does not increase Miyatani *et al.* (1971).
- in the second case the same trend as seen with Br insertion is observed Robbins *et al.* (1968); Yamashita *et al.* (1979b)

A magnetic Compton profile study showed that there are three components contributing to the magnetisation of undoped, Cl, and Br doped samples: the Cr $3d$, the Cu $3d$, and the Se $4s$ with the Cu $3d$, and the Se $4s$ moments aligned antiparallel to the Cr $3d$ moment Deb *et al.* (2007). A polarised neutron diffraction study on $CuCr_2Se_{3.5}Br_{0.5}$ showed an increase in the magnetic moment on the Cr to 2.8 μ_B/Cr while the moment on the copper had the same value as in the undoped crystal Yamagushi *et al.* (1980). The magnetic properties of the $Cu_{1+x}Cr_2Se_4$ have been studied and similarly a decrease of Curie temperature was observed Babitsyna *et al.* (1980); Schollhorn & Payer (1986). A powder neutron diffraction study showed the insertion of Cu ions in vacant tetrahedral sites in the spinel structure Payer *et al.* (1992, 1993). The domain structure in $CuCr_2Se_4$ single crystals have been studied by the Bitter technique showing stripe domain structures Szymczak *et al.* (1990). Similar patterns were observed in Br-doped samples using photoemission electron microscopy Neulinger (2006).

The electrical transport properties have been discussed and the undoped sample is found to be a p-type metal with a carrier concentration of 10^{20}cm^{-3} Robbins *et al.* (1967); Tsurkan *et al.* (1984). Anomalous Hall effect above 140 K and negative magnetoresistance were observed as expected for a metallic ferromagnet. The insertion of Br in the lattice decreases the conductivity and it has been reported that at a certain concentration the system becomes semiconducting Robbins *et al.* (1968) but the threshold value of the Br concentration to pass from metallic to semiconducting is not well defined Sleight & Jarrett (1967). It was suggested that conduction due to surface contamination could explain the origin of the observed behaviour Miyatani *et al.* (1971). Semiconducting behaviour is observed in samples with excess of Cu and with $x_{Br} > 1$ Radautsan *et al.* (1983), and longitudinal magnetoresistance of the order of 4% in similar crystals was measured Golant *et al.* (1978). The fact that the doping of $CuCr_2Se_4$ decreases

the resistivity by orders of magnitude without destroying the ferromagnetic interaction was used in recent studies to discuss the origin of the anomalous Hall effect Lee *et al.* (2004). They measured Hall effect in a series of compounds and found that all compositions are metallic, or degenerate semiconductors. Nevertheless, they verified the prediction of the anomalous-velocity theories for ferromagnets and concluded that fully polarised spin Hall currents are generated at low temperature in ferromagnets by the application of an electric field.

Studies on the magneto-optical properties of these compounds have been motivated by the room temperature ferromagnetism and a steep plasma edge in $CuCr_2Se_4$. They were found to have the largest room temperature Kerr effect Brandle *et al.* (1990, 1991).

2.4.3.3 Electronic structure

The electronic structure of $CuCr_2Se_4$ has been the centre of a controversy where two principal models have been competing to explain the electrical and magnetic properties of the compound. As described before, the copper selenochromite does not behave in the same fashion as when the cation is strictly divalent (Cd^{2+} and Hg^{2+}), yielding a relatively high Curie temperature, a saturation moment inferior to the expected 6 μ_B/mol and a metallic conduction.

The Lotgering model The author of the original magnetic measurements proposed that the phase comprises of Cu^+ and mixed valent Cr^{3+} and Cr^{4+} ions to explain the magnetic moment of $5\mu_B/mol$ at 5 K Lotgering (1964a,b). In this model, $Cu(I)$ has a nonmagnetic d^{10} configuration and does not contribute to the magnetic moment. The chromium ions configurations are d^3 and d^2 respectively, which contribute a total of five unpaired electrons per formula unit. These five spins are coupled ferromagnetically in the spinel lattice by Zener-de Gennes double exchange mechanism DeGennes (1960). The metallic conduction is due to the contribution of one hole per formula unit coming from the hopping of one electron between the Cr ions. This model was further improved following a suggestion from Haas. It was argued that the hole responsible for metallic conductivity was in the s, p valence band. Insisting on Cu^+ ions, despite the necessary reversal of the metal energy levels compared to the oxide [1], they placed the Cr^{3+} band just below the top of the anion valence band. The chromium (IV), which was so objectionable in the original model, is still included, although in the revised model it appears as variable occupancy in

[1] The second ionisation potential of copper is 20.29 eV, whereas the fourth ionisation potential of chromium is approximately 50 eV, therefore a monovalent copper ion cannot be stable in the presence of Cr^{4+} and it gives up one electron to the Cr^{4+}.

a broadened Cr t_{2g} band and accepts some electron density from the anion p band. The (monovalent) copper $3d$ orbitals are filled and lie far below the top of the valence band Lotgering & Stapele (1968).

The Goodenough model A strong argument to reject the former model is that in the oxyspinel $CuCr_2O_4$, Cu^+ cannot be stabilised in the presence of Cr^{4+}. The second model proposes the formal valency $Cu^{2+}[Cr^{3+}]_2Se_4$ Goodenough (1967, 1969), but the author insisted on the formal valency term. In this model, the copper state should be treated in a more band-like character while somewhat more localised electrons on the Cr can be discussed in an ionic model. The conduction comes from the copper band containing some chalcogen character. Each copper ion contributes one hole to the anti-bonding band just below the Fermi level. The strong covalent character of Cu^{2+} explains the absence of Jahn-Teller distortion in this compound, which is observed in the parent oxide. It was concluded that the ferromagnetism arises from the competition between 90° cation-anion-cation ferromagnetic interaction and antiferromagnetic cation-cation interaction on the Cr lattice. It is expected to find 3 μ_B/Cr. To explain the high Curie temperature and the saturation moment of 5 μ_B/mol, a net-antiparallel delocalised moment, distributed over the copper-chalcogenide band, enhances the ferromagnetic interaction via indirect exchange.

The obvious differences between these two models are:

- The valences of the cations are different and lead to different interactions being responsible for the observed ferromagnetism.
- In one case the conduction is due to hopping of an electron on the magnetic ion and in the other the conduction arises from a mixed band of copper $3d$ and selenium $4p$.

The main difference, from our point of view, is that the Lotgering model describes the compound as completely ionic compared to the Goodenough model which introduces a band model for the tetrahedral cation. A schematic representation of the two proposed models is presented in Fig.2.15. The differences in the electronic structure of the two models are significant and one might think that it should be possible to discriminate between the two models experimentally.

A number of experiments have been performed to determine whether the valency of Cr is mixed or not. The first powder neutron diffraction data obtained on $CuCr_2Se_4$ indicated that

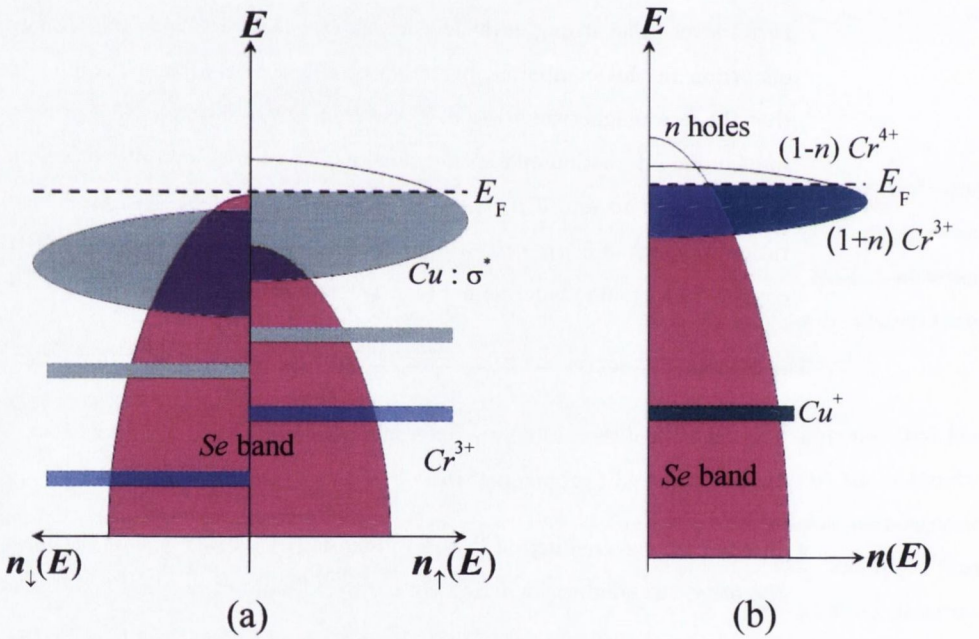

Figure 2.15: Schematic energy diagrams for $CuCr_2Se_4$, based on competing models in the literature. (a) Goodenough Goodenough (1969) (b) Lotgering and van Stapele Lotgering & Stapele (1968)

all Cr are equivalent with a magnetic moment close to 3 μ_B/Cr Colominas (1967); Robbins *et al.* (1967). They considered three different magnetic structures:

- $Cu^{+}Cr^{3+}Cr^{4+}Se_4$ corresponding to Lotgering hypothesis with an average of 2.5 μ_B/Cr for equivalent distribution on the B sites.
- $Cu^{2+}Cr_2^{3+}Se_4$ corresponding to the magnetic structure of the copper chromite oxide with an ionic ferrimagnetic configuration.
- $Cu^{2+}Cr_2^{3+}Se_4$ corresponding to the Goodenough model where 3 μ_B/Cr are expected and no localised moments on the Cu.

The results of Colominas (1967); Robbins *et al.* (1967) strongly support Goodenough's theory. Another powder neutron diffraction study found a magnetic moment on the chromium of the order of 2.8 μ_B/Cr and they concluded that there was a mixed valence +3/+4 of the Cr ions supporting the Lotgering model Rodic *et al.* (1998). A temperature dependant powder neutron diffraction study on $CuCr_2S_4$ showed that both models were valid in different temperature regions Kovtun *et al.* (1979). The observed intensities were well described for the valences $Cu^{+}_{1-n}Cu^{2+}_{n}[Cr^{3+}_{1+n}Cr^{4+}_{1-n}]X_4^{2-}$ with $n = 0.25$ at 4.2 K and with $n = 0$ at $T > 77$K. Similar findings were obtained from polarised neutron diffraction studies on a single crystal with the formal valencies $Cu^{1.07+}[Cr^{3+}_{1.28}Cr^{4+}_{0.72}]Se_4$ Yamashita *et al.* (1979a). Moreover they observed that the magnetic form factor of the Cr ions is closer to the state +1 than +3, indicating that the unpaired electron density is distributed more in the crystals than that for a free Cr^{3+} ion. Magnetometry measurements support the Lotgering hypothesis. By measuring the magnetic susceptibility of different compounds such as $CuCrRhSe_4$ and $CuCrTiS_4$, and analysing the Curie constant, they concluded that the Cr ions should have the valency +3/+4 Lotgering & van Stapele (1967); van Stapele & Lotgering (1970). These results were well supported by the data obtained on single crystals Nakatani *et al.* (1977), however another susceptibility study found that the chromium ions in the paramagnetic phase are in the oxidation states +2 and +3 Rodic *et al.* (1998). Nuclear magnetic resonance spectroscopy presents the same controversy, while some reports suggest that all chromium ions are crystallographically equivalent and trivalent Yokoyama *et al.* (1967), others observed a mixed valence and electron ordering below 60 K which is not completed even at 2 K Kovtun *et al.* (1977, 1978). Cr $2p$ x-ray absorption spectroscopy and magneto-circular dichroism on $CuCr_2Se_4$, solid solution of $Cu(Cr,Ti)_2Se_4$, and halogen-doped $CuCr_2Se_4$ showed that chromium ions are trivalent supporting the model proposed by

Goodenough, however it is pointed out that a small Cr^{4+} contribution cannot be completely ruled out since the spectra of the Cr^{3+} and Cr^{4+} are similar Kimura *et al.* (2001a,b); Liberati *et al.* (2008); Noh *et al.* (2007).

A similar range of experiments have been carried out to investigate the oxidation state of Cu. A study of the conductivity of a solid solution where Cu is introduced in the lattice, such as $M_{1-x}Cu_xCr_2Se_4$, leads to the conclusion that the p-type conductivity is due to Cu^+ even for small concentrations of Cu Lotgering & van Stapele (1967). This argument was rejected since Cu^{2+} can create shallow acceptors Goodenough (1967). Nuclear magnetic resonance on the Cu gives mixed descriptions, some concluding that the copper was monovalent Locher (1967); Locher & van Stapele (1970) while others found it divalent Yokoyama *et al.* (1967) or a mixture of both Cu^{2+} appearing at low temperature Kovtun *et al.* (1977). X-ray spectroscopic measurements assigned the spectra to monovalent copper Balal & Mande (1976); Hollander *et al.* (1974). The magneto-circular dichroism study on the Cu $2p$ shows a signal with opposite polarisation to that of the observed signal on the Cr $2p$. The valency of the copper is discussed and a mixture of monovalent and divalent oxidation states is proposed by Kimura *et al.* (2001a,b); Liberati *et al.* (2008); Noh *et al.* (2007). The analysis of the bond length was used to assess the valency of the copper. The first report concluded that copper is divalent Sleight (1967) but a later analysis came to the opposite conclusion favouring monovalent copper Riedel & Horvarth (1973). It was shown that the observed $Cu - Se$ distance can only be described using the metallic radius of Cu and the covalent radius of Se Rodic *et al.* (1998).

Despite the wide range of experimental techniques used to investigate the electronic structure of $CuCr_2Se_4$, it seems that the controversy over which model best describes the magnetic properties is still ongoing. It is therefore interesting to note that only a few calculations of the electronic structure are available in the literature. A summary of the structural and magnetic properties obtained from such theoretical studies is summarised in Table 2.3. The first band structure calculation of $CuCr_2X_4$ $(X = S, Se, Te)$ used a discrete variational X_α method previously used for magnetic semiconductors Horikawa *et al.* (1982); Ogata *et al.* (1982). One striking result from the calculation of the charge population of each atom, is the deduced formal valences of $Cu^{1.25+}[Cr^{1.41+}]_2[Se^{1.02-}]_4$. The results seem to disagree with both the Lotgering and Goodenough models. They observed a strong orbital mixing of the Se $4p$ with the Cr $3d$ bands and a smaller contribution from the Cu $3d$ orbitals. The disparity is explained by the covalent bonding effect which increases with decreasing electronegativity Horikawa *et al.* (1982). The calculated crystal field splitting for the Cr $3d$ orbitals is evaluated at about 1.3

eV, and the copper levels are found to be close to degenerate. A spin polarisation was found on each atom, the largest value being on the Cr with a value of 3.54 μ_B. A smaller negative contribution was obtained on the Cu and Se with respective values of -0.26 and -0.36 μ_B. The total calculated moment was found to be 5.38 μ_B/mol. To the author's knowledge, this electronic structure calculation provided the only available data in the literature until the point when large room-temperature magneto-optical properties of these compounds were observed. To explain the observed Kerr effect, fully relativistic spin-polarised linear muffin-tin orbital calculations were carried out Antonov *et al.* (1999). They described the band structure of $CuCr_2Se_4$ and predicted half-metallicity with a band gap for only the majority spins. The spin polarised calculation showed a moment similar to the previous calculation: a positive magnetic moment of 2.8 μ_B on Cr atoms and negative moments of -0.08 and -0.14 μ_B on Cu and Se respectively, giving a total moment of 5.28 μ_B/mol. An increase in the p bandwidth is observed upon replacing the S anion with Se and then Te successively, as previously described. They calculated the optical properties from the calculated band structure and observed a larger Kerr effect for $CuCr_2Se_4$ than for the other compounds. To support their x-ray magneto-circular dichroism results, electronic band structure calculations have been performed Kimura *et al.* (2001a,b). The main objective was to obtain the magnetic moment on each of the atoms. They reported a calculated total magnetic moment of 5.1 μ_B/mol with 2.8 μ_B on Cr, -0.1 μ_B on Cu, and -0.16 μ_B on Se. They concluded that neither of the proposed models were appropriate to describe the system since they observed Cr^{3+} and nearly monovalent copper. To further the discussion on the bonding in this material, the same electronic calculation method was used to calculate the crystal orbital Hamiltonian population, a tool for describing bonding and nonbonding interactions as a function of energy Ramesha & Seshadri (2004). They reported a total magnetic moment of 5.2 μ_B and found a small population in the minority spin. From the crystal orbital Hamiltonian population calculation they concluded that the $Cu - Se$ bonding is similar to the interaction between monovalent copper and divalent selenium. To support the claim that the anomalous Hall effect arises from Berry phases Lee *et al.* (2004), the electronic band structure has been calculated using the full-potential linearised augmented plane-wave (FLAPW) with general gradient approximation (GGA) Yao *et al.* (2007). They estimated the magnetic moment on each atom for the compositions with $x = 0.0, 0.2, 0.4, 0.6, 0.8, 1.0$ and found that the magnetic moment increases gradually from $5.1\mu_B/mol$ for $x = 0.0$ to $6\mu_B/mol$ for $x = 1.0$. Increasing the Br concentration depletes the minority spin while the calculated moment increases to a value close to 3.0 μ_B, the theoretical value for Cr^{3+} ions.

In the undoped compound, the copper is nearly monovalent, with a small spin polarisation. The crystal field splitting of the nominally Cr^{3+} is estimated to be around 3 eV. The Cr $3d$ levels are strongly mixed with the Se $4p$ states. This hybridisation is responsible for the p-type metallic conduction and stabilises the ferromagnetic ground state at the cost of a small negative spin polarisation which decreases the saturation moment. The introduction of Br in the lattice is treated as the introduction of an extra electron, *i.e.* changing the concentration of dopant is equivalent to shifting the Fermi level to higher energy. They show that, as observed experimentally, the anomalous Hall coefficient is negative for $0.15 \lesssim x \lesssim 0.25$ and positive for all other concentrations. Since the introduction of Br in the structure modifies the electrical and magnetic properties, this motivated a theoretical study on the effect of Se deficiency in thin films deposited by laser ablation, which was performed using the generalised gradient approximation Bettinger *et al.* (2008). The undoped compound possesses the same general electronic band structure as that previously described with a strong hybridisation of the Cr $3d$ and Se $4p$ states. They found a total magnetic moment slightly greater than $5\mu_B/mol$ which is slightly smaller than the value obtained using the linear density approximation (LDA). The introduction of selenium vacancies in the structure gives rise to a trigonal distortion of the crystal structure and increases the magnetic moment to 6 μ_B/mol. Another change in the band structure is that the system which was previously metallic, becomes half-metallic. The prospect of obtaining a family of electrically tunable (from metallic to semiconducting and half-metallic) ferromagnets with a relatively high Curie temperature by substitution of the chalcogen by a halogen is somewhat extraordinary. To explore these possibilities, recent electronic band structure calculations showed that solid solutions with diverse compounds would permit this flexibility. The first study examined the density of states of the solid solution $CdCr_2X_4 - CuCr_2X_4$ with $X = S, Se$ and found that compositions with low concentrations of Cd are half-metallic Wang *et al.* (2008). They extended the calculations to other hypothetical quaternary systems where the chalcogen can be replaced by a halogen or a group V element Wang *et al.* (2009), and found most of the compositions to be half-metallic.

2.4.4 Discussion on the $CuCr_2Se_4$ case

Before starting the discussion on the valences of $CuCr_2Se_4$, it is useful to recall the main characteristics of the different bonding that can occur in most inorganic crystals.

Ionic bonding To form an ionic bond two species of opposite net charge - associated with the oxidation state of the ions - exchange one or more electron. The bond is held due

Methods	Compounds	a (Å)	u	Magnetic moments (μ_B) $m(Cr)$ $m(Cu)$ $m(Se)$ m_{tot} (μ_B/mol)	References
DV X_α	$CuCr_2Se_4$	-	-	3.54 -0.26 -0.36 5.38	Ogata *et al.* (1982)
LSD LMTO ASA CC	$CuCr_2Se_4$	10.327	-	2.8 -0.08 -0.14 5.28	Antonov *et al.* (1999)
LSD LMTO ASA SOC	$CuCr_2Se_4$	-	-	2.9 -0.1 -0.16 5.0	Kimura *et al.* (2001b)
LSD LMTO ASA GGA	$CuCr_2Se_4$	-	-	2.6 - - -	Ramesha & Seshadri (2004)
FLAPW GGA	$CuCr_2Se_4$	-	-	2.79 -0.11 -0.16 5.08	Yao *et al.* (2007)
	$CuCr_2Se_3Br$			2.95 -0.024 -0.075 5.99	
DFT GGA	$CuCr_2Se_4$	10.395	0.2577	3 -0.88 5.12	Bettinger *et al.* (2008)
	$CuCr_2Se_{3.5}$	trigonal distortion		3.0 0.0 0.0 6.0	
LDA +U	$CuCr_2Se_4$	-	-	5.61	
DFT GGA PAW	$CuCr_2Se_4$	10.374	0.258	- - - 5.1	Wang *et al.* (2008)
	$Cd_{0.875}Cu_{0.125}Cr_2Se_4$	10.786	0.265	- - - 5.87	
DFT GGA PAW	$CuCr_2Se_3Br$	10.579	0.262	- - - 6.0	Wang *et al.* (2009)
	$CuCr_2Se_{3.5}$	10.520	0.260	- - - 6.0	

Table 2.3: Summary of structural and magnetic properties obtained from electronic structure calculation with different approximation.

to the attractive electrostatic interactions between the two oppositely charged ions and is strongly polarised. The overlap of the orbitals is smaller than the unit-cell. and as a direct result the electrons are localised around the atoms and ionic compounds are poor conductors.

Covalent bonding In the previous bonding one of the two atoms gains some electrons to the deficit of the other one, if two atoms with similar electronegativities and an unfilled outer shell are interacting, on the other hand, a covalent bonding can bind the two atoms. In this case electrons are shared equally between the two atoms to fill their outer shells and the overlap between the orbitals is of the order of the unit cell. This bond is much stronger than the preceding bond.

Metallic bonding The two previous bonds are both orientationally sensitive. If the orbitals overlap on a scale that is longer than the lattice parameter, this direction preference is lost and the electrons become somewhat free to move in the lattice. In the case of metallic bonding, it is hard to assign an oxidation number to the element since the electrons are not localised. Therefore these materials are generally good conductors.

Although these three different bondings are fundamentally different, most inorganic compounds can not merely be described by one single model. As with the magnetic interactions, each material will present a mixture of these different bondings, and it is important to know which member of this ternary bonding system is favoured by a compound.

The Lotgering description of the electronic structure of $CuCr_2Se_4$ is completely based on the ionic model. Most oxide compounds have been described by an ionic model and it is tempting to adopt the same view for the selenide, but the simple fact that the compound is metallic should be enough to inspire doubt that the bonding is strictly ionic. The Goodenough model introduces a covalent and metallic character of the bonding. The Cr possesses a strong ionic character with a +3 oxidation number and localised magnetic moment but the $Cu - Se$ system presents a mixture of covalent and metallic bonding. A misunderstanding of this model leads some authors to favour the Lotgering model based on the observation of a more monovalent copper than divalent. All the modern electronic structure calculations give a similar picture, with a strongly spin polarised localised Cr d band and a broad Se p band, the Fermi level cut across the Se states with the density of state at ϵ_F being populated only by the Se p.

The issue of assigning a valency to each atom exists only for the ionic model. By acknowledging that the ionic model does not accurately explain the properties of the selenide due to the

"softer" character of selenium, a more rudimentary problem is to explain the change of magnetic and electrical properties by the substitution of Se by Br.

2.5 Definition of the project

Materials exhibiting both transport and spin degrees of freedom are increasingly critical for technological applications. The chalcochromites seem to be ideal candidates. From the ongoing debate over the electronic structure of the copper-based compound, it is clear that this family of compounds provides the perfect opportunity for an exciting modern study.

In order to obtain materials suitable for spin-electronics applications, several problems have to be overcome. The first technological challenge is to produce high quality materials in a form which permits detailed and accurate characterisation of the compounds. As described in the previous section, the growth of both single crystals and thin films is highly non-trivial. Thus, the first goal of this study is to develop methods to produce high quality single crystals and thin films. Because of its high Curie temperature and tunable electrical properties we chose to focus on the growth of $CuCr_2Se_4$ thin films. The results obtained are presented in chapter 5. The growth of single crystals is always a great challenge. This sample form, however, provides us with the optimum medium for the study of the defect-minimised material. It is a step closer to the ideal case, thus analysis and characterisation of the single crystals allows us to determine the properties of the material with a high degree of accuracy. Chapter 4 is dedicated to the growth and characterisation of $CuCr_2Se_4$, $CuCr_2Se_3Br$ and $CdCr_2Se_4$ single crystals. In spite of the prospect of studying a semiconductor compound that can be described by a somewhat ionic model, the controversy between the two models for $CuCr_2Se_4$ is a more critical problem. The objectives of this project have not been solely applications-driven, the technological promise of these materials is evident, however a more fundamental problem has also been addressed in this work. In order to understand how different this system is compared to its semiconducting equivalents a detailed discussion of the available results is of primary importance.

Parameter	Compound		
	$CdCr_2Se_4$	$HgCr_2Se_4$	$CuCr_2Se_4$
Crystallo-chemical parameter			
Lattice constant (Å)	10.75	10.753	10.334
Anion parameter[1]	0.265	0.265	0.257
Density (g/cm^3)	5.675	6.670	5.818
Decomposition temperature (^oC)			
in air	542	340	700
in vacuum	564	300	532
Magnetic properties			
Curie temperature T_C (K)	129	106	430
Magnetic moment at $4.2K$ (μ_B/mol)	6	6	5-6
Optical properties			
Absorption edge (eV)			
at $300K$	1.32	0.8	N/A
at $4.2K$	1.12	0.27	N/A
Electrical properties			
Conductivity type	SC	SC	M
Resistivity ($\Omega \cdot cm$)			
at $300K$	10^2	0.7	$2 \cdot 10^{-4}$
at $4.2K$	10^5	10^2	-

Table 2.4: Some general properties of the FMS under consideration.

Chapter 3

Synthesis and characterisation of polycrystalline ACr_2Se_4 $(A = Cu, Cd, Hg)$

3.1 Solid state reaction

Traditionally, synthesis of solid state inorganic materials is viewed by many as "shake and bake" or "beat and heat" due to the high temperature processes involved in synthesising most ceramics. The obvious principle behind this caricatural description is nevertheless true, as most compounds obtained by substantial heat treatments are thermodynamically stable. Let us consider a chemical reaction where a reactant gives a stable product. Possible reaction schemes are illustrated in Fig.3.1. From this diagram it is obvious that solid state reaction is thermodynamically controlled - the reaction will not occur if the system does not acquire from an external source enough energy to overcome the activation energy. One possible drawback of this type of reaction is that it is not possible to stabilise the intermediate metastable products.

Since the heat treatment of the reactants is one of the main parameters leading to formation of the product of a chemical reaction, prior knowledge of the enthalpy of formation or the phase diagram of the desired compound is of vital importance. The phase diagram of binary and ternary systems can present different features which determine how the crystallites will form. The following section will detail these influential features.

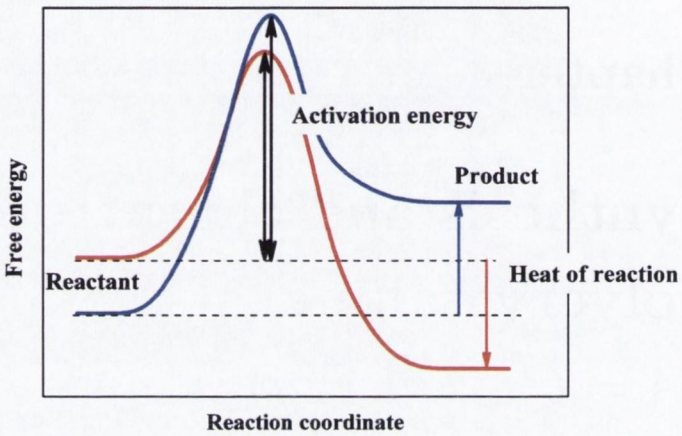

Figure 3.1: Evolution of the free energy during a chemical reaction. The blue pathway corresponds to an endothermic reaction while the red pathway corresponds to an exothermic reaction.

3.1.1 Phase diagram consideration

The most reliable (yet tedious) way of constructing phase diagrams for any compound is to exploit known values of thermodynamic parameters in combined experimental measurements [1]. Since only binary phase diagrams for the elements under study are available in the scientific literature, a description of diagrams with two components A and B is presented.

To understand how a phase diagram is built the main rules that should be kept in mind are the Gibbs phase rules from which the variance of the system v can be evaluated, and therefore the number of state parameters (P, T, or V) that are independent of each other:

$$v = C - \varphi + 2$$

where C is the number of components and φ the number of phases in thermodynamic equilibrium. In our case $C = 2$, so $v = 4 - \varphi$ and in addition to temperature and pressure, two other variables are introduced - the fractional compositions x_A and x_B. The equilibrium phase fields are constructed by minimising the Gibbs free energy. In the case of the formation of a compound, three phase equilibria can occur. The variance of the system is zero and therefore this equilibrium does not have any degrees of freedom. This implies that the phase φ_3 at the

[1] Possible methods are differential thermal analysis, thermogravimetry, x-ray diffraction (XRD), and microstructure analysis.

equilibrium temperature T_{eq} has a composition intermediate between those of φ_1 and φ_2. Two situations can arise from these three phase equilibria:

- φ_3 is only stable at $T \geq T_{eq}$ which corresponds to eutectic type equilibrium.
- φ_3 is only stable at $T \leq T_{eq}$ which corresponds to peritectic type equilibrium.

The compounds described in this thesis are all formed through a peritectic[1] type equilibrium. A more detailed description and the consequences of this type of reaction will be discussed in subsequent sections. The detailed explanation of the construction of a peritectic point from the Gibbs energy is given in appendix D. Three peritectic equilibria can be found in phase diagram depending on the nature of the phases φ_1, φ_2, and φ_3:

Peritectic equilibrium corresponds to the reaction $s_1 + L \rightleftarrows s_2$ as represented in Fig.3.2.

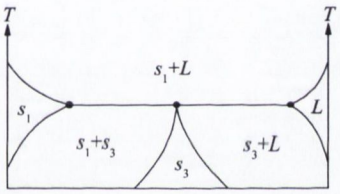

Figure 3.2: Schematic of a peritectic equilibrium.

Peritectoid equilibrium corresponds to the reaction $s_1 + s_2 \rightleftarrows s_3$ as represented in Fig.3.3.

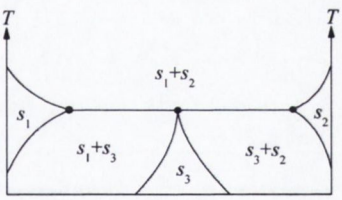

Figure 3.3: Schematic of a peritectoid equilibrium.

Syntectic equilibrium This equilibrium is much less common than the two preceding equilibria and corresponds to the demixing of two liquids through the reaction $L_1 + L_2 \rightleftarrows L$ as represented in Fig.3.4.

[1] The etymology of peritectic is melt around.

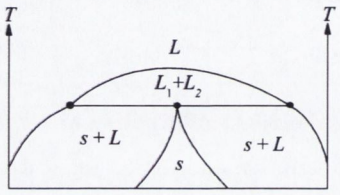

Figure 3.4: Schematic of a syntectic equilibrium.

To understand the difficulty in forming a compound through a peritectic (or peritectoid) equilibrium let us consider the liquid-solid transition of a system with the composition of the peritectic compound. The phase diagram of such a binary system is shown in Fig.3.5. This

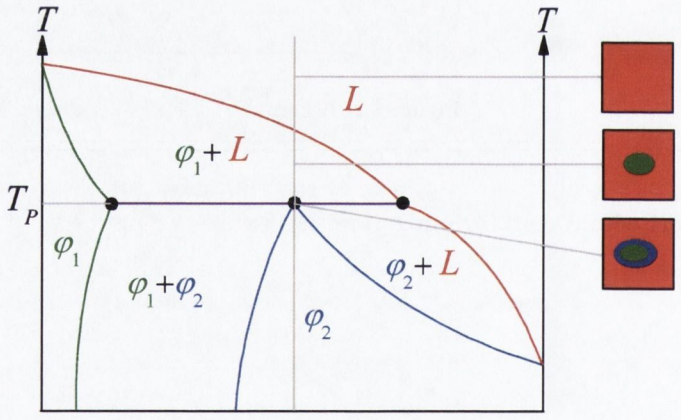

Figure 3.5: Schematic of a peritectic equilibrium. The squares on the right represent the phases present in the system at three different temperatures for a stoechiometric compound: above the liquidus, below the liquidus, and at the peritectic temperature from top to bottom.

picture illustrates clearly the complexity of a peritectic reaction. The formation of φ_2 from the reaction between φ_1 and L between the two phases creates a barrier which prevents the other two phases from reacting. This type of reaction is therefore often very slow and it is difficult to obtain the equilibrium phase in the solid state by heating the system to temperatures higher than the peritectic decomposition temperature.

3.1.2 Selenide synthesis

If solid state synthesis of selenides seems straightforward, the methodologies involved for powder preparation have most likely been underestimated. For instance, all the reactions carried out in this dissertation were performed in evacuated silica ampoules. This method has several advantages for the preparation of chalcogenide materials. Firstly, the reagents are protected from oxygen and thus from competing oxide-forming reactions. Secondly, volatile components such as the elemental chalcogens are contained in close proximity to the less volatile metal reagents. Details of the sample preparation are given in appendix B.1. According to available phase-diagram data, all chalcogenide spinels are formed by either peritectoid ($CdCr_2Se_4$) or peritectic ($HgCr_2Se_4$, $CuCr_2Se_4$) reactions[1] Fedorov *et al.* (2003). For example, the binary $CdSe - Cr_2Se_3$ and $CuSe - Cr_2Se_3$ phase diagrams are presented in Fig.3.6. The fact that these compounds decompose before they melt is one of the main reasons that crystal growth is so challenging. Moreover, it is important not to exceed the decomposition temperature while maintaining a temperature high enough to activate the reaction and to increase the mobility of the species. The characterisation methods and techniques used to analyse the polycrystalline samples are described in appendix C.

3.2 $CuCr_2Se_4$ and halogen derivative

The physical properties of the solid solution $CuCr_2Se_4 - CuCr_2Se_3Br$ were presented in chapter 2.4.3. This system is a perfect example of a more complicated solid state synthesis. In fact, the results reported in the literature vary vastly depending on the preparation conditions and starting reactants. Moreover, the formation of an unstable - moisture or air sensitive - compound was used to explain the diversity of the results. Systematic studies carried out on the solid solutions showed that the copper stoichiometry is the factor which determines the stability of the spinel. Furthermore, it is reported that compounds with a concentration of bromine up to $x = 2$ can be stabilised, compared to the generally observed solubility limit $x = 1$, but only in single crystal form Pink *et al.* (1974a,b).

3.2.1 $CuCr_2Se_4$

The synthesis and characterisation of pure $CuCr_2Se_4$ was, in the first place, motivated by the preparation of a sintered target for PLD.

[1] Also called incongruent reactions.

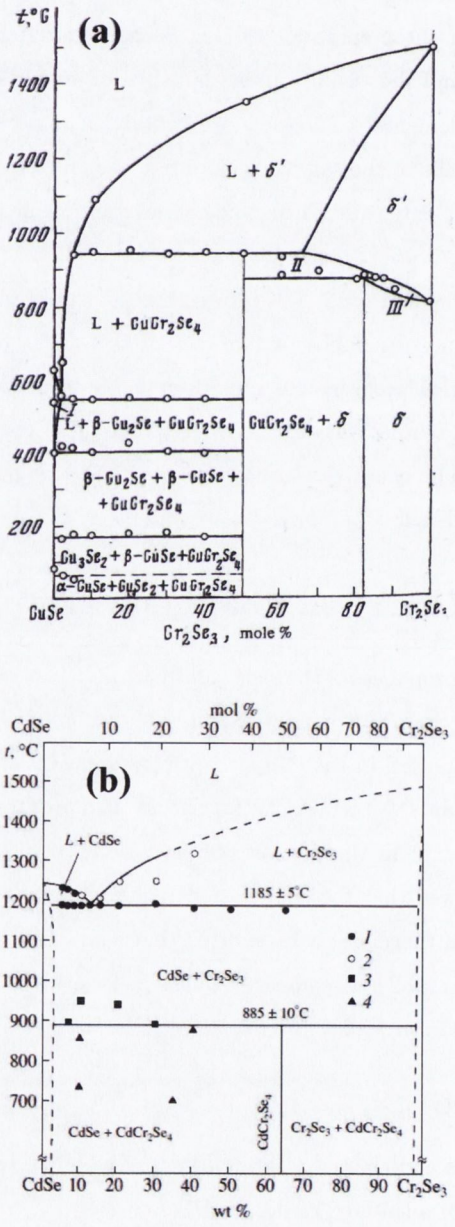

Figure 3.6: Phase diagram of (a) $CuCr_2Se_4$ reproduced from Chernitsyna *et al.* (1977) and of (b) $CdCr_2Se_4$ reproduced from Kalinnikov *et al.* (2003)

3.2.1.1 Reaction schemes

For the synthesis of $CuCr_2Se_4$, there are several possible initial reagents. The selection of initial reagents is a compromise between purity and reactivity. Finely divided reagents are more easily combined in a homogeneous reaction mixture, but are more susceptible to contamination and/or oxidation during storage and handling. Compound reagents, such as binary phases, are still more intimately mixed than the most finely divided elemental reagents, but they are subject to inhomogeneities in stoichiometry. A more detailed description of the powder synthesis can be found in appendix B.1.

In this work, two different routes to produce $CuCr_2Se_4$ powder have been used:

$$Cu + 2Cr + 4Se \longrightarrow CuCr_2Se_4 \tag{3.1}$$

$$Cu_2Se + 4Cr + 7Se \longrightarrow 2CuCr_2Se_4 \tag{3.2}$$

The product of the reaction is a soft, dark grey powder, which grinds readily and leaves no streak on an agate mortar suggesting the formation of well crystallised grains. By using a permanent magnet, one can observe that at temperatures as low as $400°C$ a ferromagnetic phase is formed. Another observation is that excess selenium does not appear to be incorporated in the compound since it condenses on the cold regions of the tube.

3.2.1.2 Structural characterisation

Powder x-ray diffraction Powder x-ray diffraction can be considered as "the eyes" of the solid-state chemist and is a conventional method for checking the phase purity of polycrystalline materials by comparing the observed spectra with those recorded in a database.

Powder diffractograms of three samples are presented in Fig.3.7 for a narrow range of 2θ with the Bragg positions obtained from the $CuCr_2Se_4$ (PDF file 33-0452).

The red diagram corresponds to a sample fired at 550 °C using reaction 3.6. Most of the diffeaction peaks are indexed with the $CuCr_2Se_4$ phase. The broadening of the full width at half maximum peak-height (FWHM) of the XRD data is completely attributed to the diffractometer. This indicates that even at low enough temperatures the reaction is complete and produces well crystallised particles. A few low intensity peaks remain unindexed, however, the presence of all expected impurity phases from the starting elements has been ruled out [1].

The green pattern corresponds to a sample prepared at 800 °C using the same reaction as the previous sample. The diagram seems to be similar to the previous one but upon closer

[1] Some peaks are due to the contamination of the x-ray tube by W and the K_β line of the Cu.

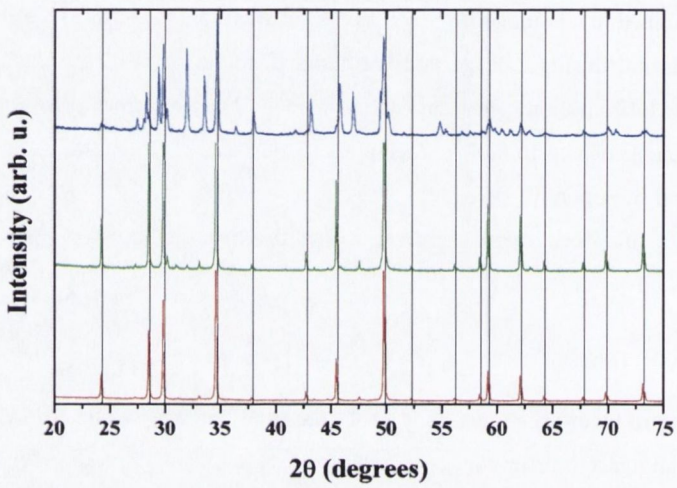

Figure 3.7: Powder diffraction patterns for $CuCr_2Se_4$: fired at 550 °C (red curve), fired at 800 °C (green curve), and with a nominal stoichiometry $CuCr_2Se_{3.75}$ (blue curve). The black vertical lines correspond to the PDF 33-0452. The data are presented in linear scale.

inspection shows the appearance of extra lines as emphasised in Fig.3.8. These reflections can be attributed to the presence of chromium deficient Cr_3Se_4.

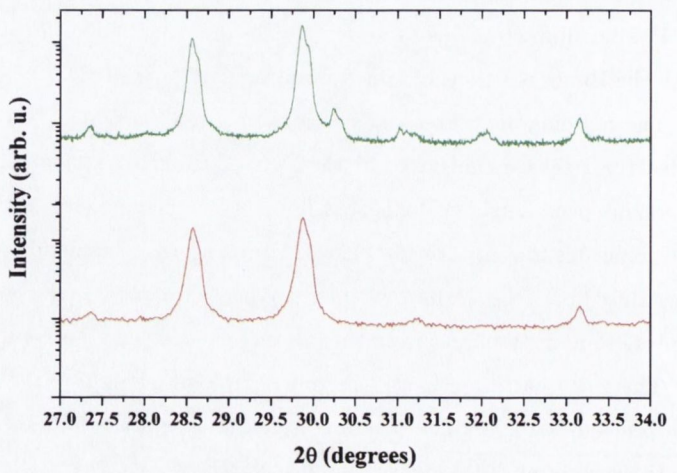

Figure 3.8: Zoom on the low angle region of the diffraction patterns of $CuCr_2Se_4$ synthesised at 550 °C (red curve), and at 800 °C (green curve). Note the logarithmic scale for the intensity.

In order to study the effect of selenium deficiency on the magnetic and transport properties, a sample with a nominal composition $CuCr_2Se_{3.75}$ was prepared. The powder obtained is a mixture of $CuCr_2Se_4$, $CuCrSe_2$ and $CrSe$. The broadening of the peaks suggest poorer crystalline quality and smaller crystallite size.

Apart from phase analysis the x-ray powder diffraction pattern can be further analysed to extract the main crystallographic parameter of the spinel structure, once the reaction has been optimised to yield phase-pure powder. The refinement of the powder diffraction patterns was performed using the Rietveld method Rietveld (1969), which is based on a least-squares fitting of the observed intensities and comparison with a structural model [1]. The structural model presented in Table 2.2 with the origin choice 2 was used. The final refinement is presented in Fig.3.9. All of the weak reflections which are not indexed with the spinel structure can

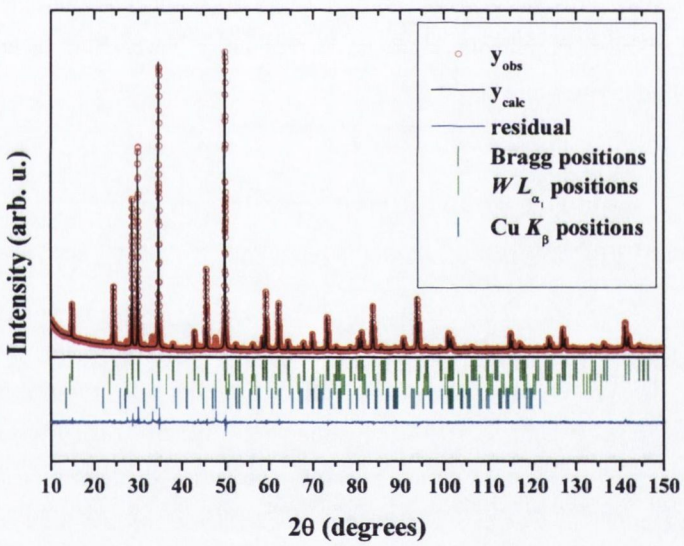

Figure 3.9: Powder x-ray diffraction pattern measured at room temperature for $CuCr_2Se_4$ powder fired at 550°C (red empty dots), the fit to the spinel structure (black solid line), and the difference plots (blue solid line). The dark green sticks represent the calculated Bragg positions, the light green sticks represent $W\ L_{\alpha_1}$ positions and the dark cyan sticks represent $Cu\ K_\beta$ positions.

be explained by the parasitic wavelengths ($Cu\ K_\beta$ and W_L) of the x-ray tube. The relevant

[1] Fullprof Suite software was used. More information on this can be found in appendix C.

refinement factors and the extracted parameters are summarised in Table 3.1. The definition of the refinement factor can be found in appendix C.

R_p		R_{wp}		R_{Bragg}	
15.1		11.8		2.96	
a (Å)	u	$d(Cu-Se)$ (Å)	$d(Cr-Se)$ (Å)	$\widehat{CuSeCr}$ (°)	$\widehat{CrSeCr}$ (°)
10.33287(2)	0.25702(3)	2.3628(3)	2.5128(3)	122.92(1)	93.25(1)

Table 3.1: Crystallographic parameters of $CuCr_2Se_4$ after structural refinement of the powder x-ray diffraction data obtained at 295 K.

Since the transparency of the samples is negligible and the overlap between the Bragg reflections is minimal, the atomic temperature factor B_{iso} for each atom have been refined. These values are listed in Table 3.2.

	T (K)	B_{iso} (Å^2)		
		Cu	Cr	Se
	295	1.03(2)	0.80(2)	0.77(1)
Rodic *et al.* (1998)	295	0.68(4)	0.57(4)	0.56(4)

Table 3.2: Cu, Cr and Se atomic temperature factor at 295 K.

The rather high value of R_p and R_{wp} results from the absence of monochromated x-ray radiation. It is, more specifically, due to the unwanted Cu K_β and W_L reflections originating from the x-ray source. Nevertheless, the prepared powder samples are completely single phase, to the limit of detection of the x-ray diffractometer, with a good crystalline quality. The values of a and u[1] agree well with the values reported in the literature. The atomic temperature factors are larger than those reported from the most recent neutron diffraction studies Rodic *et al.* (1998), however, the trend is similar: $B_{iso}(Cu)$ is slightly bigger than $B_{iso}(Cr)$ and $B_{iso}(Se)$ which are almost equal.

Powder neutron diffraction Powder XRD can provide most of the crystallographical parameters, but it is difficult to extract the atomic temperature factors accurately since the amplitude of the form factor is a function of the d spacing and the Debye-Waller factor. In the case of the neutron diffraction, the nuclear form factor does not vary with d, enabling more accurate determination of B_{iso}. The description of the two powder neutron diffraction spectrometers used for this work can be found in C.

[1] Therefore the other crystallographic parameters also.

A powder neutron diffraction pattern of $CuCr_2Se_4$ measured at 500 K on the 3T2 spectrometer is presented in Fig.3.10. This temperature, which is higher than the Curie temperature of the compound, was chosen to observe the nuclear contribution only. A measurement was also performed at 2 K where the nuclear and magnetic parts were refined. The residual of the refinement is better than that obtained with the laboratory XRD because of the more monochromatic wavelength used for the data collection. Moreover, the shorter wavelength, compared to the $Cu\ K_{\alpha_{1,2}}$, used on the 3T2 spectrometer permits the investigation of the structure on a wider range of d. The same crystallographic parameters that have been extracted from XRD data have been refined with the neutron data and are presented in Table 3.3. The calculated atomic factor at 500 K and 2 K for each atom is presented in Table 3.4. The high value of the B_{iso} at 500 K compared to that for most oxides suggests a low decomposition temperature for this compound.

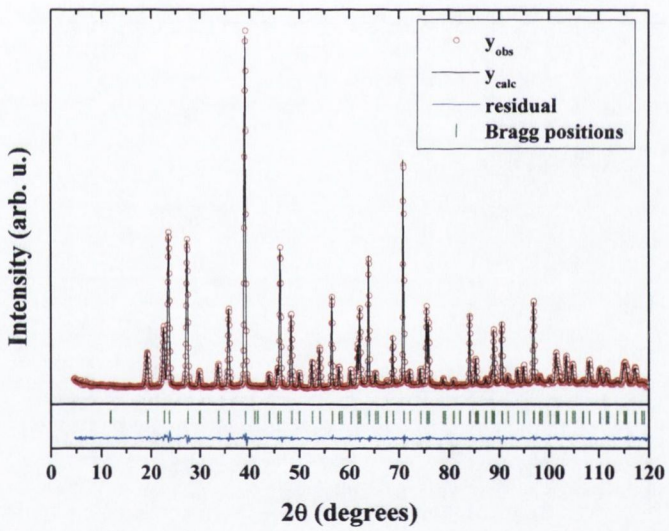

Figure 3.10: Powder neutron diffraction pattern measured at 500 K with $\lambda = 1.225270$ Å for $CuCr_2Se_4$ powder fired at 550°C (red empty dots), the fit to the spinel structure (black solid line), and the difference plots (blue solid line). The dark green sticks represent the calculated Bragg positions.

The temperature dependance of the lattice parameter has been studied using the data collected from the G4.1 diffractometer and is presented in Fig.3.11[1]. A typical parabolic trend in

[1]The value of the wavelength of the G4.1 spectrometer is not well defined and to correct this effect, the

	R_p		R_{wp}		R_{Bragg}	
500 K	7.34		6.27		1.67	
	a (Å)	u	$d(Cu-Se)$ (Å)	$d(Cr-Se)$ (Å)	$\widehat{CrSeCr}$ (°)	$\widehat{CuSeCr}$ (°)
	10.35361(4)	0.25736(2)	2.3736(3)	2.5145(3)	122.81(1)	93.42(1)
	R_p		R_{wp}		R_{Bragg}	
2 K	5.27		5.27		1.20	
	a (Å)	u	$d(Cu-Se)$ (Å)	$d(Cr-Se)$ (Å)	$\widehat{CrSeCr}$ (°)	$\widehat{CuSeCr}$ (°)
	10.31745(3)	0.25717(1)	2.3619(2)	2.5076(2)	122.873(6)	93.330(6)

Table 3.3: Crystallographic parameters of $CuCr_2Se_4$ at 500 K and 2 K after refinement of the powder neutron diffraction data collected from the diffractometer 3T2.

the evolution of the lattice parameter is observed, and the vanishing of the expansion coefficient at 0 K Kittel (2005).

T (K)	B_{iso} (Å^2)		
	Cu	Cr	Se
500	1.61(2)	1.20(2)	1.205(7)
2	0.177(9)	0.15(1)	0.150(4)
Rodic *et al.* (1998) 10	0.08(3)	0.08(3)	0.07(1)

Table 3.4: Cu, Cr, and Se atomic temperature factor at 500 and 2 K.

The least-squares fitting gives a lattice parameter dependence as a function of temperature according to the equation:

$$a(T) = 10.3181(3) + 1.6(4) \cdot 10^{-5}T + 1.2(2) \cdot 10^{-7}T^2$$

The coefficient of thermal expansion is given by :

$$\alpha(T) = \frac{1}{a}\left(\frac{da(T)}{dT}\right) = \frac{d}{dT}(\ln(a(T)))$$

A linear coefficient of expansion of $6.6(2) \cdot 10^{-5}K^{-1}$ between 90 K - 300 K is found, which is similar to the literature value calculated from XRD data Kanomata & Ido (1974).

lattice parameter has been adjusted to match those obtained by XRD and on the 3T2 spectrometer

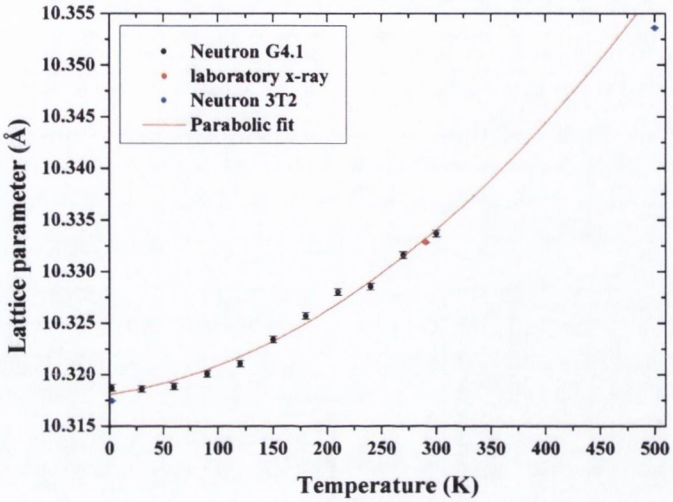

Figure 3.11: Evolution of the lattice parameter of $CuCr_2Se_4$ with temperature. The black dots are from data collected on the G4.1 neutron diffractometer, the blue dots are extracted from the data collected on the 3T2 neutron diffractometer, the red dot is from the laboratory x-ray measurements. The red line is a fit to the data with a second order polynomial function.

3.2.1.3 Magnetic properties

The magnetic properties of the synthesised powders have been studied by DC SQUID magnetometry, AC susceptibility, and powder neutron diffraction [1].

DC magnetometry To obtain the saturation magnetic moment, the evolution of the magnetic moment in an applied field from -5 T to 5 T at 4 K has been measured. The curves presented in Fig.3.12 have the typical ferromagnetic signature at both 300 K (red curve) and 5 K (blue curve). The value of the saturation magnetic moment is found to be 5.7 μ_B/mol which is closer to the theoretical 6 μ_B/mol for the spin only value of Cr^{3+} ions than other figures reported in the literature Lotgering (1964b). Nevertheless, absolute magnetisation values are difficult to obtain by the method used, and this value has to be considered critically.

The evolution of the magnetic moment with temperature was also studied to examine the magnetic transition of the sample. Fig.3.13 represents the evolution of the magnetic moment under an applied field of 1 mT between 4 K and 600 K of a polycrystalline powder prepared

[1] All DC and AC magnetometry measurements in this chapter were performed with Dr. P. Stamenov, some DC measurements were also performed with Dr. M. Venkatesan.

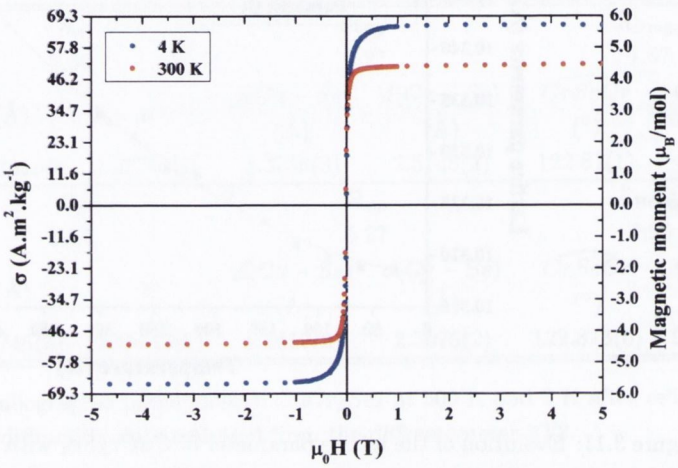

Figure 3.12: Magnetic moment as a function of applied field of $CuCr_2Se_4$ powder prepared at 550 °C measured at 4 K (blue curve) and 300 K (red curve).

at 550 °C. The extracted Curie temperature is 478(1) K, this is higher than the usual 460 K reported Lotgering (1964b). The Curie temperature of the sample prepared at 800 °C is slightly higher (481(1) K) than for powder prepared at 550 °C and the plot of the magnetisation as a function of temperature exhibits a bump around 150 K as shown in Fig.3.14. This behaviour could be due to the presence of an antiferromagnetic impurity phase such as Se deficient Cr_3Se_4.

AC susceptibility To investigate the magnetic transition and the presence of other magnetic phases, AC susceptibility has been measured on powder synthesised at low and high temperatures. In AC measurement, a small AC driven magnetic field is superimposed on the DC field causing a time-dependent moment in the sample. In the low frequency limit the AC magnetisation follows the DC magnetisation. At higher frequency the AC moment of the sample does not follow the DC magnetisation curve due to the dynamic effects on the sample. That is why the AC susceptibility is often known as the dynamic susceptibility. The magnetic susceptibility is defined as :

$$\chi = \frac{dM}{dH} \tag{3.3}$$

and the AC susceptibility is defined as :

$$\chi = \chi' + i\chi'' \tag{3.4}$$

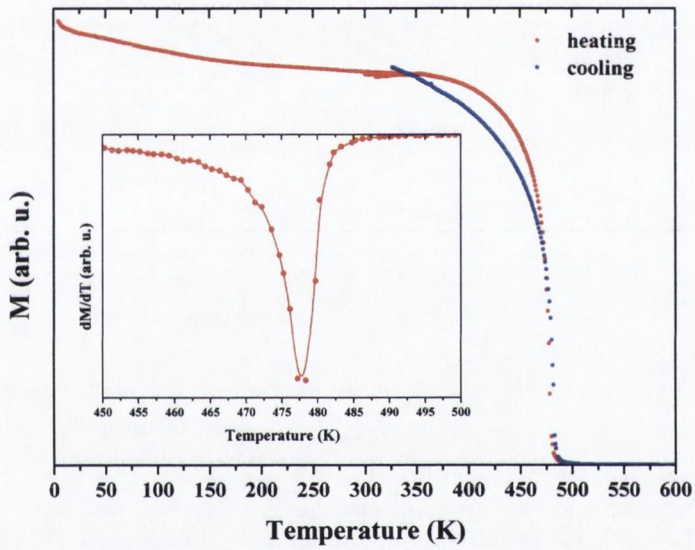

Figure 3.13: Evolution of the magnetic moment as a function of temperature in an applied field of 1 mT for $CuCr_2Se_4$ powder prepared at 550 °C. The red dots are from data collected upon heating the powder, the blue dots were collected when cooling. The inset shows the derivative of the magnetisation as a function of temperature obtained from the heating curve.

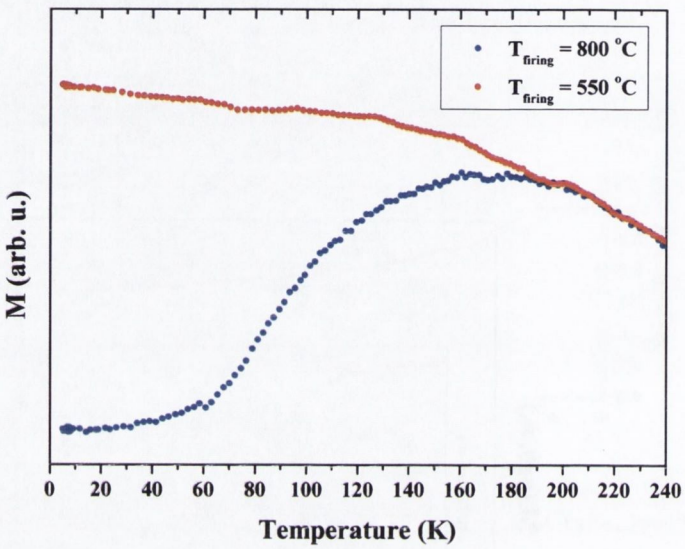

Figure 3.14: Evolution of the magnetic moment with temperature in an applied field of 1 mT for $CuCr_2Se_4$ powder prepared at 550 °C (blue dots) and 800°C (red dots).

where χ' is the real part (or dynamical susceptibility), and χ'' is the imaginary part. A more detailed description of the experiment is given in appendix C.

The real and imaginary parts of the susceptibility of a sample prepared at low temperature are presented in Fig.3.15.

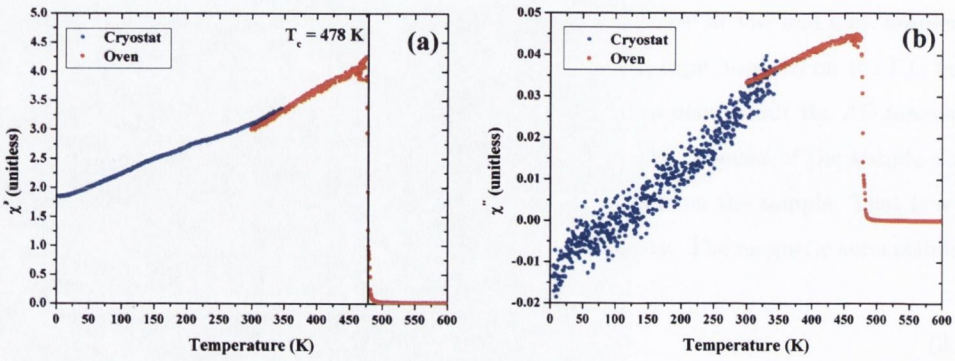

Figure 3.15: (a) Real and (b) imaginary parts of the susceptibility of $CuCr_2Se_4$ powder prepared at low temperature.

The behaviour of the powder prepared at high temperature is similar in the low temperature region, however the transition temperature is different as shown in Fig.3.16.

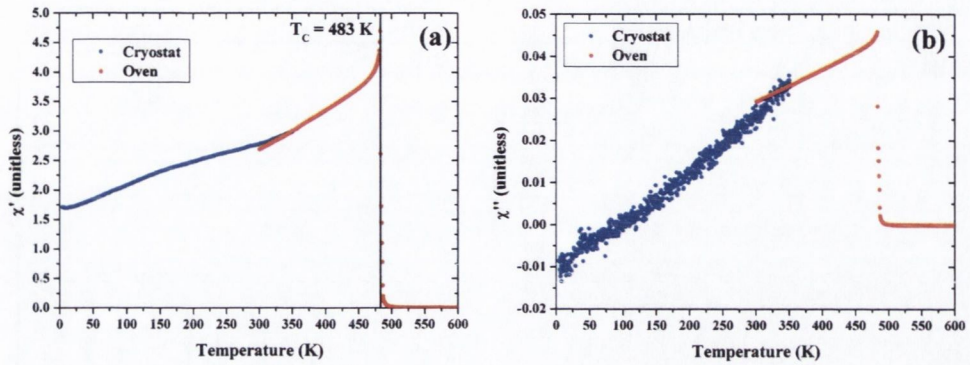

Figure 3.16: (a) Real and (b) imaginary part of the susceptibility of $CuCr_2Se_4$ powder prepared at high temperature.

Powder neutron diffraction Previously, the structural properties extracted from powder neutron diffraction have been described. Taking advantage of the fact that the neutron possesses a spin, magnetic structures can be solved using neutron diffraction technique. Although there are few reports of neutron diffraction in the literature Colominas (1967); Robbins *et al.* (1967); Rodic *et al.* (1998), none of the authors measured the sample in the paramagnetic state. The spectrum in the paramagnetic state is vital for a correct integration of the magnetic intensity, especially in the case of a simple ferromagnet, where the propagation vector is (0,0,0), and therefore all the magnetic peaks overlap with nuclear ones. A spectrum of $CuCr_2Se_4$ is presented in Fig.3.10 and the extracted parameters will serve as a starting point to refine the magnetic structure. As expected for a simple ferromagnet, all the magnetic peaks are overlapping with nuclear peaks as seen in Fig.3.17. The first nuclear peak at 11° is accidentally extinct[1], emphasising the purely magnetic peak.

Fig.3.18 shows the powder neutron diffraction pattern of $CuCr_2Se_4$ prepared at 550 °C measured on the G4.1 spectrometer. The same value of B_{iso} as given in Table 3.4 have been used.

[1]This is due to the similar values of the coherent scattering length of Cu and Se, $0.77 \cdot 10^{-12}\text{cm}^{-1}$ and $0.79 \cdot 10^{-12}\text{cm}^{-1}$ respectively.

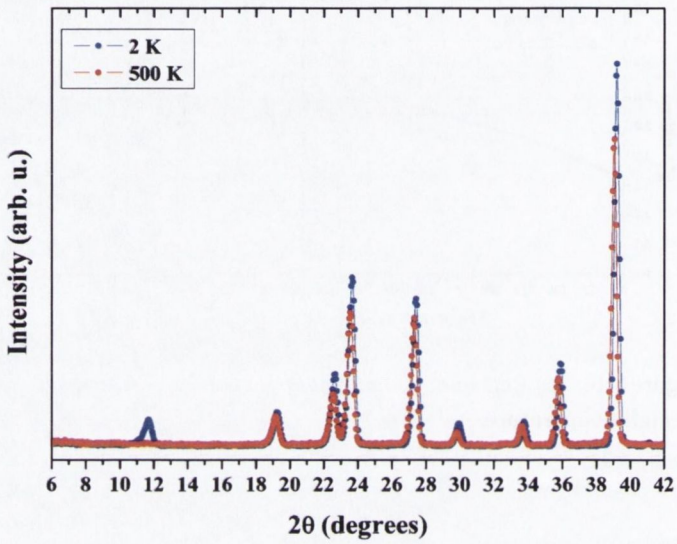

Figure 3.17: Low angle part of powder neutron diffraction pattern of $CuCr_2Se_4$ powder at 500 K (red dots) and 2 K (blue dots) on the 3T2 diffractometer.

The refinement of the magnetic structure was done with a magnetic propagation vector $k = (0, 0, 0)$ and the magnitude of the magnetic moment on both Cu atoms and Cr atoms has been determined. Several combinations of magnetic form factors were used to compare with the data reported in the literature. Polarised neutron diffraction study on single crystals showed that the magnetic form factor of the chromium atom is closer to Cr^{+} than the expected Cr^{3+} in the ionic model Yamashita *et al.* (1979a). Rodic *et al.* (1998) found that the moment on the Cr ions is 2.8 μ_B with the Cr^{3+} magnetic form factor and this increases to 3 μ_B with a Cr^{0} magnetic form factor. Their arguments completely reject the Goodenough model to describe the electronic structure since there is no observation of a negative moment on the Cu. On the contrary, they measure a small positive contribution using a Cu^{2+} magnetic form factor. The results of the polarised neutron diffraction are to be expected; in fact the compound in question seems to be more covalent (even metallic) than ionic and a reduced intensity of the form factor in the forward direction is expected with increasing covalency Hubbard & Marshall (1965).

The nuclear and magnetic refinement factors obtained on the sample measured at 2 K are presented in Table 3.5 along with the calculated moment amplitudes [1].

[1] Since the structure is cubic, the directions of the magnetic moments are equivalent and are assigned to the z axis.

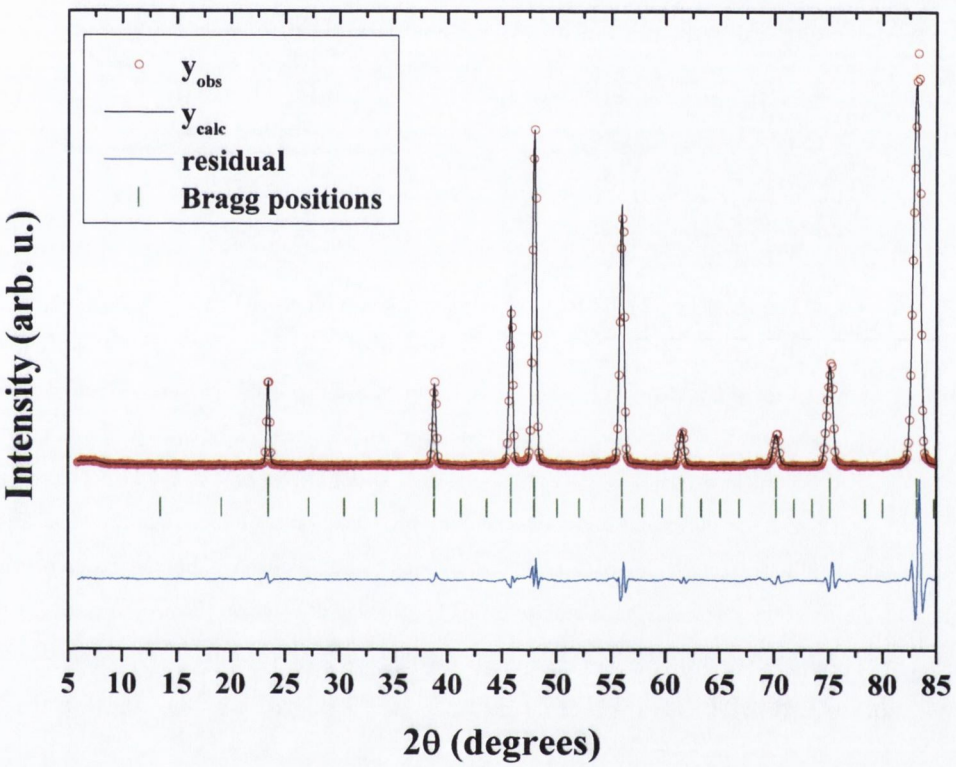

Figure 3.18: Powder neutron diffraction pattern measured at 2 K with $\lambda = 2.4226$ Å for $CuCr_2Se_4$ powder fired at 550°C (red empty dots), the fit to the spinel structure (black solid line), and the difference plots (blue solid line). The upper dark green sticks represent the calculated Bragg positions and the lower ones indicate the calculated magnetic Bragg positions.

R_p	R_{wp}	R_{Bragg}	R_{mag}
14.5	14.9	3.44	3.37
	magnetic moments (μ_B)		
	$m(Cu)$	$m(Cr)$	$m(Se)$
Magnetic form factor	Cu^{2+}	Cr^{3+}	Se^{2-}
G4.1	0.01(2)	2.97(5)	-
3T2	0.01(3)	2.83(3)	-

Table 3.5: Refinement factors and calculated magnetic moment obtained on $CuCr_2Se_4$ at 2 K on the G4.1 spectrometer.

The values obtained from G4.1 are very similar to the values reported by Colominas (1967) and Robbins *et al.* (1967), whereas the moment found on 3T2 differs slightly from the expected 3 μ_B for a Cr^{3+} but agrees well with the values reported by Rodic *et al.* (1998). Changing the magnetic form factor of Cu, Cr, or Se does not drastically change the magnetic moment and does not improve R_{mag}. The resolution at small angles on the G4.1 spectrometer is better than that of the 3T2, making this spectrometer more suitable for magnetic structure determination and hence, the value of 2.97(5) μ_B/Cr has to be favoured. The discussion on the assignment of different form factors is not relevant to powder diffraction data. Moreover, it does not change the amplitude of the magnetic moments within the error limit. The magnetic correlation length can be estimated from the FWHM of the magnetic peak by:

$$L_{mag} = K/y \tag{3.5}$$

where L_{mag} is the magnetic correlation length in Å , $K = 89$ is a constant specific to the diffractometer, and y is the profile size parameter using a modified pseudo-Voigt profile. The value found at 2 K is $L_{mag} = 180(70)$nm and $L_{mag} = 150(50)$nm at 300 K. The error on the values is large due to the broadening of the magnetic peak at the limit of the resolution of the instrument. This suggests that the magnetic order is long range. The temperature evolution of the magnetic moments on the Cu and Cr sites is compared in Fig.3.19.

The expected total moment, from powder neutron diffraction, in $CuCr_2Se_4$ is 6.0 μ_B/mol which is different from the value obtained by DC magnetometry. The Lotgering model with a mixed Cr valence is therefore not supported by the data analysis, however the Goodenough model, with a formal valence of Cr^{3+}, matches well. In this model, a negative magnetic moment is expected to arise from the hybridisation of the Cu and the Se bands at the Fermi level. The electrons are responsible for the metallic conduction and are therefore delocalised in the lattice.

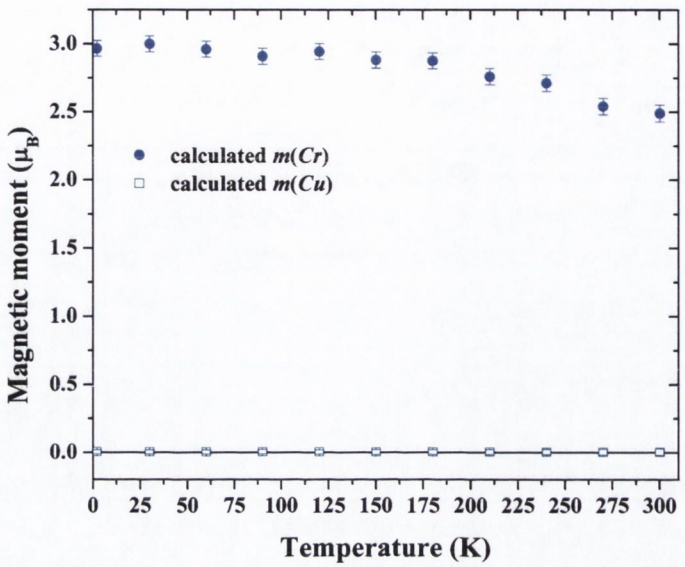

Figure 3.19: Evolution of the calculated magnetic moment on Cu (teal square) and Cr (blue dot) from powder neutron diffraction as a function of temperature.

The magnetic information obtained by powder neutron diffraction is due to localised spin around the nuclei, however if a delocalised spin is present in the lattice, this method will be insensitive to it. It can be envisaged to measure the delocalised component using polarised small angle neutron scattering on particles with a diameter of around 150 nm, or by polarised neutron diffraction on a single crystal from which an electronic density map can be obtained. It may be difficult to estimate accurately the covalency effect by standard Bragg scattering for this compound because of the small number of reflections in the $\sin(\theta)/\lambda \sim 0.1$ Å. If it is clear that a delocalised moment will be difficult to determine by elastic scattering, then perhaps a localised magnetic moment on the Cu antiparallel to the moment of the Cr atoms can be observed. The simulated patterns of two models have been calculated and are presented in Fig.3.20. Model 1 corresponds to a magnetic moment of 3 μ_B on Cr atoms and 0 μ_B on the Cu atoms, and the second model corresponds to a magnetic moment of 3 μ_B on Cr atoms and -1 μ_B on the Cu atoms.

From the difference plot, it is clear that it should be easy to see a negative magnetic moment on the Cu atoms if it is localised.

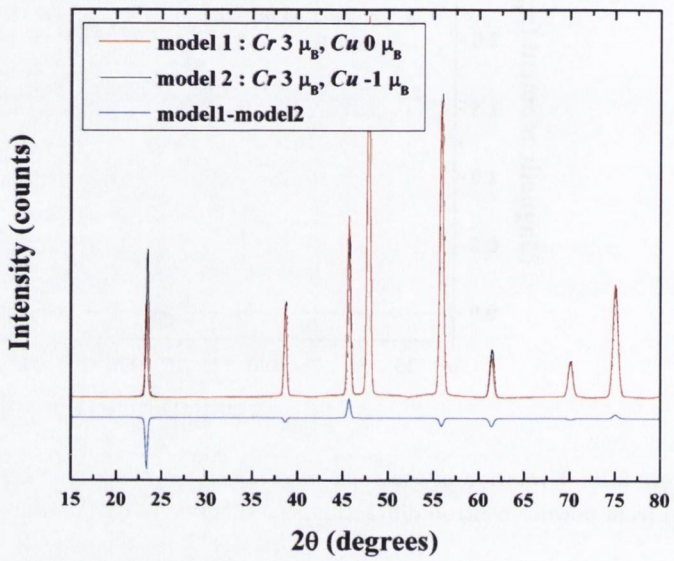

Figure 3.20: Simulation of diffraction pattern for the model magnetic structure 1 (red curve) and 2 (black curve) and the difference (blue curve).

3.2.2 $CuCr_2Se_4 - CuCr_2Se_3Br$ solid solution

The preparation of the solid solution $CuCr_2Se_4 - CuCr_2Se_3Br$ is not as straightforward as the pure compound, judging from the discrepancy in reported results. To understand the evolution of the magnetic properties of these materials, the preparation and characterisation of the solid solution was carried out.

3.2.2.1 Reaction schemes

For the synthesis of $CuCr_2Se_{4-x}Br_x$, the initial reactants play an important role since it was reported that the use of $CuBr$ led to unstable spinels Pink *et al.* (1974a,b). In order to reproduce these results, two reaction schemes have been employed:

$$(1-x)Cu + xCuBr + 2Cr + (4-x)Se \longrightarrow CuCr_2Se_{4-x}Br_x \tag{3.6}$$

$$\left(2-\frac{x}{2}\right)Cu + \frac{x}{2}CuBr_2 + 4Cr + (4-x)Se \longrightarrow 2CuCr_2Se_{4-x}Br_x \tag{3.7}$$

Compounds with nominal molar concentration from $x = 0.0$ to $x = 1.0$ in increments of 0.1 have been prepared. The powders prepared from $CuBr$ were fired at 750 °C whereas the powders prepared from $CuBr_2$ were fired at 550 °C.

The product obtained is a dark grey color with a trace of green powder which increases with increasing Br concentration. The texture of the powder changes compared to the undoped compound and leaves some trace marks in the mortar indicating a loss in crystalline quality. The powders are not attracted to a permanent magnet, revealing that the Curie point is below room temperature for a composition higher than $x = 0.5$ and $x = 0.8$ for powders prepared from $CuBr$ and $CuBr_2$ respectively. After dipping the silica tube in a container of liquid nitrogen, the powder is strongly attracted to a permanent magnet.

These simple observations show that the preparation conditions can drastically affect the magnetic properties of the compound. Because of the rather poor stability in air the detailed characterisation of these compounds is extremely difficult.

3.2.2.2 Structural characterisation

The same procedure as followed for the undoped compound was used to characterise the series of Br-doped powders.

Powder x-ray diffraction The emergence of a green-tinged powder and the textural changes observed upon increased doping are reflected in the measured XRD spectra. The appearance of a new peak that can be attributed to $CuBr$ is observed as shown in Fig.3.21. The broadening of the peak at high angles presented in Fig.3.22 suggests that the powder is of poorer crystalline quality (either due to the size of the particles or the strain due to the insertion of Br). A relative change in the peak positions is observed, which indicates a change of the lattice parameters.

All XRD patterns have been refined in the same manner as before, and the extracted parameters (lattice parameter, anion position, bond lengths, bond angles, and Cu site occupancy $s(Cu)$, are summarised in Table 3.6. In both cases the stoichiometry of the Cu had to be adjusted for the fitting to converge to a certain value. The under-stoichiometry increases with increasing concentration of Br. This result is similar to that reported in the literature, where Cu-poor spinels are found to be stable and the same range of stoichiometry is found Pink *et al.* (1974a). The values of anion parameter, bond angle and bond length do not show a significant variation with the insertion of Br in the lattice but the lattice parameter, on the other hand, is drastically changed with a variation of 0.5% for the series prepared from $CuBr_2$ and 0.8% for the series prepared from $CuBr$. The variation of the lattice parameter as a function of the nominal Br concentration is presented in Fig.3.23.

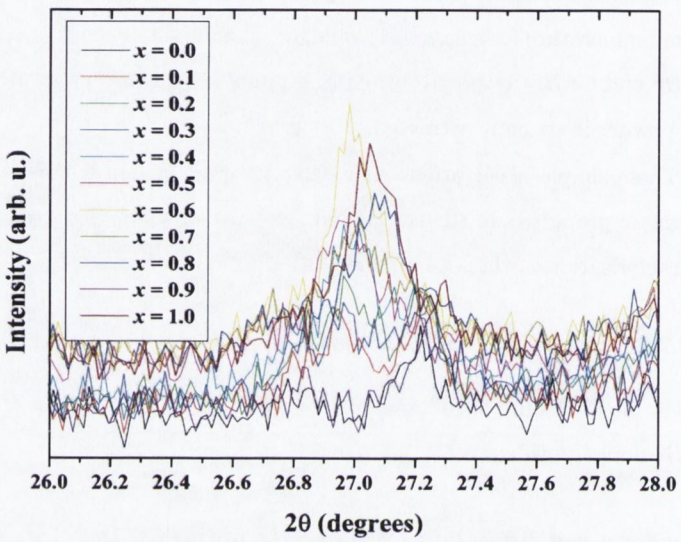

Figure 3.21: Zoom on a 2θ range of the XRD patterns of Br doped $CuCr_2Se_4$ showing the appearance of a $CuBr$ impurity phase.

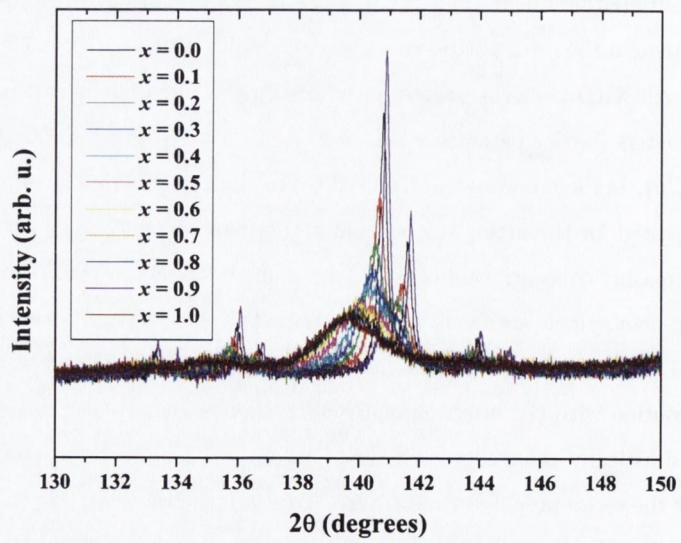

Figure 3.22: Zoom of a narrow range of the XRD pattern at high angle of Br-doped $CuCr_2Se_4$ showing the broadening of the peaks.

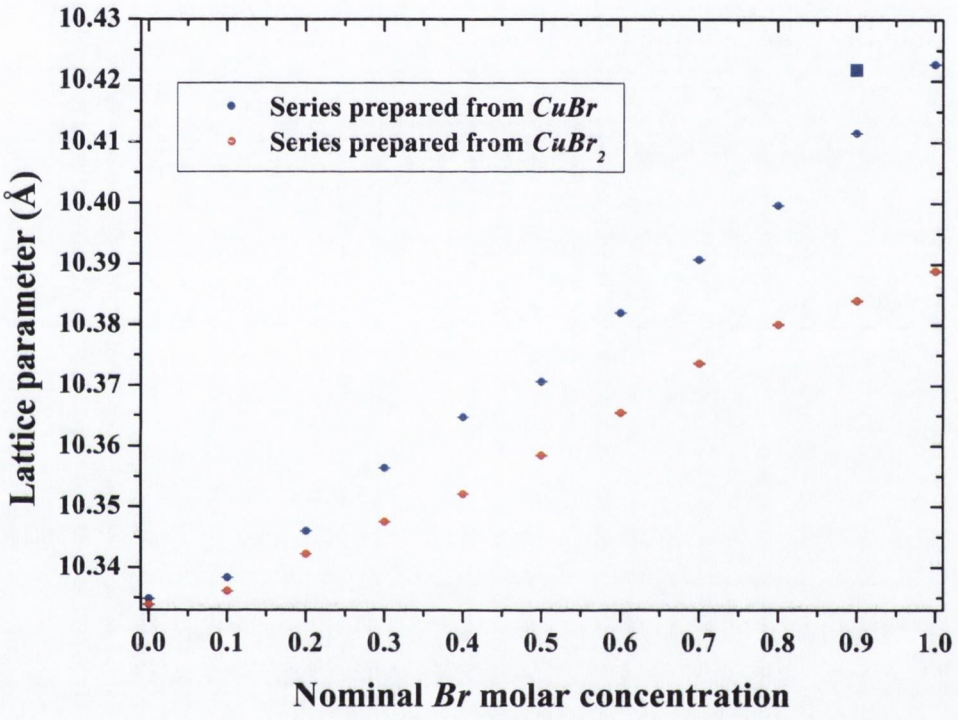

Figure 3.23: Evolution of the lattice parameter as a function of the Br concentration for the two initial reactants: the red dots are for the series prepared from $CuBr_2$ and the blue dots and squares are for the series prepared from $CuBr$. The square point corresponds to a powder measured just after breaking the evacuated ampoule, and the dots correspond to powders measured more than 48 h after opening the tube.

			Bond length (Å)		Bond angle (°)					
x	a (Å)	u	$Cr-Se$	$Cu-Se$	$\widehat{CrSeCr}$	$\widehat{CuSeCr}$	$s(Cu)$	R_p	R_{wp}	R_{Bragg}
Series prepared from $CuBr_2$ at 550°										
0.0	10.33388(1)	0.25675(4)	2.5157(4)	2.3582(4)	93.13(1)	123.02(1)	-	15.4	12.4	2.90
0.1	10.33610(2)	0.25696(4)	2.5141(4)	2.3624(5)	93.23(2)	122.94(2)	-	17.1	14.8	3.23
0.2	10.34224(2)	0.25666(4)	2.5186(4)	2.3585(5)	93.09(2)	123.05(1)	-	15.2	12.1	3.19
0.3	10.34754(4)	0.25667(4)	2.5198(5)	2.3599(5)	93.09(2)	123.04(2)	0.995(3)	15.8	13.1	3.40
0.4	10.35216(5)	0.25670(4)	2.5206(5)	2.3614(5)	93.11(2)	123.03(2)	0.979(3)	15.2	12.7	2.63
0.5	10.35849(6)	0.25656(4)	2.5235(5)	2.3604(5)	93.04(2)	123.08(2)	0.951(3)	15.3	13.0	2.61
0.6	10.36551(9)	0.25626(6)	2.5282(7)	2.3566(7)	92.90(2)	123.18(2)	0.895(4)	18.1	15.8	3.30
0.7	10.3737(1)	0.25605(7)	2.5322(7)	2.3547(7)	92.80(2)	123.26(2)	0.888(5)	18.2	16.2	3.01
0.8	10.3801(1)	0.25602(7)	2.5341(8)	2.3556(8)	92.79(3)	123.27(3)	0.866(5)	18.9	16.7	3.06
0.9	10.3840(1)	0.25592(7)	2.5360(8)	2.3547(8)	92.74(3)	123.30(3)	0.856(5)	19.1	16.8	3.07
1.0	10.3889(1)	0.25569(8)	2.5395(8)	2.3516(8)	92.64(3)	123.38(3)	0.833(5)	19.6	16.9	3.10
Series prepared from $CuBr$ at 750°										
0.0	10.33482(3)	0.25729(5)	2.5106(6)	2.3680(6)	93.39(2)	123.83(2)	-	10.7	10.1	1.96
0.1	10.33831(3)	0.25737(5)	2.5107(6)	2.3703(6)	93.42(2)	122.80(2)	-	10.8	10.0	1.99
0.2	10.34598(2)	0.25708(4)	2.5154(4)	2.3668(4)	93.29(1)	122.90(1)	-	10.7	10.2	1.91
0.3	10.35638(2)	0.25706(2)	2.5181(2)	2.3689(2)	93.278(7)	122.911(7)	0.936(3)	7.93	7.26	1.56
0.4	10.36459(3)	0.25703(3)	2.5204(4)	2.3702(5)	93.26(1)	122.92(1)	0.922(3)	7.70	6.96	1.28
0.5	10.37057(4)	0.25721(4)	2.5201(5)	2.3748(5)	93.35(2)	122.86(2)	0.854(2)	9.22	8.31	2.71
0.6	10.38197(3)	0.25700(3)	2.5249(3)	2.3736(3)	93.25(1)	122.93(1)	0.882(2)	8.99	8.40	1.38
0.7	10.39072(6)	0.25697(5)	2.5273(6)	2.3751(6)	93.23(2)	122.94(2)	0.861(4)	9.69	9.05	1.50
0.8	10.39965(4)	0.25695(4)	2.5297(8)	2.3768(4)	93.22(1)	122.95(1)	0.848(3)	10.4	9.77	1.39
0.9	10.42182(3)	0.25726(3)	2.5321(4)	2.3874(4)	93.37(1)	122.84(1)	0.797(3)	8.85	8.90	1.10
1.0	10.42270(4)	0.25743(5)	2.5306(5)	2.3907(5)	93.45(2)	122.78(2)	0.756(4)	8.68	8.75	1.48

Table 3.6: Crystallographic parameters and refinement factors for the two solid solutions synthesised.

The powders prepared from $CuBr$ exhibited poor stability, as indicated in Fig.3.23, with a lattice contraction of 0.1 % in 48 hr., this result is supported in the literature Pink *et al.* (1974a). Pink *et al.* (1974a) claimed that the spinels prepared from $CuBr_2$ are stable, however, contrasting results have been obtained in this study. In fact, the same shift in the Bragg peaks is observed when a sample is measured just after opening the tube and 24 hr. later without removing the sample from the XRD. This effect is clearly visible in Fig.3.24 where the small peak of the $CuBr$ impurity phase does not shift and yet the (311) peak from $CuCr_2Se_3Br$ shifts towards higher 2θ and hence smaller a. A small variation in the intensity of the peaks is also observed.

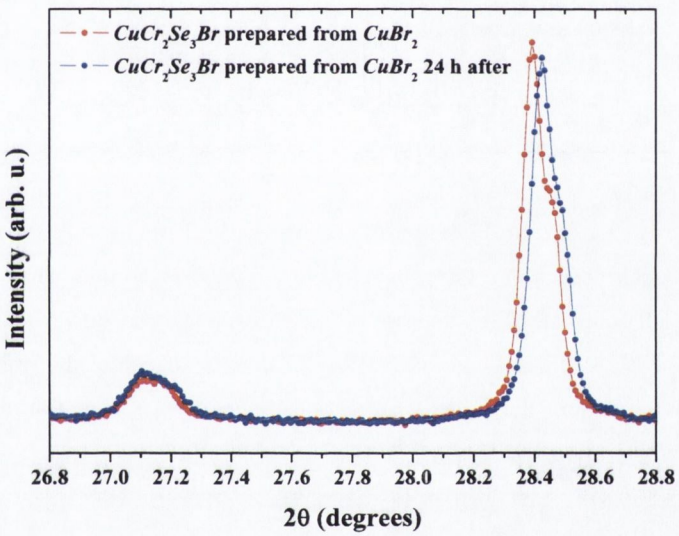

Figure 3.24: XRD pattern of $CuCr_2Se_3Br$ prepared from $CuBr_2$ just after opening the tube (red dots) and 24 h after (blue dots).

The calculated crystallographic parameters from the powder diffraction patterns shown in Fig.3.24, of a powder prepared from $CuBr_2$ at 750 °C are compared in Table 3.7.

The value of $B_{iso}(Cu)$ was high compared to the two other atoms for the normal stoichiometry. Even with the under-stoichiometry of Cu, the atomic thermal factor of the Cu is relatively high. The improvement in the refinement factor is an indication that the Cu-deficient model is more appropriate. A decrease in the lattice parameter is also observed after 24 h, this implies that the compound is not quite stable in air. The amount of $CuBr$ is calculated by introducing

t				B_{iso} (Å^2)					
(hr.)	a (Å)	u	$s(Cu)$	Cu	Cr	Se	R_p	R_{wp}	R_{Bragg}
0	10.39893(3)	0.25703(4)	1.0	4.20(7)	0.90(3)	0.77(1)	23.9	18.9	5.37
	10.39891(2)	0.25654(4)	0.876(3)	1.99(8)	0.91(3)	0.87(1)	23.4	18.3	4.17
24	10.39508(2)	0.25698(3)	1.0	3.93(6)	0.84(2)	0.68(1)	19.4	15.4	4.19
	10.39506(2)	0.25654(3)	0.881(1)	1.89(6)	0.86(2)	0.78(1)	18.5	14.7	2.92

Table 3.7: Crystallographic parameters extracted from XRD patterns of a $CuCr_2Se_3Br$ sample prepared from $CuBr_2$ at 750°C recorded immediately upon exposure of the powder to atmosphere and after a 24 h delay.

it as a second phase in the refinement. After opening the tube, the amount of $CuBr$ in the powder increases from 4.7(1) mass% to 5.6 mass% after 24 hr.

Powder neutron diffraction The structural properties have also been studied by powder neutron diffraction. The refinement of a $CuCr_2Se_3Br$ sample at 300 K prepared from $CuBr_2$ and fired at 750°C is presented in Fig.3.25 and the crystallographic parameters are summarised in Table 3.8 [1]. In contrast to the XRD measurements, the sample should not undergo any change during the neutron diffraction measurements since the measurements were performed in He atmosphere.

	R_p		R_{wp}		R_{Bragg}	
300 K	12.4		9.25		4.14	
	a (Å)	u	$d(Cu-Se)$ (Å)	$d(Cr-Se)$ (Å)	$\widehat{CuSeCr}$ (°)	$\widehat{CrSeCr}$ (°)
	10.41752(7)	0.25724(3)	2.3861(4)	2.5312(4)	122.85(1)	93.36(1)
	R_p		R_{wp}		R_{Bragg}	
2 K	9.18		7.67		2.00	
	a (Å)	u	$d(Cu-Se)$ (Å)	$d(Cr-Se)$ (Å)	$\widehat{CuSeCr}$ (°)	$\widehat{CrSeCr}$ (°)
	10.40029(2)	0.25731(1)	2.3834(1)	2.52634(1)	122.825(1)	93.395(1)

Table 3.8: Crystallographic parameters of $CuCr_2Se_3Br$ prepared from $CuBr_2$ at 750 °C extracted from the refinement of the powder neutron diffraction data, measured at 300 K and at 2 K, on the 3T2 diffractometer.

In this case, a large value of $B_{iso}(Cu)$ is obtained compared to the two other atomic thermal factors confirming the observations of the XRD study. Moreover, residuals in the difference

[1] The sample was kept in its evacuated quartz tube until the measurement.

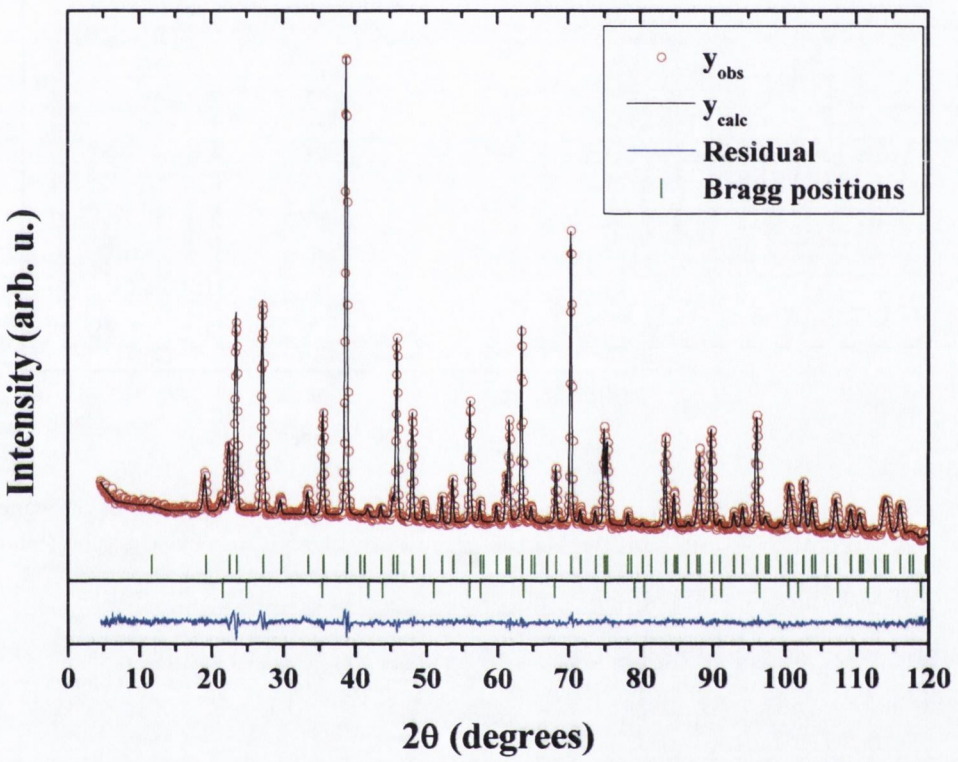

Figure 3.25: Powder neutron diffraction pattern measured at 300 K with $\lambda = 1.225270$ Å for $CuCr_2Se_3Br$ powders prepared from $CuBr_2$ and fired at 750°C (red empty dots), the fit to the spinel and $CuBr$ structures (black solid line), and the difference plots (blue solid line). The upper dark green sticks represent the calculated Bragg positions for $CuCr_2Se_3Br$, and the lower ones correspond to the calculated Bragg positions for $CuBr$.

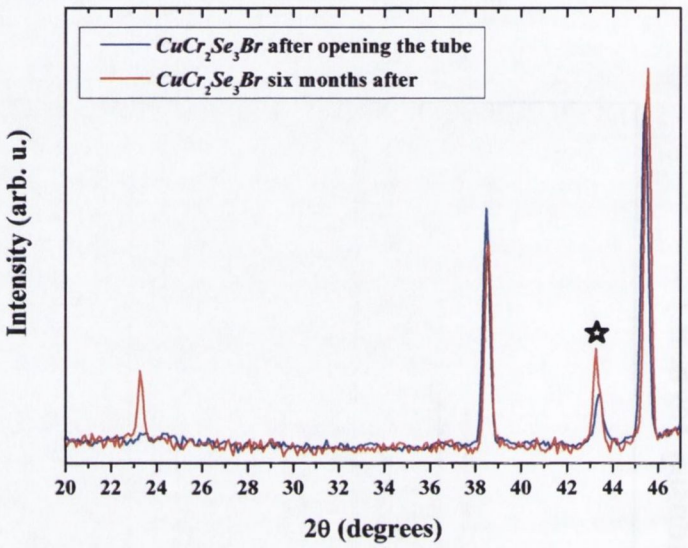

Figure 3.26: Powder neutron diffraction pattern measured at 290 K of the same powder as in Fig.3.25 measured on the G4.1 spectrometer just after opening the tube (blue curve) and 6 months later (red curve). The $CuBr$ impurity is marked with a star.

Fourier map are observed around the Cu peaks[1]. The refined Cu stoichiometry and the atomic thermal factors are presented in Table 3.9.

T (K)	B_{iso} (Å^2)			$s(Cu)$
	Cu	Cr	Se	
300	1.50(4)	0.65(2)	0.697(9)	0.863(6)
2	0.63(2)	0.102(9)	0.079(4)	0.87(1)

Table 3.9: Cu occupation factor, and atomic temperature factors for Cu, Cr and Se at 300 K and 2 K.

The negative slope of the observed background provides further evidence for the reaction of the sample in air. In fact, the sample was exposed to air during the transfer from one spectrometer to the other. This exposure time seems to have been enough for the measurement to show a typical background of a sample with some hydrogen, presumably due to the presence of water. The measurement of the same sample after a period of six months in air (Fig.3.26) leads us to the same conclusion as obtained with the XRD study: a reduction in the lattice

[1]This could be due to the presence of the impurity phase

parameter, and an increase in the $CuBr$ content. Moreover, the appearance of the magnetic peak signifies that the ordering temperature has increased above room temperature.

The evolution of the lattice parameter has been studied as a function of temperature on the G4.2 spectrometer and is presented in Fig.3.27. The same parabolic behaviour as found in samples with no bromine, is observed. The discrepancy between the lattice parameters obtained on the two instruments is not only due to the definition of the wavelength, but also the sample clearly changed during the transfer from one spectrometer to the other. Therefore, no further data analysis has been attempted.

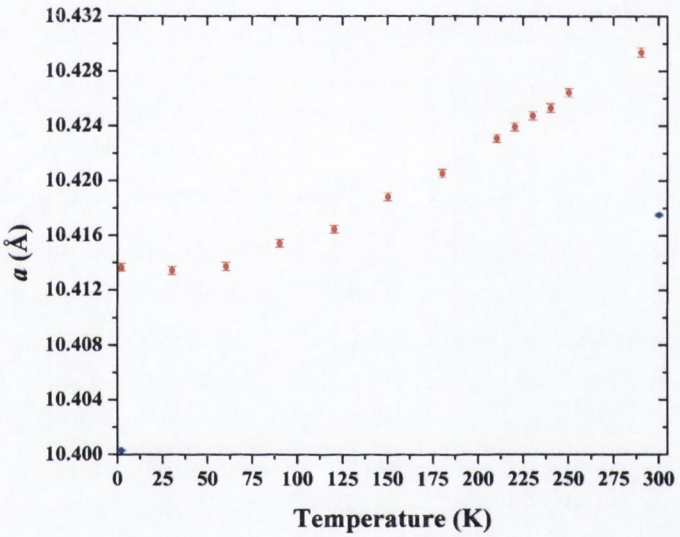

Figure 3.27: Evolution of the lattice parameter of $CuCr_2Se_3Br$ as a function of the temperature. The red dots are from data collected on the G4.1 neutron diffractometer, and the blue dots are extracted from the data collected on the 3T2 neutron diffractometer.

3.2.2.3 Magnetic properties

The magnetic properties of the solid solution have been studied by DC magnetometry and neutron diffraction.

DC magnetometry The magnetisation as a function of the applied field has been measured for all the samples prepared from $CuBr$. The linear increase in the saturation moment with doping concentration, reported in the literature Miyatani *et al.* (1971); Robbins *et al.* (1968)

is not obvious due to the formation of impurity phases observed by XRD as described earlier. The temperature dependence of the magnetisation is plotted in Fig.3.28. The magnetisation exhibits an anomaly around 120 K due to the $CuBr$ impurity phase in the powder. The Curie

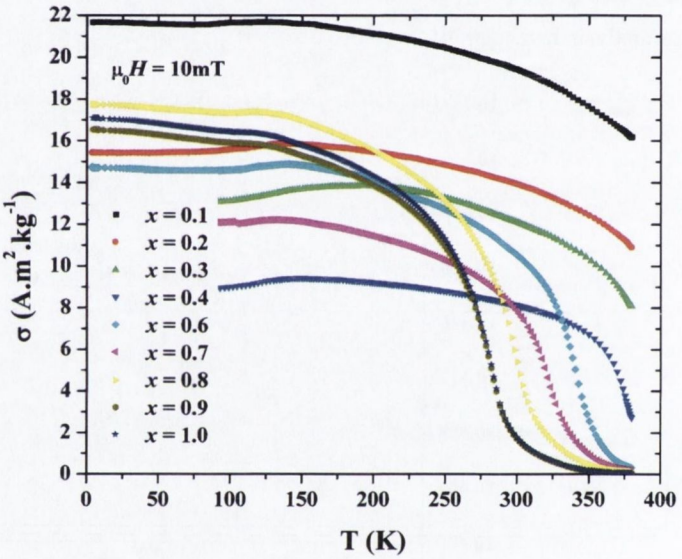

Figure 3.28: Evolution of the magnetisation under an external field of 10 mT of the solid solution series $CuCr_2Se_4 - CuCr_2Se_4Br$ as a function of the temperature.

temperature of the compound decreases with increasing Br content, this data is contrary to the behaviour reported in the literature Miyatani *et al.* (1971); Robbins *et al.* (1968). T_C does not decrease linearly but instead tends to saturate just below room temperature for $x \geq 0.8$. This difference may be explained by the fact that the magnetisations of the powder were measured more than one month after their synthesis and the samples were exposed to air throughout this period. It seems that the chemical decomposition tends towards an equilibrium composition of Br.

Powder neutron diffraction In order to understand the effect of the introduction of Br on the magnetic structure, three intermediate compositions $x = 0.5, 0.8, 1.0$ have been studied by powder neutron diffraction.

The evolution of the spectra recorded on the G4.1 spectrometer as a function of temperature for $CuCr_2Se_3Br$ is shown in Fig.3.29.

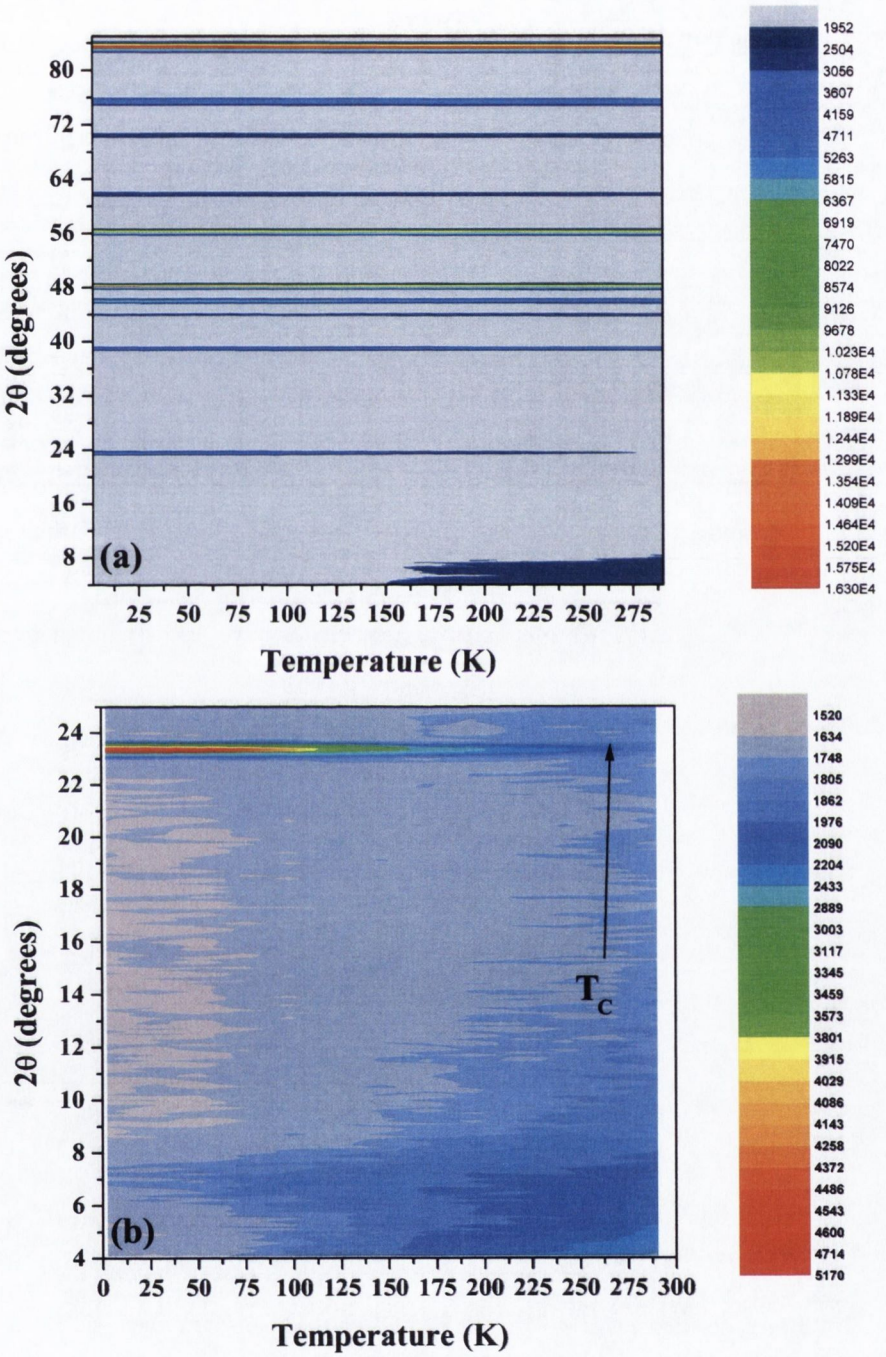

Figure 3.29: (a) Evolution of the powder neutron diffraction pattern of $CuCr_2Se_3Br$ recorded on the G4.1 spectrometer as a function of temperature. (b) Zoom on the low angle part of the diffraction pattern, the Curie temperature is marked with an arrow where the intensity of the (111) peak becomes constant.

This graph shows that the overall magnetic structure of the compound did not change drastically compared to the end member, since no new magnetic peaks appeared. The transition temperature of this compound, however, is just below room temperature as measured by magnetometry as reflected by the decreasing intensity of the (111) peak around 23 °C.

To refine the magnetic structure, the structural values extracted from the data of the 3T2 diffractometer have been used. To begin the magnetic structure refinement, the same model that was determined for $CuCr_2Se_4$ was used and a $R_{mag} = 3.50$ was obtained. The residual showed peaks corresponding to a small magnetic moment on the Cu as in the model shown in Fig.3.20. The inclusion of the copper atom in the magnetic model leads to a detectable moment antiparallel to the moment on the Cr and gives $R_{mag} = 1.44$. The result of the fitting using this final model is presented in Fig.3.30.

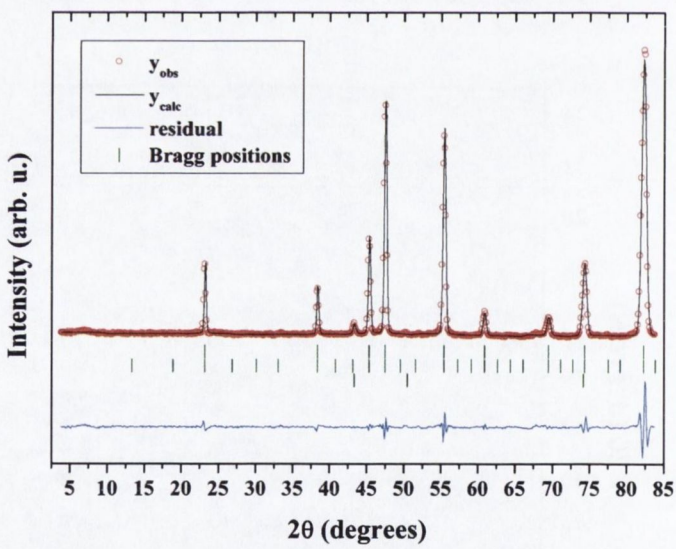

Figure 3.30: Powder neutron diffraction pattern measured at 2 K using the G4.1 spectrometer of $CuCr_2Se_3Br$ (red empty dots), the fit to the spinel and $CuBr$ structures (black solid line), and the difference plots (blue solid line). The first line of dark green sticks represent the calculated Bragg positions, the second corresponds to the calculated magnetic Bragg positions and the third to the Bragg positions of $CuBr$.

Similar results were obtained for the $x = 0.8$ and $x = 0.5$ compositions, the latter having a transition temperature above room temperature. The Cu stoichiometry, magnetic moments on the Cu and Cr sites, and the corresponding refinement factors are given in Table 3.10.

	$s(Cu)$	m (μ_B)		R_p	R_{wp}	R_{Bragg}	R_{mag}
		Cu	Cr				
$x = 1.0$	0.87(1)	-0.54(9)	2.68(8)	14.3	12.0	1.68	1.44
		0	2.97(6)	14.9	12.3	2.76	3.50
$x = 0.8$	0.88(1)	-0.3(1)	2.92(9)	15.7	15.4	2.62	1.85
		0	3.06(7)	15.8	15.4	3.23	2.89
$x = 0.5$	0.93(1)	-0.2(1)	2.9(1)	17.2	17.8	3.98	2.72
		0	3.07(8)	17.3	17.8	4.31	3.13

Table 3.10: Calculated magnetic moments and copper stoichiometry obtained by powder neutron diffraction for different Br concentrations.

The magnetic correlation length is determined as a function of temperature using equation 3.5 and its evolution is shown in Fig.3.31.

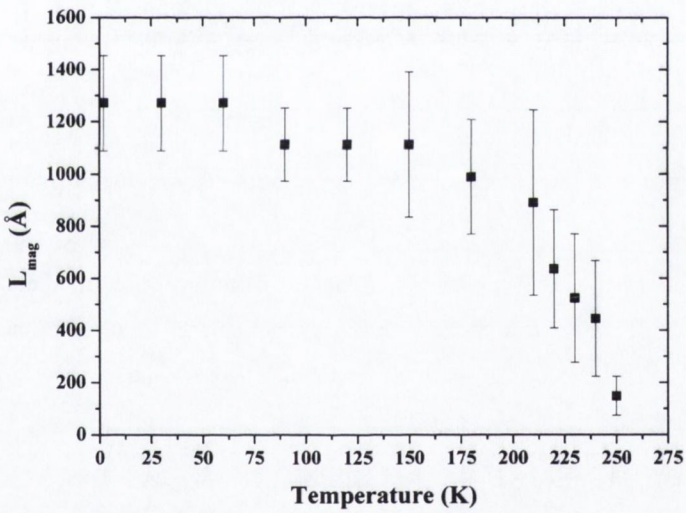

Figure 3.31: Magnetic correlation length as a function of temperature for $CuCr_2Se_3Br$

Another phenomenon which occurs close to the magnetic transition is the balance between the ordered magnetic moment and the excitation of magnons. The coherent scattering expressed in the Bragg reflection gives information on the magnitude of the ordered moment, whereas the magnon population is related to incoherent scattering. When the temperature is increased close to the Curie point, the background level increases at small angles as illustrated in Fig.3.32.

The area under the curve is proportional to the incoherent magnetic scattering. The evolu-

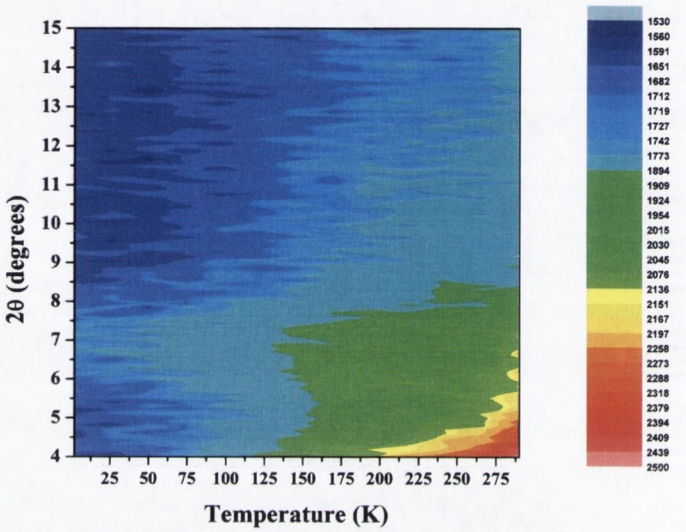

Figure 3.32: Low angle zoom on the background as a function of temperature for $CuCr_2Se_3Br$.

tion of the ordered moments is correlated with the excitation of magnons by comparing the area with the integrated intensity of the magnetic peaks. The variation of the magnetic moments is plotted in Fig.3.33, assuming that the incoherent magnetic scattering is null at 2 K.

3.2.3 Discussion

The magnetic and structural properties of $CuCr_2Se_4$ and its solid solution with $CuCr_2Se_3Br$ has been studied by conventional diffraction and magnetometry. The saturation magnetic moment measured in this system depends on the preparation conditions. The powder neutron diffraction carried out on $CuCr_2Se_4$ confirmed the first results obtained in that system Colominas (1967), where the Cr magnetic moment is measured to be 3 μ_B/mol. There is no evidence of an antiferromagnetic moment localised on the Cu, and the hypothesis of a delocalised moment seems to be reasonable since the system is metallic. The study of the Br-doped composition gave a new picture of the magnetic properties of the system. In fact, if no net magnetic moment is localised on the Cu in the pure composition, the introduction of one more electron in the system leads to the appearance of a local magnetic moment on the Cu which is aligned antiparallel to the Cr moment. The magnetic structure of $CuCr_2Se_3Br$ is plotted on Fig.3.34 with the magnetic atom and their moments on scale. Another result from this study is the

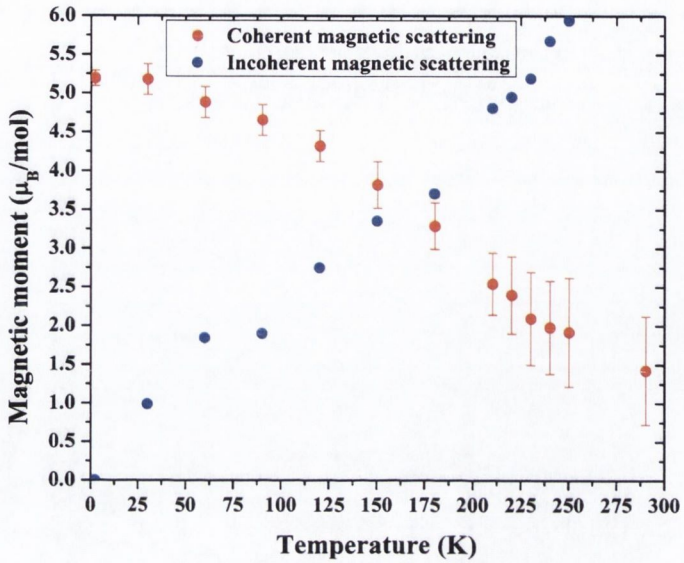

Figure 3.33: Evolution of the coherent (red curve) and incoherent (blue curve) integrated magnetic intensity. The right hand scale is normalised to the total magnetic moment found at 2 K.

observation of the Cu deficiency in the Br-doped composition and a B_{iso} with a high value compared to the rest of the atoms.

3.3 $CdCr_2Se_4$ and its solid solution with Ag and In

Of the three compounds studied in the present work, $CdCr_2Se_4$ may be the most promising because of the possibility of doping it both p- and n-type. It is therefore important to prepare the compound and investigate, in detail, the solubility of each of the dopants.

3.3.1 Pure $CdCr_2Se_4$

Before studying the solid solution of $CdCr_2Se_4$ with different dopants it is important to know the precise conditions for preparation and the properties of the end member.

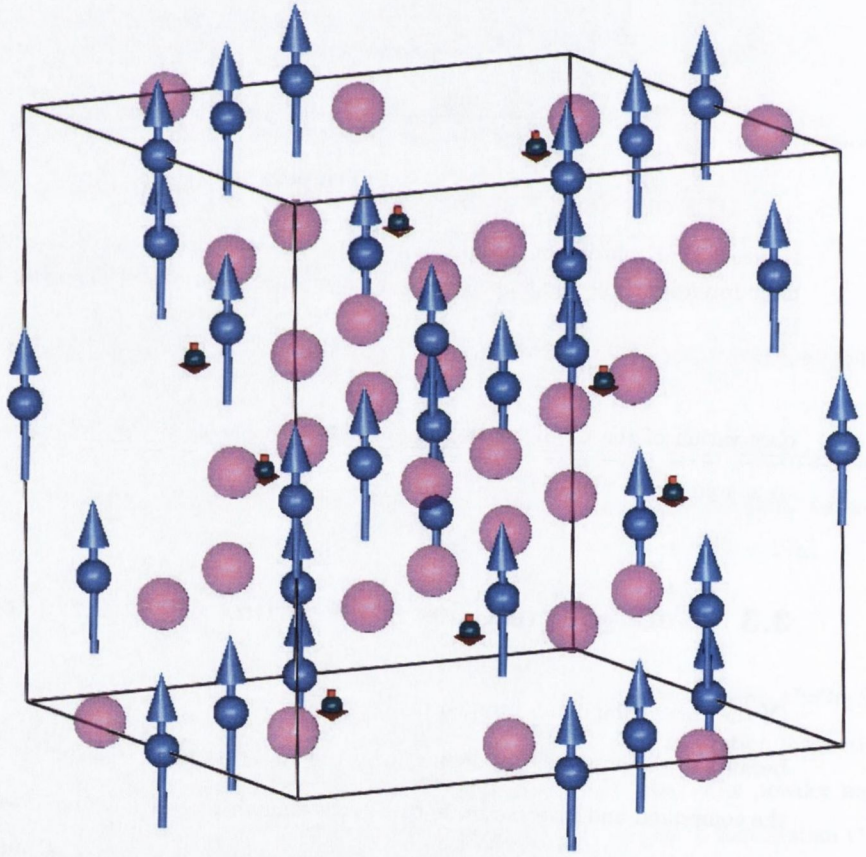

Figure 3.34: Magnetic structure of $CuCr_2Se_3Br$ as determined by powder neutron diffraction. The magnetic moment are represented on scale by arrows on the magnetic atoms.

3.3.1.1 Reaction scheme

The preparation of $CdCr_2Se_4$ has been performed by solid state reaction from $CdSe$, Cr, and Se according to the equation:

$$CdSe + 2Cr + 3Se \longrightarrow CdCr_2Se_4 \tag{3.8}$$

The reaction temperature was 750°C, just below the peritectoid decomposition temperature. The product is a fine, metallic grey powder. The powder is not attracted to a magnet at room temperature but becomes magnetic upon cooling it in liquid nitrogen.

3.3.1.2 Structural characterisation

Powder x-ray diffraction The XRD pattern of $CdCr_2Se_4$ is shown in Fig.3.35 along with the refinement based on a spinel model and the extracted parameters are listed in Table 3.11. The refinement is of rather poor quality because of the coincidence of the peak due to the tungsten wavelength and the peak due to the copper wavelength as illustrated in Fig.C.4 in appendix C.

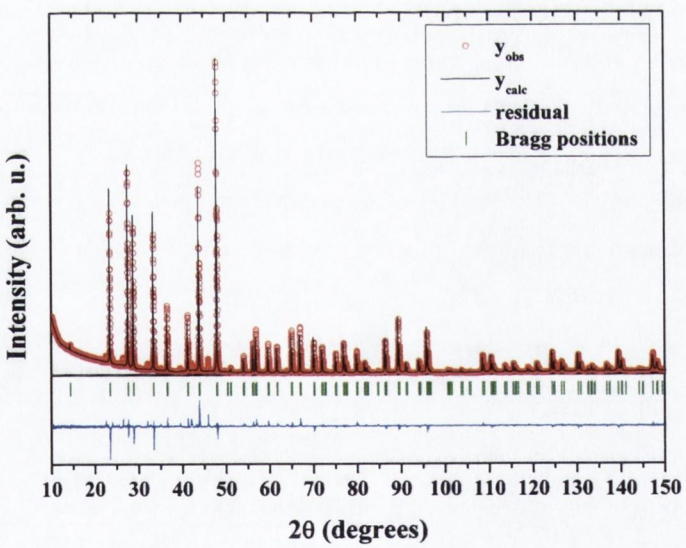

Figure 3.35: Powder x-ray diffraction pattern measured at room temperature for $CdCr_2Se_4$ powder fired at 750°C (red empty dots), the fit to the spinel structure (black solid line), and the difference plots (blue solid line). The dark green sticks represent the calculated Bragg positions.

R_p		R_{wp}		R_{Bragg}	
13.0		13.9		7.21	
a (Å)	u	$d(Cd-Se)$ (Å)	$d(Cr-Se)$ (Å)	$\widehat{CdSeCr}$ (°)	$\widehat{CrSeCr}$ (°)
10.74259(2)	0.26458(4)	2.5971(3)	2.5387(3)	120.26(1)	96.84(1)
$B_{overall}$ (Å^2)					
0.16(1)					

Table 3.11: Crystallographic parameters of $CdCr_2Se_4$ after refinement of the powder x-ray diffraction data obtained at 295 K.

The powder appears to be single phase, but the parasitic wavelength arising from the x-ray tube prevents proper analysis of the data.

Powder neutron diffraction To date there is no report of powder neutron diffraction on $CdCr_2Se_4$ in the literature, one of the obvious reasons for this is the high absorption coefficient ($b(Cd) = 2520$ barns) of Cd by neutrons [1], the linear absorption coefficient of $CdCr_2Se_4$ was calculated to be 1.16 mm^{-1} . Nevertheless, an attempt to measure powder neutron diffraction data on this material has been carried out in this study. The spectrum together with its refinement obtained at 300 K on the 3T2 spectrometer are presented in Fig.3.36. The extracted parameters and refinement factors are summarised in Table 3.12, while the temperature factors are reported in Table 3.13.

	R_p		R_{wp}		R_{Bragg}	
300 K	25.4		15.0		7.16	
	a (Å)	u	$d(Cd-Se)$ (Å)	$d(Cr-Se)$ (Å)	$\widehat{CrSeCr}$ (°)	$\widehat{CdSeCr}$ (°)
	10.7479(1)	0.26416(5)	2.5906(6)	2.5439(6)	96.64(2)	120.41(2)
	R_p		R_{wp}		R_{Bragg}	
2 K	21.7		14.0		5.90	
	a (Å)	u	$d(Cd-Se)$ (Å)	$d(Cr-Se)$ (Å)	$\widehat{CrSeCr}$ (°)	$\widehat{CdSeCr}$ (°)
	10.73405(8)	0.26418(5)	2.5876(5)	2.5404(5)	120.40(2)	96.65(2)

Table 3.12: Crystallographic parameters of $CdCr_2Se_4$ after refinement of the powder neutron diffraction data from the diffractometer 3T2 obtained at 300 K and 2 K.

[1] Cd metal is used as a beam stopper.

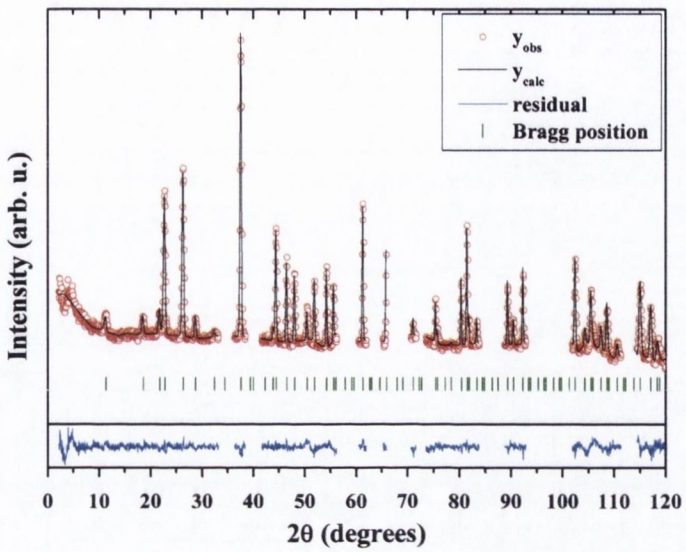

Figure 3.36: Powder neutron diffraction pattern measured at 300 K of $CdCr_2Se_4$ powder (red empty dots), the fit to the spinel (black solid line), and the difference plots (blue solid line). The dark green sticks represent the calculated Bragg positions for $CdCr_2Se_4$.

T (K)	B_{iso} (Å^2)		
	Cu	Cr	Se
300	1.70(9)	1.08(7)	0.73(2)
2	0.76(7)	0.87(7)	0.30(2)

Table 3.13: Atomic temperature factors of Cd, Cr and Se at 300 and 2 K.

3.3.1.3 Magnetic properties

The magnetic properties of $CdCr_2Se_4$ were studied by DC and AC magnetometry and powder neutron diffraction.

DC magnetometry The variation of the magnetisation as a function of the applied field is plotted in Fig.3.37 at 300 K and 4 K. A typical paramagnetic curve is observed at 300 K whereas ferromagnetic behaviour is detected at 4 K. A saturation magnetic moment of 5.6 μ_B/mol is found on the $CdCr_2Se_4$ sample at 4 K under an applied magnetic field of 5 T. The value obtained is close to the theoretical value for Cr^{3+}. The evolution in the magnetic moment as a function of temperature under an applied magnetic field was also measured, this is presented

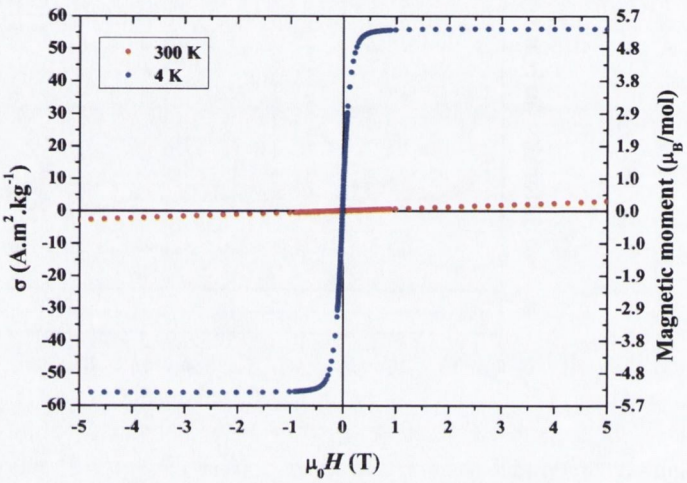

Figure 3.37: Magnetisation in function of the applied field of $CdCr_2Se_4$ at 300 K (red dots) and 4 K (blue dots)

in Fig.3.38. The only magnetic transition visible is due to $CdCr_2Se_4$, this indicates that the powder is magnetically single phase. The extracted Curie temperature is 129(1) K, which is similar to the values reported in the literature Pinch & Berger (1968).

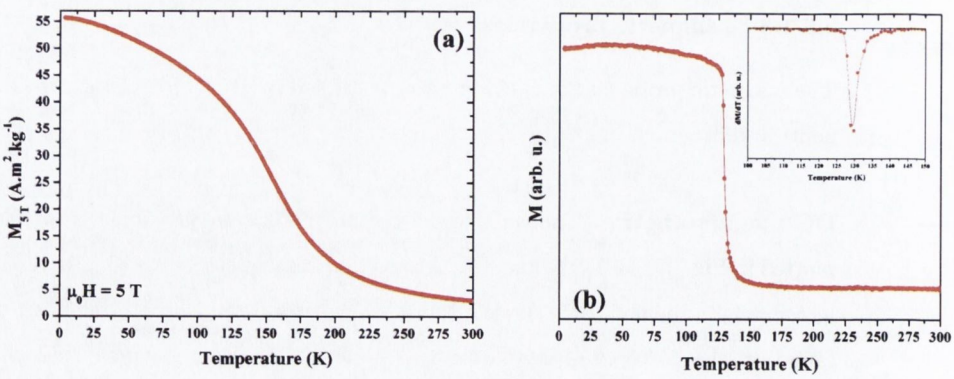

Figure 3.38: (a) Saturation magnetisation as a function of temperature and (b) Thermoremanent curve of $CdCr_2Se_4$, the inset shows the derivative of the magnetisation around the transition temperature.

AC susceptibility The real and imaginary part of the AC susceptibility of $CdCr_2Se_4$ is presented on Fig.3.39 (a) and (b) respectively. A sharp transition at 129 K is observed. The decrease in the susceptibility observed at low temperature might be due to the presence of antifferomagnetic compounds on the surface of the powder.

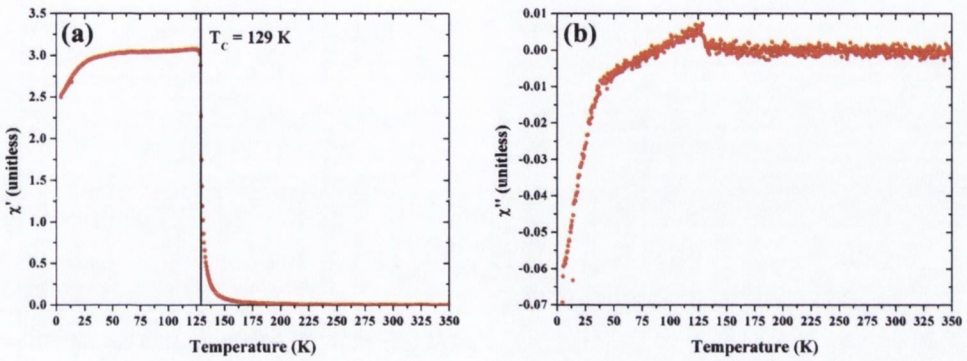

Figure 3.39: (a) Real and (b) imaginary part of the susceptibility of the $CdCr_2Se_4$ powder.

Powder neutron diffraction The magnetic properties of pure $CdCr_2Se_4$ have been investigated by powder neutron diffraction, the pattern obtained on the 3T2 spectrometer at 2 K is shown in Fig.3.40 together with the structural and magnetic refinement. The magnetic agreement factor was found to be $R_{\text{mag}} = 3.88$ and the magnitude of the moment on the Cr atoms was $m(Cr) = 2.90(7)\ \mu_B$/mol which is close to the theoretical spin only value of Cr^{3+} ions. The temperature evolution of the magnetic moment was obtained from data collected on the G4.1 spectrometer and is presented in Fig.3.41

3.3.2 Ag and In doped $CdCr_2Se_4$

It would be useful to have a magnetic semiconductor that could be doped both p- and n-type [1] without degrading the crystal quality. It has been reported that Ag and In are p- and n-dopants respectively for $CdCr_2Se_4$ Lehmann (1967). To investigate the solubility limit of these two dopants, series of powders have been synthesised by solid state reaction following the equations:

$$(1-x)CdSe + \frac{x}{2}In_2Se_3 + 2Cr + \left(3 - \frac{x}{2}\right)Se \longrightarrow Cd_{1-x}In_xCr_2Se_4 \tag{3.9}$$

[1] Assuming that the compound is an intrinsic semiconductor.

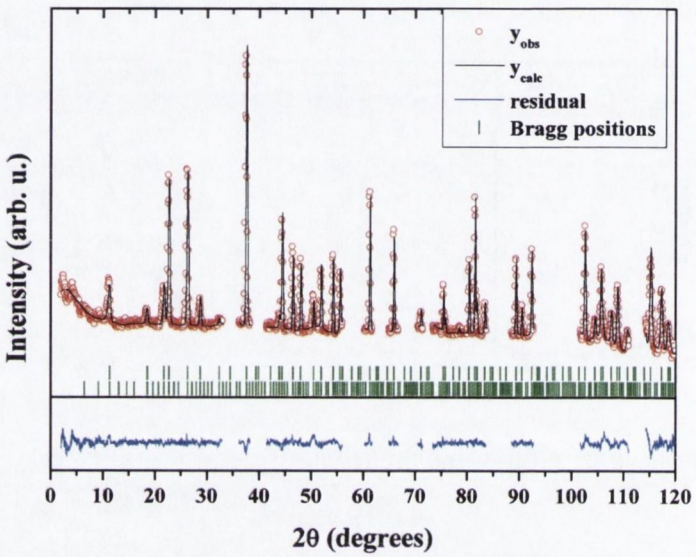

Figure 3.40: Powder neutron diffraction pattern measured at 2 K of $CdCr_2Se_4$ powder (red empty dots), the fit to the spinel (black solid line), and the difference plots (blue solid line). The dark green sticks represent the calculated Bragg positions for $CdCr_2Se_4$.

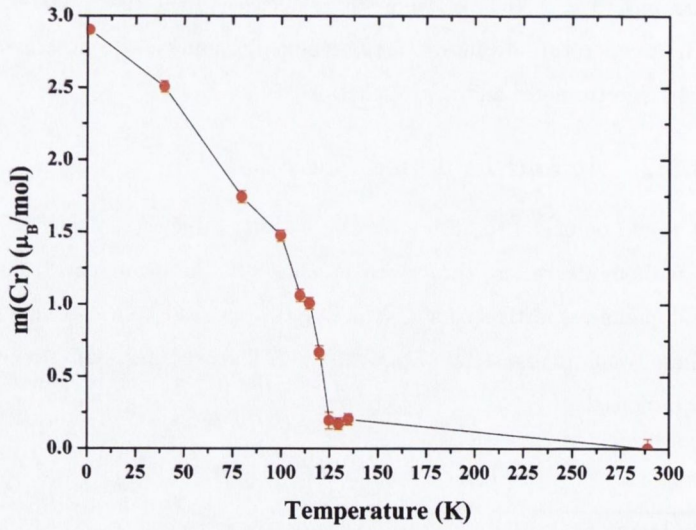

Figure 3.41: Evolution of the Cr magnetic moment as a function of the temperature measured by powder neutron diffraction on the G4.1 spectrometer.

$$(1-x)CdSe + xAg + 2Cr + (x+3)Se \longrightarrow Cd_{1-x}Ag_xCr_2Se_4 \tag{3.10}$$

with $x = 0.02, 0.04, 0.06, 0.08, 0.01$ for Ag-doping and $x = 0.01, 0.03, 0.05, 0.07, 0.09$ for In-doping $CdCr_2Se_4$. The synthesised powders are all grey, metallic powders with very fine grains.

3.3.3 Structural characterisation

The phase purity of the synthesised powders was checked by XRD and the lattice parameters were extracted from the refinement. The Ag-doped samples were found to be single phase for all compositions, whereas a $InCr_2Se_4$ impurity phase was found in In-doped $CdCr_2Se_4$ for $x > 0.03$ as illustrated in Fig.3.42.

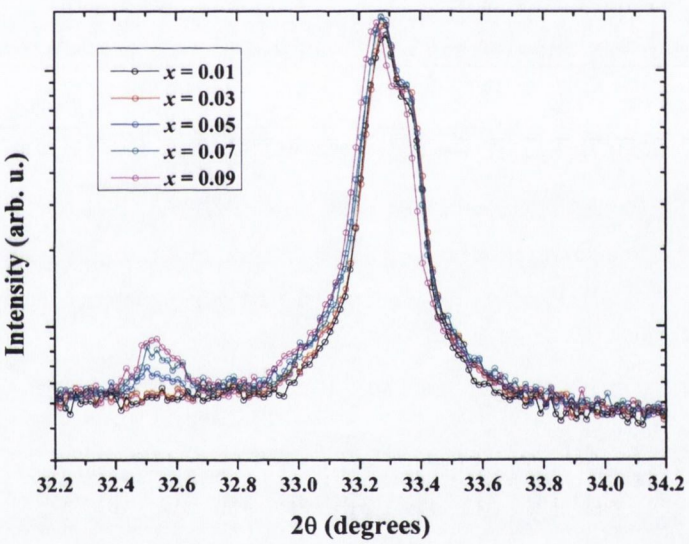

Figure 3.42: Zoom of the XRD pattern of In-doped $CdCr_2Se_4$ where an impurity peak identified as a $InCr_2Se_4$ peak appears. Note the logarithmic intensity scale.

The evolution of the lattice parameter is compared for both series of Ag- and In-doped samples, as shown in Fig.3.43. The introduction of Ag does not seem to disturb the lattice, a strong increase if the lattice parameter, on the other hand, is observed when the compound is doped by In.

Although the lattice parameter continues to increase after the appearance of the impurity phase, the solubility limit of In in $CdCr_2Se_4$ ($x \approx 0.03$) seems to be very low compared to Ag-doped samples.

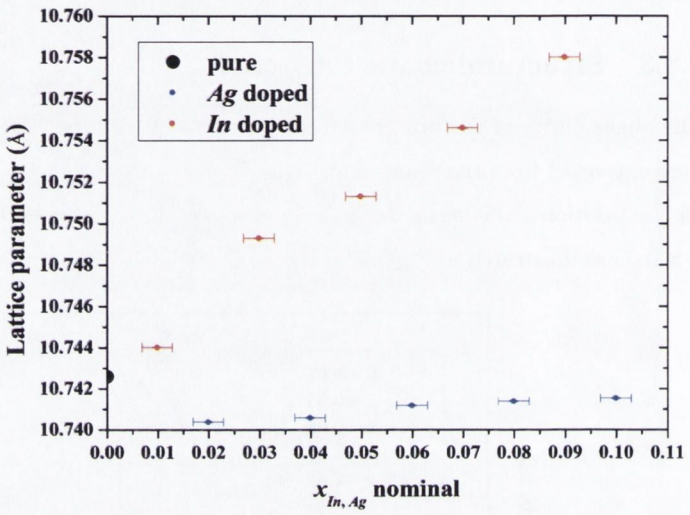

Figure 3.43: Evolution of the lattice parameter as a function of the nominal concentration of In (red dots) and Ag (blue dots). The lattice parameter of the pure compound (black dot) is provided as reference.

3.4 $HgCr_2Se_4$

There are very few reports in the literature on the preparation and characterisation of $HgCr_2Se_4$ Baltzer *et al.* (1966). In this work, $HgCr_2Se_4$ powders have been synthesised and characterised structurally and magnetically.

3.4.1 Reaction scheme

In order to prepare $HgCr_2Se_4$ by solid state reaction, $HgSe$, Cr, and Se have been used as reactants following the equation:

$$HgSe + 2Cr + 3Se \longrightarrow HgCr_2Se_4 \tag{3.11}$$

The reaction temperature was 550°C, just under the peritectic decomposition temperature. The resulting product was a fine, metallic black powder. The powders are not attracted to a magnet at room temperature but become magnetic after cooling the samples in liquid nitrogen.

3.4.2 Structural characterisation

The XRD pattern of $HgCr_2Se_4$ is presented in Fig.3.44 together with the refinement based on a spinel model and the extracted parameters are listed in Table 3.14.

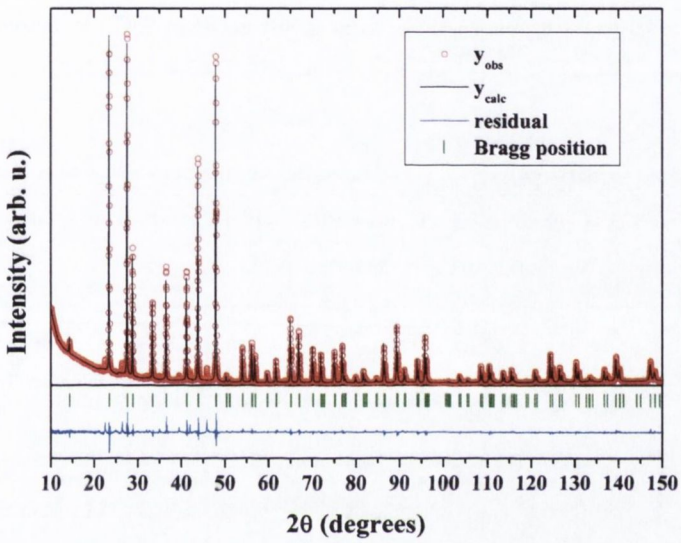

Figure 3.44: Powder x-ray diffraction pattern measured at room temperature for $HgCr_2Se_4$ powder fired at 550°C (red empty dots), the fit to the spinel structure (black solid line), and the difference plots (blue solid line). The dark green sticks represent the calculated Bragg positions.

R_p		R_{wp}		R_{Bragg}	
10.3		11.5		2.52	
a (Å)	u	$d(Hg-Se)$ (Å)	$d(Cr-Se)$ (Å)	$\widehat{HgSeCr}$ (°)	$\widehat{CrSeCr}$ (°)
10.74189(2)	0.26464(4)	2.5981(5)	2.5380(5)	120.24(2)	96.87(2)
		B_{iso} (Å^2)			
Hg		Cr		Se	
0.58(2)		0.70(4)		0.39(2)	

Table 3.14: Crystallographic parameters of $HgCr_2Se_4$ after refinement of the powder x-ray diffraction data obtained at 295 K.

X-ray diffraction analysis confirmed that the obtained powders are single phase. The sample is therefore suitable for magnetic study.

3.4.3 Magnetic properties

The magnetic properties have been investigated by DC magnetometry and AC susceptibility measurements.

DC magnetisation The variation of the magnetisation as a function of the applied field is plotted in Fig.3.45 at 300 K and 4 K. A typical paramagnetic curve is observed at 300 K, while ferromagnetic behaviour is detected at 4 K.

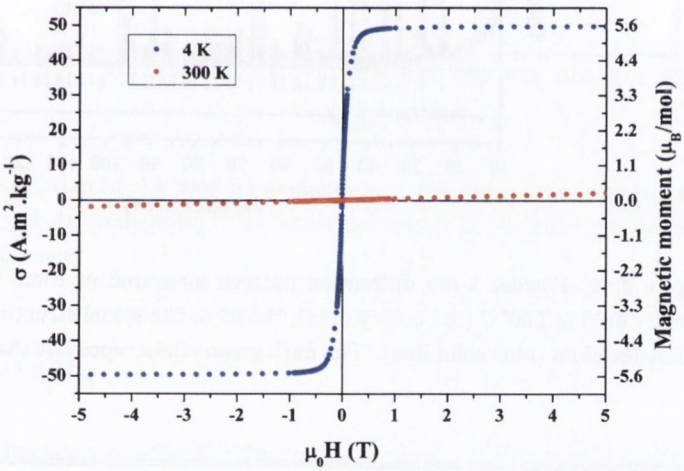

Figure 3.45: Magnetisation as a function of the applied field of $HgCr_2Se_4$ at 300 K (red dots) and 4 K (blue dots)

A saturation magnetic moment of 5.6 μ_B/mol is found at 4 K under an applied magnetic field of 5 T. The thermoremanent curve of the synthesised powder is shown in Fig.3.46. No other magnetic transitions are observed. The extracted Curie temperature is 105(1) K which is lower than the reported 109 K Baltzer *et al.* (1965).

AC susceptibility The real and imaginary part of the AC susceptibility of $CdCr_2Se_4$ is presented on Fig.3.47 (a) and (b) respectively. A sharp transition at 106 K is observed. The decrease in the susceptibility observed at low temperature might be due to the presence of antifferomagnetic compounds on the surface of the powder.

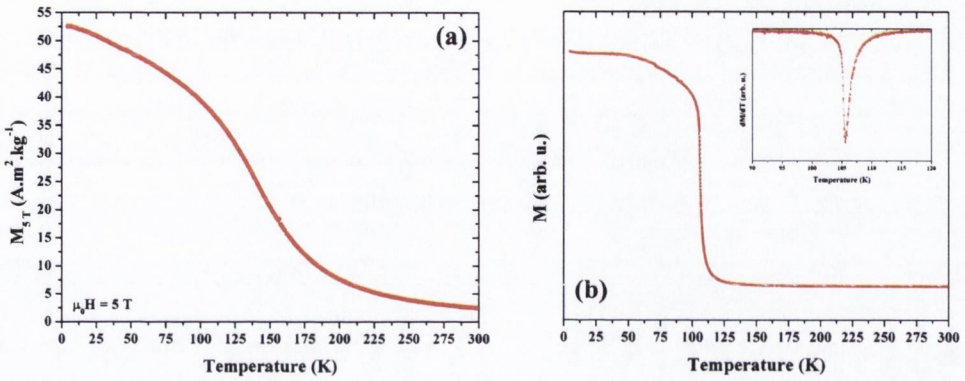

Figure 3.46: (a) Saturation magnetisation as a function of temperature and (b) Thermoremanent curve of $HgCr_2Se_4$, the inset shows the derivative of the magnetisation around the transition temperature.

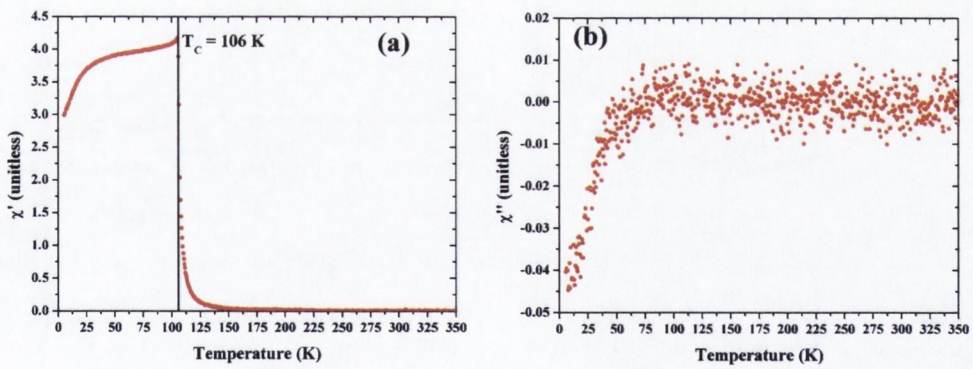

Figure 3.47: (a) Real and (b) imaginary part of if the susceptibility of $HgCr_2Se_4$ powder.

3.5 Low temperature magnetisation exponent

The low temperature part of the saturation magnetisation is increased due to the magnon contribution. When the magnon dispersion is quadratic, it can be described according to the Bloch law where the magnetisation follows the relation:

$$M(T) = M_S - (1 - B \cdot T^{3/2}) \tag{3.12}$$

and the coefficient B is related to the spin-wave stiffness constant D by the relation

$$B = \frac{0.059 g \mu_B}{M_s} \cdot \left(\frac{k}{D}\right) \tag{3.13}$$

The low temperature saturation magnetisation as a function of $(T/T_C)^{3/2}$ is plotted in Fig.3.48(a) for $CuCr_2Se_4$, $CuCr_2Se_3Br$, $CdCr_2Se_4$, and $HgCr_2Se_4$ with the respective linear fits between 5 K and 20 K. It can be seen from Fig.3.48 that this expression does not describe the low tem-

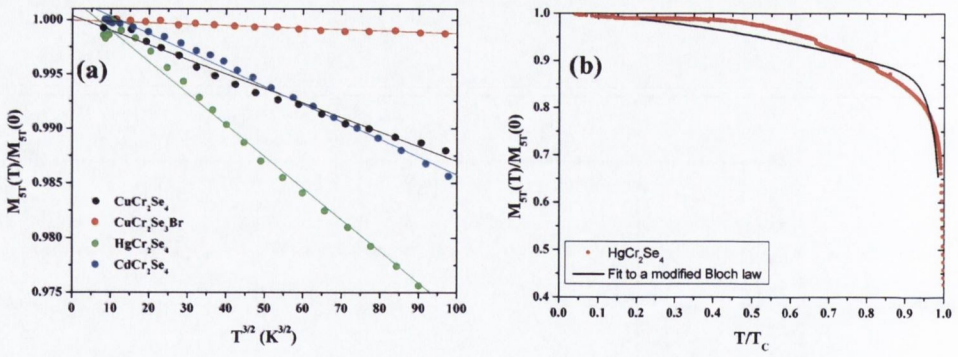

Figure 3.48: Plot for the determination of the stiffness constant using (a) Bloch law and (b) modified Bloch law (Kuz'min (2005)).

perature magnetisation behaviour accurately. The contribution of the spin-wave to the magnetisation can be determined by describing the low temperature magnetisation by the relation :

$$M_s(5K) - M_s(T) \sim T^n \tag{3.14}$$

The exponents of the low temperature saturation magnetisation n have been calculated for these four systems (Fig.3.49). The figures of the spin-wave stiffness constant and the low temperature exponent are summarised in Table 3.15.

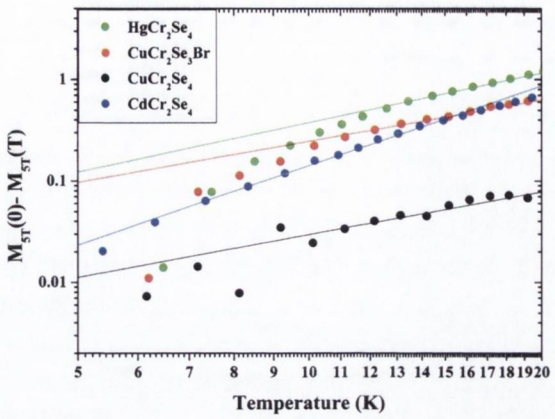

Figure 3.49: Low temperature behaviour of the saturation magnetisation.

	$CuCr_2Se_4$	$CuCr_2Se_3Br$	$CdCr_2Se_4$	$HgCr_2Se_4$
n	1.4(2)	1.4(1)	1.9(1)	1.6(2)
D (meV·Å^2)	72(2)	263(5)	81(4)	45(1)

Table 3.15: Low temperature exponents of the saturation magnetisation.

The saturation magnetisations do not follow the classical $T/T_C^{3/2}$ law, to extend the study further it was proposed by Kuz'min (2005) to approximate the spontaneous magnetisation with the expression:

$$\frac{M(T)}{M(0)} = \left(1 - s \cdot \frac{T}{T_C}^{3/2} - (1-s) \cdot \left(\frac{T}{T_C}\right)^p\right)^{1/3} \tag{3.15}$$

where s and p are parameters, $p > 3/2$ and $s > 0$. The coefficient s is related to the spin-wave stiffness constant by the relation Kuz'min (2005):

$$s = 0.176 \frac{\mu_B}{M(0)} \cdot \left(\frac{kT_C}{D}\right)^{3/2} \tag{3.16}$$

The fit to this model for the $HgCr_2Se_4$ is shown in Fig.3.48(b), and the spin-wave stiffness constant is found to be 48(1) meV·Å^2.

3.6 Conclusions

In this chapter polycrystalline samples of several chalcochromite spinels have been prepared and their magnetic and structural characterisation is presented. Although these compounds

have been studied in the past, the study presented in this thesis presents several new aspects to these materials :

1. The Curie temperature of $CuCr_2Se_4$ was measured by AC susceptibility for the first time and was measured to be 20 K higher than the reported values bringing the transition temperature to 478 K.

2. The magnetic structure of $CuCr_2Se_3Br$ was determined for the first time by powder neutron diffraction revealing that the insertion of Br in the lattice change the order from ferromagnetic to ferrimagnetic with a moment on the Cu aligned antiparallel to the Cr moment. Moreover the magnitude of the moment measured on the Cu varies with the Br concentration.

3. The magnetic structure of $CdCr_2Se_4$ was measured for the first time by powder neutron diffraction confirming the ferromagnetic state of the compound. The amplitude of the moment calculated on the Cr atoms agrees well with the magnetisation measurements.

Chapter 4

Single crystal growth and characterisation of ACr_2Se_4 $(A = Cu, Cd)$

4.1 Single crystal growth

4.1.1 Introduction

Although most of the solids tend towards a certain degree of crystallinity, single crystals are the most ordered form that can be achieved. The preparation of such materials is commonly thought to be more of an art than a science. Nevertheless, single crystal growth is at the heart of modern technology (especially the semiconductor industry), and for some well known elements and compounds the growth processes are completely understood. The crystal grower is often secluded from the scientific scene, however the crystal grower's role must not be diminished since it is very relevant in each of the following interdependent disciplines - engineering, chemistry, and physics. Nowadays crystals in thin film form are preferred by industry for integration into devices. Nevertheless, it is important to have bulk single crystals for thorough fundamental investigation of the properties of the material for two main reasons:

- many physical properties of solids are obscured or complicated by the effects of grain boundaries
- the full range of tensor relationships between applied physical cause and observed effect can be obtained only if the full internal symmetry of the crystal structure is maintained

throughout the specimen

Despite the wide variety of crystal growth methods, the main steps in the formation of a crystal are the following:

1. Generation of reactants
2. Transport of reactants to the growth surface
3. Nucleation
4. Adsorption at the growth surface
5. Growth
6. Removal of unwanted reaction products from the growth surface

4.1.2 Single crystal growth method

Methods for crystal growth can be classified according to various criteria; in this dissertation it makes sense to use the state of matter, therefore techniques are tabulated under the following headings : from melts, from solution, from vapour. A general description of each of these technologies is given below.

Growth from melts This is the most widespread technique to grow large bulk single crystals in industry and research. It consists of melting the element or the solid state product and crystallising the liquid in a single crystal form. Well known melt techniques are: the Czochralski Czocharlski (1918) method, where the crystal is pulled from the melt; and Bridgeman method were the crucible is slowly moved out of the furnace Bridgeman (1925); Stockbarger (1938). These two methods involve the use of a crucible, which can introduce contaminants in the crystal or worse, can react with the melt. If no suitable crucible can be found, methods were the melt is only in contact with a seed or its own solid have been developed. The Verneuil process Verneuil (1902, 1904) involves the use of a seed and a gas flame which melts the solid state compound onto the seed forming a liquid film. Another widely used method in the research laboratory is the floating-zone method Theurer (1952) where a molten zone is maintained between two rods of the solid. By moving the zone relative to the rods, one rod grows, and if a single crystal seed is used, a crystal can be grown. The main disadvantage of these techniques is that they are

limited to compounds that will not decompose before melting, which is not the case for the compounds studied in this thesis.

Growth from solution Although growth from the melts is the most common technique used to grow high quality crystals, growth from solution would be the most popular to the general public. Most people probably enjoyed growing their own sugar or salt crystals from saturated solution at home. The description in this section will focus on high temperature solution growth (HTS) (also called flux growth) by slow cooling process[1] but the discussion is also valid for the low temperature solution growth. In these techniques the crystal is grown from supersaturated solution, and the crystal is completely immersed in the solution. All solution growth involves a solvent, which is used as a flux (to lower the melting point) for the compound. This changes the situation from a one component (melt growth) to at least a two component system, where the crystal and the flux form a eutectic[2]. The slow cooling procedure consists in soaking the binary system at high enough temperature to have a homogeneous liquid and cooling the melt until crystallisation begins. The liquid composition typically changes during the process as presented in Fig.4.1, which corresponds to a certain liquidus temperature drop. The typical cooling rate varies from a fraction of a degree up to 20 degrees per hour. To control the nucleation properly it is therefore important to control the temperature accurately, this requires special equipment. Other requirements for HTS growth are the choice of a good solvent and vessel. There is no general rule to find a good solvent, but generally low melting temperature salts are used. The possibility of contaminating the crystal with the solvent or the crucible is always a risk using this method. The extraction of the crystal from the flux can be a problem if there is no solvent to dissolve it.

Growth from the vapour phase In this growth process, the crystal is grown from volatile species that are transported across a reactor. There is a considerable variety of vapour phase processes depending on how the vapour phase is formed, the nature of the reactor (closed or open system), and the formation of bulk monocrystals or epitaxial films. A possible arrangement for the different processes is presented in Fig.4.2. The production of thin films is often referred to as chemical vapour deposition (CVD) which is mainly done

[1] Other processes such as temperature difference, high pressure, and solvent evaporation processes are other solution growth methods.

[2] The solutions in oxides are called fluxed melts because the solvents are the ones used for welding, brazing, and soldering.

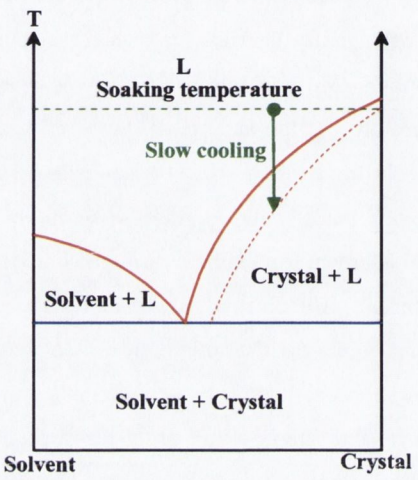

Figure 4.1: Phase relations in a binary system illustrating the formation of crystals by the slow cooling method in HTS growth.

in open systems, in contrast to the production of bulk crystals done in closed systems and referred to as chemical vapour transport (CVT). Since all the crystals obtained by vapour

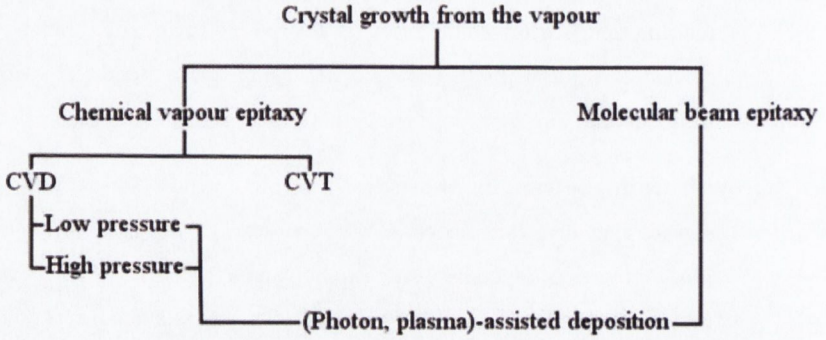

Figure 4.2: Classification of the different vapour growth processes.

growth in this work have been synthesised in a closed tube system, only the principles of CVT will be described. The growth of bulk single crystals by vapour transport is a phenomenon known for a long time Bunsen (1852); Deville (1861), but the experimental and theoretical description of chemical vapour transport started with the work of Schäfer Schaffer (1964). The principle of the chemical transport lies in a reversible reaction

between solids and liquids $A_{i(s,l)}$ with a transport agent $B_{(g)}$ to form gaseous species $C_{i(g)}$ similar to sublimation or distillation, but the substance $A_{i(s,l)}$ does not possess an appreciable vapour pressure. The chemical equation of the reaction can be written as :

$$a_1 A_{1(s,l)} + bB_{(g)} + a_2 A_{2(s,l)} + \cdots = c_1 C_{2(g)} + \cdots \tag{4.1}$$

The driving force of the reaction is the difference in pressures inside the closed system achieved with a temperature gradient. A schematic of a closed tube CVT experiment is given in Fig.4.3. Simple thermodynamic considerations have led to ten rules determining the feasibility of a transport reactionSchaffer (1964).

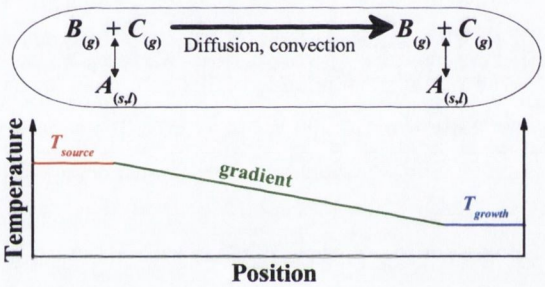

Figure 4.3: Schematic of a closed tube CVT experiment with the ideal temperature gradient across the tube for an endothermic reaction.

4.1.3 $CuCr_2Se_{4-x}X_x$ $(X = Cl, Br, I)$ crystal growth by CVT

The growth of ternary chalcogenide spinel single crystals was studied intensively and a vast literature is available von Philisborn (1971). Since the system studied here decomposes before melting, only solution growth and vapour transport are suitable methods to grow single crystals. An accurate temperature control is crucial to the growth of single crystals of $CuCr_2Se_4$ from high temperature solution (see appendix B.4), therefore the accessible chemical vapour transport method was investigated.

4.1.3.1 Transport agent chemistry

A good transport agent is critical to the success of a chemical transport reaction. Although the driving mechanism of the reaction is an imbalance in partial pressure at either end of the reactor, the temperature at which this condition is reached can be drastically changed by the

volatile species Pierson (1999). Moreover, contamination (or doping) of the crystal with the transport agent (similar to the solvent in HTS growth) has to be considered. As pointed out by Schäfer, a case by case study has to be considered but it is recommended to use one of the components of the crystal as transport agent to synthesise a pure compound Schaffer (1964).

In the case of $CuCr_2Se_4$, Br and Cl based transport agents are useful since they will create volatile species in the system and also dope the crystal. The control of the doping concentration, however, is not very accurate, and this aspect of chemical transport has not been studied. The concentrations of Br and Cl always exceeded the solubility limit of the halogen in the mother compounds. Therefore, the concentration of dopant in this study is considered to be the maximum for that growth temperature. Despite the warning given in Schaffer (1964)[1], iodine is widely used as a transport agent for chalcospinels on the basis that it will dope the crystal only to a very small extent (in the ppm region) as it was proposed in the original method Nitsche (1960). In chapter 2, there is a discussion of the change of magnetic (lowering of the Curie point) and electrical properties (reduction of the electrical conductivity) induced by halogen doping. It is interesting to note at this point that all the properties measured in "pure" single crystals might have been altered by the introduction of iodine in the lattice. One argument for this assertion is that the measured Curie point on "pure" single crystal was determined to be 440 K Nakatani *et al.* (1977) which is lower than that for the polycrystalline sample Lotgering (1964a).

In this study several transport agents have been used to obtain the single crystals. The first transport agent tested was I_2, following the procedure of Nakatani *et al.* (1977), the second was $CuBr_2$ following the procedure of Miyatani *et al.* (1968), next was $CrCl_3$ inspired from the $HgCr_2Se_4$ growth Gibart (1978), and finally without external element (Se can be considered as the transport agent) inspired by the growth of $CdCr_2S_4$ Barraclough & Meyer (1972) and Neulinger (2006). The starting chemical equations for each of the aforementioned reactions are respectively:

$$Cu + 2Cr + 4Se + I_2 \longrightarrow CuCr_2Se_{4-x}I_x + I_{2-x} + xSe \tag{4.2}$$

$$\frac{1}{2}CuBr_2 + \frac{1}{2}Cu + 2Cr + 3Se \longrightarrow CuCr_2Se_3Br_x + (1-x)Br_2 \tag{4.3}$$

$$CuSe + \frac{1}{3}CrCl_3 + \frac{5}{3}Cr + 2Se \longrightarrow CuCr_2Se_3Cl_x + (1-x)Cl_2 \tag{4.4}$$

$$Cu + 2Cr + (4+x)Se \longrightarrow CuCr_2Se_4 + xSe \tag{4.5}$$

[1] Especially in a compound where mixed valence can be induced by substitution of the chalcogen.

4.1.3.2 Thermodynamic feasibility of reactions

The chemical transport has two physico-chemical obstacles: the reaction feasibility is a thermodynamic equilibrium problem, while the mass transport rate is a kinetic problem. Both of these problems are complicated in reality. The first step is to define the chemical reactions and to compute the equilibrium constant (from known thermochemical data). The transport reaction will be favourable if the equilibrium constant is close to unity.

Since the system is in equilibrium the change in free Gibbs energy is zero, therefore:

$$\Delta G_i = -R \cdot T \cdot \ln(K_i) \tag{4.6}$$

where ΔG_i is the free Gibbs energy of the reaction i, R is the gas constant, and K_i is the equilibrium constant.

System $Cu : Cr : Se : Br$ The reactions considered in this system are listed below.

$$CuCr_2Se_3Br_{(s)} + 4Br_{2(g)} = CuBr_{(g)} + 2CrBr_{4(g)} + \frac{3}{2}Se_{2(g)} \tag{4.7}$$

$$CuBr_{2(s)} = CuBr_{(g)} + \frac{1}{2}Br_{2(g)} \tag{4.8}$$

$$CuBr_{(s)} = \frac{1}{3}Cu_3Br_{3(g)} \tag{4.9}$$

$$\frac{1}{2}Cr_{(s)} + Br_{2(g)} = \frac{1}{2}CrBr_{4(g)} \tag{4.10}$$

$$CuSe_{(s)} + \frac{1}{2}Br_{2(g)} = CuBr_{(g)} + \frac{1}{2}Se_{2(g)} \tag{4.11}$$

$$\frac{1}{4}Cr_2Se_{3(s)} + Br_{2(g)} = \frac{1}{2}CrBr_{4(g)} + \frac{3}{8}Se_{2(g)} \tag{4.12}$$

$$Se_{(s)} + Br_{2(g)} = SeBr_{2(g)} \tag{4.13}$$

$$Se_{(s)} + \frac{1}{2}Br_{2(g)} = \frac{1}{2}Se_2Br_{2(g)} \tag{4.14}$$

$$Se_{2(g)} = \frac{1}{3}Se_{6(g)} \tag{4.15}$$

System $Cu : Cr : Se : Cl$ The reactions considered in this system are listed below.

$$CuCr_2Se_3Cl_{(s)} + 3Cl_{2(g)} = CuCl_{(g)} + 2CrCl3_{2(g)} + \frac{3}{2}Se_{2(g)} \tag{4.16}$$

$$CuCl_{2(g)} = CuCl_{(g)} + \frac{1}{2}Cl_{2(g)} \tag{4.17}$$

$$CrCl_{2(g)} + \frac{1}{2}Cl_{2(g)} = CrCl_{3(g)} \tag{4.18}$$

$$CrCl_{3(g)} + \frac{1}{2}Cl_{2(g)} = CrCl_{4(g)} \tag{4.19}$$

$$CrCl_{2(g)} = \frac{1}{2}Cr_2Cl_{4(g)} \tag{4.20}$$

$$CuCl_{(g)} = \frac{1}{3}Cu_3Cl_{3(g)} \tag{4.21}$$

$$CuSe_{(s)} + \frac{1}{2}Cl_{2(g)} = CuCl_{(g)} + \frac{1}{2}Se_{2(g)} \tag{4.22}$$

$$\frac{1}{2}Cr_2Se_{3(s)} + Cl_{2(g)} = CrCl_{2(g)} + \frac{3}{4}Se_{2(g)} \tag{4.23}$$

$$Se_{2(g)} = \frac{1}{3}Se_{6(g)} \tag{4.24}$$

$$\frac{1}{2}Se_{2(g)} + Cl_{2(g)} = SeCl_{2(g)} \tag{4.25}$$

$$Se_{2(g)} + Cl_{2(g)} = Se_2Cl_{2(g)} \tag{4.26}$$

System $Cu : Cr : Se : I$ The reactions considered in this system are listed below. All the thermodynamic values used in this section can be found in appendix A.2.

$$CuCr_2Se_{4(s)} + \frac{5}{2}I_{2(g)} = CuI_{(g)} + 2CrI_{2(g)} + 2Se_{2(g)} \tag{4.27}$$

$$Cu_{(s)} + \frac{1}{2}I_{2(g)} = CuI_{(g)} \tag{4.28}$$

$$CuI_{(g)} = \frac{1}{3}Cu_3I_{3(g)} \tag{4.29}$$

$$Cr_{(s)} + I_{2(g)} = CrI_{2(g)} \tag{4.30}$$

$$Cr_{(s)} + I_{2(g)} = \frac{1}{2}Cr_2I_{4(g)} \tag{4.31}$$

$$CrI_{2(g)} + \frac{1}{2}I_{2(g)} = CrI_{3(g)} \tag{4.32}$$

$$CuSe_{(s)} + \frac{1}{2}I_{2(g)} = CuI_{(g)} + \frac{1}{2}Se_{2(g)} \tag{4.33}$$

$$\frac{1}{2}Cr_2Se_3(s) + I_{2(g)} = CrI_{2(g)} + \frac{3}{4}Se_{2(g)} \tag{4.34}$$

$$Se_{2(g)} = \frac{1}{3}Se_{6(g)} \tag{4.35}$$

The Ellingham diagrams for the three respective systems are given in Fig.4.4. The chemical equilibrium constants involved in the formation of $CuCr_2Se_4$ could not be calculated because thermodynamic data is not available for the possible species formed. Moreover, this analysis is simplified and some unknown gaseous complexes can play an important role in the vapour transport Emmenegger (1972).

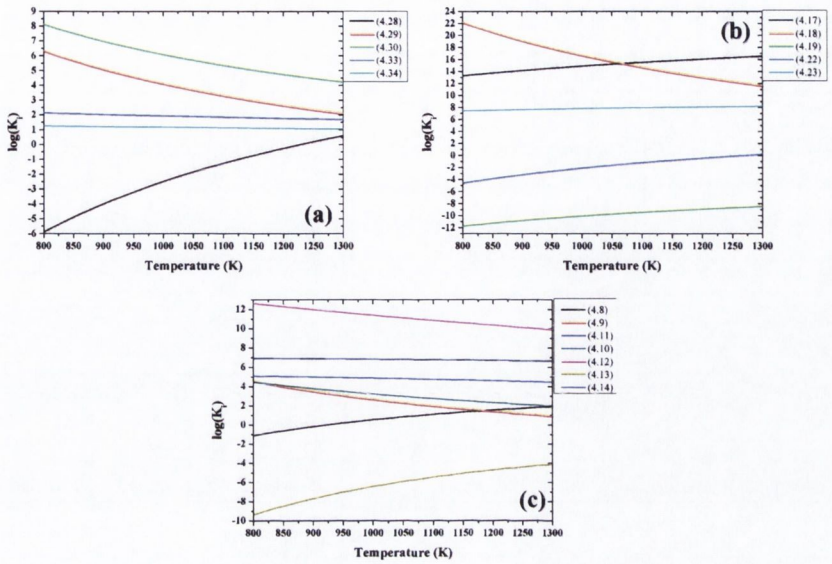

Figure 4.4: Ellingham diagram for selected reactions presented in the text for (a) Br_2 as a transport agent, (b) Cl_2 as a transport agent, and (c) I_2.

4.1.3.3 Growth optimisation

Although knowledge of the feasibility of the reactions is important, the driving process of chemical vapour transport rests in the difference in partial pressures of the species between the source and the growth zone. The calculation of the partial pressures for the three systems was carried out using the CVTrans software based on the minimisation of the free energy Gruehn & Glaum (1997). The results are presented in Fig.4.5 for the three transport agents.

The bromine and chlorine systems present similar behaviour and the difference of pressure is relatively large, the most abundant gaseous species being $Se_{2(g)}$. Therefore, $CuBr_2$ and $CrCl_3$ seem to be good transport agents. In the case of the iodine system, $Se_{2(g)}$ has the highest partial pressure but is constant up to 825°C before it starts to increase. From this calculation it seems that the vapour transport will work for source temperatures higher than in the case of the bromine or chlorine system.

4.1.4 $CdCr_2Se_4$ crystal growth by HTS

The crystal growth of $CdCr_2Se_4$ is by far the most studied among the chalcochromites, and from the variety of techniques developed to grow this compound, HTS growth seems to be

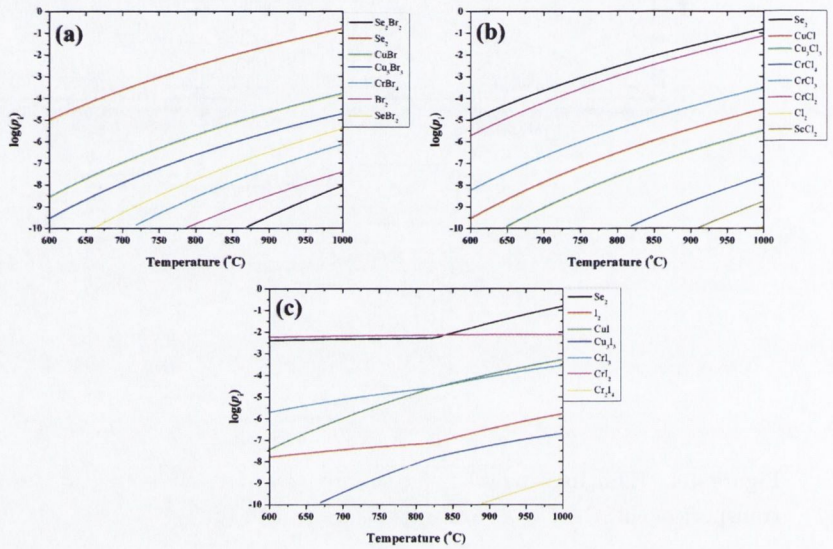

Figure 4.5: Partial pressure for selected gaseous species for (a) Br_2 as a transport agent, (b) Cl_2 as a transport agent, and (c) I_2.

strikingly effective as it is reported in an inorganic synthesis textbook Wold & Rulff (1973).

The procedure described in Wold & Rulff (1973) does not require special furnaces since the cooling rate is approximately 3 °/h from 900 °C. The full experimental procedure is explained in appendix B.4. The chemical reaction involved in this process is the following:

$$4Cd + 2CrCl_3 + 4Se \longrightarrow CdCr_2Se_4 + 3CdCl_2 \tag{4.36}$$

The difference with the HTS procedure is that the solvent ($CdCl_2$) is not introduced in the system in the first place but is created during the heating of the system. To optimise the growth the system $CdCr_2Se_4 - solvent$ was investigated Luzhnaya *et al.* (1981), and it was demonstrated that the primary crystallisation region of $CdCr_2Se_4$ is around 540°C. The insertion of a dopant in the lattice, such as Ag, In, or Ga from the elements that have been investigated, modifies the electrical properties of the parent compound. The insertion of silver was a success, but In, which has a low solubility limit, and Ga doping partly failed as described in appendix B.4. Annealing the crystals, as described in a recent report Vinogradova *et al.* (2007) in a mixture of $Ga(In)/Ga(In)_2Se_3$ vapour, did not change the bulk electrical conductivity in our experimental conditions. But neither the annealing temperature nor the annealing time, which are crucial for the experiment, are reported in the experimental details of this paper.

4.2 Single crystal characterisation

One of the main reasons for growing single crystals is the possibility of characterising the material better than with any other form. In the scope of this study, the magnetic and electrical properties of $CuCr_2Se_4$ and $CdCr_2Se_4$ single crystals have been studied.

4.2.1 Structural characterisation

Before measuring any properties on a system, the first step is to assess the crystal quality (and make sure that it is the right phase)[1].

4.2.1.1 Crystal morphology

The structural characterisation of powders requires special tools (such as a microscope and XRD), but in the case of single crystals the simple observation of the morphology with the naked eye will give a good deal of information on the quality, and sometimes the crystalline structure of the crystal.

The morphology of a single crystal is determined by internal factors (the crystal structure) and external factors (growth process and conditions). Polyhedral crystals bound by flat faces usually adopt characteristic shape controlled by the symmetry (point group/space group) of the crystal. A description of the different crystal systems and their habits can be found in Hahn (1996). In the case of the chalcochromite spinels, the crystal system is cubic (or isometric). The expected shape for these crystals is octahedral (similar to magnetite).

$CdCr_2Se_4$ Crystal grown by HTS present a typical octahedral habit as represented in Fig.4.6. Some of them present some intergrowth indicating that the cooling and the reaction vessel are not optimised perfectly. Moreover, the bigger crystals presents some traces of inclusions in the forms of holes and cracks. These inclusions are suspected to be $CdCl_2$ which is dissolved in the separation from the solvent process.

$CuCr_2Se_4$ The pure $CuCr_2Se_4$ grown by vapour transport presents a mixture of habits which seems to correlate with the size of the crystals. The smaller crystals tend to have a polyhedral habit close to octahedral whereas the bigger crystals tend to form agglomerated platelets as shown in Fig.4.7. In this system the crystal growth is slow and the yield is very small. The flat

[1] One of the advantages of single crystals is that they are single phase most of the time, compared to polycrystalline samples which contain impurity phases most of the time.

Figure 4.6: Single crystal of (a) pure $CdCr_2Se_4$, (b) Ag-doped $CdCr_2Se_4$, and (c) cut along the [111] direction of a $CdCr_2Se_4$ crystal showing the traces of inclusions. The grid has a 1 mm scale.

faces observed correspond to the (111) and ($\bar{1}$ $\bar{1}$ $\bar{1}$) of the original octahedron which are more developed than the 6 other faces and delimit these two triangular/hexagonal faces. The fact that the smaller crystals tend to be octahedrons suggests that the platelet shape of the bigger crystal is due to the growth conditions.

$CuCr_2Se_3Br$ Crystals grown with bromine as a transport agent form needles as presented in Fig.4.8. Although this prismatic habit is reproducible, the size distribution varies from run to run. As described previously the 8 faces of the octahedron can be seen with one set of faces that grows faster than the other.

$CuCr_2Se_3Cl$ This system produces the biggest crystals, but the shape is not very well defined, this is certainly due to intergrowth. The crystals are polyhedrons (Fig.4.9) which can be related to distorted octahedrons.

$CuCr_2Se_4 : I$ The crystals obtained with iodine as transport agent are similar to what is described in the literature: plates perpendicular to [111] Lotgering (1964a) as represented in Fig.4.10. Step growth can be observed as well as twins. The fact that the habit of all Cu containing crystals is not octahedral compared to the expected octahedral form of $CdCr_2Se_4$ is a hint that the two systems might have different crystal structures. The elevated atomic thermal factor of the Cu calculated by powder neutron diffraction might also be due to a small distortion of the lattice. Nevertheless, the observation of non-equiax habits has often been observed for cubic crystals depending on the external factors Faust *et al.* (1968).

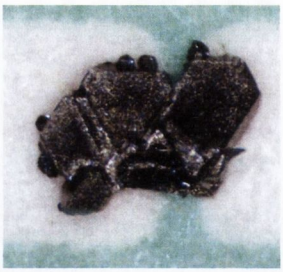

Figure 4.7: Pure $CuCr_2Se_4$ single crystal grown by CVT using Se as transport agent.

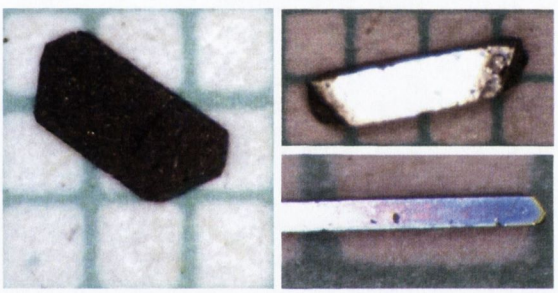

Figure 4.8: $CuCr_2Se_3Br$ single crystals grown by CVT using bromine as transport agent.

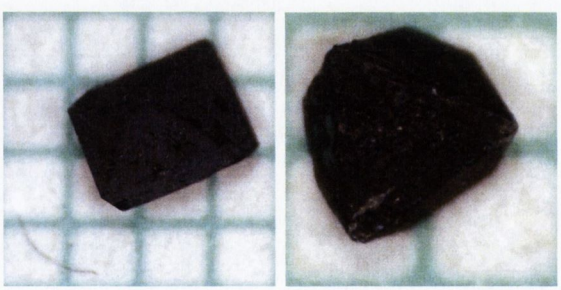

Figure 4.9: $CuCr_2Se_3Cl$ single crystals grown by CVT using chlorine as transport agent.

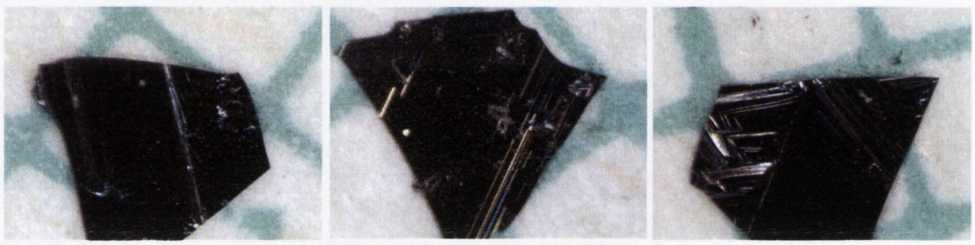

Figure 4.10: $CuCr_2Se_3Cl$ single crystals grown by CVT using iodine as transport agent.

4.2.1.2 Single crystal x-ray diffraction

There is no report in the literature of single crystal XRD on pure $CdCr_2Se_4$ and Br doped $CuCr_2Se_4$. The samples were cut in spheres, where possible, to correct the absorption analytically. The description of the collection method is detailed in appendix C [1]. Two different $CuCr_2Se_3Br$ single crystals were measured, $CuCr_2Se_3Br^{low}$ was grown at lower temperature than $CuCr_2Se_3Br^{high}$ and was cut into a sphere whereas $CuCr_2Se_3Br^{high}$ could not cut into a sphere[2]. The lattice parameters and refinement information are summarised in Table 4.1. The quality of the refinement for both crystals can be checked visually by plotting F_{obs} against

	$CuCr_2Se_3Br^{low}$	$CuCr_2Se_3Br^{high}$	$CdCr_2Se_4$
Lattice parameter (Å)	10.3822(2)	10.4325(2)	10.75653(9)
Wavelength	$Mo\ K_\alpha$, $\lambda = 0.7107$ Å		
Shape	distorted octahedron	metallic needle	metallic octahedron
μ (mm^{-1}), R (μm)	33.53, 60	-	43.97, 56
$< \frac{\sin(\theta)}{\lambda} <$	0.41, 0.85	0.38, 0.86	0.340, 0.772
Space group	$Fd\bar{3}m$	$Fd\bar{3}m$	$Fd\bar{3}m$
N_{meas}/N_{unique}/Redundancy	9345/168/76	8928/170/68	8190/142/66
Refinement method	Full-matrix least-squares on F^2		
R_{int}	4.73	4.74	2.79
R, R_w (all data)	1.80, 2.70	3.41, 4.60	1.17, 2.35
Largest difference ($e^-/Å^3$)	1.91, -1.23	3.11, -2.35	0.47, -0.28

Table 4.1: Single crystal refinement parameters for $CdCr_2Se_4$ and $CuCr_2Se_3Br$. μ is the linear absorption coefficient, and R is the radius of the sphere.

F_{calc} as presented on Fig.4.11.

[1] The data collection was performed by Dr. Florence Porcher in Service Commun de Diffraction X CRM2 Institut Jean Barriol Nancy Université

[2] The superscript *low* and *high* denotes the growth temperature of the crystals.

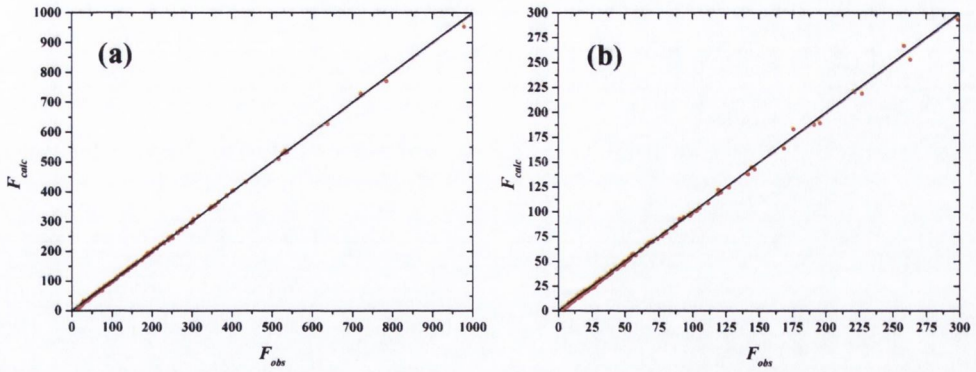

Figure 4.11: Plots of F_{calc} and F_{obs} for (a) $CdCr_2Se_4$ and (b) $CuCr_2Se_3Br^{high}$.

$CdCr_2Se_4$ The reconstructed $(0,k,l)$, $(h,0,l)$, and $(h,k,0)$ reciprocal planes from $CdCr_2Se_4$ are represented in Fig.4.12 (a), (b), and (c) respectively. The symmetry of the lattice is cubic

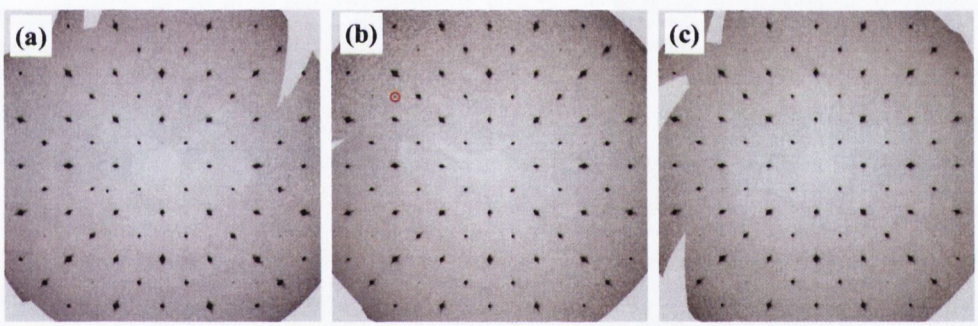

Figure 4.12: Reconstructed reciprocal planes of $CdCr_2Se_4$ single crystal (a)$(0,k,l)$, (b)$(h,0,l)$, and (c)$(h,k,0)$. The red circle in (a) shows a (-4 0 3) spot not indexed for the $Fd\bar{3}m$ space group.

with a mode F, but some weak systematic peaks are observed corresponding to a violation of the d mirror. This could suggest a reduced symmetry of the structure in a non-isomorphic subgroup of $Fd\bar{3}m$. A possible solution could be $F\bar{4}3m$, in fact the literature on the true space group of spinels is abundant and it was proposed, based on experimental and theoretical evidence Lutz *et al.* (2000) (and references therein), that Cr containing spinels would present a lower symmetry than the usual spinels with a space group $F\bar{4}3m$. The refined atomic positions

and displacement parameters[1] are summarised in Table 4.2. The calculated bond lengths and angles are summarised in Table 4.3.

Atom	Wyckoff position	x	y	z	U_{eq} (Å^2)
Cd	*8a*	0.125	0.125	0.125	0.0135(2)
Cr	*16d*	0.5	0.5	0.5	0.0098(2)
Se	*32e*	0.26420(2)	0.26420(2)	0.26420(2)	0.0106(2)

Table 4.2: Atomic coordinates, and displacement parameters for $CdCr_2Se_4$ single crystals.

A difference Fourier map in a Cd plane is represented in Fig.4.13. The residual electron density varies from -0.28 to 0.47 e-/Å^3, and is found around the Cd atoms (green dot on Fig.4.13). The residual is weak and suggest that the general refinement of the structure is good.

Bond lengths (Å)		
$Cd-Se$	$Cr-Se$	
2.5900(2)	2.5423(2)	
Bond angles (°)		
$\widehat{CrSeCr}$	$\widehat{SeCdSe}$	$\widehat{CdSeCr}$
96.659(8)	109.471(7)	120.397(9)

Table 4.3: Calculated bond lengths and angles for $CdCr_2Se_4$ single crystals.

$CuCr_2Se_3Br$ The morphology and size of bromine doped single crystals made them suitable for use with the laboratory x-ray diffractometer modified for thin films described in appendix C for preliminary measurements. The diagram obtained for the needle flat on the stage is represented in the bottom panel of Fig.4.14. Only the (111) family of planes is observed when the crystal is flat on the sample stage. Assuming that the crystal has cubic symmetry, the (100) planes were observed by tilting the sample 53.56° from the initial position[2]. The rocking curve of the (222) peak is presented in Fig.4.15. By fitting the curve with a Lorentzian, a FWHM of 0.025° which is the resolution limit for the optics used to measure the curve.

Conventional single crystal XRD was also carried out on a bromine doped sample, the reconstructed sections $(0,k,l)$, $(h,0,l)$, and $(h,k,0)$ are represented on Fig.4.16. In this case a cubic lattice is also found and the reciprocal lattice reconstructions show that the lattice

[1] U_{eq} is defined as one third of the orthogonalised U_{ij} tensor. $B = 8\pi^2 U_{eq}$, for comparison with x-ray and neutrons.

[2] The method to calculate the interplane angles is described in appendix C.

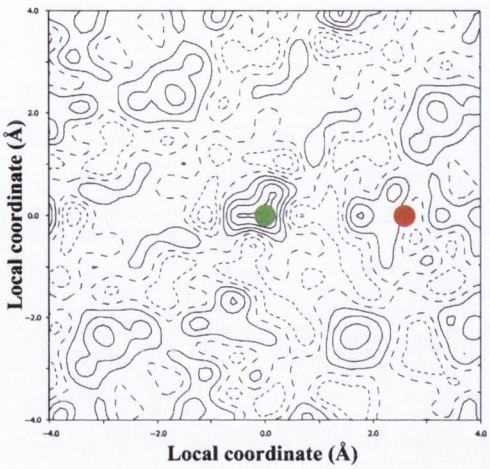

Figure 4.13: General section difference Fourier map centred on a Cd atom trough a (1 1 0) plane with a scope of (8 8 0). The green dot represents a Cd atom, and the red dot the Se atom.

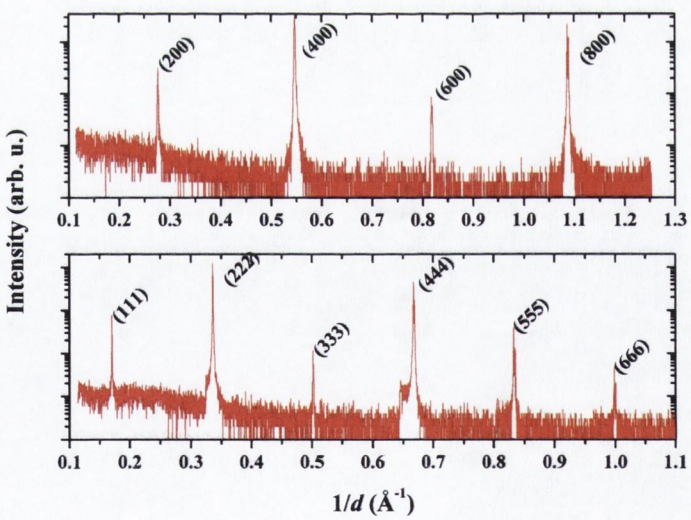

Figure 4.14: XRD diagrams of a $CuCr_2Se_3Br^{high}$ needle flat on the sample stage (bottom panel) and in-plane (top panel).

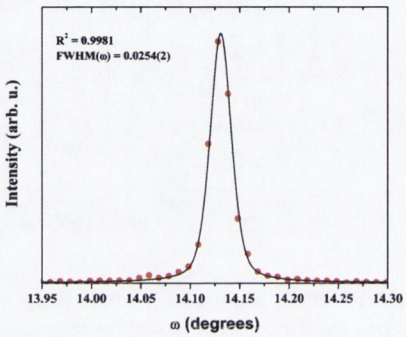

Figure 4.15: Rocking curve of the (222) peak measured on a $CuCr_2Se_3Br^{high}$ needle.

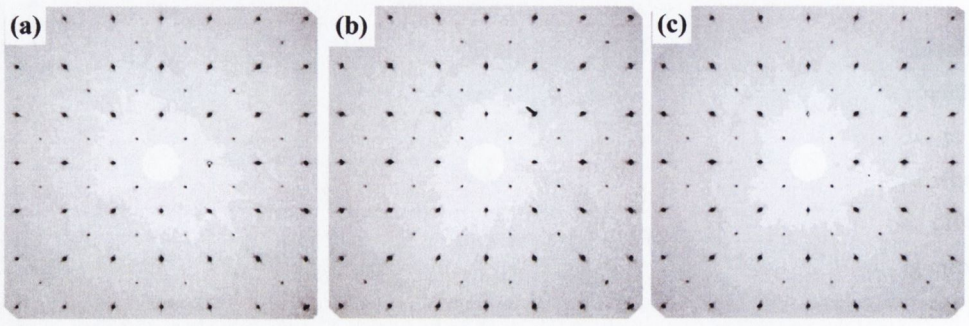

Figure 4.16: Reconstructed section of $CuCr_2Se_3Br^{high}$ single crystal (a)$(0, k, l)$, (b)$(h, 0, l)$, and (c)$(h, k, 0)$.

Crystal	Atom	x	y	z	U_{eq} (Å^2)
$CuCr_2Se_3Br^{high}$	Cu	0.125	0.125	0.125	0.0188(5)
$CuCr_2Se_3Br^{low}$					0.0136(3)
$CuCr_2Se_3Br^{high}$	Cr	0.5	0.5	0.5	0.0084(4)
$CuCr_2Se_3Br^{low}$					0.0084(2)
$CuCr_2Se_3Br^{high}$	Se, Br	0.25772(4)	0.25772(4)	0.25772(4)	0.0079(3)
$CuCr_2Se_3Br^{low}$		0.25713(3)	0.25713(3)	0.25713(3)	0.0085(2)

Table 4.4: Atomic coordinates, and displacement parameters for a $CuCr_2Se_3Br$ single crystals.

	Bond lengths (Å)		
	$Cu-Se$	$Cr-Se$	
$CuCr_2Se_3Br^{high}$	2.3904(4)	2.5221(4)	
$CuCr_2Se_3Br^{low}$	2.3791(3)	2.5282(3)	
	Bond angles (°)		
	$\widehat{CrSeCr}$	$\widehat{SeCuCr}$	$\widehat{CuSeCr}$
$CuCr_2Se_3Br^{high}$	93.59(1)	109.47(1)	122.68(2)
$CuCr_2Se_3Br^{low}$	93.290(9)	109.471(9)	122.90(1)

Table 4.5: Calculated bond lengths and angles for $CuCr_2Se_3Br$ single crystals.

mode F and glide d mirrors are observed in contrast to the $CdCr_2Se_4$. The refined atomic positions and displacement parameters are summarised in Table 4.4. Similar features with the polycrystalline study are found: a copper under-stoechiometry (0.9 instead of 1) improves the agreement factor, and the atomic displacement factor of copper is bigger than the other atoms. The calculated bond lengths and angles are summarised in Table 4.5. A difference Fourier map in a Cu plane is presented in Fig.4.17 similar to the one presented for $CdCr_2Se_4$. But in this case, the residual electron density varies from -2.35 to 3.11 e$^-$/Å^3, for $CuCr_2Se_3Br^{high}$ and between -1.23 to 1.91 e$^-$/Å^3 for $CuCr_2Se_3Br^{low}$, which is not insignificant. The residual density is mainly observed around Cu atoms (negative and positive contributions). To verify that this behaviour is not due to a small distortion of the cubic cell as reported in Neulinger (2006), a test with a rhombohedral distortion has been carried out. The agreement factor for each generator is given in Table 4.6. To test if one of the space groups has more significance, the Hamilton test was carried out Hamilton (1965). At the 25% significance level no other space group is better. A possible disorder of the copper atoms could explain this behaviour, and the origin of this behaviour is still under investigation.

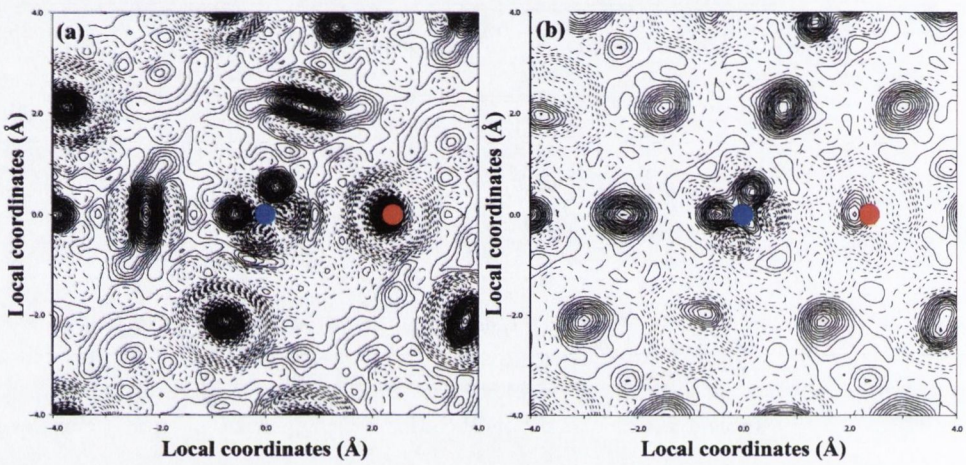

Figure 4.17: Difference Fourier map centred on a Cu atom through a (1 1 0) plane for (a) $CuCr_2Se_3Br^{high}$ (b) $CuCr_2Se_3Br^{low}$. The blue dot represents a Cu atom, and the red dot the Se atom.

R_{int}	$R\ (I > 4\sigma(I))$	$R_w\ (I > 4\sigma(I))$	Generator
		$Fd\bar{3}m$	
4.7	1.76	2.66	
		$R\bar{3}m$	
4.7	2.34	2.83	(-1,1,0)(0,-1,1)(1,1,1)
4.9	2.24	3.02	(0,-1,-1)(1,1,0)(1,-1,1)
4.8	2.38	3.07	(-1,-1,0)(0,-1,0)(-1,-1,-1)
4.7	2.29	3.03	(0,1,1)(1,-1,0)(1,1,-1)

Table 4.6: Agreement factors for the subgroup $R\bar{3}m$ on $CuCr_2Se_3Br$ single crystal data.

4.2.2 Magnetic properties

Single crystals are the best samples to investigate the magnetic properties of a material. They are, in most cases, single phase, and are crystallographically perfectly oriented (if no twins are present), which makes absolute magnetisation and magnetocrystalline anisotropy studies possible.

4.2.2.1 DC magnetisation data

The magnetic properties of $CdCr_2Se_4$, $CuCr_2Se_4$, and $CuCr_2Se_3Br$ have been reported in chapter 3 and the difficulty of measuring absolute magnetisation values with powder samples was noted. In this section, absolute magnetisation has been measured on single crystal samples[1]. The magnetisation as a function of applied magnetic field is presented in Fig.4.18. The absolute saturation magnetic moments are found to be 4.8 μ_B/mol, 5.6 μ_B/mol, and 5.9 μ_B/mol for pure $CuCr_2Se_4$, $CuCr_2Se_3Br$, and $CdCr_2Se_4$ single crystals respectively with a accuracy of 0.2 %. The magnetic moment of $CdCr_2Se_4$ is very close to the 6.0 μ_B/mol expected for the system, and shows that it is possible, with great care, to obtain the absolute magnetisation value. The Br doped single crystal presents a magnetic moment smaller than $CdCr_2Se_4$ but much higher than the $CuCr_2Se_4$ crystals. The reported value of the magnetic moment of crystals obtained by a similar reaction is 5.54 μ_B/mol (Miyatani *et al.* (1968)) which is in good agreement with the measured moment. The moment of the pure single crystal is much lower than what has been measured in chapter 3, and lower than all of the reported moments of $CuCr_2Se_4$ single crystals (4.96 μ_B/mol in Miyatani *et al.* (1968), 5.07 μ_B/mol in Nakatani *et al.* (1977), and 5.4 μ_B/mol in Ohgushi *et al.* (2008)). It is important to stress that all the $CuCr_2Se_4$ crystals described in the literature have been grown with I_2 as transport agent. It is believed that I_2 does not substitute Se in the lattice for steric reasons, nevertheless, it has been shown that a small percentage of iodine is present in these crystals and that the concentration can vary from 0.177 to 0.393 weight % Neulinger (2006). The crystals synthesised in this study without any transport agent have a lower saturation magnetisation and a higher Curie temperature than the single crystals prepared with I_2. This follows the trend of the increased magnetisation with decreased the Curie temperature upon halogen insertion into the lattice. This is a proof that I_2 is doping the lattice and changes the physical properties of the crystals in contradiction to what is reported in the literature Nitsche (1960).

[1] All DC and AC magnetometry measurements in this chapter were performed with Dr. P. Stamenov

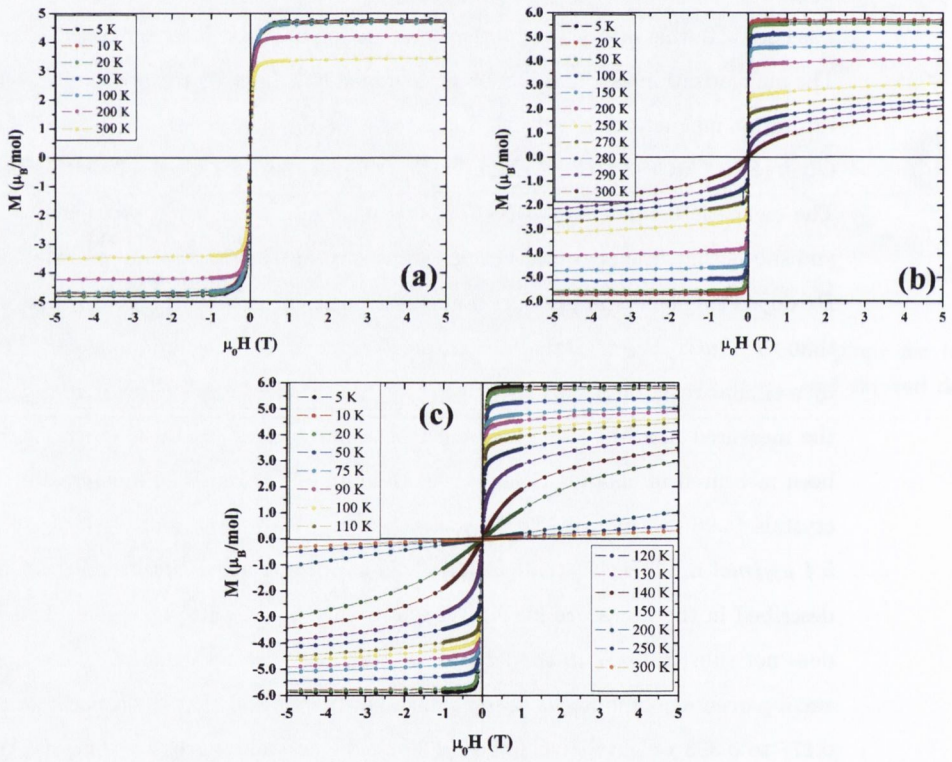

Figure 4.18: Absolute magnetisation as a function of field and temperature for (a) $CuCr_2Se_4$, (b) $CuCr_2Se_3Br$, and (c) $CdCr_2Se_4$ single crystals.

The saturation magnetisations of $CuCr_2Se_3Br$ and $CdCr_2Se_4$ are presented on Fig.4.20(a) and Fig.4.20 (a) respectively.

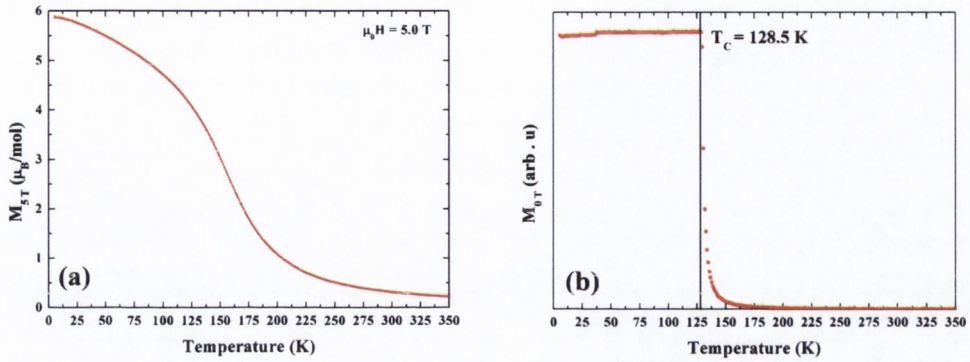

Figure 4.19: (a) Absolute saturation magnetisation at 5 T as a function of temperature (b) thermoremanent curve of a $CdCr_2Se_4$ single crystal.

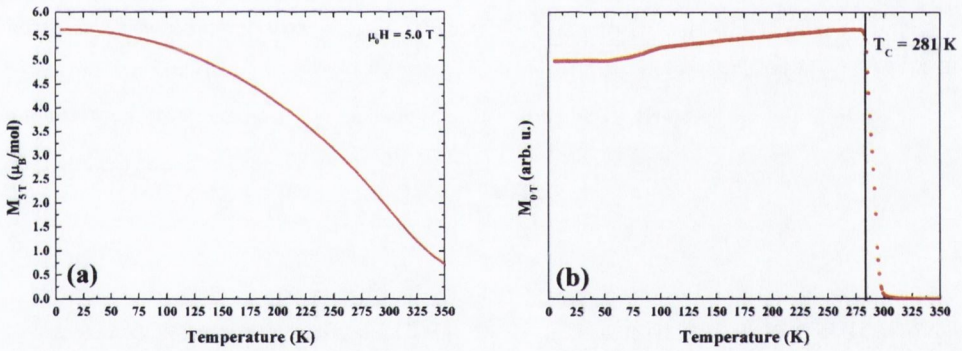

Figure 4.20: (a) Absolute saturation magnetisation at 5 T as a function of temperature (b) thermoremanent curve of a $CuCr_2Se_3Br$ single crystal.

A similar analysis as presented in chapter 3 has been carried out and is presented in Table 4.7.

The thermoremanent curves for both systems are presented in Fig.4.20 (b) and Fig.4.20 (b). The magnetic transition of $CdCr_2Se_4$ is very sharp and the T_C is evaluated to be 128(1) K whereas the magnetic transition of $CuCr_2Se_3Br$ is broader and measured to be 281(2) K. The small decrease observed in the thermoremanent magnetisation around 120 K and 40 K for $CuCr_2Se_3Br$ and $CdCr_2Se_4$ respectively is due to the anisotropy of the material.

The magnon stiffness constant and the low temperature magnetisation exponent (using equation 3.14) were calculated in the same fashion as described in the chapter 3. The values for the three single crystals are reported in Table 4.7

	$CuCr_2Se_4$	$CuCr_2Se_3Br$	$CdCr_2Se_4$
n	1.8(3)	2.4(5)	1.7(2)
D (meV·Å^2)	56(3)	280(6)	60(2)

Table 4.7: Low temperature magnetisation exponent n, and magnon stiffness constant for $CuCr_2Se_4$, $CuCr_2Se_3Br$, and $CdCr_2Se_4$ single crystals.

4.2.2.2 AC susceptibility data

To investigate the magnetic transitions of $CuCr_2Se_3Br$ and $CdCr_2Se_4$ single crystals, AC susceptibility has been measured with the same experimental setup used for polycrystalline sample. The real and imaginary parts of $CdCr_2Se_4$ single crystal are presented in Fig.4.21 (a) and (b) respectively. The susceptibility of $CdCr_2Se_4$ single crystals presents a small decrease

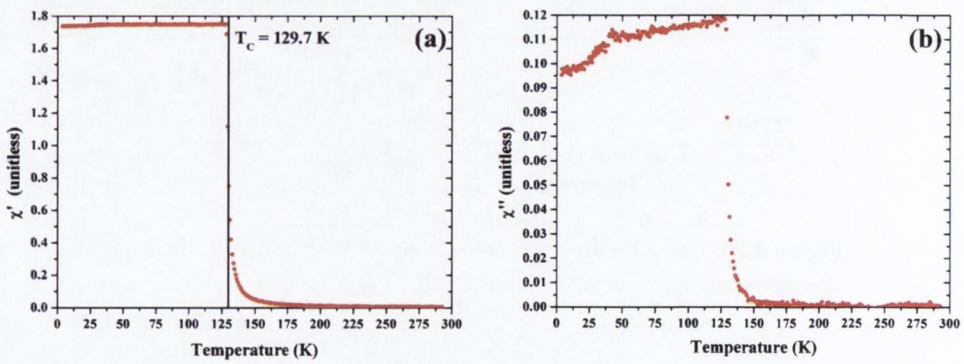

Figure 4.21: (a) Real and (b) imaginary parts of $CdCr_2Se_4$ single crystal.

in the imaginary part at low temperature which might be due to the presence of a layer of antiferromagnetic oxide on the surface of the sample. The estimated Curie temperature from the susceptibility is 129(1) K which is a little bit higher than that obtained from the thermoremanent curve. The influence of a small magnetic field on the magnetic transition was studied on both compositions. The real and imaginary parts of the susceptibility of $CdCr_2Se_4$ around the magnetic transition under 5 mT and 10 mT are shown in Fig.4.22. No major changes are observed in the susceptibility.

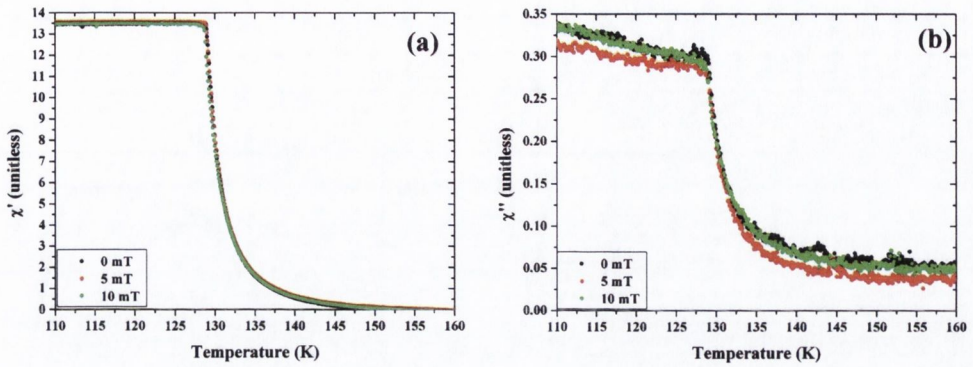

Figure 4.22: (a) Real and (b) imaginary parts of $CdCr_2Se_4$ single crystal under no magnetic field (black dots), 5 mT (red dots), and 10 mT (green dots).

The temperature dependance of $CuCr_2Se_3Br$ susceptibility is presented in Fig.4.23. The magnetic transition is measured at 287(1) K which is almost 10 K higher than the one obtained from the thermoremanent curve. In addition to the main magnetic transition, the real and imaginary parts of the susceptibility present two features at 100 K and just below 200 K. For

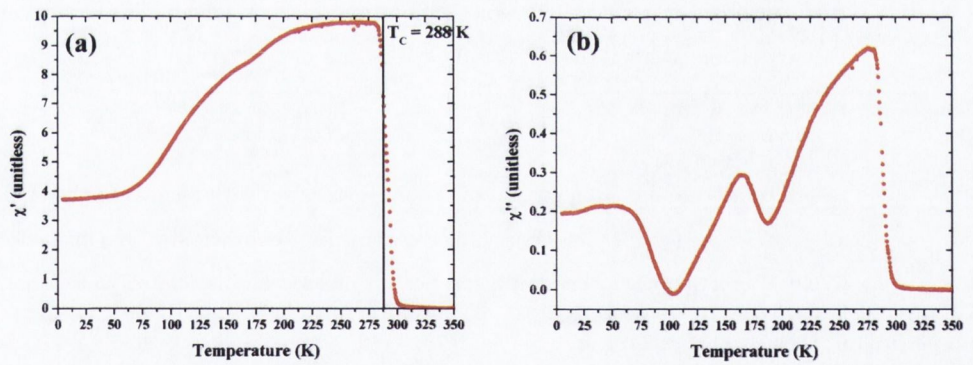

Figure 4.23: (a) Real and (b) imaginary parst of $CuCr_2Se_3Br$ single crystal.

this crystal composition, the susceptibility is much more sensitive to the external magnetic field. The magnetic transition becomes broader and shift towards lower temperature with an applied DC magnetic field.

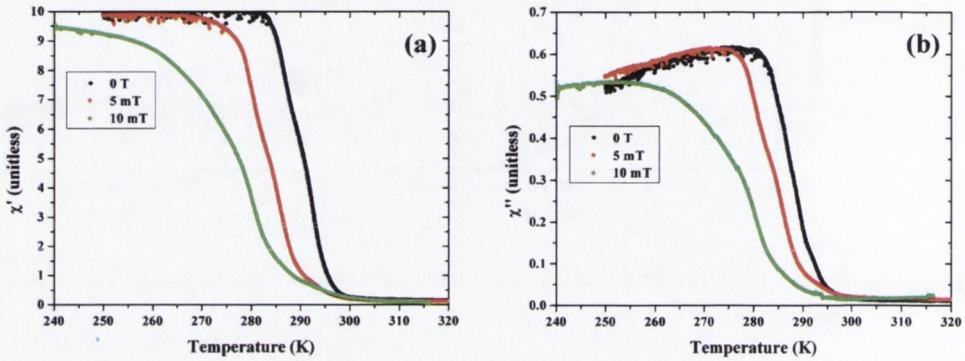

Figure 4.24: (a) Real and (b) imaginary parts of $CuCr_2Se_3Br$ single crystal under no magnetic field (black dots), 5 mT (red dots), and 10 mT (green dots).

4.2.2.3 Magnetocrystalline anisotropy measurements

Magnetocrystallline anisotropy is an intrinsic property of a ferromagnet, it corresponds to the free energy E_a to rotate the magnetisation from one crystallographic axis to an other. In the case of a cubic system, the anisotropy energy can be written as:

$$E_a = K_0 + K_1(\alpha_1^2\alpha_2^2 + \alpha_2^2\alpha_3^2 + \alpha_3^2\alpha_1^2) + K_2\alpha_1^2\alpha_2^2\alpha_3^2 \tag{4.37}$$

where α_i are the direction cosines of the magnetisation with respect to the cubic axes and K_0, K_1, and K_2 are the magnetocrystalline constants for a cubic crystal. If a magnetic field is applied along a direction of the crystal, a torque L is created and is related to the magnetocrystalline energy by :

$$L = -\left(\frac{\partial E_a}{\partial \theta}\right) \tag{4.38}$$

where θ is the angle between the magnetisation and the reference direction. Torque measurement has been carried out on $CuCr_2Se_3Br$ and $CdCr_2Se_4$ single crystals. The detail of the experiment can be found in appendix C[1]. The configuration of the $CdCr_2Se_4$ single crystal on the cantilever is represented on Fig.4.25, where the angle between the main axis of the crystal and the normal of the cantilever is from left to right 60° (third axis), 0° (main axis), and 45° (secondary axis). For the $CuCr_2Se_3Br$ crystal, the needle shape give only two positions, one where the angle between the two axis is 0 ° and one with the angle between the two axis is 60 °.

[1]Torque magnetometry was performed with Dr. P. Stamenov.

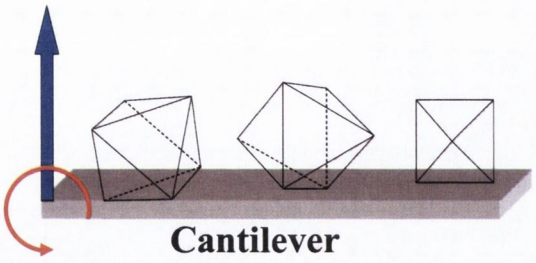

Figure 4.25: Schematic of the crystal mounting on the cantilever for torque measurement. The blue arrow is the normal to the cantilever, and the red arrow represents the rotation of the cantilever.

The torque amplitude of the $CdCr_2Se_4$ is represented on Fig.4.26 as a function of temperature. The main axis has a negative torque amplitude which means that it is the hard axis. The

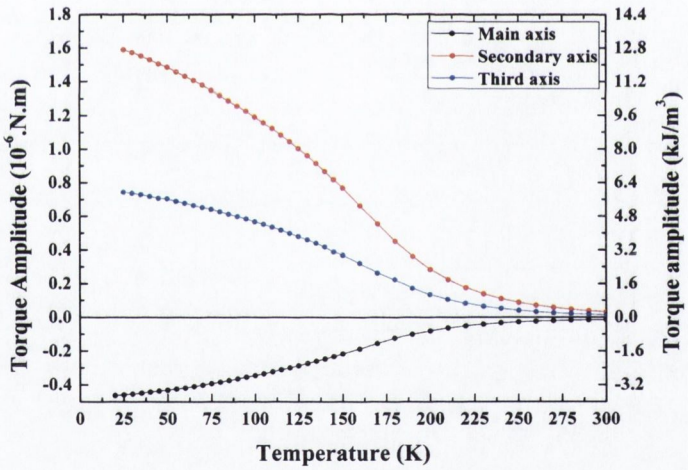

Figure 4.26: Torque amplitude as a function of temperature for a $CdCr_2Se_4$ crystal along the three axes defined in the text in 14 T.

ratio between each curve compared to the main axis correspond to the projection of the cosine of the angle between the main axis and the axis considered. In the case presented here, the ratio of the torque amplitude between the main axis and the secondary axis is $\cos(45°) \approx 0.7$ while the ratio between the main axis and the third axis is $\cos(60°) = 0.5$.

The torque amplitude of the $CuCr_2Se_3Br$ is represented on Fig.4.27 as a function of tem-

perature. The first observation is that the torque amplitude in this crystal is five times bigger

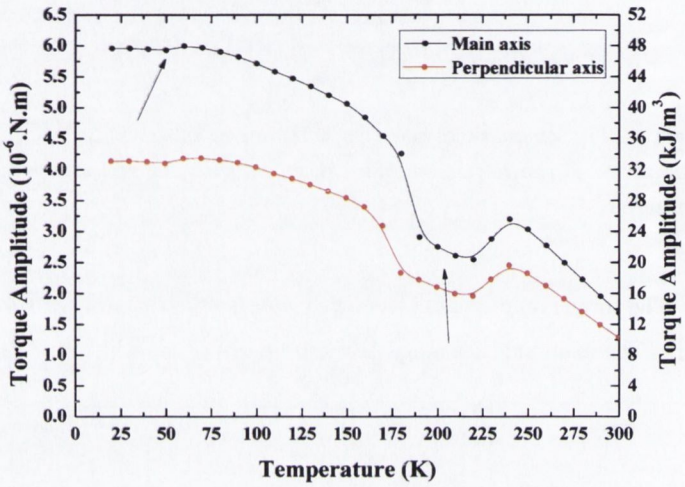

Figure 4.27: Torque amplitude as a function of temperature for a $CuCr_2Se_3Br$ crystal along two axis in 14 T.

than for $CdCr_2Se_4$. The second striking observation is the behaviour of the temperature dependance of the torque amplitude where two peaks are observed (marked with an arrow on Fig.4.27). These two anomalies appear at the same temperatures as those observed in the susceptibility measurement.

4.2.3 Heat capacity

The heat capacity at constant volume of a solid[1] can be defined as:

$$C_V \equiv \left(\frac{\partial U}{\partial T}\right)_V \tag{4.39}$$

where U is the internal energy of the system and T is the temperature. Although the specific heat is a valuable thermodynamic information for the material, it also can give an insight into the microscopic behaviour of systems. By definition, the specific heat arises from the combination of several types of atomic interactions. In the case of the system under study, three different contributions can be considered:

[1]The heat capacity at constant volume is considered even though the heat capacity at constant pressure (C_p) is experimentally determined. They are related by the relation $C_p = C_V + B \cdot V_m \cdot \alpha^2 \cdot T$.

Lattice contribution This term corresponds to the specific heat due to phonons and in the Debye model which assumes that the density of states of the phonon follows a quadratic distribution up to a characteristic frequency (related to the Debye temperature T_D) at which point the density of states drop to zero. From this approximation the specific heat can be derived and is given by:

$$C_V = 9nN_A k \left(\frac{T}{T_D}\right)^3 \int_0^{\theta/T} \frac{x^4 e^x}{(e^x - 1)^2} dx \tag{4.40}$$

This model works well at low temperature, and the equation 4.40 can be simplified for $T \ll T_D$ and reduces to:

$$C_V = \frac{12\pi^4 n N_A k T^3}{5T_D^3} \tag{4.41}$$

and the Debye temperature can be calculated by fitting the heat capacity at low temperature with a cubic function $C_V = \beta T^3$ and given by the relation:

$$T_D = \sqrt[3]{\frac{12\pi^4 n N_A k}{5\beta}} \tag{4.42}$$

The Debye temperature gives a semi-quantitative measure of the stiffness of the bonds between atoms in different materials, and allows comparison of the nature of the bonding between similar materials.

Conduction electron contribution In a metallic system, the electrons are considered to be nearly free to move in the lattice and should behave like an ideal gas. However, the contribution of electrons to the specific heat is smaller than expected and as a result of quantum mechanics, only the electrons that are able to change energy states contribute to the specific heat. For a free electron gas, the electronic heat capacity can be expressed as :

$$C_{el} = \frac{\pi^2 n}{2\epsilon_F} k^2 \cdot T \tag{4.43}$$

Experimentally, the contribution of the electronic part is obtained by considering the low temperature region which is described by :

$$C_V = \gamma T + AT^3 \tag{4.44}$$

Magnetic contribution The contribution of the magnetism to the specific heat can be divided in two parts. The first is related to a phase transition, and therefore is related to the entropy of the system. Quantum mechanics predicts that the entropy per mole for a

cooperative order-disorder transition should be $S_M = R \cdot \ln(2S+1)$ Gopal (1966). If the magnetic specific heat can be isolated by substracting the lattice and the electron specific heat contribution, then the entropy due to order-disorder change in spin alignments can be calculated and compared to the theoretical value. A lambda shaped anomaly is observed at the magnetic ordering temperature. In addition to the specific heat associated with the magnetic transition, the periodicity of the magnetic spins in the lattice (similarly to the periodicity of the atoms) contribute to the specific heat at low temperature. Assuming a quadratic dispersion of the magnon spectrum, the heat capacity due to the magnon at low temperature will be proportional to $T^{3/2}$.

The specific heat of $CuCr_2Se_3Br$ and $CdCr_2Se_4$ have been measured[1] and are presented in Fig.4.28 and Fig.4.29. A description of the experimental method can be found in appendix C.

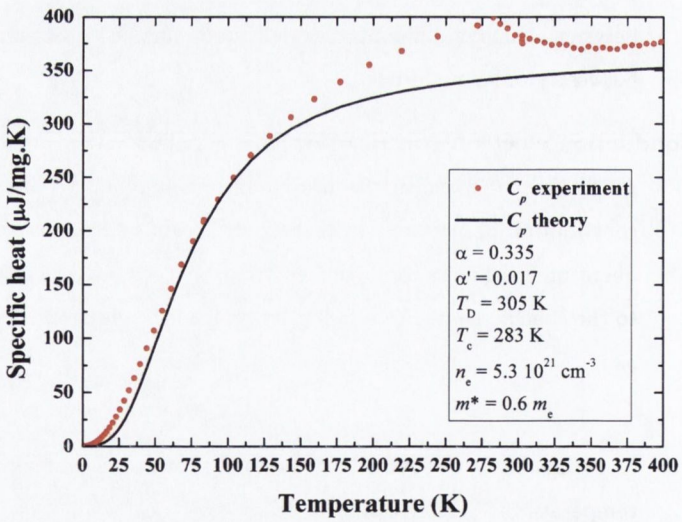

Figure 4.28: Specific heat of $CuCr_2Se_3Br$ single crystal (red dots) and the calculated heat capacity with the three contributions described in the main text.

The characteristic lambda shaped anomaly at the magnetic phase transition are observed for $CuCr_2Se_3Br$ and $CdCr_2Se_4$ compounds at 283 K and 128 K respectively. The Debye temperatures are estimated to be 305 K and 328 K for $CuCr_2Se_3Br$ and $CdCr_2Se_4$ respectively using the Debye model described above.

[1] Heat capacity measurements were performed with Dr. P. Stamenov.

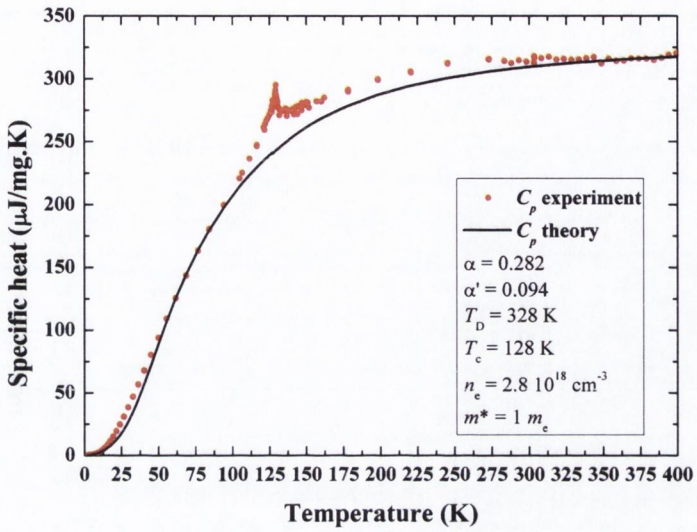

Figure 4.29: Specific heat of $CdCr_2Se_4$ single crystal (red dots) and the calculated heat capacity with the three contributions described in the main text.

4.2.4 Scaling analysis

In the Landau theory, the free energy is expended as a function of the average magnetisation and critical exponent can be defined Landau & Lifshitz (1980). The critical properties of a magnetic system showing a second order phase transition are characterized by static critical exponents α, β, γ, δ. The exponent α is obtained from specific heat measurements. The mathematical definitions of the exponents are given below :

- Above T_C, the initial susceptibility is given by :

$$\chi_0 \sim \frac{1}{|T - T_c|^\gamma} \tag{4.45}$$

- Below T_C the temperature dependence of the spontaneous magnetisation M_0 is given by :

$$M_0 \sim |T_c - T|^\beta \tag{4.46}$$

- For $T = T_C$ the variation of the magnetisation with small fields is described by the critical point exponent δ defined by :

$$M \sim H^{\frac{1}{\delta}} \tag{4.47}$$

- The specific heat, like the magnetic susceptibility, exhibits a divergence at the critical point. The specific heat at constant field is given by :

$$C \sim \frac{1}{|T - T_c|^{\alpha}} \tag{4.48}$$

The scaling theory predicts equalities between the critical point exponents, such as :

- The Rushbrooke relation $\alpha + 2\beta + \gamma = 2$
- The Widom relation $\gamma = \beta(\delta - 1)$

The scaling approach leads to a "scaled magnetisation" expressed in term of scaled parameters. The magnetic equation of state in the critical region can be written as :

$$M(H,t) = |t|^{\beta} f_{\pm}\left(\frac{H}{|t|^{\beta+\gamma}}\right) \tag{4.49}$$

where f_+ for $T > T_c$ and f_- for $T < T_c$, respectively, are regular functions, and $t = |T - T_c|/T_c$ is the reduced temperature. Equation 4.49 implies that the $M \cdot |t|^{-\beta}$ as a function of $H \cdot |t|^{-(\beta+\gamma)}$ produces two universal curves : one for temperature below T_c and the other for temperatures above T_c.

We limited the study of the critical exponents to $CdCr_2Se_4$ since the transition of $CuCr_2Se_3Br$ is more complicated. The critical temperature was determined to be 130.0(5) K. The isothermal magnetic susceptibility exponent γ was determined to be 1.3(1) as presented on Fig.4.30(a), and the critical isotherm exponent δ was extracted from the magnetisation curve as presented on Fig.4.30(b). A value of $\delta = 4.1(2)$ was obtained and the zero-field magnetic exponent β was calculated using the Widom relation and found to be $\beta = 0.3(1)$. The "scaled magnetisation" plot is useful to verify that the exponent obtained are correct. Such a plot is presented on Fig.4.31, the fact that the isotherms curve falls on two different branches shows that the exponents are correct. The specific heat critical exponent α was determined using the anomaly observed at the critical temperature and found to be 0.06(2), as presented on Fig.4.30(c). This exponent compared well with the expected value (0.1) calculated from the Rushbrooke relation.

The value obtained are summarised in table 4.8 together with the theoretical value for the mean field and Heisenberg model. The value obtained are closer to the 3D Heisenberg model than the mean field model.

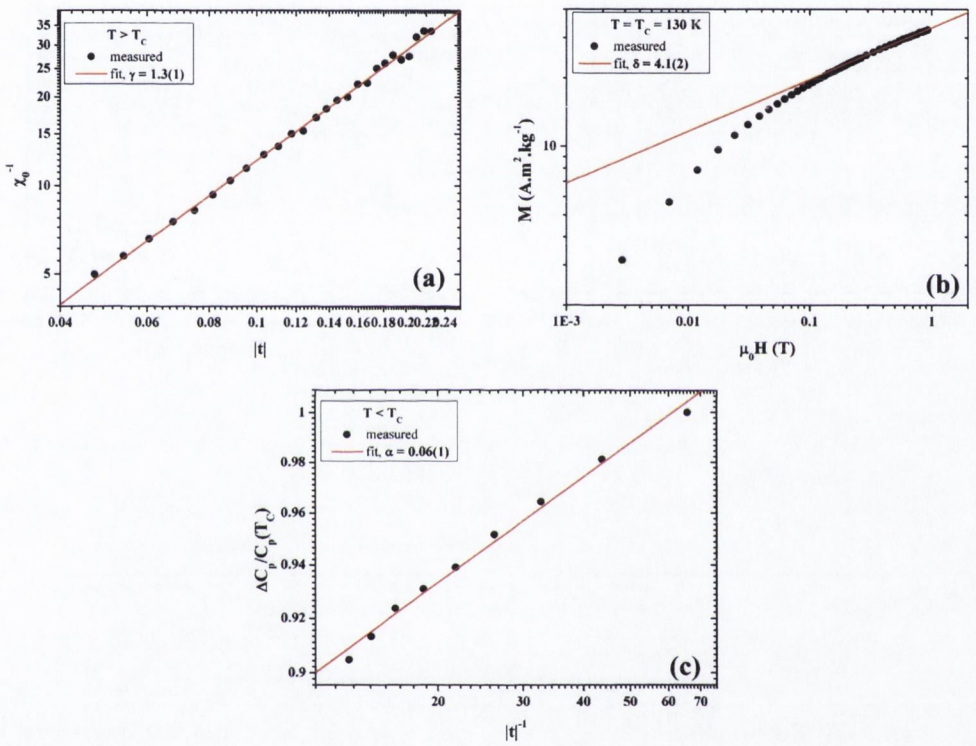

Figure 4.30: log-log plots of (a) magnetic susceptibility for $T > T_c$, (b) isothermal magnetisation at $T = T_c$, and (c) specific heat for $T < T_c$

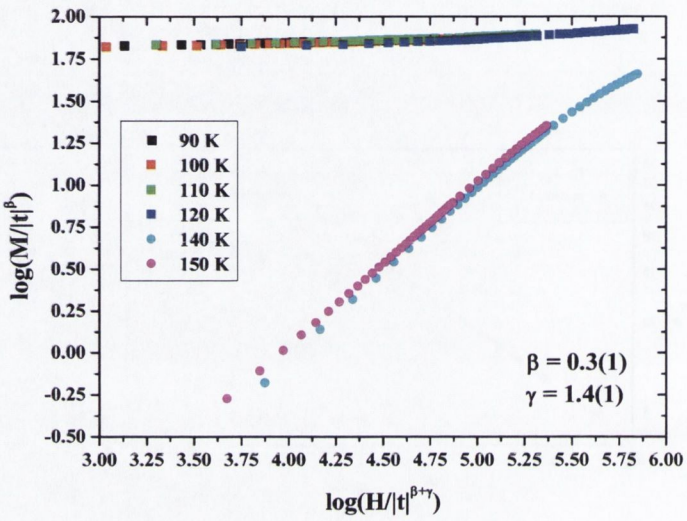

Figure 4.31: Scaling plot of the magnetic isotherm in logarithmic form below and above Curie temperature.

	α	β	γ	δ
Mean field	0	0.5	1	3
3D Heisenberg	-0.1	0.365	1.386	4.78
$CdCr_2Se_4$	0.06(2)	0.3(1)	1.3(1)	4.1(2)

Table 4.8: Static critical-point exponent values for mean field, 3D Heisenberg, and $CdCr_2Se_4$ single crystals.

4.2.5 Magneto-transport data

The electrical properties of these systems have been the centre of attention since $CdCr_2Se_4$ has been reported to be ferromagnetic and semiconductor Lehmann (1967) and presents some interesting features such as bipolar dopability and anomaly in the conductivity in the n-type samples Aminov *et al.* (1980); Haas (1968). $CuCr_2Se_4$ is an exciting system for the tunability of its conduction, which is reported to be metallic in the parent system Tsurkan *et al.* (1984) and semiconducting in the end member $CuCr_2Se_3Br$ Miyatani *et al.* (1971).

This section will describes the magnetotransport properties measured on the single crystals described above[1]. Before presenting the main results obtained on each system a general

[1] All the magnetotransport measurements presented in this section were performed with Dr. P. Stamenov.

introduction to the different magnetoresistive contributions relevant to the study is necessary.

4.2.5.1 Introduction

The current density **j** and electric field **E** inside a conducting material are related by Ohm's law :

$$\mathbf{j} = \hat{\sigma}\mathbf{E} = \hat{\rho}^{-1}\mathbf{E} \tag{4.50}$$

where $\hat{\sigma}$ represent the conductivity tensor and its inverse $\hat{\rho}$ is the resistivity tensor. In general for non magnetic metals, the resistance change in a small applied magnetic field is positive and quadratic in low field and in the high field limits saturate quadratically. The simplest model to explain this behaviour considers two bands, and splits the traditional current densities into two separate current density (one for the holes and one for the electrons). This magnetoresistance effect is called closed orbit magnetoresistance and it follows the expression:

$$\frac{\Delta\rho^{CO}}{\rho} = \frac{aH^2}{b + cH^2} \tag{4.51}$$

where a, b, and c are parameters dependent on the carrier partial conductivity $\sigma_{1,2}$, and mobilities $\beta_{1,2}$.

If this contribution is always positive, negative magnetoresistance can be observed. In the ionised impurity scattering model, the mobility of the carrier is limited by spin disorder, and the magnetoresistance contribution is negative and quadratic at low field. The expression for the ionised impurity scattering is given by:

$$\frac{\Delta\rho^{LS}}{\rho} = A_{IS}\cosh\left(\frac{g\mu_B H}{kT}\right)^{-1} \tag{4.52}$$

A negative magnetoresistance is also observed in ferromagnetic system due to the magnetic scattering from the magnetic moment, and varies as the square of the magnetisation:

$$\frac{\Delta\rho^{MS}}{\rho} = A_{MS}M(H)^2 \tag{4.53}$$

An analogous term in the Hall coefficient is associated with the spontaneous (anomalous) Hall effect. The Hall resistivity is then the sum of the normal contribution and the spontaneous part. For a recent review on anomalous Hall effect see Nagaosa *et al.* (2009). Another phenomenon related to the magnetic scattering is the anisotropic magnetoresistance (AMR). It was observed that the resistivity of bulk ferromagnetic metals depends on the relative angle between the

electric current and the magnetisation direction Thomson (1857) and the magnetoresistance contribution can be expressed as:

$$\frac{\Delta\rho^{AMR}}{\rho} = \sum_{i=0,1,\cdots} A_{2i}\cos^{2i}(\theta) \tag{4.54}$$

where θ is the angle between the current and the magnetisation, A_{2i} are constants dependent on the density of d-like states at the Fermi level, sample quality, temperature, *etc.* The first term of the series is usually defined as:

$$A_2 = \frac{\rho_{\parallel} - \rho_{\perp}}{\rho_{\perp}} \tag{4.55}$$

where $\parallel$ and $\perp$ refer to the mutual orientation of the current and the magnetisation of the sample.

Another contribution to the magnetoresistance can be due to weak localisation phenomenon, where the carrier is delocalised when a magnetic field is applied. In this case the magnetoresistance for the 3D case can be expressed to the first order as:

$$\frac{\Delta\sigma}{\sigma_0} \propto -f^{3D}\left(\frac{H_{eff}}{H}\right) \tag{4.56}$$

where $\sigma_0 = \frac{q^2}{\pi h}$ is the conductance quantum and f^{3D} is defined as :

$$f^{3D}\left(\frac{H_{eff}}{H}\right) = \psi\left(\frac{1}{2} + \frac{H_{eff}}{H}\right) \tag{4.57}$$

where H_{eff} is the effective field related to the elastic scattering and ψ the digamma function.

4.2.5.2 $CuCr_2Se_4$

The magnetoresistance and Hall effect between -14 T and 14 T have been measured on a pure single crystal in a Van der Pauw geometry. Details of the experimental setup are given in appendix C. The evolution of the resistance of the sample as a function of the temperature is shown in Fig.4.32. The resistance decreases when the temperature decreases wich is similar as in a metal. The magnetoresistance seems to have several contributions: a magnetic contribution, a closed orbit contribution, and an ionised impurity scattering contribution. The fact that several bendings are observed in the Hall resistance shows that the system contains at least two different types of carrier. A combined fitting including the three contributions in the magnetoresistance, one majority hole, and one minority hole has been carried out. The magnetoresistance and Hall effect measured at 5 K with the combined fit is shown in Fig.4.33. The fitted conductivity coefficient at different temperatures are summarised in Table 4.9, where n_0 and n_1 are the

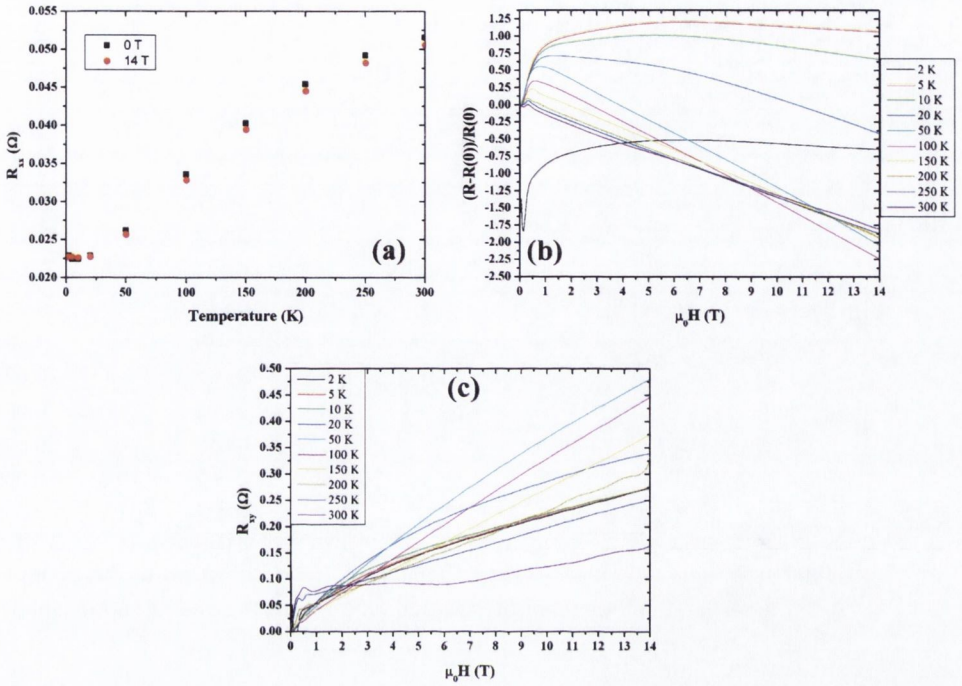

Figure 4.32: (a) Evolution of the resistance as a function of the temperature in 0 T (black dots) and in 14 T (red dots), (b) magnetoresistance at different temperature, and (c) Hall resistance at different temperature of a pure $CuCr_2Se_4$

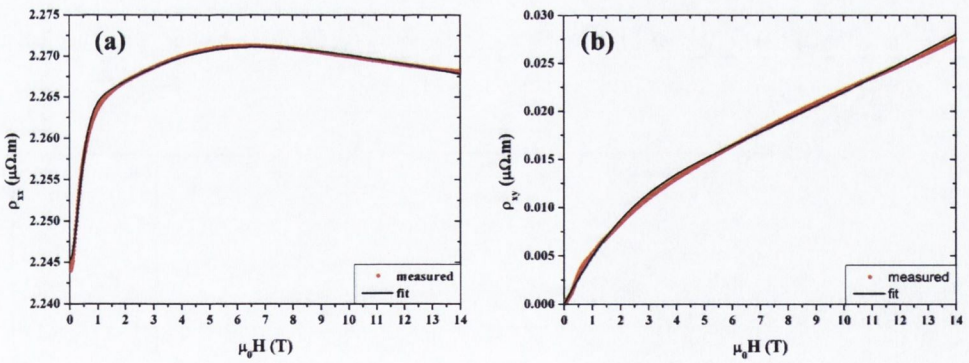

Figure 4.33: Measured (red dots) and fitted (black line) (a) magnetoresistance and (b) Hall effect of a pure $CuCr_2Se_4$ single crystal.

T (K)	n_0 $10^{27}\mathrm{m}^{-3}$	n_1 10^{22} m^{-3}	τ_0 $10^{-15}s$	τ_1 $10^{-13}s$	A_{IS} part/unit	H_{IS} T	A_{MS} part/unit	H_{MS} T
300	-4.8	-	0.9	-	0.027	10.2	-	-
250	-4.8	-	1.0	-	0.027	9.0	-	-
200	-3.3	-	1.6	-	0.031	10.3	-	-
150	-2.5	-	2.4	-	0.041	12.2	-	-
100	-2.1	-5.4	3.3	0.5	0.039	7.8	0.003	0.15
50	-2.3	-22	4.0	0.5	0.044	7.9	0.005	0.20
20	-3.4	-19	3.0	0.8	0.032	9.1	0.007	0.34
10	-3.7	-7.8	2.8	1.3	0.012	9.0	0.008	0.41
5	-3.6	-6.2	2.9	1.5	0.007	10.4	0.009	0.46
2	-3.6	-5.9	2.9	1.4	0.008	11.3	0.007	0.57

Table 4.9: Conductivity coefficients for the majority and minority holes obtained with a two band model and parameters from the ionised impurity scattering and magnetic scattering contribution.

electronic carrier concentration of the majority and minority holes respectively, τ_0 and τ_1 are the scattering time of the majority and minority holes respectively, A_{IS} and H_{IS} the amplitude and effective field for the ionised impurity contribution, and finally A_{MS} and H_{MS} the amplitude and effective field for the magnetic scattering contribution. The calculated band dispersion obtained by Bettinger *et al.* (2008) is represented on Fig.4.34. The effective masses of the majority and minority holes used in the fitting were obtained from their band structure calculation, and are $0.65m_e$ and $0.25m_e$ respectively.

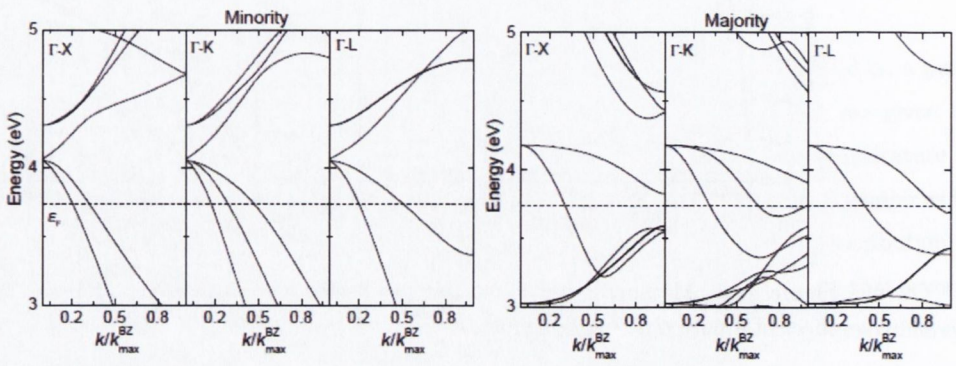

Figure 4.34: Majority and minority energy bands near the Fermi Energy (dashed line) along Γ-X, Γ-K, and Γ-L directions. Adapted from Bettinger *et al.* (2008)

4.2.5.3 $CuCr_2Se_3Br$

The magnetoresistance, Hall effect and AMR were measured on a $CuCr_2Se_3Br$ single crystal as described in appendix C. The magnetoresistance and Hall resistance are presented on Fig.4.35 (a) and (b) respectively. The behaviour of the magnetoresistance presents two components, a

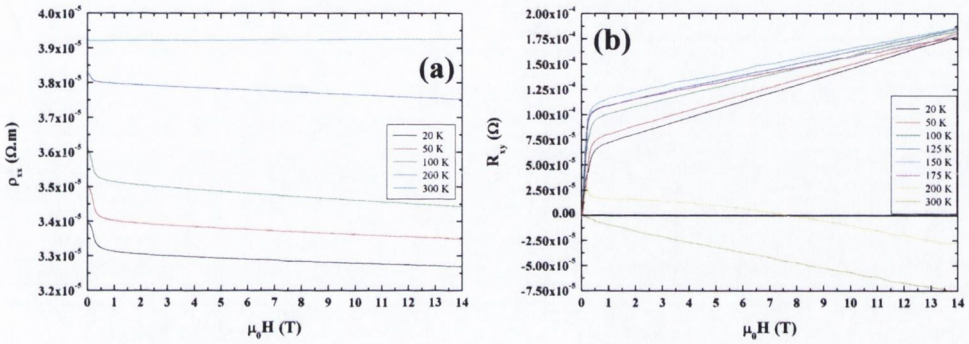

Figure 4.35: (a) Magnetoresistance (b) Hall resistance of a $CuCr_2Se_3Br$ single crystal.

conventional two band magnetoresistance which is temperature independent in the interval 20 K to 200 K demonstrating the fact the crystals are extremely degenerate (essentially metallic). The second component is the spontaneous magnetoresistance expected for a ferromagnetic metal, its magnitude being proportional to the square of the magnetisation. Its amplitude increases from $0.5 \cdot 10^{-7}$ to about $1 \cdot 10^{-6}$ at 200 K. This increase is in contradiction with the expectation of downward trend of the same amplitude following the temperature behaviour of the saturation magnetisation. Similar amplitude dependence as a function of the temperature is observed in the spontaneous coefficient of the Hall effect as seen in Fig.4.35(b). Despite the very high carrier concentration (of the order of 10^{27} m^3) there is substantial temperature dependence of the normal Hall effect which corresponds to a change in the effective carrier concentration of about three times. The change of sign of the normal Hall voltage above the Curie temperature (280 K) is not a true property of the crystal rather than an artefact related to the presence of substantial (more than 50% in amplitude) resistive contribution to the voltage measured at the Hall contacts. Resistance and Hall voltage have been measured simultaneously while applied magnetic field was rotated in a plane containing the current and the (111) crystal axis. The characteristic angular dependence of the AMR (Eq. 4.54) is clearly seen in Fig.4.36 and is simultaneously regressed with the angular dependance of the Hall voltage. The unintuitive

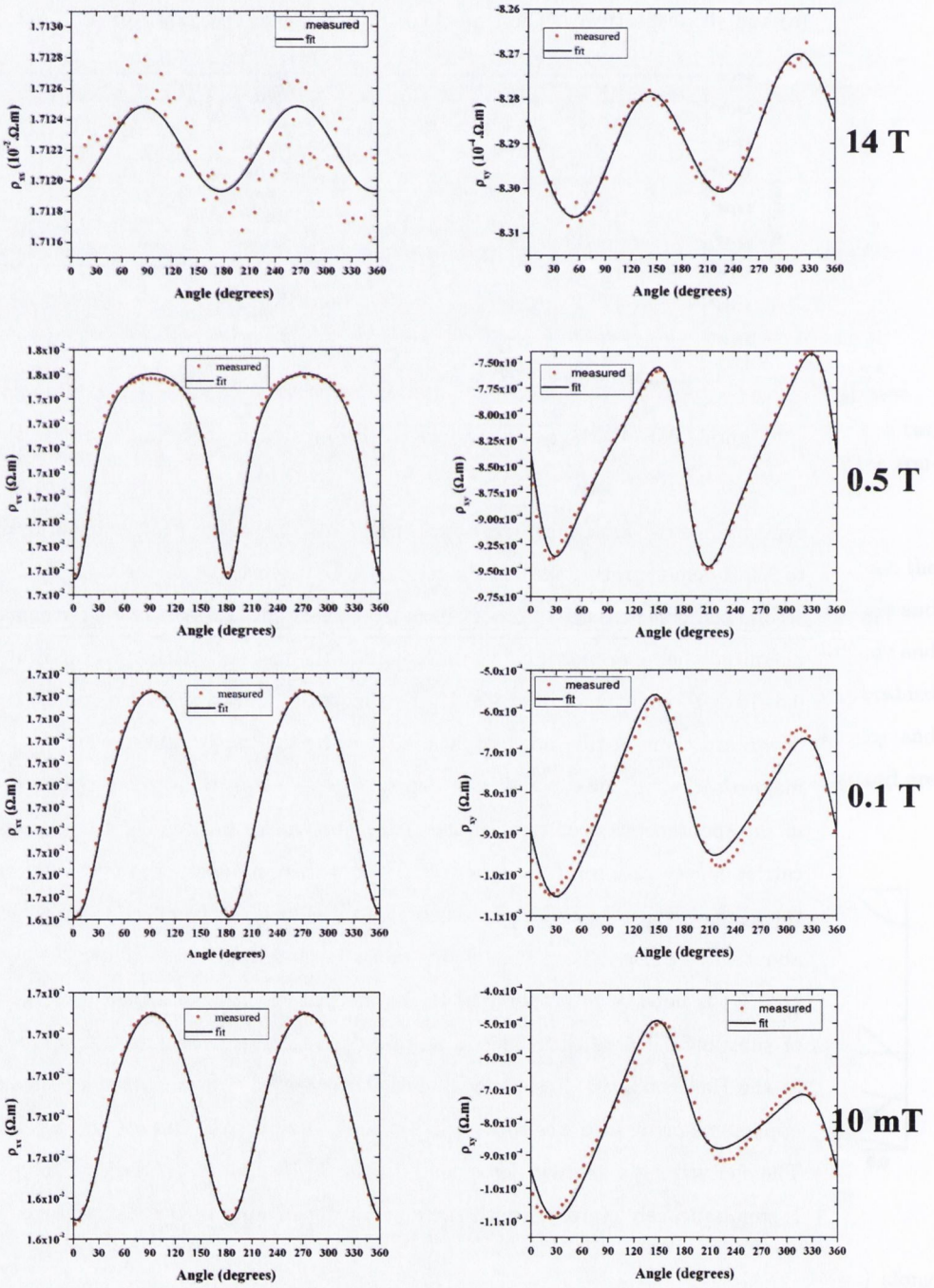

Figure 4.36: Angular dependance of ρ_{xx} (left column) and ρ_{xy} (right column) measured at 10 K and at 10 mT, 0.1T, 5T, and 14 T from top to bottom. The red dots are the measured resistivities and the black line is the fit.

shape of the angular dependances of the voltage drop across the Hall contacts is due to the different angular phase offset of two of the three contacts used for the physical substraction of the resistive component. The only other term present has the normal cosine angular dependence of the Hall voltage and its amplitude is the sum of the normal and spontaneous Hall amplitude. Excellent agreement is observed in the angular dependences and experimental data as seen in Fig.4.36.

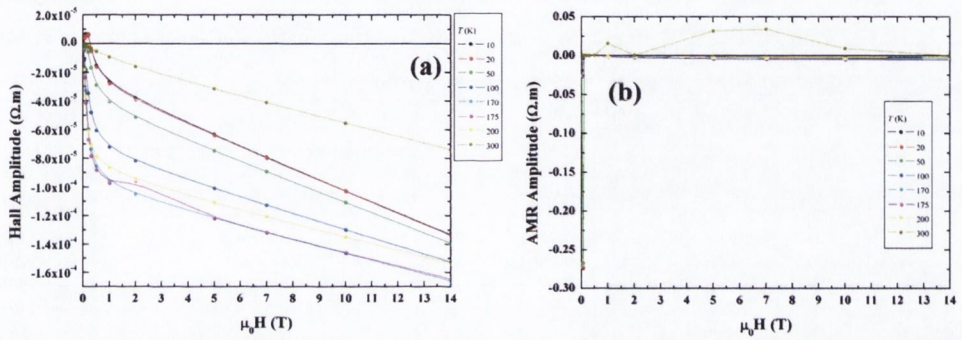

Figure 4.37: (a) Hall amplitude and (b) AMR amplitude of a $CuCr_2Se_3Br$ single crystal extracted from the angular dependance of ρ_{xx} and ρ_{xy}.

The extracted Hall and AMR amplitude are visualised in Fig.4.37 and represent the true field and temperature dependences of the anomalous scattering coefficients. It is important to note, the non -monotonic field dependence of the anomalous Hall coefficient when temperature is below 50 K and also its non vanishing magnitude above the Curie point (280 K). The same may be associated with the existence of finite size ferromagnetic clusters in the paramagnetic phase after long range spin-coherence has been lost. Similar high field reentrant behaviour of the infinite ferromagnetic cluster is evidenced in Fig.4.37(b) as the AMR amplitude at 300 K and 14 T approaches the values observed below the Curie temperature at arbitrary fields above saturation.

4.2.5.4 $CdCr_2Se_4$

The magnetoresistance of the cadmium based composition is apparently dominated by the weak delocalisation component (Fig.4.38,4.39,4.41, 4.42). The absolute amplitude of the resistance change remains essentially constant below 140 K, thus substantiating the quantum mechanical

nature of the observed effect. The magnetoresistance above this temperature obeys the conventional two bands picture due to the sufficient (10^{17} per cc) number of carriers. The good agreement between the conventional 3D weak localisation theory (equation 4.56) and the experimental data is demonstrated in Fig.4.39 for the same sample at the relatively high temperature of 50 K. The characteristic magnetic localisation length obtained from the effective field by the relation $L_B = \sqrt{\frac{\hbar}{eH_{eff}}}$ is found to be 83 nm.

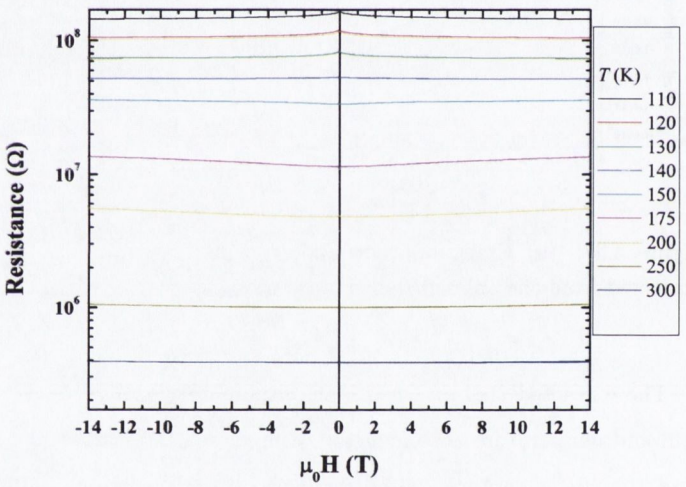

Figure 4.38: Magnetoresistance of pure $CdCr_2Se_4$ single crystals between 110 K and 300 K.

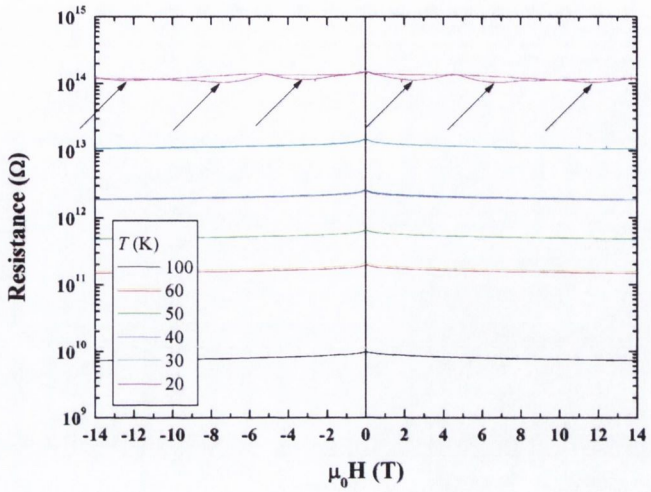

Figure 4.39: Magnetoresistance of pure $CdCr_2Se_4$ single crystals between 100 K and 20 K. The anomaly pointed by the arrows corresponds to temperature fluctuation.

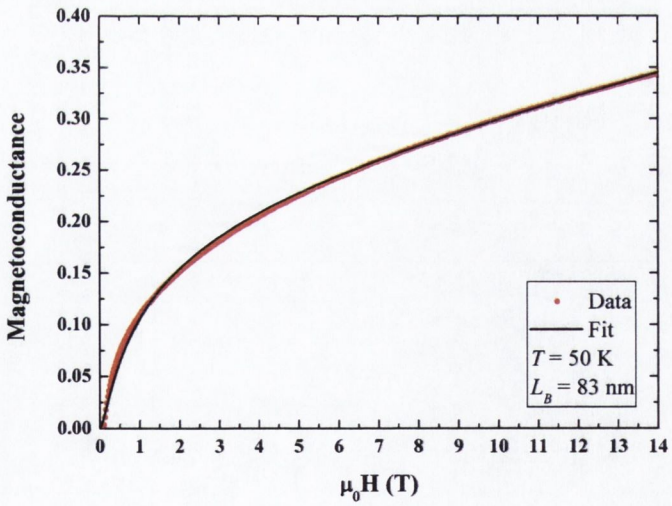

Figure 4.40: Magnetoconductance of pure $CdCr_2Se_4$ at 50 K (red dots) and its fit to a weak localisation magnetoresistance (equation 4.56).

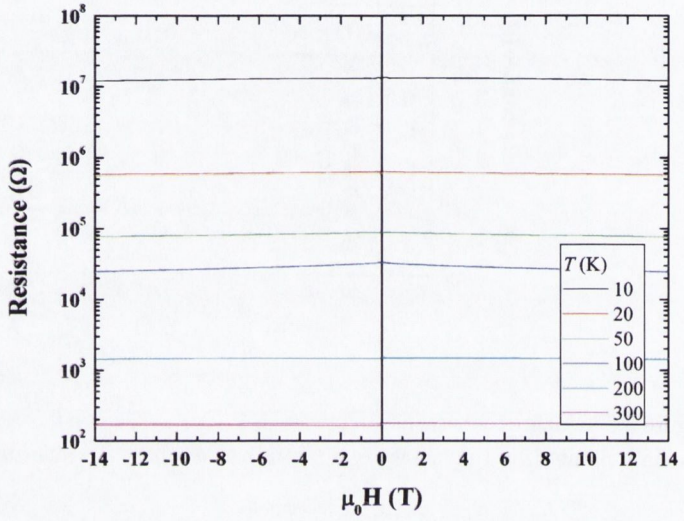

Figure 4.41: Magnetoresistance of Ag-doped $CdCr_2Se_4$ between 10 K and 300 K.

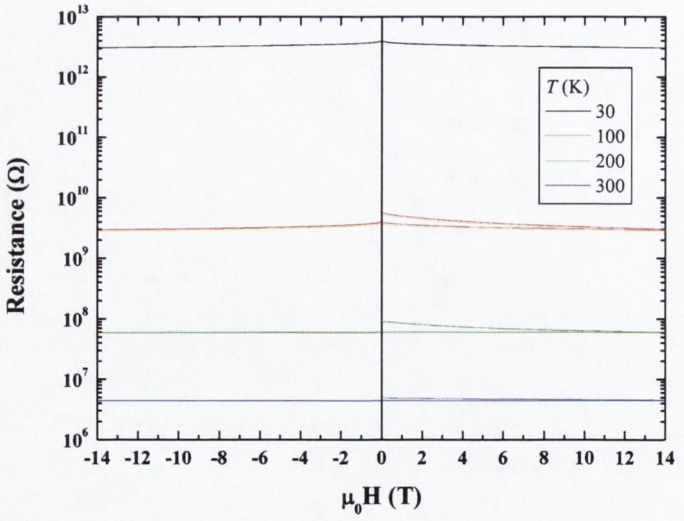

Figure 4.42: Magnetoresistance of In-doped $CdCr_2Se_4$ between 10 K and 300 K.

4.2.6 Spin polarisation measurement

In ferromagnets there exists an imbalance between the number of charge carriers having a particular spin orientation at the Fermi level, E_F, leading to a net spin polarisation P of the conduction electrons. A relatively new method to measure the spin polarisation is to analyse the Andreev reflection at the ferromagnetic/semiconductor interface in point contact (PCAR). This method permits to determine the magnitude of P (not the sign) of metallic system. Andreev reflection is the process in which an electron in a normal metal at a S/N interface pairs with an electron of opposite spin and momentum in order to form a Cooper pair and enter the superconducting condensate at the other side of the interface, doubling the subgap electrical conduction of the system. A hole is then reflected into the normal metal in order to conserve charge, spin and momentum. Blonder, Tinkham and Klapwijk (BTK) developed a theory that incorporates the effects of all transport processes (Andreev reflaction, normal reflection, and single particle tunneling) and an interfacial barrier of arbitrary strength (Z)Blonder *et al.* (1982). The BTK model identifies four processes that can occur at a normal metal/superconductor interface: Andreev reflection (A), normal reflection (B), transmission with branch crossing(C), and transmission without branch crossing (D). The probabilities of these processes are determined from the Bogoluibov transport equations Tinkham (1996) and the current is then computed from these probabilities weighted by the Fermi-Dirac function, $f(E)$, at a given temperature T :

$$I_u \propto \int (f(E-V) - f(E))(1 + A_u(E) - B_u(E))\, dE \tag{4.58}$$

This model has since been modified to include the effects of a ferromagnetic metal/superconductor junction Soulen *et al.* (1998); Upadhyay *et al.* (1998). This is done through a two current model, one spin polarised (I_p) and one unpolarised (I_u), where the total current is given by :

$$I_t = (1 - |P|)\, I_u + |P| I_p \tag{4.59}$$

I_u behaves exactly as described in the BTK model. However, with I_p the imbalance of carriers of a particular spin of the ferromagnet results in some electrons not being able to pair with electrons of opposite spin, suppressing Andreev reflection (forcing $A_p = 0$). In the limit of $Z = 0$, $|P|$ can be simply determined from the zero bias conductance by the suppression of Andreev reflection by :

$$\frac{G(0)}{G_N} = 2(1 - |P|) \tag{4.60}$$

However at finite Z the entire conductance spectrum must be fit to extract $|P|$.

PCAR of a $CuCr_2Se_3Br$ single crystal was measured with a niobium superconducting tip in the experimental setup described in appendix C. A PCAR spectrum of a $CuCr_2Se_3Br$ at 3.1 K and its evolution in function of temperature is presented on Fig.4.43 and Fig.4.44 respectively with fits to a modified BTK model[1]. The fitting is in excellent agreement with the

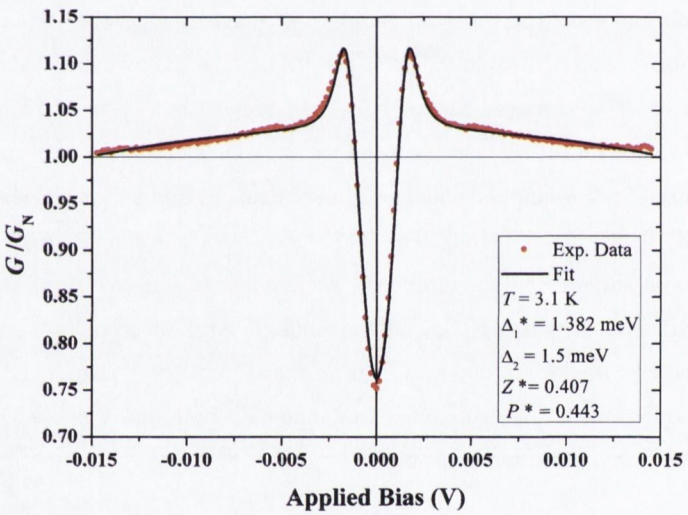

Figure 4.43: Measured normalised differential conductance as a function of applied bias (red dots) at 3.1 K of a $CuCr_2Se_3Br$ single crystal. The black line represent the fit to the experimental data with a modified BTK model.

experimental data and a spin polarisation $|P|$=44.3% is obtained with a quite high Z value of 0.41. The superconducting gap within the proximity region [2] is found to be Δ_1=1.38meV is a little bit smaller than the bulk value Δ_2=1.5meV which is a fix parameter and is used as an energy reference.

[1] PCAR was measured with Dr. P. Stamenov, the fitting algorithm was written by Dr. P. Stamenov.

[2] This value is characteristic to the material and the junction. The proximity region corresponds to the space where the Cooper pairs are present in the ferromagnetic material.

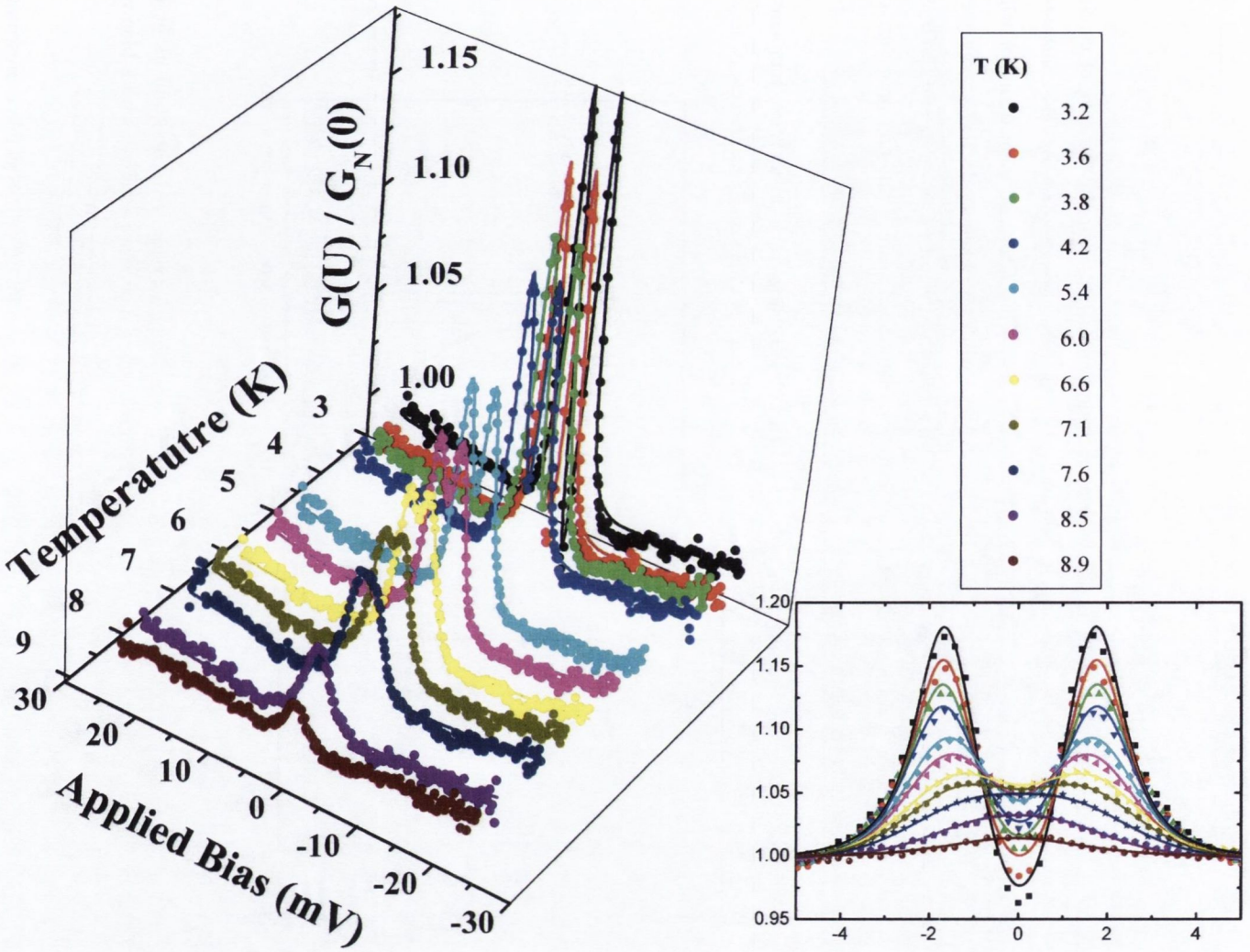

Figure 4.44: Measured normalised differential conductance as a function of applied bias and temperature of a $CuCr_2Se_3Br$ single crystal. The solid lines represent the fit to the experimental data with a modified BTK model.

4.2.7 Optical properties

Useful information can be obtained from optical measurements. In the case of conducting materials, the optical conductivity can be obtained by measuring the optical constants over a wide frequency range. The absorption edge of the insulator and semiconductor will give information on the nature and the value of the band gap whereas the low energy part will contain vibrational information. A study of the reflectivity of pure $CdCr_2Se_4$ and $CuCr_2Se_3Br$ is described in this section[1]. The description of the experimental setup and procedure can be found in appendix C.

$CdCr_2Se_4$ The reflectivity spectrum of a $CdCr_2Se_4$ single crystal at room temperature is shown in Fig.4.45. Four peaks are observed and can be attributed to phonons. Considering

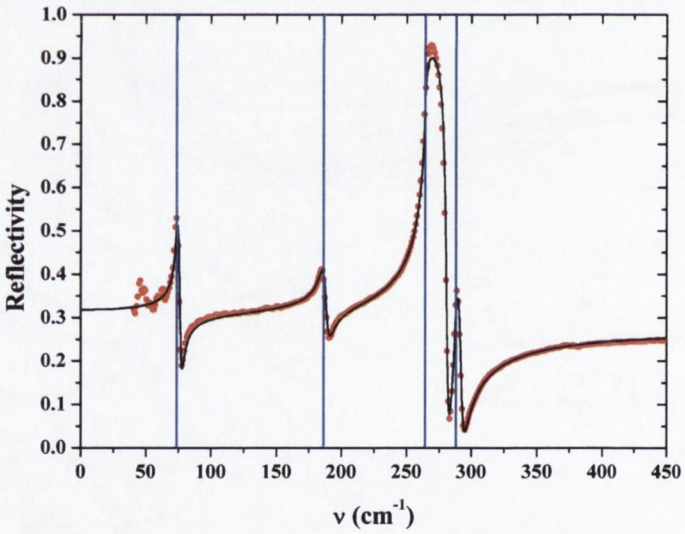

Figure 4.45: Infra-red reflectivity of a $CdCr_2Se_4$ single crystal (red dots) and its fit with a classical oscillator (black curve). The 4 infrared active modes are assigned with a blue vertical line.

that the crystal structure is cubic with a space group $Fd\bar{3}m$, the irreducible representation of the spinel will be:

$$\Gamma = A_{1g} + E_g + T_{1g} + 3T_{2g} + 2A_{2u} + 2E_u + 5T_{1u} + 2T_{2u} \tag{4.61}$$

[1]The measurements were performed in the Basov Infrared Spectroscopy Lab (University of California San Diego) with the help of A. LaForge and A. Schafgans.

where the only infrared active modes are 4 of the 5 triply degenerated T_{1u}. The experimental curve was therefore fitted with the Drude-Lorentz model:

$$\epsilon(\nu) = \epsilon_\infty + \sum_{i=1}^{n} \frac{\nu_{pi}^2}{\nu_{0i}^2 - \nu^2 - i \cdot \gamma_i \cdot \nu} \tag{4.62}$$

It describes the optical response of a set of harmonic (damped) oscillators. Here ϵ_∞ is the high-frequency dielectric constant, which represents the contribution of all oscillators at very high frequencies. The parameters ν_{pi}, ν_{0i}, and γ_i are the plasma frequency, the transverse frequency (eigenfrequency) and the linewidth (damping factor) respectively of the i^{th} Lorentz oscillator. For the Drude term, which describes to response of the unbound (free) charge carriers, the ν_{0i} is zero. The value of each parameter is summarised in Table 4.10 and are in accordance with the values reported previously in Wagner *et al.* (1971). All the modes observed are consistent with the O_h point group symmetry, and no other modes were measured at room temperature to confirm the lowering of the symmetry observed by single crystal XRD. Nevertheless, an additional mode was observed in Wagner *et al.* (1971) below the Curie temperature which was attributed to a tetragonal distortion.

i	1	2	3	4	ϵ_∞
ν_{0i} (cm^{-1})	288.32	264.71	186.66	74.22	10.1
Wagner *et al.* (1971)	286.6	264.5	188.0	74.5	11.0
ν_{pi} (cm^{-1})	87.45	327.3	107.18	67.63	
γ_i (cm^{-1})	4.22	2.17	5.69	2.65	

Table 4.10: Values of ν_p, ν_0, and γ for the 4 identified infrared T_{1u} vibrations in $CdCr_2Se_4$

$CuCr_2Se_3Br$ Since the Hall effect is small in $CuCr_2Se_3Br$, the estimation of the carrier concentration is not easy. To confirm the order of magnitude, spectroscopy in the far infrared was carried out on a single crystal of $CuCr_2Se_3Br$. The spectra covering far (blue dots), mid (green dots), and near (red dots) infrared is represented in Fig.4.46. To obtain the carrier concentration from the Drude model, the far infrared part is fitted with equation 4.62 with no oscillator (Fig.4.47). The relation between the carrier density n and the plasma frequency ω_p is given by the relation:

$$n = \frac{\omega_p^2 \cdot m^* \cdot \epsilon_0}{e^2} \tag{4.63}$$

The carrier concentration does not vary much as a function of temperature, and at 300 K a plasma ordinary frequency of 14000 cm^{-1} and a damping factor of 3720 cm^{-1} are found. This

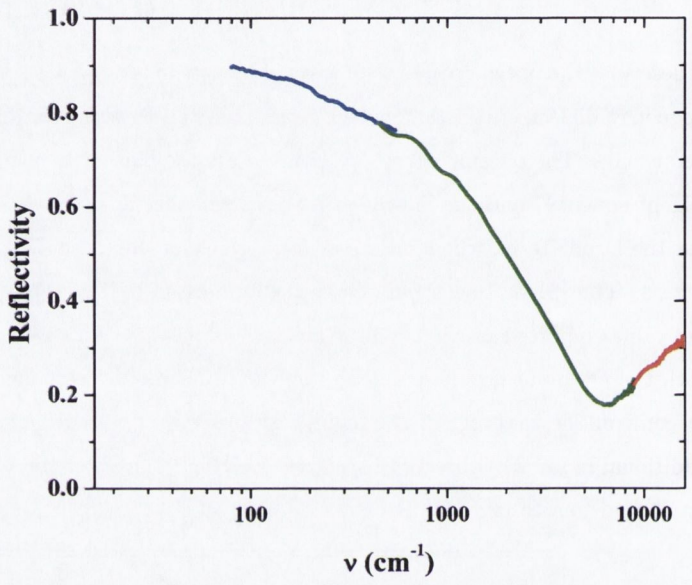

Figure 4.46: Infra-red reflectivity of a $CuCr_2Se_3Br$ single crystal. The blue, green, and red dots correspond to the far, mid, and near infrared region.

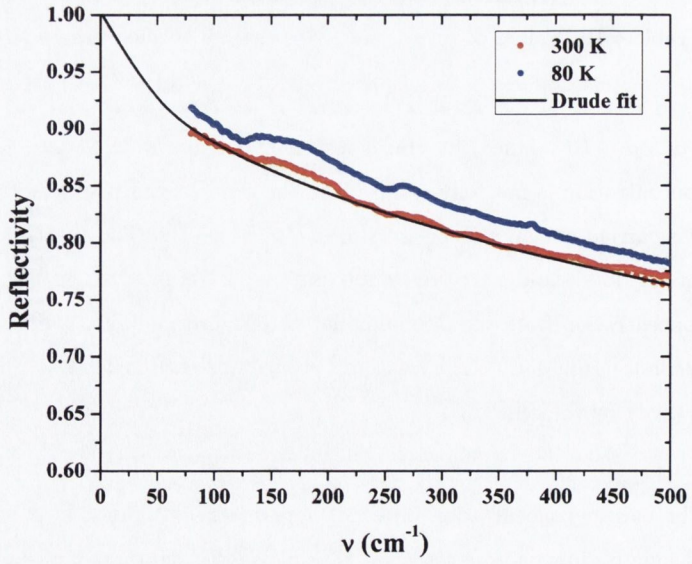

Figure 4.47: Far infrared reflectivity of a $CuCr_2Se_3Br$ single crystal at 80 K (blue dots) and 300 K (red dots).The black line correspond to a fit with the Drude model of the 300 K data.

plasma frequency corresponds to an effective carrier concentration $n = 2.2(3) \cdot 10^{21}\text{cm}^{-3}$ which is in good agreement with what is obtained by Hall measurement.

4.3 Conclusion

This chapter presents the preparation and the characterisation of $CdCr_2Se_4$, $CuCr_2Se_Br$, and $CuCr_2Se_4$ single crystals.

4.3.1 $CdCr_2Se_4$: a prototype magnetic semiconductor

The crystal growth of $CdCr_2Se_4$ was achieved by HTS and the insertion of dopants such as Ag, In, and Ga was studied. The magnetic and structural properties were investigated showing that the compound is a cubic ferromagnet with only Cr^{3+} carrying the magnetic moment. The scaling analysis study shows that it behaves like an Heisenberg magnet. The magnetotransport study shows that the system is semiconducting, the positive magnetoresistance below the Curie temperature indicate the reasonable mobility in the pure compound. The magnetotransport at low temperature were investigated for the first time. The low temperature magnetoresistance (below the Curie temperature) is dominated by the weak localisation phenomenon, and no magnetic scattering magnetoresistance is observed.

The insertion of Ag was a success and the electrical properties of the crystal were modified. In fact, the pure compound was found to be an intrinsic semiconductor and the carrier concentration was increased by introduction of Ag dopant. The insertion of In and Ga is more problematic because of the poor solubility of the respective ions as illustrated in chapter 3. In view of the transport properties measured on this system, it is important to continue to investigate other doping methods such as growth from vapour.

4.3.2 $CuCr_2Se_4 - CuCr_2Se_3Br$: another ferromagnetic metal

The crystal growth of $CuCr_2Se_3Br$ was optimised by chemical vapour transport. The single crystal x-ray characterisation confirmed the trend observed by powder neutron diffraction with a disorder on the Cu atoms. The magnetic properties were investigated and the magnetic transition is broad compared to the parent compound and very sensitive to an external field. The magnetotransport properties were also investigated. This study revealed that this compound is a highly degenerate semiconductor and the potential application of this material in devices is limited since its mobility is quite low. The main contribution in the magnetoresistance is

due to magnetic scattering and ionised impurities scattering. The angular dependance of the longitudinal and transverse resistivity have been measured and used to reconstruct the true Hall amplitude. The spin polarisation was measured for the first time in this compound by PCAR, and a moderate value of 44.3% was found which is contradiction with the band structure calculation predicting half metallicity.

The crystal growth of pure $CuCr_2Se_4$ by chemical vapour transport is reported for the first time and its magnetotransport properties were studied. The mobility in this compound is higher than in the Br doped composition. The main contribution to the magnetoresistance are the closed orbit, ionised impurity and magnetic scattering magnetoresistance, and the Hall effect is dominated by the normal Hall contribution in opposition with the Br doped compound where the spontaneous Hall effect dominate. It was therefore possible to fit together the longitudinal and transverse component of the resistivity tensor using a two band model, including the contribution from the magnetic scattering and the ionised impurities. The conductivity coefficients of two carriers (majority holes, and minority holes) were extracted from 2 K to 100 K for the first time and an effective mobility of 10 $cm^2\ V^{-1}\ s^{-1}$.

Chapter 5

Fabrication of $CuCr_2Se_4$ thin films

An important technological aspect of integrating materials in a microelectronic industrial process is the ability to fabricate high quality thin films. In a research environment, a versatile technique for the deposition of thin films is pulsed laser deposition (PLD). This technique, although marked by its adaptability, is not easily implemented in mass production. Sputtering, on the other hand, is widely used for its control over the deposition parameters and since it can be integrated on a production line.

5.1 Pulsed Laser Deposition

Pulsed laser deposition is classed as a physical vapour deposition process where the vapour is created by the interaction of a focused laser beam and the material to be deposited. The vapour can be made to react with a background gas to adjust the stoichiometry of a volatile element. The vapour of ablated material travels towards a heated substrate with an appropriate lattice constant, upon which it forms a film. Most of the time, the deposition is done in high-vacuum and the pressure is maintained at a level conducive to the molecular flow regime. A monograph of the application of PLD for the deposition of complex materials can be found in Eason (2007).

A part of the project was to set up a PLD system for oxide and chalcogenide deposition. A more detailed description of PLD as a thin film deposition tool is provided in appendix B.5. Different source targets have been employed and various configurations have been used in order to prepare the chalcogenide thin films. The sample preparation procedure is thoroughly explained in appendix B.5.2.3. Characterisation of the structural and magnetic properties of the thin film samples will be detailed in following sections.

5.1.1 Deposition from ceramic and alloy targets

Typically ceramic targets of the stoichiometric compound are used to grow films by PLD. After investigating the growth of $CuCr_2Se_4$ from sintered polycrystalline pellets, it was found that alloys with starting composition $CuCr_2$ were more successful in yielding the desired phase in a two-step process which also involved post-deposition annealing of the films in Se atmosphere.

5.1.1.1 Ceramic targets

The targets used in this section were made by pressing and sintering pellets of the powders described in chapter 3. The obtained films were then characterised by XRD and SQUID magnetometry.

Structural characterisation The XRD pattern of an as-deposited film using a $CuCr_2Se_4$ source target is presented in Fig.5.1.

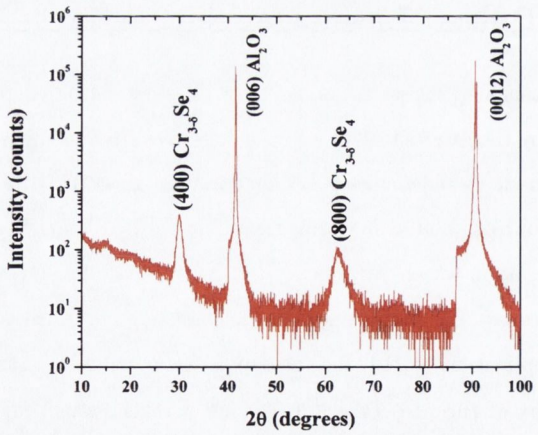

Figure 5.1: XRD pattern of a thin film prepared from a $CuCr_2Se_4$ ceramic target on a sapphire substrate at 650°C.

The thickness of the films was determined by x-ray reflectivity when possible, and all of the samples were approximately 30 nm thick. For all growth temperatures investigated the films present an oriented phase of $Cr_{3-\delta}Se_4$ instead of the expected $CuCr_2Se_4$ as illustrated in Fig.5.1. Possible explanations for the non-formation of the desired phase are:

- Decomposition of the phase on the surface of the substrate since the temperature is higher than the peritectic point. However, even at a substrate temperature as low as 300°C the same phase is observed.
- The pressure used during the deposition may fall into a reducing regime, however, the same results are obtained with higher Ar background pressure.
- A loss of selenium during the deposition at the target-laser interface and/or the ions-substrate interface.

Magnetic properties The magnetic moment of the thin films described above as a function of the applied field is shown in Fig.5.2.

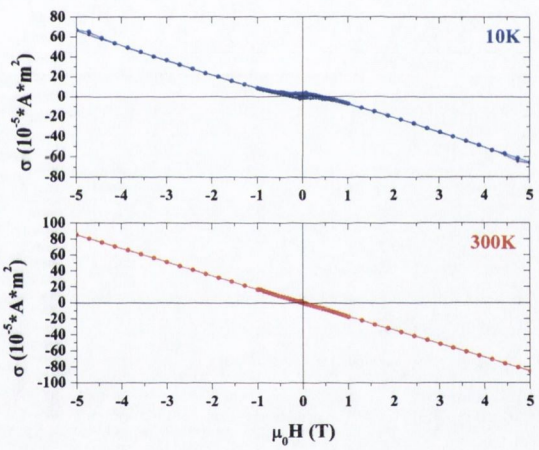

Figure 5.2: Magnetisation as a function of applied field of a film prepared from a $CuCr_2Se_4$ ceramic target at 650°C on a sapphire substrate. The measurements were carried out at 10 K (top panel) and 300 K (bottom panel).

As expected from the XRD analysis the films are not ferromagnetic at room temperature but present a well developed hysteresis loop at 10 K. The observed phase $Cr_{3-\delta}Se_4$ is an off-stoichiometric compound of Cr_3Se_4. It has been shown that, by changing the Cr content, it is possible to obtain an antiferromagnet or a ferrimagnet Maurer & Collin (1980). This explains the appearance of the hysteresis behaviour observed at low temperature with a large coercive field of 0.33 T.

The desired $CuCr_2Se_4$ phase was not found in any of the as-deposited films. To investigate the possibility of producing $CuCr_2Se_4$ from a precursor film, a target of the metallic alloy $CuCr_2$ was prepared[1].

5.1.1.2 Metallic alloy targets

All the films were deposited from the $CuCr_2$ target on various substrates at a temperature of 300 °C. They are all amorphous and do not show any magnetic ordering down to low temperature (4 K). An XRD pattern of the as-deposited film on a (001) MgO substrate is presented in Fig.5.3, none of the reflections correspond to $CuCr_2Se_4$.

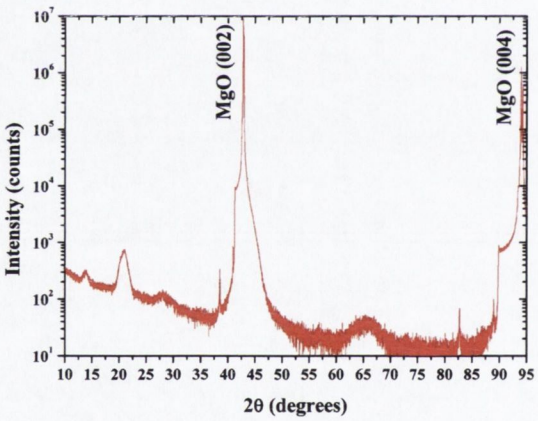

Figure 5.3: XRD pattern of a film prepared from a $CuCr_2$ metallic alloy on a (001) MgO substrate at 300°C . The unindexed peaks correspond to forbidden Bragg peaks of MgO and wavelength contamination from the Cu K_β and W L_α.

5.2 Cu/Cr multilayer produced by sputtering

PLD may be an ideal technique for producing high quality ceramic materials with a smooth surface, the deposition of metals, however, is more complicated due to the formation of nanoparticle droplets on the substrate surface. In contrast, DC sputtering is very much suited to the fabrication of smooth metallic films.

[1]The $CuCr_2$ alloy was prepared by Dr. M. Venkatesan by arc melting.

5.2.1 Multilayer production

Bilayers of Cu/Cr have been produced by sputtering[1] on different substrates from individual Cu and Cr targets. The thickness of each layer was calculated so as to give a Cu:Cr stoichiometric ratio of 1:2.

5.2.2 Multilayer characterisation

The as deposited films were analysed by XRD, x-ray reflectivity (XRR), and magnetometry. The x-ray reflectivity curve of such a film is presented in Fig.5.4.

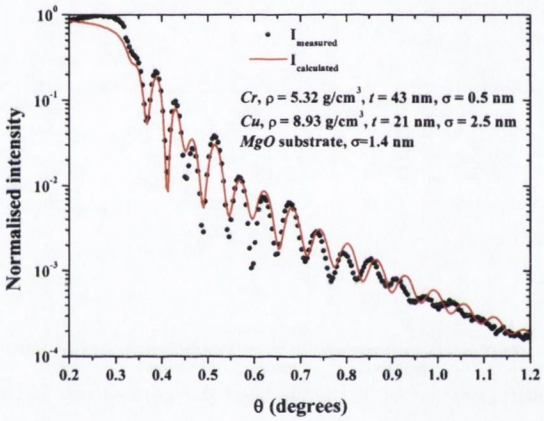

Figure 5.4: X-ray reflectivity of a Cu/Cr bilayer deposited on MgO by sputtering. The black dots are the measured intensity and the red line is the calculated curve for the 21 nm of Cu and 43 nm of Cr.

The room temperature magnetisation curve as a function of applied field is presented in Fig.5.5. As expected, only a diamagnetic signal is measured at room temperature.

5.3 Selenisation process

To understand whether the deficiency of selenium in $CuCr_2Se_4$ during the PLD process causes the formation of the undesired binary phase in the films, annealing of the samples under various selenium pressures was carried out. All the results presented in this section have been obtained using the optimum annealing temperature of 600 °C.

[1] Ciarán Fowley deposited the films in the Shamrock sputtering system.

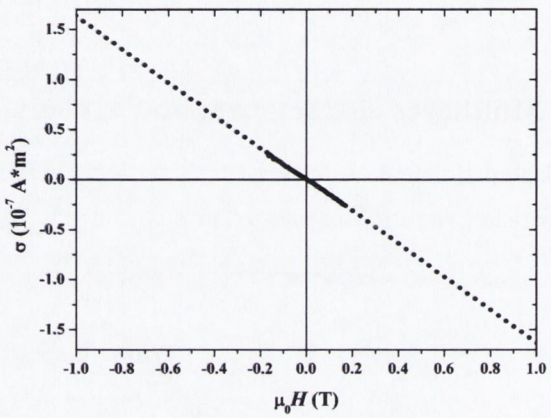

Figure 5.5: Magnetisation as a function of applied field of a Cu/Cr bilayer deposited by sputtering.

The precursor films prepared from both the metallic alloy (by PLD) and the bilayer prepared by sputtering were annealed using the same procedure. In this case, a solid state reaction occurs on the films.

5.3.1 Structural characterisation

All the annealed films exhibit a powdery surface with almost no adherence of the film to the substrate. This indicates that the films have reacted with the Se atmosphere, since annealing in vacuum did not change the morphology of the surfaces. The poor adhesion of the films to the substrate makes electrical transport characterisation unreliable.

The phases present in the thin films were determined by XRD. The XRD pattern of a film prepared by PLD from the ceramic target after annealing under Se is plotted in Fig.5.6. We observe the appearance of a second peak, corresponding to the desired $CuCr_2Se_4$ phase, together with the impurity phase Cr_3Se_4. Only the (111) orientation of $CuCr_2Se_4$ is observed suggesting that the grains are somewhat preferentially oriented.

In the case of the films prepared from a precursor film, the situation is even worse. The XRD pattern of a bilayer prepared by sputtering after annealing is shown in Fig.5.7 and the positions of the Bragg peaks characteristic of $CuCr_2Se_4$ are indicated. Some of the diffraction peaks correspond to the desired phase but it is clear that there are other phases present. The film obtained is completely polycrystalline and presents minimal adhesion to the substrate.

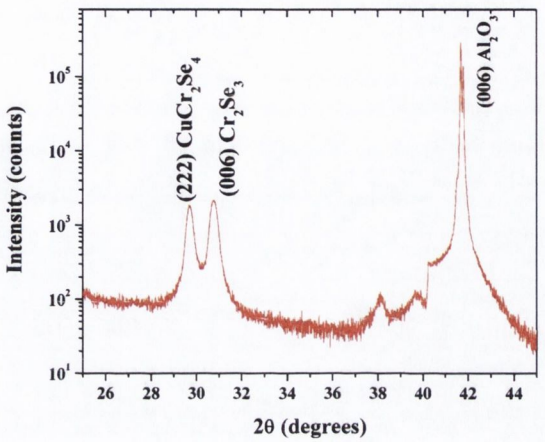

Figure 5.6: XRD pattern of a film prepared from a $CuCr_2Se_4$ ceramic target at 650°C on a c-cut sapphire substrate after annealing under a Se atmosphere.

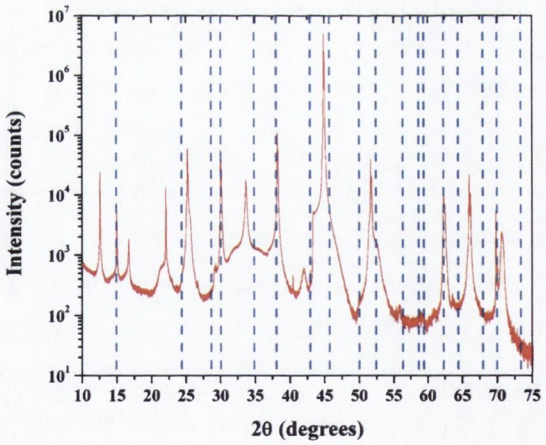

Figure 5.7: XRD pattern of a bilayer deposited by sputtering on (001) MgO after annealing under a Se atmosphere. The blue lines correspond to the Bragg positions of $CuCr_2Se_4$.

5.3.2 Magnetic properties

The magnetisation as a function of applied field of an annealed film prepared by PLD from a ceramic target is presented in Fig.5.8. A typical ferromagnetic signal (superposed on a diamag-

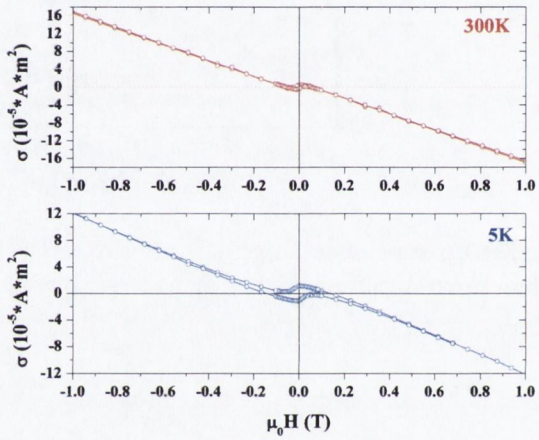

Figure 5.8: Magnetisation as a function of applied field of a film prepared from a $CuCr_2Se_4$ ceramic target at 650°C on a sapphire substrate at 5 K (bottom panel) and 300 K (top panel) after annealing in a Se atmosphere.

netic signal arising from the Al_2O_3 substrate) is observed at room temperature consistent the XRD observations. A small coercive field of 13 mT is observed at 300 K, and this increases to 30 mT at 5 K. The evolution of the magnetisation with temperature in an external field of 20 mT is shown in Fig.5.9. The sample has a Curie temperature just above 400 K. A significant increase in the magnetisation is observed at around 70 K, this is followed by a decrease upon further cooling. This behaviour is attributed to the antiferromagnetic transition of one of the impurity phases present in the film.

The same behaviour is observed for films prepared from precursor films. The applied field dependence and the temperature dependence of the magnetisation for an annealed bilayer prepared by sputtering are presented in Fig.5.10 and Fig.5.11 respectively.

The only differences compared to the films prepared from the ceramic target are that the transition appears to be smoother, and that the contribution of the antiferromagnetic impurity is reduced.

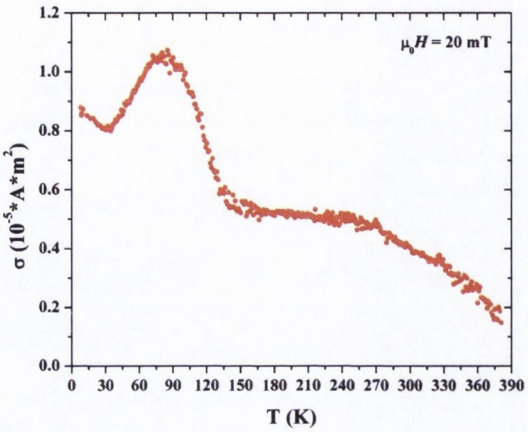

Figure 5.9: Temperature dependence of the magnetisation measured in an external magnetic field of 20 mT of a film prepared by PLD from a $CuCr_2Se_4$ ceramic target at 650°C on a sapphire substrate after annealing in a Se atmosphere.

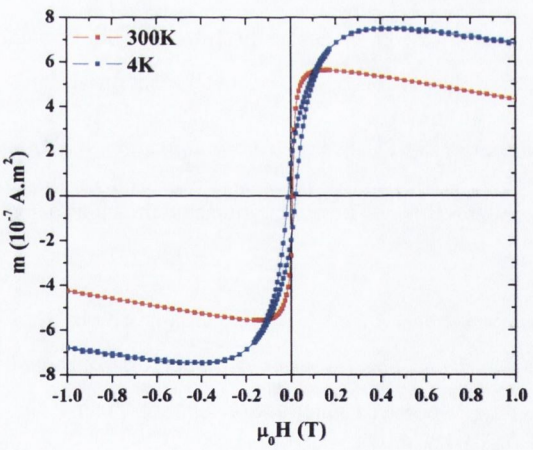

Figure 5.10: Magnetisation as a function of applied field of a bilayer prepared by sputtering with post-annealing in a Se atmosphere, at 5 K (blue curve) and 300 K (red curve).

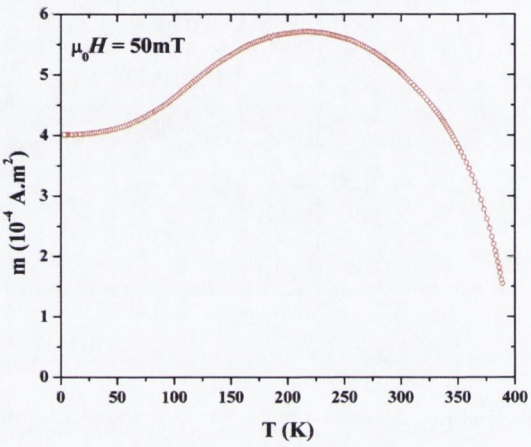

Figure 5.11: Magnetisation as a function of temperature in an external magnetic field of 50 mT of a bilayer prepared by sputtering and subsequently annealed in Se atmosphere.

5.4 Conclusions

The preparation of copper chalcochromite thin films was investigated by both PLD and sputtering. Two different methods have been attempted:

- direct growth of the films from a stoichiometric target
- a two-step process involving subsequent selenisation of a previously fabricated precursor film

It has been established that it is not possible to obtain a single phase film by these processes. Nevertheless, films with the desired phase were obtained after annealing the samples in a Se atmosphere. A possible explanation is that during the deposition a large amount of Se is lost. The Se is lost in the plume of the plasma and at the substrate surface when it is heated to elevated temperatures. Even when the film is deposited at room temperature, annealing under vacuum does not produce $CuCr_2Se_4$. A Se-enriched target was prepared and used, but the crystalline quality of the films deteriorated since the target was not as dense as the pure compound and droplets were formed at the surface of the films.

In order to minimise the loss of the highly volatile Se, pulsed laser deposition was carried out in a confined plasma configuration. The first conclusion of this study is that the loss of Se is still too significant to permit the formation of $CuCr_2Se_4$. This study provides only a

preliminary investigation of the deposition of single phase $CuCr_2Se_4$ thin films. Although the more direct methods for deposition of these films have been ruled out, innovative adaptations of the techniques are under constant development, and there is plenty of scope for further work in this area (e.g. combinatorial PLD).

During the time of the project two reports of the deposition of $CuCr_2Se_4$ thin films have been published Bettinger *et al.* (2008); Kim *et al.* (2008). In both reports they obtain multiphase films were obtained, and a post-deposition treatment was necessary to obtain the spinel phase. We did not investigate the electrical properties of our films since the film quality was deemed insufficient and the presence of several impurity phases might compromise the interpretation and the accuracy of the results.

Chapter 6

ZnO based diluted magnetic oxides

6.1 Transition metal doped ZnO

Another approach to develop a magnetic semiconductor is to insert a magnetic dopant inside a well known semiconductor matrix. The success of the Mn doped $III-V$ semiconductors is an example of such a system. The possibility of using an oxide semiconductor in magneto-electronic applications emerged after the first report of room temperature ferromagnetism in Co-doped anatase TiO_2 Matsumoto *et al.* (2001). The first part of the study presented here addresses the synthesis and the characterisation of TM-doped ZnO nanoparticles while the second part focuses on reproducing the results on thin films obtained in the laboratory with a new PLD system. The possibility of finding and developing new materials exhibiting ferromagnetism at or above room temperature for spinelectroncs applications is explored.

6.1.1 Literature review

An exhaustive literature review on TM-doped ZnO would be rather difficult as the reports are too numerous, and a number of reviews articles are available Pan *et al.* (2008).

The main conclusion that can be drawn from the plentiful supply of scientific literature, is that the observed high temperature ferromagnetism is highly non-reproducible and that the question of whether this magnetism is due to intrinsic magnetic interaction or due to the presence of magnetic clusters is sill under debate.

6.1.2 TM-doped ZnO nanoparticles

Preparation of nanoparticles would appear to be an easy way to produce ferromagnetism in oxide materials. It has been argued that no dopant is needed to induce a magnetic moment in a wide range of oxide materials Sundaresan & Rao (2009a,b); Sundaresan *et al.* (2006). The study undertaken here is an extension of a previous work attempting to reproduce some reports of ferromagnetism in TM-doped ZnO Alaria *et al.* (2005, 2006a,b). The experimental details for each section can be found in appendix B.1.

6.1.2.1 Sol-gel method

An attempt to reproduce the report of high temperature ferromagnetism in sol-gel synthesised, Li co-doped Co-ZnO is presented in this section Sluiter *et al.* (2005). To determine the effect of the heating rate on the magnetic properties, two experiments were carried out. The first one adopted the same "fast" heating rate used in the original report, and the second used a "slower" heating rate, with a gelling time of 12 h instead of 4 h. XRD patterns of both samples were similar, one of them is presented in Fig.6.1. All of the peaks can be indexed with the

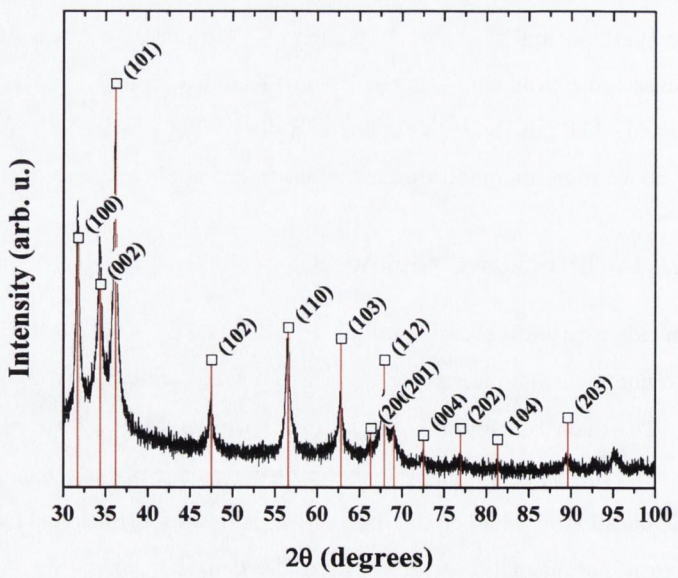

Figure 6.1: XRD pattern of Li co-doped Co-ZnO nanoparticles prepared by sol-gel method, with a "fast" heating rate, and fired at 400°C.

würtzite *ZnO* structure. The broadening of the peaks is due to the small crystallite size which is estimated to be about 20 nm by the Williamson-Hall method.

There is no clear difference between the two methods from the XRD analysis, however, a slight difference is observed in the magnetic properties. Fig.6.2 shows the magnetic moment as a function of applied field. Samples prepared by the "slow" heating rate exhibit paramagnetism,

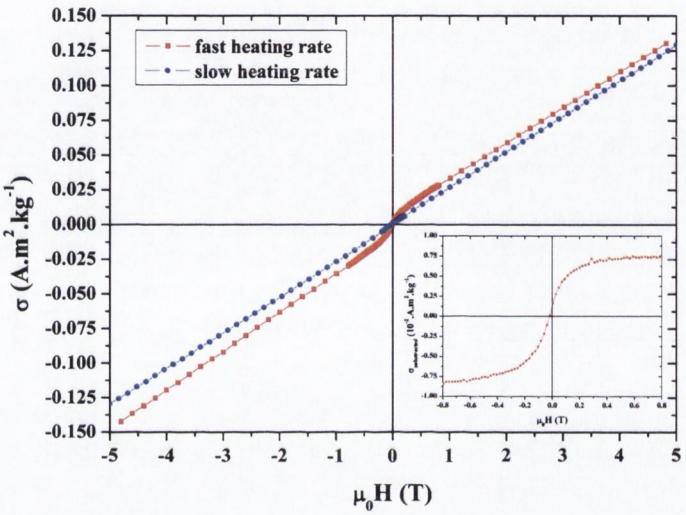

Figure 6.2: Magnetisation as a function of applied magnetic field for *Li* co-doped *Co-ZnO* nanoparticles prepared by sol-gel method with a "fast" heating rate (red square) and "slow" heating rate (blue dots) and fired at 400°C. The inset is a zoom of the "fast" heating rate curve corrected from the paramagnetic contribution.

whereas the "fast" heating rate yields particles presenting a mixture of paramagnetism and ferromagnetism. The saturation magnetic moment observed is nevertheless much lower than that reported in Sluiter *et al.* (2005).

6.1.2.2 Hydro/solvo-thermal method

***ZnO* rods grown by hydrothermal method** The observation of ferromagnetism in oxide thin films in the absence of any dopant is puzzling Venkatesan *et al.* (2004). A possible explanation could be that the aspect ratio between the thickness and the length of the grains is larger than in normal materials. To investigate the truth in this hypothesis, nano- and micro-rods of pure *ZnO* were synthesised by hydrothermal method using ethylenediamine and CTAB (Cetyl TrimethylAmmonium Bromide) as surfactants.

Scanning electron microscopy (SEM) was used to check the morphology of the obtained powders and the micrographs are compared in Fig.6.3.

Figure 6.3: SEM pictures of (a) pure ZnO microrods prepared with CTAB, (b) pure ZnO nanorods prepared with ethylenediamine, and (c) Co-doped ZnO platelets prepared with CTAB.

The magnetic properties of the pure ZnO exhibit only diamagnetism whereas the nominally 5 % Co-doped ZnO powder is paramagnetic at room temperature as indicated by Fig.6.4.

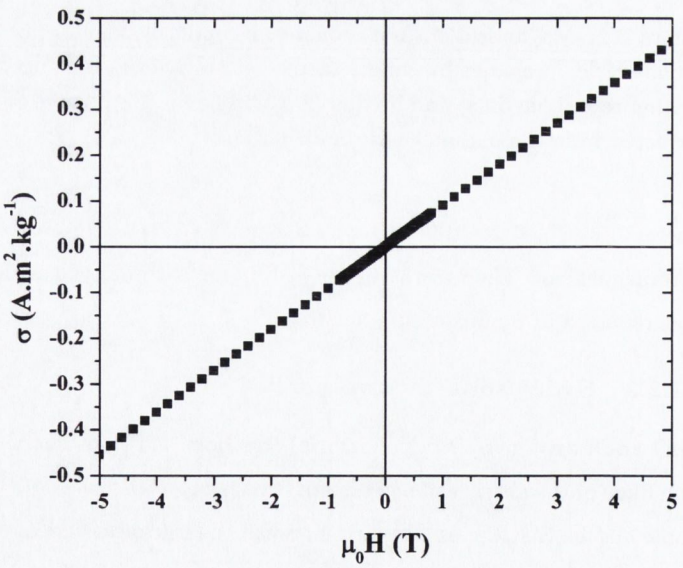

Figure 6.4: Magnetisation as a function of applied field of ZnO nanoparticles doped with 5 % Co at room temperature.

We did not observe any signature of ferromagnetism in pure ZnO particles with an aspect ratio of up to 10 for the microrods and in Co doped ZnO particles with an aspect ratio of

4. The observed aspect ratios are still very small compared to those in thin films, even if the lateral grain size is only few microns.

TM-doped ZnO synthesised by solvothermal method Another aspect of hydrothermal synthesis that can be used in the investigation, is the fact that it is possible to work outside thermodynamic equilibrium. One possible origin of the ferromagnetism observed in these TM-doped oxides could be the presence of defects in the materials. A report of high temperature ferromagnetism in Co-doped ZnO nanoparticles synthesised by solvothermal method explained the origin of the ferromagnetism by the creation of defects at the interfaces of two overlapping nanocrystals Wang *et al.* (2006).

A detailed and systematic study of the structural and magnetic properties of (Sc, Ti, V, Cr, Mn, Fe, Co, Ni, Cu) doped ZnO nanocrystals with a nominal concentration of 5%, prepared by a solvothermal process was carried out. For each dopant two different batches of sample were prepared as described by the flowchart in Fig.6.5. The phase purity of all the obtained

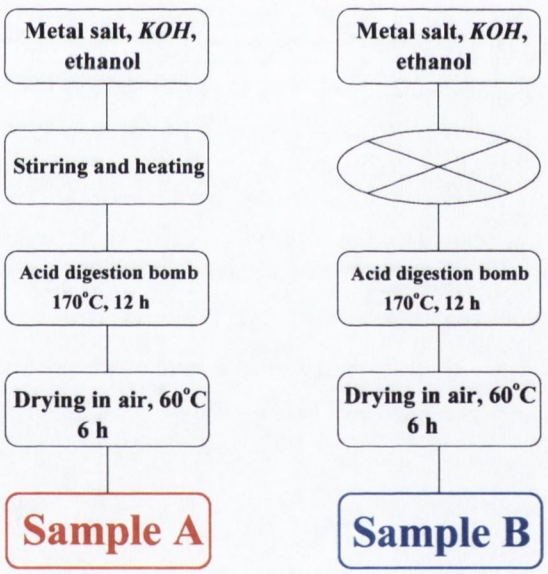

Figure 6.5: Flowchart of the sample preparation, series A (left) and series B (right).

powders was analysed by XRD and all but Ni-doped ZnO particles were found to be single phase. The XRD patterns of the pure and Ni-doped ZnO are refined[1] and presented in Fig.6.6.

[1]The software XpertPlus was used to refine these XRD scans.

For Ni-doped samples (both series A or B) the presence of a secondary phase is identified as Ni

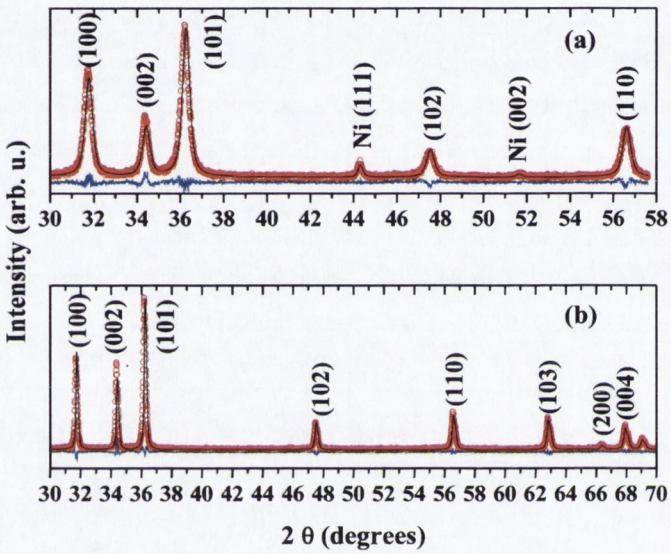

Figure 6.6: Refined XRD patterns of (a) Ni-doped ZnO with a nominal concentration of 5% and (b) pure ZnO at room temperature. The red circles represent the observed pattern, the continuous black line represents calculated intensities and the blue line is the residual.

metal, the quantitative analysis gives a ratio of 96.7(7)% of ZnO and 3.3(7)% of metallic Ni. The main difference observed between sample A and B for each TM is the presence of unreacted zinc hydroxide and a bigger particles size for samples prepared without premixing (series B). For samples prepared in series B, a longer reaction time (24 h at 170°C) or a higher temperature is needed to obtain the full reaction. The average crystallite size was determined from the broadening of the x-ray diffraction peaks of the sample using Williamson-Hall method. The average crystallite sizes of samples prepared via route A is around 20 nm whereas the average crystallite sizes of sample prepared via route B is around 50 nm.

Fig.6.7 (a) summarises the magnetic properties of the TM-doped ZnO prepared by a solvothermal method by presenting the mass magnetisation at 5 T for each TM. All the samples prepared in series A, except for $TM = Ni$, are diamagnetic or paramagnetic as expected for the dilution of the TM in the ZnO matrix. No ferromagnetic component is observed down to 4.2 K. A ferromagnetic behavior is observed for sample $Zn_{0.95}Fe_{0.05}O$ B with a saturation magnetisation of 1.7 A m^2 kg^{-1} whereas sample A presents only paramagnetism (Fig.6.7

(d)). Similar behavior is observed for the Co-doped sample : room temperature ferromagnetism with a saturation magnetisation of 0.3 A m^2 kg^{-1} for the sample prepared in series B and pure paramagnetism for sample A (Fig.6.7 (b)). This magnetisation value is high compared to other reports in the literature but ten times smaller than the 3 A m^2 kg^{-1} reported by Wang *et al.* (2006). A supplementary experiment was carried out to see the evolution of the magnetisation with the temperature growth and an increase of 100% of the magnetisation is observed by increasing the temperature reaction to 190°C as presented on Fig.6.8. In the case of $Zn_{0.95}Ni_{0.05}O$ room temperature ferromagnetism for both samples A and B (Fig.6.7 (c)) is observed. This ferromagnetism is explained by the presence of Ni metal observed by x-rays. Nickel segregation is explained by the poor solubility of Ni in ZnO, and moreover, the solubility of Nickel (II) acetate in ethanol is very low, so it is difficult to obtain a homogeneous mixture of Zn^{2+} and Ni^{2+} ions. To confirm this hypothesis, $Zn_{0.95}Ni_{0.05}O$ was prepared by a hydrothermal method, using the same procedure as sample A, but replacing ethanol by water. The M-H curve at room temperature presented purely paramagnetic behavior (Fig.6.7 (c), green star symbol)

Fig.6.9 (a) and (b) show the Mössbauer spectra[1] of $Zn_{0.95}Fe_{0.05}$O A and B samples respectively. For sample A no magnetic ordering of the iron is observed, which is in a +(III) states with an isomer shift of 0.37 mm s^{-1} relative to α-Fe, and a quadrupole splitting of 0.46 mm s^{-1}, as expected for substituted Fe^{3+} on tetrahedral site in ZnO Ahn *et al.* (2004). For sample B 70 % of the iron is a similar +(III) state. However 30 % of the iron appears in a magnetically ordered form, identified from the spectrum as magnetite and hematite.

6.1.3 Co-doped ZnO thin films

As described in the introduction of this chapter, a vast number of experimental studies showed that Co-doped ZnO presents room temperature ferromagnetism. The aim of the study presented below was to reproduce the results obtained by PLD in the laboratory with a different deposition chamber.

The system used and the experimental condition for the deposition of the films are described in details in appendix B.5.2.1. The nominal concentration of Co in the target was set to 5% and a systematic study of the structural and magnetic properties of the films as a function of deposition temperature was carried out.

[1] Mössbauer spectroscopy on the samples was measured and analysed by Dr. Gunning.

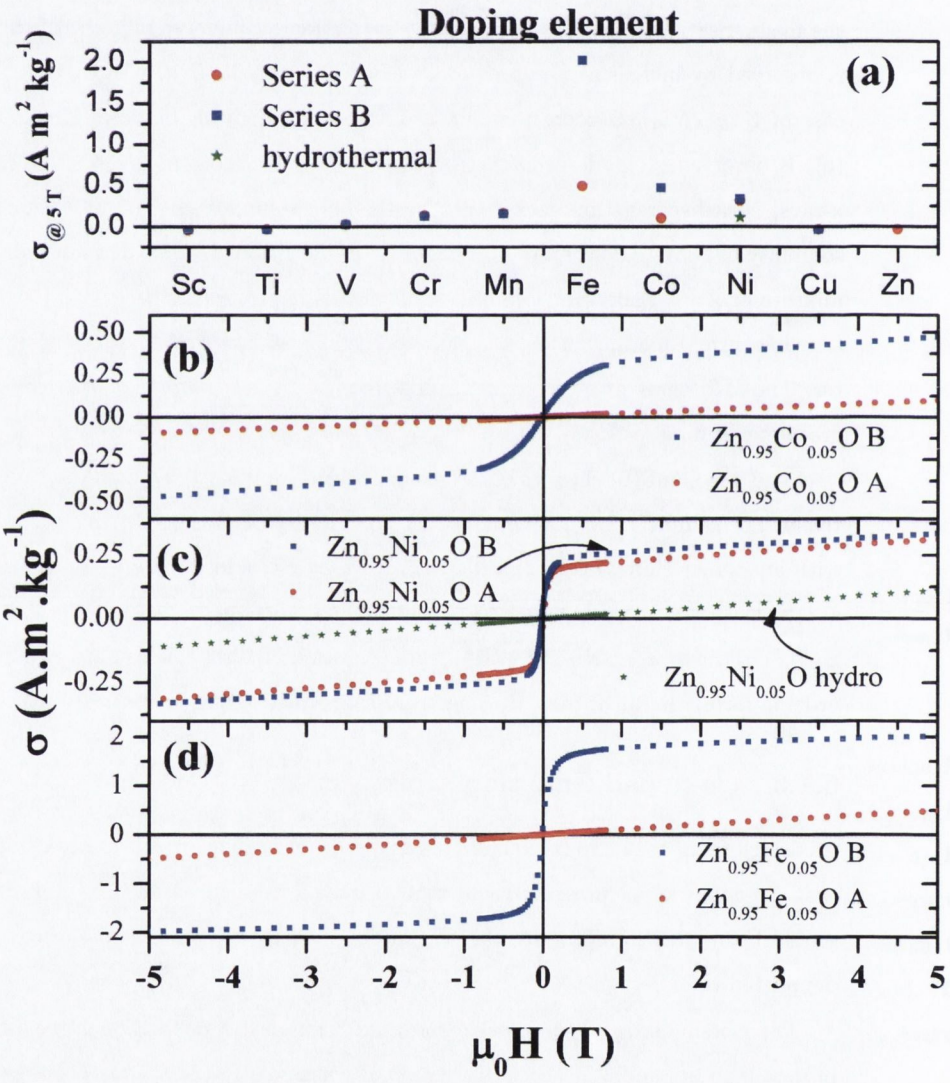

Figure 6.7: (a) Summary of the mass magnetisation at 5 T for the different TM. (b), (c) and (d) Room temperature magnetisation curves for ZnO doped with 5% of Co, Ni and Fe respectively. Red circles represent samples prepared in series A, blue squares samples of series B and the green star 5% Ni doped ZnO by hydrothermal reaction.

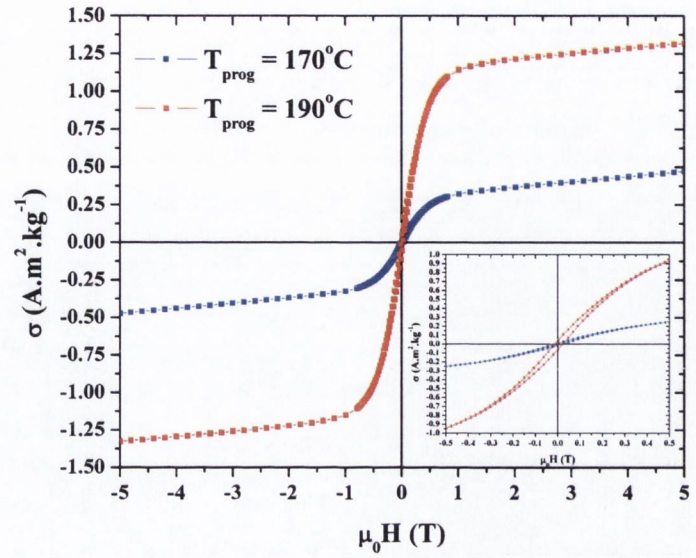

Figure 6.8: Magnetisation as a function of applied field of Co-doped ZnO series B prepared at 170°C (blue squares) and 190°C (red squares). The inset is a zoom at low field.

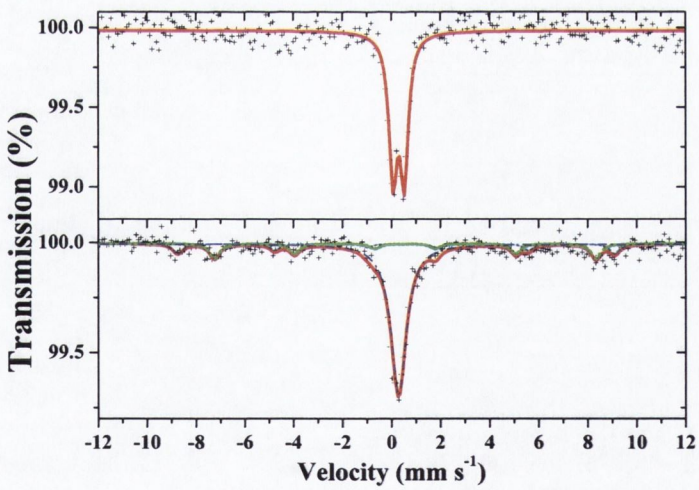

Figure 6.9: Mössbauer spectra of (a) $Zn_{0.95}Fe_{0.05}O$ prepared via route A and (b) prepared via route B. Continuous lines represent the total calculated spectrum, the dashed lines represent the contribution of magnetite and hematite.

6.1.3.1 Structural characterisation

A typical XRD diagram of the obtained films is shown on Fig.6.10. The c lattice constant

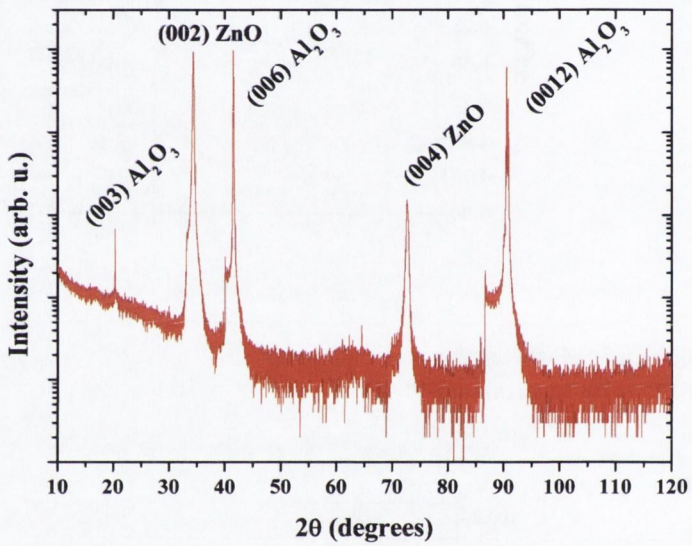

Figure 6.10: XRD pattern of a ZnO thin film deposited on c-Al_2O_3 by PLD.

was calculated, and its evolution as a function of the deposition temperature is presented on Fig.6.11.

6.1.3.2 Optical properties

To check the substitution of Co ions in the ZnO matrix, optical spectroscopy can be a useful tool. In fact, the $d-d$ transitions of most $3d$ ions are available in the literature. In particular, the transition for Co^{2+} in tetrahedral coordination have been measured Koidl (1977). The spectra between 200-800 nm of pure and Co-doped ZnO are represented Fig.6.12. Three absorptions peaks are present in the Co-doped films between 500 and 700 nm. These three peaks are attributed to the transition $^4A_2(F) \rightarrow^4 T_1$. The strong spin-orbit coupling lift the degeneracy of the $^4T_1$ in three energy levels so the three absorptions corresponds to the transitions : $^4A_2(F) \rightarrow^2 E(G)$, $^4A_2(F) \rightarrow^4 T_1(P)$, and $^4A_2(F) \rightarrow^2 A_1(G)$ as represented on Fig.6.13.

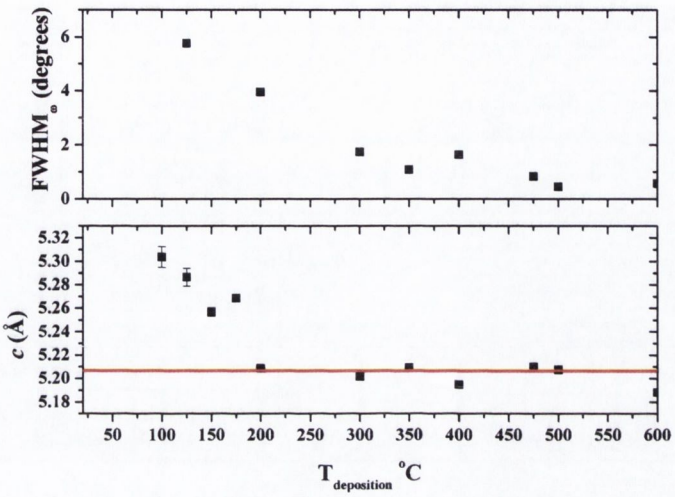

Figure 6.11: Evolution of the ZnO (002) rocking curve FWHM (top panel) and c lattice parameter (bottom panel) as a function of deposition temperature.

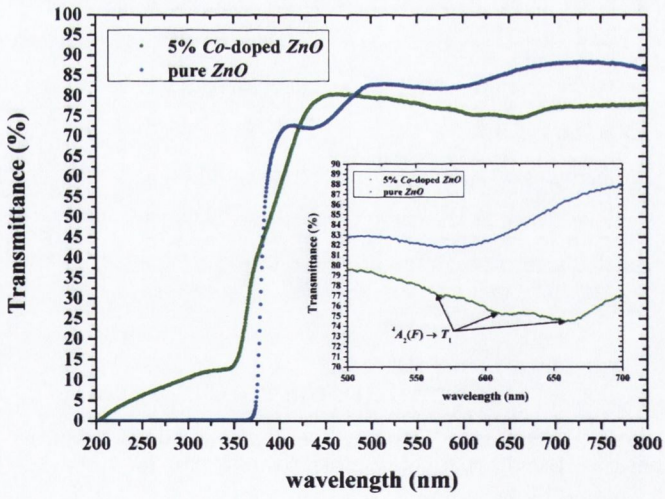

Figure 6.12: Transmittance spectra of a pure ZnO films (blue dots) and a nominally 5% Co-doped ZnO films. The inset emphasis the $d-d$ transitions due to the Co^{2+} inserted in the ZnO matrix.

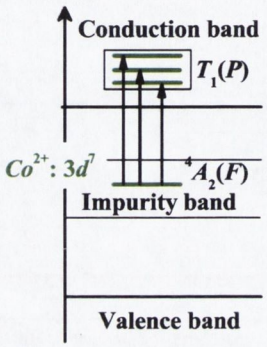

Figure 6.13: Diagram showing the transition in Co-doped ZnO.

6.1.3.3 Magnetic properties

The goal of this study was to reproduce the magnetic properties of Co-doped ZnO films produced in a different ablation chamber. It was shown that the ferromagnetism appears only in a small temperature region, therefore magnetisation as a function of applied field was measured for the films prepared for different deposition temperature in the new system. The result is presented on Fig.6.14.

No ferromagnetism was observed in the films prepared, in contrary to what was observed in previous study in the same laboratory. The small ferromagnetic feature observed on some curves is due to the contamination of the substrate by the substrate holder as described in appendix B.5.

6.2 $w - CoO$ thin films and related

Some reports show that the origin of the magnetic properties observed in DMOs can be metallic inclusion in the host matrix Dorneles *et al.* (2007); Kim *et al.* (2004); Rode *et al.* (2008). The observation of such clusters by conventional techniques may be difficult because ZnO and Co metal both crystalize in an hexagonal structure and coherent cobalt nanoinclusions may form in ZnO. Other possible secondary phases in this compound are Co_3O_4 and cubic CoO, but both are antiferromagnetic with Néel temperatures of 40 and 287 K respectively Rao & Rao (1974).

Recently several groups reported the preparation of hexagonal CoO nanoparticles Risbud *et al.* (2005b); Seo *et al.* (2005). The authors concluded that no magnetic ordering is present

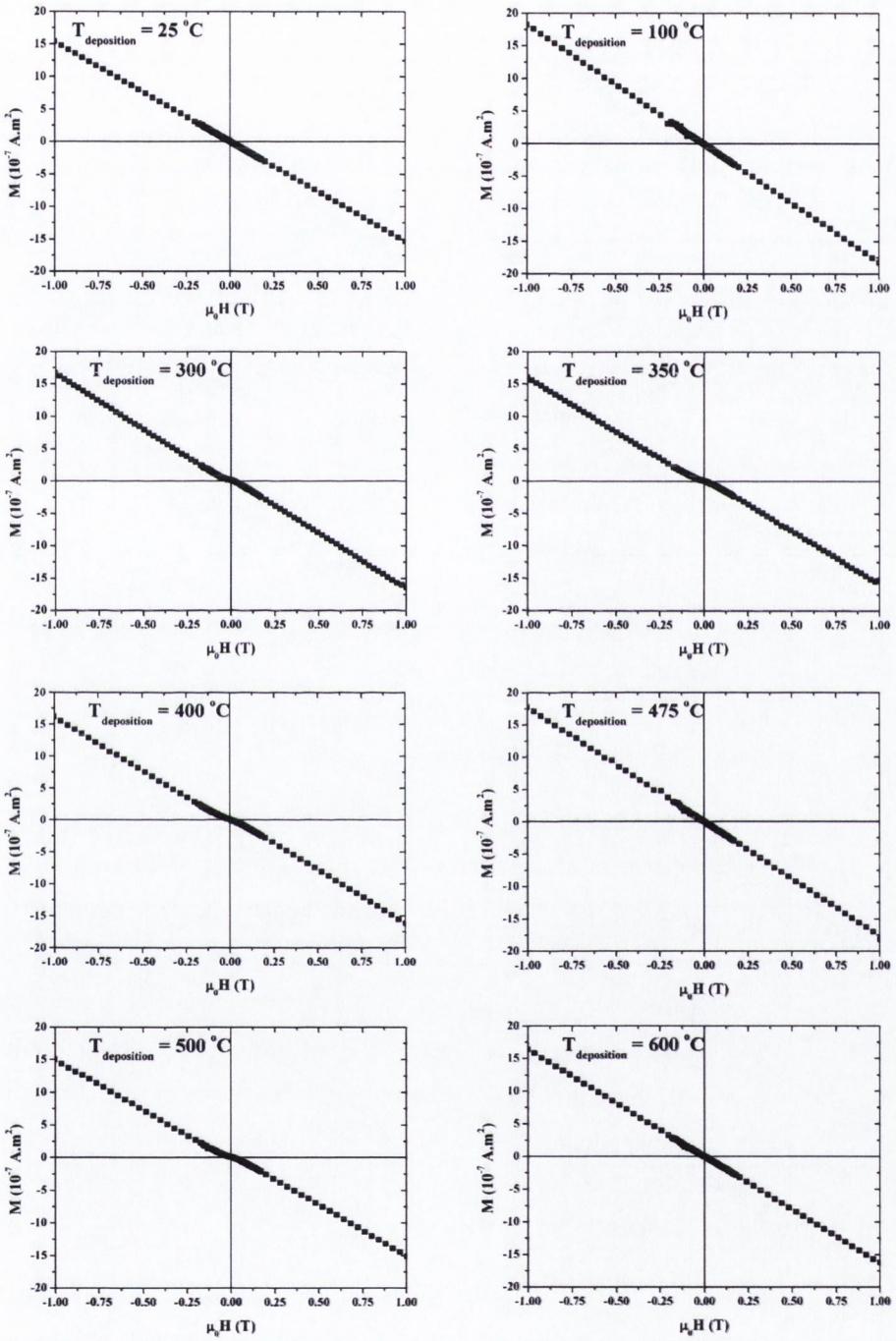

Figure 6.14: Magnetisation as a function of applied field for 5% Co-doped ZnO prepared at various temperature.

in this structure, although electronic structure calculations led to a different conclusion Han & Yu (2006); Risbud *et al.* (2005b). Furthermore, it has been postulated that hexagonal CoO nanoparticles with a high Néel temperature contribute to the observed magnetic moment via uncompensated cobalt spins at the surface Dietl *et al.* (2004).

To investigate the possibility of the formation of new $Co-O$ phases in thin films, two different PLD geometry (on-axis and off-axis) have been used to grow CoO thin films on sapphire substrate and ZnO buffer layer. The detail of the experimental procedure can be found in appendix B.5.2.2.

6.2.1 CoO thin films

The films described in this section have been prepared with the classical geometry of PLD (substrate and target aligned).

6.2.1.1 XRD characterisation

We present in Fig. 6.15 the XRD patterns obtained for the films deposited on a ZnO buffer layer at different substrate temperatures. For the film deposited at 600°C the main reflection is attributed to ZnO (Fig. 6.15(a)). A small peak of CoO is also observed. As soon as we began the deposition of CoO, the RHEED pattern started to be spotty (inset Fig. 6.15(a)). Fig. 6.15(b) presents the XRD pattern of a film deposited with the substrate temperature at 500°C. Two main phases are observed : ZnO with a (002) preferred orientation and Co_3O_4 with a (400) orientation. For the samples grown at lower temperature a mixture of oriented ZnO and polycrystalline Co_3O_4 (Fig. 6.15(c)) is observed.

6.2.1.2 Magnetic properties

The samples prepared above 400°C present only diamagnetic behaviour at room temperature. In contrast, the samples prepared at 400°C and 300°C include a ferromagnetic contribution (Fig. 6.16). After the diamagnetic correction, the magnetisation observed is in the range of 0.5 to 1.25 $\cdot 10^5$ A$\cdot$m^{-1}. We recorded the time dependance of the magnetic properties of the sample prepared at 400°C (inset of Fig. 6.16). There is a decay with time of the magnetic moment which might be due to the oxidation of Co particles.

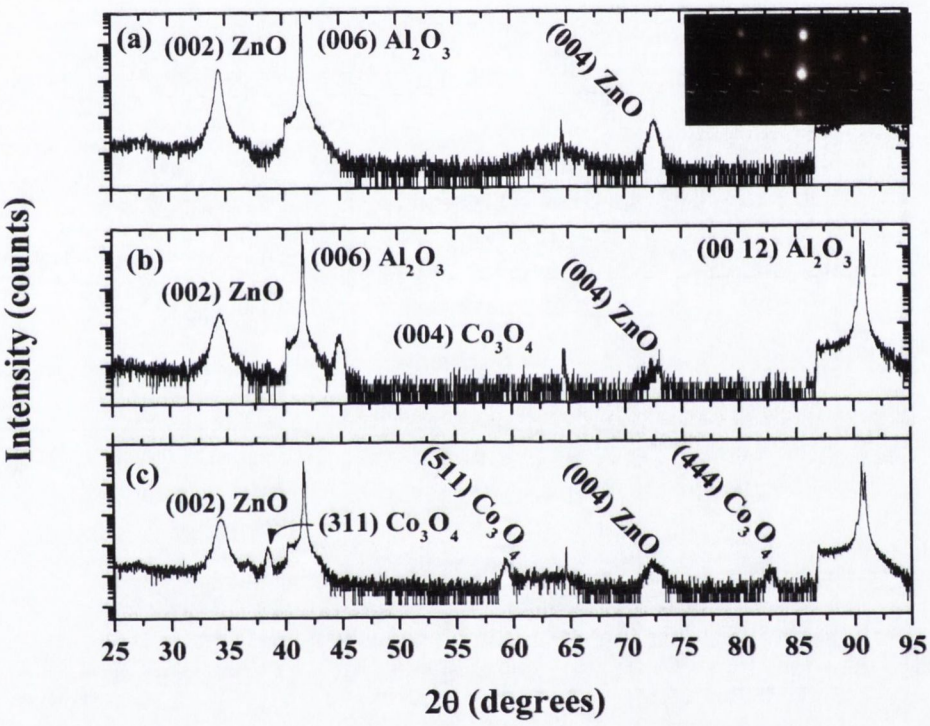

Figure 6.15: XRD pattern of CoO-ZnO-c Al_2O_3 deposited on axis at (a) 600°C (inset : RHEED pattern after the deposition) (b) 500°C and (c)400°C.

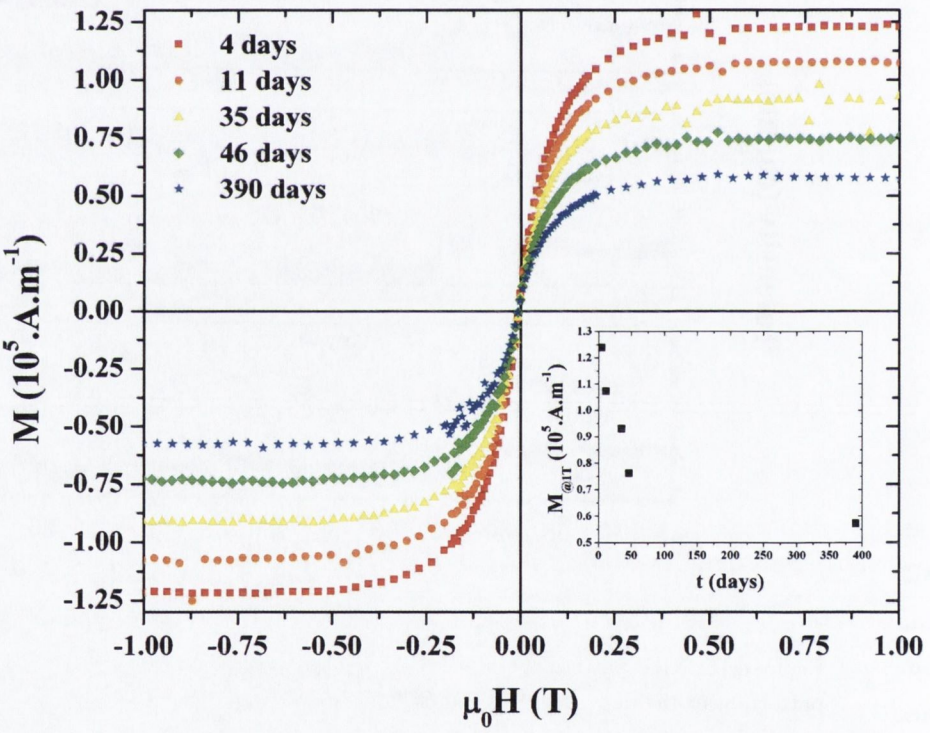

Figure 6.16: Magnetisation curves of a sample prepared at 400°C measured after different times (inset : evolution of the saturation magnetisation as a function of time.) Data have been corrected for the background diamagnetic slope.

6.2.2 Off-axis PLD

In the off-axis geometry the target and the substrate are misaligned with an angle of 5° and the energy of the species reaching the substrate is lower than in a normal geometry. Two type of thin films have been produced : CoO on (0001) Al_2O_3 and CoO on a ZnO buffer layer.

6.2.2.1 RHEED analysis

Fig. 6.17 (a) presents the RHEED diffraction pattern obtained with the electron beam parallel to the $[1\bar{1}00]$ and the Fig. 6.17 (b) with the electron beam parallel to the $[11\bar{2}0]$ direction of the sapphire substrate after surface preparation. Fig. 6.17 (c) and (d) represent the RHEED diffraction pattern after the deposition of a ZnO buffer layer, a CoO layer and a ZnO capping layer. The streaky patterns observed show that the growth is two-dimensional. During the growth of the CoO layer, the general aspect of the RHEED pattern does not evolve, suggesting that the CoO is growing with a würtzite structure. Fig. 6.17 (a) and (b) show an epitaxial relationship $[1\bar{1}00]_{Al_2O_3}//[11\bar{2}0]_{ZnO}$ as reported by Vispute *et al.* (1997). Fig. 6.17 (e) and (f) represent the RHEED diffraction patterns of CoO grown directly on the sapphire. In this case we observe spotty patterns, characteristic of three-dimensional growth.

Although, the general RHEED patterns are similar in both cases, we can observe a variation of the in-plane lattice parameter. Fig. 6.18 presents the real time a lattice parameter variation. The lattice parameter is calculated by using the sapphire as reference. For the ZnO buffer layer, we stopped the deposition when the a parameter of ZnO is completely relaxed (Fig. 6.18 blue curve). During the deposition of the CoO layer on ZnO we observe a slight variation of the in-plane lattice parameter (Fig. 6.18 red curve).

6.2.2.2 XRD characterisation

Fig. 6.19 shows XRD patterns for the CoO films grown on (a) sapphire and (b-c) ZnO seed layers. The sample grown directly on sapphire shows a reflection of cubic CoO with a (111) preferred orientation at $2\theta = 36.5°$ in Fig. 6.19 (a). A careful analysis of the (111) peak shows that we have some trace of Co_3O_4. In Fig. 6.19 (b), the peak observed at 34.42° is attributed to the (002) ZnO and w-CoO reflections. The 2θ value shows that the ZnO film is completely relaxed as expected from the RHEED investigation. A "mean crystallite size" in the [002] direction was calculated applying the Scherrer formula. The crystallite size are evaluated to be 18.7 nm. The crystallite size is found to be close to the total sample thickness (18.9 nm) determined by x-ray reflectivity indicating coherent growth of CoO on the ZnO seed-layer. The

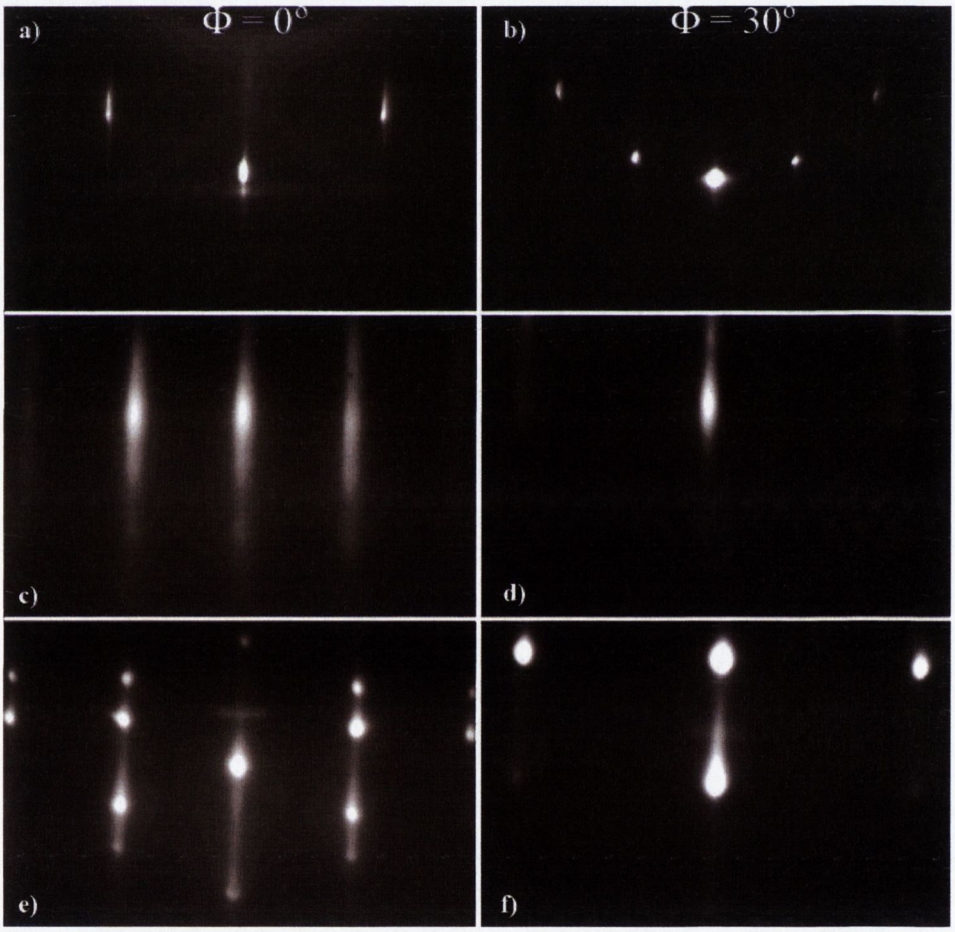

Figure 6.17: RHEED diffraction patterns of surface prepared sapphire (a),(b) final picture after the deposition of 15 nm of *ZnO* buffer layer, 5 nm of *w-CoO*, 2 nm of *ZnO* (c),(d) 15 nm of *CoO* directly on sapphire (e),(f). The left column picture represent diffraction pattern with the electron beam parallel to the $[1\bar{1}00]_{Al_2O_3}$ $\Phi = 0°$ and the right column with the electron beam parallel to the $[11\bar{2}0]_{Al_2O_3}$ $\Phi = 30°$

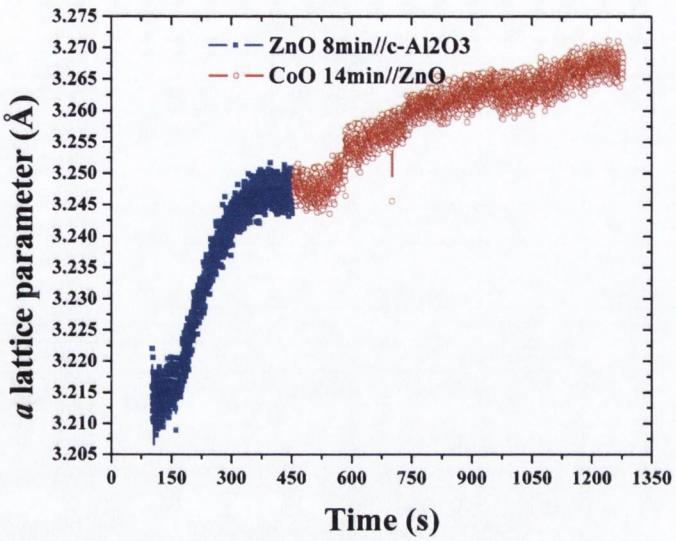

Figure 6.18: Plot of in-plane lattice parameter for ZnO buffer layer (blue curve) and CoO (red curve) layers against growth time.

smaller peak at 36.5° is attributed to the (111) reflection of cubic CoO. Fig. 6.19 (c) shows the x-ray diffraction diagram of the same films a year later. We observe a broadening of the (002) peak and the appearance of additional reflections at 38.51°, 59.35° and 82.61° attributed to Co_3O_4. The morphology of the film has completely changed; inhomogeneous agglomerates on the surface of the film can be observed with an optical microscope (inset of Fig. 6.19 (c)). The conclusion is that the w-CoO is not stable when synthesised by this method and that the decomposition products include Co_3O_4.

6.2.2.3 Magnetic properties

Fig. 6.20 presents the magnetic properties of the CoO deposited directly on sapphire. We observed a diamagnetic behaviour at room temperature due to the contribution of the substrate as presented Fig. 6.20 (a). No evidence of ferromagnetism is detected down to 4 K. Fig. 6.20 (b) represents the evolution of the volume susceptibility as a function of the temperature.

For the sample prepared with a ZnO seed layer, the same behaviour for the susceptibility is observed. This observation is similar to those on w-CoO nanoparticles Risbud *et al.* (2005b); Seo *et al.* (2005). Fig. 6.21 (b) presents the evolution of the magnetisation curves at room

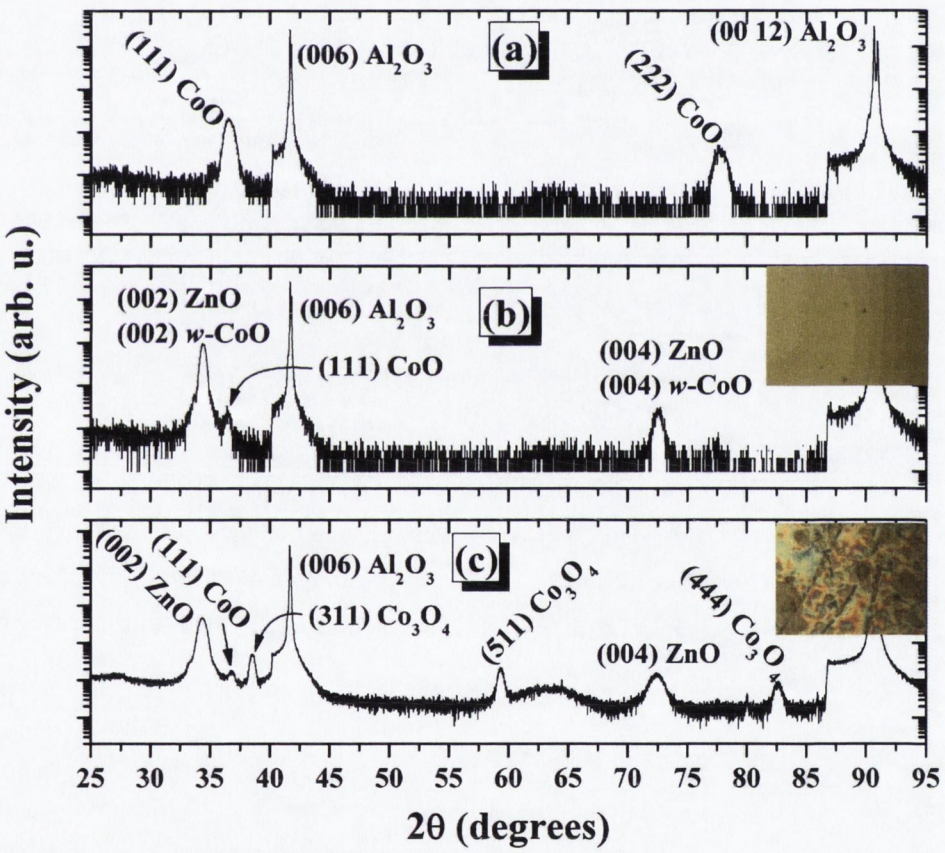

Figure 6.19: XRD patterns of (a) *CoO* grown directly on sapphire. (b) *ZnO-CoO-ZnO* trilayer just after deposition (c) the same film a year later. The pictures in the inset of (b) and (c) are optical micrographs.

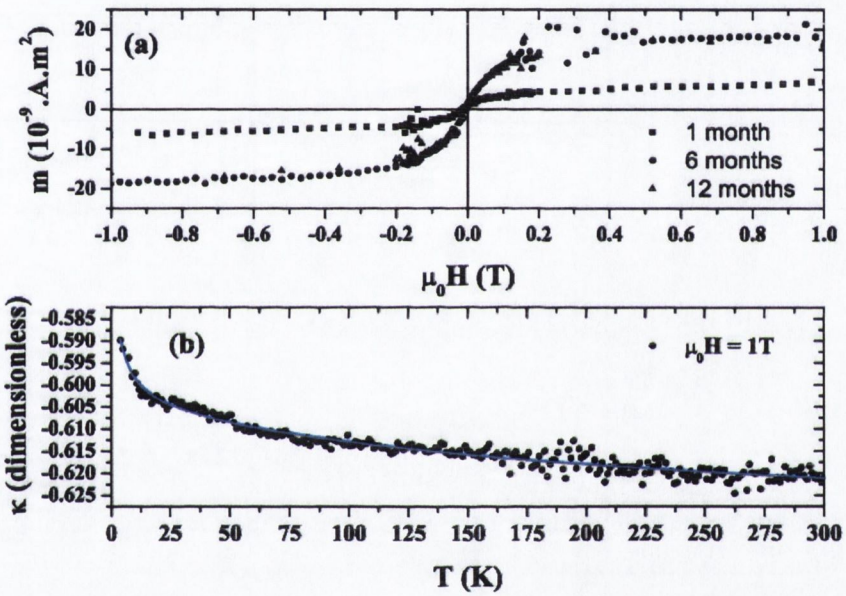

Figure 6.20: (a) Magnetisation curve at 300 K of CoO grown directly on sapphire. (b) Variation of the dimensionless volume susceptibility against the temperature under an applied field μ_0H=1 T.

temperature after one, six, and twelve months. The data have been corrected for the diamagnetic background contribution. The slope is calculated from the data between 3 T and 5 T. We observe the appearance of a small ferromagnetic moment which is stable with time.

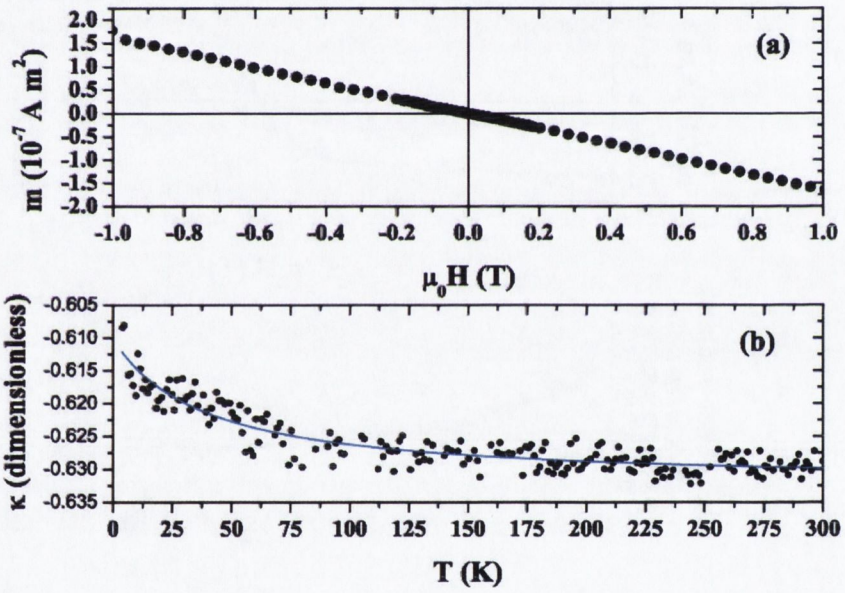

Figure 6.21: (a) Room temperature magnetisation curves of the sample grown with a ZnO seed layer. Data are corrected for the diamagnetic substrate signal (b) Temperature variation of the susceptibility under an applied field μ_0H=1 T.

6.2.3 Discussion

The thin film of pure w-CoO shows no trace of ferromagnetism in the as-deposited state (Fig. 6.21). This is in agreement with previous reports on w-CoO nanoparticles Risbud *et al.* (2005b); Seo *et al.* (2005). There is a small upturn in the susceptibility below 10 K, which is attributed to a few weakly-coupled Co^{2+} ions. The data can be fitted by a Curie-Weiss law with $\Theta_p \approx -200$ K indicating strong antiferromagnetic interaction. This magnetic behaviour can be understood in terms of the würtzite structure, which consist of sheets with hexagonal rings of alternating

Co^{2+} and O^{2-} ions, in an $ABAB$ stacking sequence which leads to a tetrahedral lattice of Co. The antiferromagnetic superexchange in each individual layer is fully frustrated. The individual $Co^{2+} - O^{2-} - Co^{2+}$ 110° superexchange may be strong, but there is no way to arrange the spins to satisfy all the interactions simultaneously.

The time dependent evolution of the w-CoO film is quite surprising. A magnetic moment appears, which increases with time and saturates after several months. At the same time, x-rays shows the appearance of Co_3O_4. Co_3O_4 is a normal spinel with Co^{2+} (e^4, t_2^3, $S = 3/2$) on A sites and Co^{3+} on B sites, where it adopts a low spin state (t_{2g}^6, $S = 0$). The $A - A$ interactions are weak, and the Néel temperature is 40 K Rao & Rao (1974). There would seem to be no reason to suppose that Co_3O_4 could be the origin of the ferromagnetic signal. Two other possibilities suggest themselves :

- The reaction of w-CoO film in air is not oxidation but decomposition : $4CoO \longrightarrow Co_3O_4 + Co$
- The frustration in w-CoO is somehow relieved by oxidation, and an uncompensated, ordered moment appears.

Both of these possibilities seem implausible. One can argue that the second can be eliminated by the lack of easy-plane anisotropy in the magnetisation curve of the oxidised film. The crystal field parameter at the tetrahedral cation site is D≈2 cm^{-1} Du & Zhao (1988).

As regards the samples prepared in the normal geometry, which show a moment when the substrate is at 400°C or lower, but not at 500°C or more, in no case is there evidence for the presence of w-CoO. In the 600°C films, antiferromagnetic c-CoO is observed. In the ferromagnetic samples produced at 400°C, Co_3O_4 is observed and the moment in this case decays with time, as it does in some films of Co-doped ZnO Fitzgerald *et al.* (2005). The possibility of ferromagnetic Co_3O_4 is therefore reconsidered. There is some evidence that this oxide can develop a net moment when doped with Sr Tay *et al.* (2006). This is attributed to a change from the low spin to the high spin state of Co^{3+}. We propose that Co_3O_4 produced by oxidation of w-CoO, or by low temperature deposition conditions has different magnetic properties than the bulk. Surface or defect sites may have a weaker B-site crystal field, producing a mixture of low spin and high spin Co^{3+}. Co^{3+} is known to adopt either a high spin or a low spin state when octahedrally coordinated with oxygen in different structures Goodenough (1963). The same effect at defect associated B-sites and normal B-sites in the same Co_3O_4 might be the origin of the observed moment and the high Curie temperature.

Chapter 7

Conclusions and Outlook

This thesis focused on the preparation and characterisation of materials which presents potential application in the field of spin electronics. Three different materials have been prepared in powder and single crystalline form. The main results obtained for each materials is presented below :

$CuCr_2Se_4$ The polycrystalline preparation of single phase $CuCr_2Se_4$ was demonstrated by XRD, powder neutron diffraction, and magnetometry. A Curie temperature higher by 20 K compared to the reported values in the literature has been measured by AC susceptibility. The powder neutron diffraction confirmed that the magnetic moment localised on the Cr is 3 μ_B, and no evidence of a localised moment was measured on the other atoms. Single crystals of pure $CuCr_2Se_4$ were grown for the first time and the magnetotransport properties were measured. The conductivities coefficient for the majority holes and minority holes were calculated from a two bands model.

$CuCr_2Se_3Br$ The powder neutron diffraction study of polycrystalline $CuCr_2Se_3Br$ revealed that the assumed delocalised antiferromagnetic moment in the parent compound appears on the Cu site and increases with the Br content. Moreover the insertion of Br in the lattice introduces some disorder on the Cu site. The origin of this disorder is not fully understood and complementary experiments such as the evolution of the atomic displacement parameters in function of the temperature might give a better picture of the true nature of this disorder. The magnetotransport properties have been studied and showed that the system is a highly degenerate semiconductor and confirmed by infrared measurements. The spin polarisation was determined for the first time in this compound by PCAR and found to be 44.3%.

$CdCr_2Se_4$ The magnetic structure of $CdCr_2Se_4$ has been determined for the first time by powder neutron diffraction and confirmed the assumed ferromagnetic state of the compound. The value of the moment measured on the Cr atom agrees well with the magnetic moment measured by standard magnetisation. The magnetotransport study confirmed that the system is a semiconductor and in the context of our project is the best candidate for future development of spin electronic devices. In fact Ag-doped single crystal have been synthesised and the insertion of Ag is the lattice increases the carrier concentration. An attempt to produce n-type $CdCr_2Se_4$ by doping with In and Ga failed by HTS. In fact the polycrystalline study showed that the solubility limit of In is very low. The next step is to investigate the growth of this system by vapour transport.

Apart for the general properties described above, physical properties such as heat capacity and magnetocrystalline anisotropy of $CdCr_2Se_4$ and $CuCr_2Se_3Br$ were measured for the first time

.

Another aspect of this study was to investigate the possibility of producing $CuCr_2Se_4$ thin films with reasonable quality by pulsed laser deposition. The outcome of this study is that the selenium partial pressure is not high enough to condense the desired phase on the substrate. Several possibilities have been investigated to diminish the loss of selenium during the process.

The last chapter of this thesis deals with a problem related to the origin of ferromagnetism in diluted magnetic oxide. The problem has been investigated in nanocrystalline powder and in thin films. The main results from the preparation of ZnO nanoparticles doped with various dopant is that an homogeneous precursor is vital for the production of impurity precipitate in the host matrix. The thin films study was based on the possibility to grow metastable compound by pulsed laser deposition, and hexagonal CoO was grown for the first time in thin films by including a ZnO buffer layer. The aim of this study was to study the magnetic properties of this new compound which could explain the origin of the high temperature ferromagnetism observed in some Co-doped ZnO. The study revealed that hexagonal CoO is a frustrated antiferromagnet and the phase was unstable in thin films form.

In the context of the search for a ferromagnetic semiconductor, as described in the introduction, the detailed characterisation of several potential compounds revealed $CdCr_2Se_4$ to be the candidate with the greatest potential for demonstration of an all ferromagnetic junction. In fact, $CuCr_2Se_4$ is metallic and when doped with Br, as investigated in this thesis, does not exhibit any semiconducting properties. $CdCr_2Se_4$, on the other hand, showed both

semiconducting and ferromagnetic properties and so the obvious next step is to find suitable dopants to produce p and n type samples. It is important to note that this compound would make a good example at research level, however its low Curie temperature in conjunction with its composition, Cd being one of the six substances banned by the European Union's Restriction on Hazardous Substances directive which bans certain hazardous substances in electronics, precludes its commercial application.

In conclusion, a strong candidate for an all ferromagnetic semiconductor device has been investigated but the quest for a room temperature ferromagnetic semiconductor is still open.

Appendix A

Chemicals informations

A.1 Origin and purity

Here we list all the informations on the chemicals used to synthesise the samples described in the main text of the thesis.

Name	Formula	Origin	Purity (%)
Zinc oxide	ZnO	Sigma Aldrich	99.995
Copper (mesh)	Cu	Sigma Aldrich	99.9
Chromium (mesh)	Cr	Sigma Aldrich	99+
Selenium (mesh)	Se	Cerac/Pur	99.95
Copper (II) bromide	$CuBr_2$	Fluka	99+
Copper (I) bromide	$CuBr$	Sigma Aldrich	99.999
Indium (mesh)	In	Sigma Aldrich	99.9
Silver (mesh)	Ag	Cerac/Plus	99.9
Cadmium (mesh)	Cd	Sigma Aldrich	99.9
Cobalt (II) acetate	$(C_2H_3O_2)Co, 4H_2O$	Sigma Aldrich	98+
Zinc (II) acetate	$(C_2H_3O_2)Zn, 4H_2O$	Sigma Aldrich	99
Sodium hydroxide	$NaOH$	Sigma Aldrich	99.9
Potassium hydroxide	KOH	Sigma Aldrich	99.9
Oxalic acid	$C_2H_2O_4$	Sigma Aldrich	98
CTAB		Sigma Aldrich	70
Toluene	C_7H_9		60
Ethanol	C_2H_5OH		60
Copper (II) acetate	$(C_2H_3O_2)Cu, 4H_2O$	Sigma Aldrich	99
Scandium (II) acetate	$(C_2H_3O_2)Sc, 4H_2O$	Sigma Aldrich	90
Vanadium oxide	V_2O_3	Sigma Aldrich	99
Chromium (II) acetate	$(C_2H_3O_2)Cr, 4H_2O$	Sigma Aldrich	98
Manganese (II) acetate	$(C_2H_3O_2)Mn, 4H_2O$	Sigma Aldrich	99.9

Continued on next page ···

Name	Formula	Origin	Purity
Continued ···			
Iron (II) acetate	$(C_2H_3O_2)Fe, 4H_2O$	Sigma Aldrich	99.9
Nickel (II) acetate	$(C_2H_3O_2)Ni, 4H_2O$	Sigma Aldrich	99.9
sitosterol	$C_{29}H_{50}O$	Fluka	70
Chromium (III) chloride	$CrCl_3$	Sigma Aldrich	99.9
Iodine	I_2	Sigma Aldrich	95
Cadmium shots	Cd	Cerac/Pur	99.995
Selenium shots	Se	Cerac/Pur	99.995
Galium	Ga	Sigma Aldrich	99.99

Table A.1: Name, formula, origin, and purity of chemicals used for the synthesis of the samples presented in the main text.

A.2 Thermodynamics value

Here we list the thermochemical data used to calculate the equilibrium in chapter 4. All the data were obtained from Binnewies & Milke (1999), except from the data for $CuCr_2Se_4$ obtained from Tret'yakov *et al.* (1977) and the heat capacity calculated using the Dulong-Petit law. The data of Cr_2Se_3 were obtained from the Common Thermodynamic Database Project website.

Compound	ΔH^0_{298}	ΔS^0_{298}	c_p ($\mathrm{J \cdot mol^{-1} \cdot K^{-1}}$)		
	$\mathrm{kJ \cdot mol^{-1}}$	$\mathrm{J \cdot mol^{-1} \cdot K^{-1}}$	a	b	c
$CuBr_{2(s)}$	-138.5	128.9	76.36	5.19	-0.19
$CuBr_{(g)}$	122.6	248.3	37.31	0.59	-0.12
$Br_{2(g)}$	30.9	245.4	37.36	0.46	-1.3
$Cu_3Br_{3(g)}$	-151.5	452	132.88	0.34	-0.46
$Cr_{(s)}$	0	23.6	24.51	2.05	-0.18
$CrBr_{4(g)}$	-258.6	417.4	107.64	0.34	-0.46
$Se_{(s)}$	0	42.3	17.89	25.1	
$Se_{2(g)}$	136.7	243.6	44.6	-2.66	-0.25
$Se_{6(g)}$	35.38	110	30.74	0.75	0.18
$SeBr_{2(g)}$	-20.9	317.1	58.12	0.05	-0.24
$Se_2Br_{2(g)}$	29.3	378.1	82.43	1.83	-0.29
$Cu_{(s)}$	0	33.2	20.53	8.61	0.16
$I_{2(s)}$	0	116.1	30.13	81.63	
$I_{2(g)}$	62.2	260.2	37.25	0.78	-0.05
$CuI_{(g)}$	142.3	255.7	37.41	0.5	-0.1
$Cu_3I_{3(g)}$	-16.7	464.5	133.18	-0.08	-0.36
$Cr_2I_{4(g)}$	15.9	532	132.92	0.06	-0.49
$CrI_{2(g)}$	-158.2	169	66.94	22.59	
$CrI_{3(g)}$	-48.86	408.3	68.87	3.26	-0.16
$CuSe_{(s)}$	-41.8	78.2	54.81		
$CrCl_{3(g)}$	-325.2	317.7	83.35	3.16	-0.74

Continued on next page ···

compound Continued ...	ΔH^0_{298}	ΔS^0_{298}	c_p		
$CrCl_{3(s)}$	-556.5	123	98.83	13.98	-1
$CuCl_{(g)}$	91.1	237.2	37.36	0.5	-0.22
$CrCl_{2(g)}$	-136.3	308	61.12	1.36	-0.34
$Cu_3Cl_{3(g)}$	-263.7	429.5	132.88	0.08	-0.77
$CrCl_{4(g)}$	-426.8	364.4	106.43	1.31	-0.95
$SeCl_{2(g)}$	-33.5	295.7	57.95	0.13	-0.39
$Se_2Cl_{2(g)}$	-21.8	353.9	82.38	1.57	-0.45
$CuBr_{(s)}$	-105.6	96.1	-52	206.4	4.02
$CrBr_{2(s)}$	-302.1	134.7	65.9	22.18	
$CrBr_{3(s)}$	-432.6	159.7	99.34	8.71	-0.49
$SeBr_{4(s)}$	-73.3	265.9	134.93		
$CuCl_{(s)}$	-136.8	87.4	51.09	17.66	-0.27
$Cl_{2(g)}$	0	223.1	36.61	1.08	-0.47
$CrCl_{2(s)}$	-395.4	115.3	71.36	13	-0.53
$CuCl_{2(s)}$	-218	108	78.87	2.93	-0.71
$CuI_{(s)}$	-36.2	159.1	59.41		
$CrI_{2(s)}$	-158.2	169	66.94	22.59	
$CrI_{3(s)}$	-205	199.6	105.44	20.92	
$Cr_2Se_{3(s)}$	-78.3	188	121		
$CuCr_2Se_{4(s)}$	-50	80	200		

Table A.2: Thermochemical data used for the calculation of equilibria in chemical vapour transport.

Appendix B

Samples preparations

This appendix presents the different method used to prepared the materials characterised in this thesis.

B.1 Solid state reaction

Solid state reactions were used to prepare polycrystalline chalcogenide spinels as well as In_2Se_3 and Ga_2Se_3. Since all these compounds contain Se, it is necessary to avoid the presence of oxygen during the reaction. To achieve this, the reactants were sealed in a silica tube under dynamic vacuum. The preparation procedure can be divided in several steps :

Reactant mixing After weighing the different reactants needed for the reaction in the desired stoechiometric proportion (usually to obtain 3 g of the product), the chemicals are dry grinded in an agate mortar until the mixture is visually homogeneous.

Ampoule loading The mixture is then transferred to a fused silica tube with one rounded end purchased from Baumbach Ltd. with dimensions of 14 mm outside diameter, 250 mm length, and 1.5-2 mm wall thickness. To avoid the loss of material on the side of the wall, a weighing paper funnel can be used.

Making a constriction In order to seal the tube under dynamic vacuum, a small constriction is made around 8 cm from the open end of the tube with an acetylene/oxygen torch.

Compound	$T_{soaking}$ (°C)	$t_{soaking}(h)$	$m_{product}$ (g)
$CuCr_2Se_4$	$550 \rightarrow 850$	48	3,6
$CuCr_2Se_{4-x}Br_x$	550/750	48	3,6
$CdCr_2Se_4$	700/800	72	3
$(Ag, In) : CdCr_2Se_4$	750	72	3
$HgCr_2Se_4$	550	72	3
In_2Se_3	700	72	1
Ga_2Se_3	700	72	1

Table B.1: Summary of the experimental conditions for the synthesis of the prepared powder.

Evacuating the tube Once the constriction is small enough to be closed safely, the open end of the tube is connected to the pumping system constituted of a rotary and a small diffusion pump.

Sealing the tube When the pressure is around 10^{-5} mbar, the constriction is closed while pumping with the acetylene/oxygen torch.

Firing The ampoule is then placed vertically in a box furnace and is heated with the desired temperature program.

Collection of the product To collect the product of the reaction, the ampoule was opened by, first cutting a rim with a diamond saw, and then breaking the top part of the ampoule with a screwdriver. A strong smell of $HeSe_2$ can occur, so the operation should be done under a fume hood. When the sample is ferromagnetic at room temperature the small broken silica pieces were separated by using a permanent magnet. In the other cases they had to be picked manually. The sample is then grinded and stored into a glass vial.

The temperature program is chosen depending on the chemical compound. In the case of the selenide it is important to control the heating rate to control the pressure inside the ampoule and avoid explosion. In all the synthesis carried out in this thesis a heating rate smaller than 40 K/h. A summary of the soaking temperature and time is presented in table B.1

B.2 Soft chemistry

As described in the main text of this thesis (chapter 3), one of the limitations of solid state reaction is that the compound obtained corresponds to the thermodynamically stable phase. A possible approach to synthesise metastable compounds (such as zeolites) is to use milder conditions. New synthesis routes were introduced by French chemist and are known as *chimie douce* Livage (1997). Nowadays methods such as sol-gel, hydrothermal, and co-precipitation are widely used, not only for metastable compound, but also for nanoparticles synthesis. In this section we describe the preparation of the oxide nanoparticles characterised in the main text of the thesis and the first results on chalcogenide nanoparticles preparation. A recent review on soft chemistry for inorganic nanoparticles synthesis can be found in Cushing *et al.* (2004).

B.2.1 Oxides preparation

B.2.1.1 Co-precipitation method

A mixture of starting powders is co-precipitated from a solution of salts (chlorides, nitrates, sulphates or organometallic precursors) by using some precipitating agent (a base in most cases). The feasibility of the reaction depends on the solubility of the complexes formed between the cations and the precipitating agent . The method gives a high degree of homogenisation resulting in lower temperatures or shorter times for synthesis compared to the conventional solid-state reaction method. The Co-doped ZnO target used for the deposition of thin films were prepared from co-precipited Co and Zn oxalate.

The first step in the preparation of the powder is to obtain a solution of the two cations that we want to precipitate. $Zn(II)$ acetate and $Co(II)$ acetate were mixed in the required quantity in deionised water until completely dissolved. A solution of oxalic acid is prepared in a separate beaker, the concentration of both solution is 0.4 mol/L. The oxalic acid was then added to the cations solution with constant stirring until a precipitate of $Zn_{0.95}Co_{0.05}C_2O_4, 2H_2O$ forms. The precipitate is stirred for 30 min before leaving it set for typically 2 hr. The precursor is filtered on a Büchner filter and the light pink powder obtained is dried overnight at 60 °C. The desired oxide is obtained by decomposing the organic precursor at temperature as low as 450 °C. The powder used in this thesis were prepared by introducing the precursor in a muffle oven set at 800 °C for 15 min. After calcination the color of the precursor changed to green.

B.2.1.2 Sol-gel method

The preparation of inorganic material from a colloidal solution of metal salts (sol) in a polymeric network (gel) is widely used to prepare ceramic materials as well as thin film and is called sol-gel process. This process involve several steps :

Hydrolysis It correspond to the formation of hydroxide seed by precipitation of the metal cations with a base or an acid.

Polymerisation A network is formed in the liquid by metal oxide bonding between the solvent and the seed which grows to colloidal dimension and forms a sol.

Gelation/aging The density of bond in the polymeric network increases with time and the viscosity of the solution increases.

Dehydratation The removal of the water or solvent leaves a porous network called xerogel.

Densification A heat treatment can remove the organic and produce dense oxide ceramic.

A variation of the classical sol-gel method which uses metal-alkoxide as precursor is the Pechini method Pechini (1967). Instead of using alkoxide, inorganic salts can be used and the polymerisation process is done via a chelating agent (usually citric acid).

The powder (Li,Co)- co-doped ZnO prepared by a modified Pechini method described in the thesis have been synthesised following the procedure reported in Sluiter *et al.* (2005). The concentration of Li and Co were chosen to 10% and 5% since the highest moment were measured for these concentrations. Typically zinc acetate, cobalt acetate and lithium chloride are mixed in deionised water in the required molar ratio. A separate solution of citric acid is prepared in deionised water and added slowly to the first one with a weight ratio 5:1. The pH of the solution is then adjusted from 2 to 7.5 slow addition of ammonia. The color of the solution changed from light pink to brown. The solution was then heated to 80 °C to chelate the solution and a gel is formed in 4 hr (this sample is called fast heating rate in the main text). The same experiment was carried out but the gelling temperature was set to 40 °C and left for 12 hr to set (this sample is called slow heating rate in the main text). The gel was then dried at 160 °C for 12 hr and finally fired at 400 °C for 30 min and the obtained powder is black.

B.2.1.3 Hydro/solvothermal method

Hydrothermal and more generally solvothermal method refer to high temperature and pressure reaction, close to the critical point of the solvent in a closed vessel. The high pressure involved increases the solubility of the reactants and enable to reduce the temperature of the reaction. If the first hydrothermal reaction were used to produce bulk single crystal, its application to nanostructure synthesis is widely spread Rajamathi & Seshadri (2002). All the hydro/solvothermal reaction to produce oxides particles were carried out in a Parr acid digestion bomb presented on Fig.B.1.

Figure B.1: Parr digestion bomb with the Teflon vessel and the stainless steel jacket, and high temperature solvothermal autoclave.

ZnO nano/micro-rods The preparation of the ZnO micro/nano-rods presented in the text were synthesised using hydrothermal method with a surfactant agent as described in Liu & Zeng (2003); Zhang *et al.* (2004). The micro-rods were synthesised by introducing an aqueous solution of zinc acetate, sodium hydroxide, and saturated CTAB in the autoclave. The autoclave was then sealed and heated to 120 °C for 20 hr. After the reaction a white powder was filtered, washed and dried overnight at 60 °C. The nano-rods were synthesised by preparing a solution of Zn^{2+} and HO^{-} with molar ratio $[Zn^{2+}]/[HO^{-}] = 1/20$. 10 mL of this solution was then introduced in the teflon container and the volume was filled to 80% with ethanol and 3 mL of ethylenediamine were added.The teflon vessel was then pretreated in an ultrasonic bath. The

autoclave was then sealed and heated to 180 °C for 20 h. The white product of the reaction was filtered and washed.

TM-doped ZnO prepared by solvothermal method TM-doped ZnO were synthesised via a solvothermal method from zinc acetate, a transition metal salt, and potassium hydroxide. Absolute ethanol was used as solvent similar to the one proposed by Wang *et al.* (2006). We prepared two batches as presented in the main text (Fig.6.5).

Series A : $Zn(OAc)_2, 2H_2O$ and the TM salt were mixed in ethanol until we obtained a homogeneous solution (for a complete dissolution of some TM in ethanol, heating was required). After stirring, an excess of alcoholic KOH solution was added to the previous solution, resulting in the precipitation of the hydroxide. The mixture was then transferred in the autoclave, sealed and kept at 170°C for 12 hr. It was then allowed to cool down naturally to room temperature. The resulting solid products were filtered, washed with ethanol and dried at 60°C for 12 hr.

Series B : $Zn(OAc)_2, 2H_2O$ and the TM salt and KOH were loaded directly in the autoclave without pre-mixing, then the same procedure was used to obtain the samples.

B.2.2 Chalcogenides preparation

The preparation of complex chalcogenide by solvothermal reaction has been reported at low temperature Li *et al.* (1999) but in the case of $CuCr_2Se_4$ reaction temperature above the melting point of teflon have been reported Ramesha & Seshadri (2004) and the pressure inside the volume would be too high for a silica vessel. An autoclave was designed in stainless steel 316 L with Swagelok cap (Fig.B.1). The starting salt were copper (0.25 mmol) and chromium (0.5 mmol) acetylacetonate mixed with Se (1.5 mmol), and β-sitosterol. The mixture was transferred in the autoclave which was then filled with toluene up to 60% of the total volume. The autoclave was then heated in a box furnace at 350°C for 12 hr. The product obtained was then filtered, washed and dried overnight at 60°C. The powder is a mixture of black and green particles. XRD measurement shows that the product is a mixture of $CuCr_2Se_4$, $CuSe$, and Cr_2Se_3 as presented on Fig.B.2.

B.3 Chemical vapour transport

All the crystal grown by vapour transport in this thesis were carried in a two zone furnace (gradient furnace) purchased from Elite Thermal Systems Ltd. The preparation of the ampoule

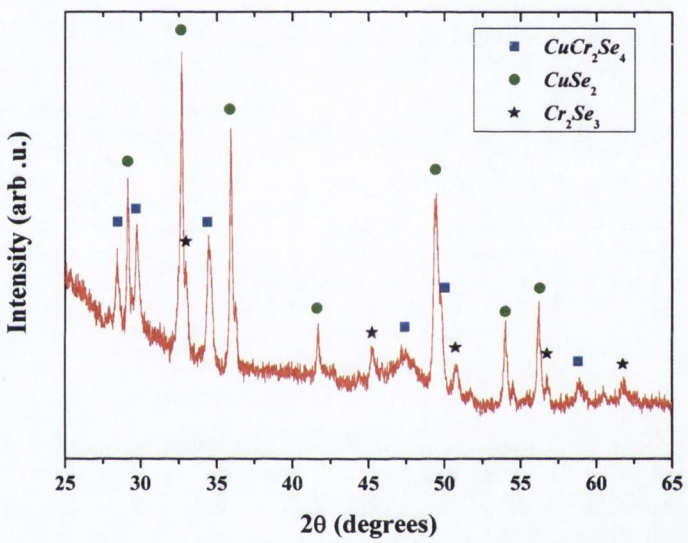

Figure B.2: XRD pattern of the powder obtained by solvothermal reaction. Peaks indexed with a blue square correspond to $CuCr_2Se_4$, the green dots correspond to $CuSe_2$, and the black star to Cr_2Se_3

System	m (g)			
$CuCr_2Se_4 : I_2$	Cu	Cr	Se	I_2
	0.3944	0.6454	1.9602	0.3
$CuCr_2Se_3Br$	Cu	Cr	Se	$CuBr_2$
	0.1312	0.4295	0.9782	0.4612
	Cu	Cr	Se	$SeBr_4$
	0.2624	0.4295	0.8967	0.4115
$CuCr_2Se_3Cl$	Cu	Cr	Se	$CrCl_3$
	0.4334	0.5911	1.6155	0.3600
$CuCr_2Se_4 : Se$	Cu	Cr	Se	Se
	0.3944	0.6454	1.9602	0.05

Table B.2: Masses of reactants introduced for the different CVT reactions

was done in a similar fashion as for the solid state reaction but with an initial tube length of 350 mm and a final length of the ampoule is 20 cm.. The typical load for each transport agent is summarised in table B.2.

B.3.1 Furnace temperature profile

The control and knowledge of the temperature profile during a chemical transport experiment is critical. A careful calibration of the furnace was carried out before starting any experiments[1]. The temperature profile for each zone is presented on Fig.B.3. Series of measurement where the left zone temperature was varied while the right zone was set at a constant temperature was carried out. An example is given on Fig.B.4 where the right zone is set to 950 °C and the left zone is varied from 900 °C down to 650 °C. The common linear gradient is between 20 cm and 40 cm inside the furnace, and the ampoule is set inside this zone for the experiments. To be able to choose the sink, the growth temperature, and the gradient we interpolated the linear gradient with the series of measurement described previously. The result is shown on Fig.B.5. The relation between the linear gradient and the programmed temperature difference is given by :

$$G = 1.7(2) + 0.034(1) \cdot \Delta T_{prog} \tag{B.1}$$

[1]The profile presented in this section are from the heater with which most of the crystal were produced.

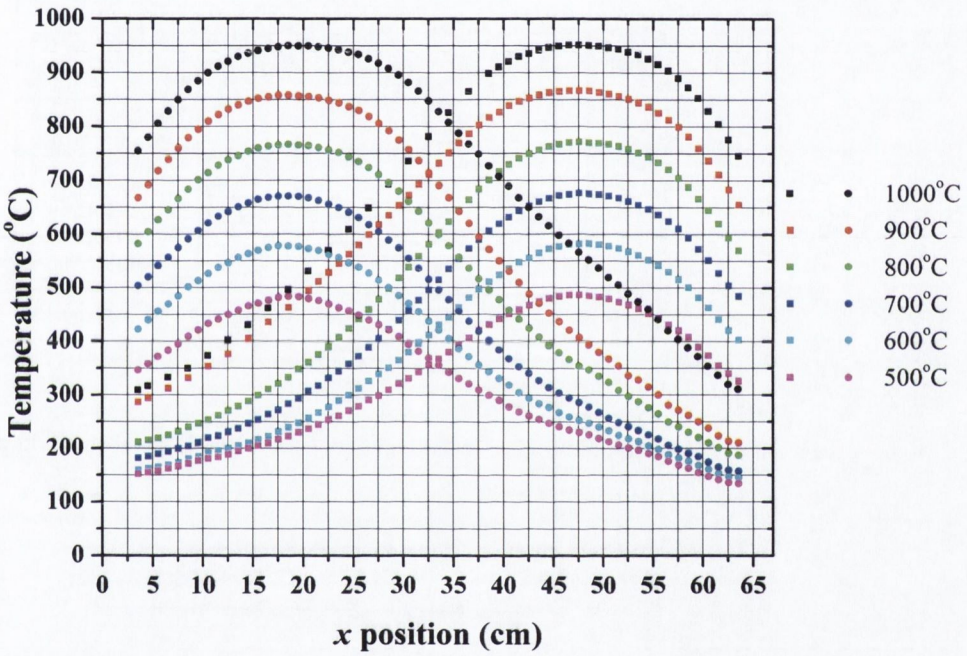

Figure B.3: Temperature profile of individual zone.

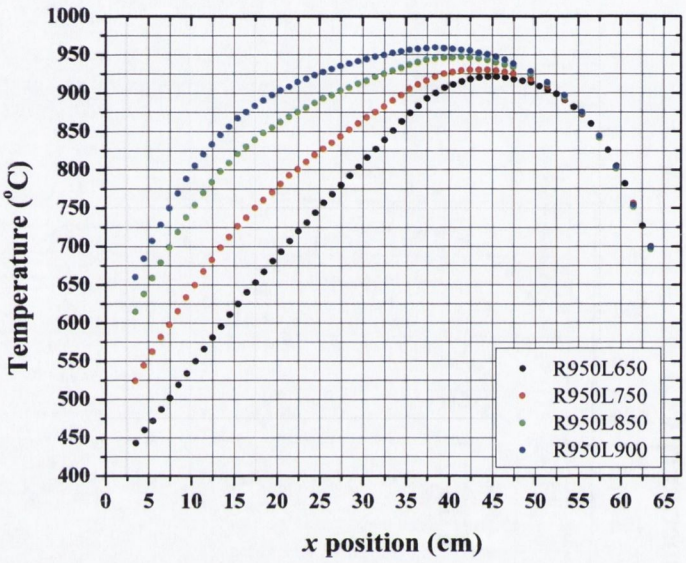

Figure B.4: Temperature profiles for the right zone set at 950 °C and the right zone at 900 °C, 850 °C, 750 °C, and 650 °C.

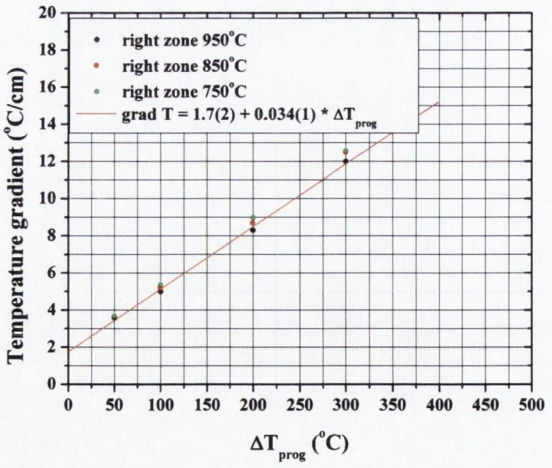

Figure B.5: Interpolation between the linear gradient and the programmed temperature difference.

where G is the linear gradient in °C/cm and $\Delta T_{prog} = T_{right} - T_{left}$.

B.3.2 Reaction optimisation

If literature is available for most of the transport agent used in this study the exact experimental conditions are never explicitly described Lotgering (1964a); Miyatani *et al.* (1968); Nakatani *et al.* (1977); Radautsan (1983); Tsurkan *et al.* (1984). Therefore a temperature reaction optimisation was carried out to find out at what feed and sink temperature the crystal growth was more efficient. To improve the nucleation control the ampoule was first heated to an equilibrium temperature ($T_{source} = T_{growth}$) for 12 hr followed by a reverse gradient ($T_{source} < T_{growth}$) for 6 hr in order to clean the wall on the growth side. The growth condition were then applied. A typical temperature program is represented on Fig.B.6 where the blue curve correspond to T_{growth} and the red curve correspond to T_{source}. When the program is finished, a visual inspec-

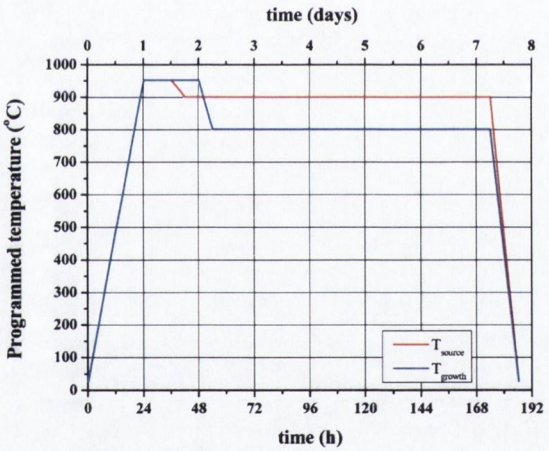

Figure B.6: Typical temperature program of a CVT reaction, the red curve represents the source zone temperature and the blue curve the growth zone temperature.

tion of the ampoule will define the next step. If the product at the growth end is an agglomerate mass, the temperature growth zone is increased. If no transport is observed across the reaction vessel the temperature growth zone is decreased. In the case of the growth with Se transport agent, the concentration of Se excess was varied. If the vapour pressure of Se is too high at the growth zone, Se condenses and the Se excess is diminished in the next experiment. In the

best case, well faceted crystals are observed in the growth zone, the tube is then cut carefully with a diamond saw and the crystal harvested.

B.4 High temperature solution growth

All the $CdCr_2Se_4$ crystals described in the main text have been grown by HTS growth using the convenient method described in Wold & Rulff (1973). The chemicals are introduced in the same kind of tube used for the CVT growth with a weighing paper funnel[1]. Typically the total charge is around 8 g with 3.3792 g of Cd, 2.3803 g of $CrCl_3$, and 2.3737 g of Se. The tube is then prepared in the same fashion as for solid state, or CVT reactions with a final length of 25 cm. It is then placed vertically in a box furnace and fired following the temperature program described on Fig.B.7.

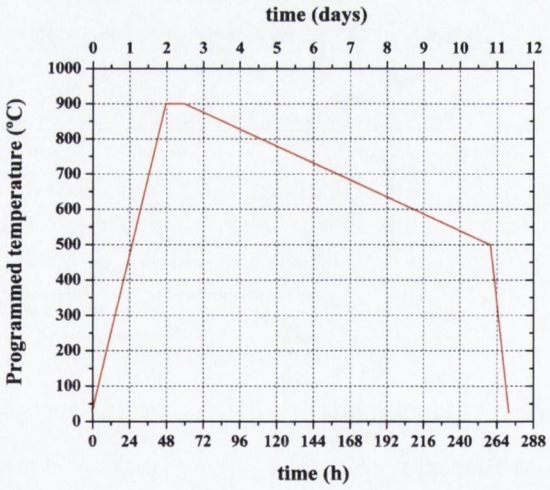

Figure B.7: Temperature program of a HTS growth run.

When the reaction is finished the tube is cut with a diamond saw close to where the flux solidified and this piece is broken with a hammer. The biggest silica pieces are removed manually and the rest od the solid mass is cleaned in boiling water. The crystallised flux $CdCl_2$ is soluble in water, which is convenient for the extraction of the product. The mixture is filtered and the operation is repeated until the filtrate is clear which indicate that all the flux is removed. The

[1]For $CrCl_3$ a long funnel is used to avoid too much loss on the wall since it tends to stick on surfaces.

collected solids are then inspected under a binocular and the best single crystal specimens are separated from the rest.

Attempt of growing Ag, In, Ga-doped $CdCr_2Se_4$ have been made by introducing the dopant in its elemental form in the charge. The introduction of silver was a success, but in the case of In and Ga the product of the reaction contained several phases (see green and yellow compounds on Fig.B.8), and only a minimum amount of In has been successfully introduced as described in the main text. A gas phase doping has also been tried following the procedure of Vinogradova

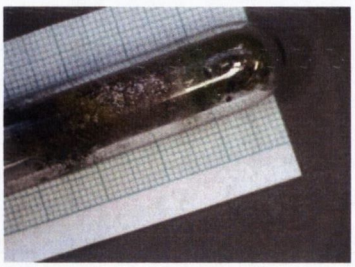

Figure B.8: Product of a Ga-doped $CdCr_2Se_4$ HTS reaction where we clearly see the presence of other phases (green and yellow products).

et al. (2007). A single crystal is introduced in the designed vessel (inset of Fig.B.9) with $In(Ga)$ and $In(Ga)_2Se_3$ prepared from the elements at 750 °C in a vacuum sealed ampoule. The formation of the phases was checked by XRD (Fig.B.9). A mixture of $\alpha - In_2Se_3$ and $\beta - In_2Se_3$ and a mixture of Ga_2Se_3, Ga and Se have been identified (using *XpertIdentify* provided by Panalytical) for the two systems. The annealing was done in a closed tube sealed under vacuum at a temperature of 550 °C and 750 °C for 72 hr[1]. The surface conductivity of the crystal is affected by the annealing but after shaving a face of the crystal the same conductivity as in the undoped crystal is found.

B.5 Pulsed laser deposition

The popularity of PLD in research laboratory is due to two main reasons : the possibility to grow a wide range of material with high crystalline quality and the good cationic stoechiometry transfer between the target and the substrate.

[1]Higher temperature were not investigated since the decomposition temperature of $CdCr_2Se_4$ is 800 °C.

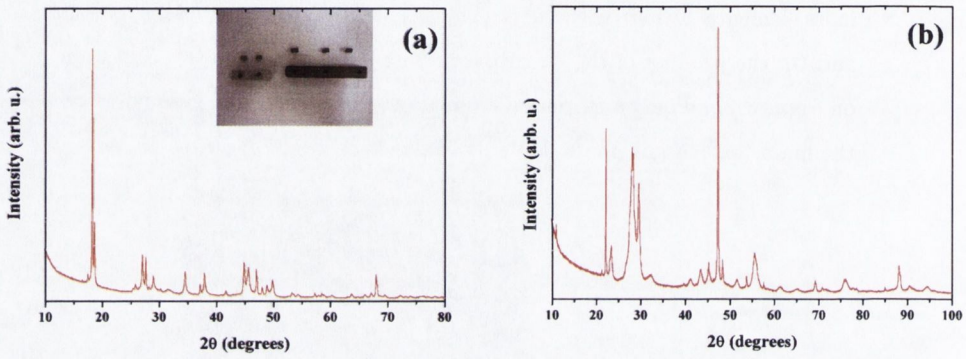

Figure B.9: XRD powder diagram of (a) In_2Se_3 and (b) Ga_2Se_3. The inset is a picture of the annealing vessel designed from Vinogradova *et al.* (2007).

The processes involved in laser ablation are complex and several physical phenomena of different nature occur. Several step can be considered for the deposition of a thin film on a substrate :

Interaction photon/solid When the fluence of the beam is high enough (ablation threshold) the electric field created between the photon and the solid will break the atomic bonds in the solid and ionic species will be ejected from the target.

Plasma formation and expansion The ejected atoms form a plasma which expand, transporting high energy species from the target to the substrate. The energy of the ions in the plasma can be monitored with a Langmuir probe. Plasma diagnostic is one of the main activity of the Laser and Plasma Application Group in Trinity College Dublin. A typical Langmuir probe signal obtained at different O_2 partial pressure during the deposition of $CuAlO_2$ films is presented on Fig.B.10.

Condensation on the substrate The high energy species present in the plasma will react with the background gas and etch atoms that condense on the substrate. When the thermal equilibrium is reached, the flux of high energy incoming ions is lower than the condensation rate and a nucleation centre will appear.

Nucleation and growth Nucleation is a thermodynamic problem and is mainly governed by the temperature of the substrate and the supersaturation pressure. When the energy is

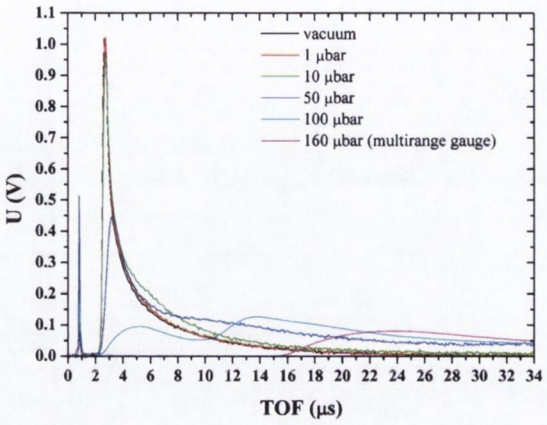

Figure B.10: Langmuir probe signal obtained at different O_2 partial pressure during the deposition of $CuAlO_2$ films.

minimised, a seed will start to grow, and the growth mode (layer by layer, step flow, or 3D) will depend on the size of the nucleation centre.

B.5.1 *Héloïse* deposition chamber set-up

All the thin films prepared by pulsed laser deposition in this dissertation have been produced in a high vacuum chamber engineered by Surface. The complete set-up is pictured on Fig.B.11. It is composed of :

A KrF excimer laser It consist of Compex Pro 102 (Lambda Physik) with a wavelength of 248 nm and a pulse duration of 25 ns. The output energy can be varied from 130 to 450 mJ and the repetition rate from 1 to 20 Hz.

Optical path The laser beam is directed from the laser to the deposition chamber by 2 mirrors and focused on the target with a convergent lens with a nominal focal length of 350 mm[1] and enter the chamber through a fused silica window. The optical path was set in a fashion that the laser beam is incident to the target at an angle of approximately 45°.

Surface chamber The deposition chamber consist of a pumping unit (a diaphragm pump and a turbo molecular pump with a capacity of 250 L/s) reaching a base pressure of $\approx 2 \cdot 10^{-7}$

[1] All the optic component where purchased from Elliot Scientific.

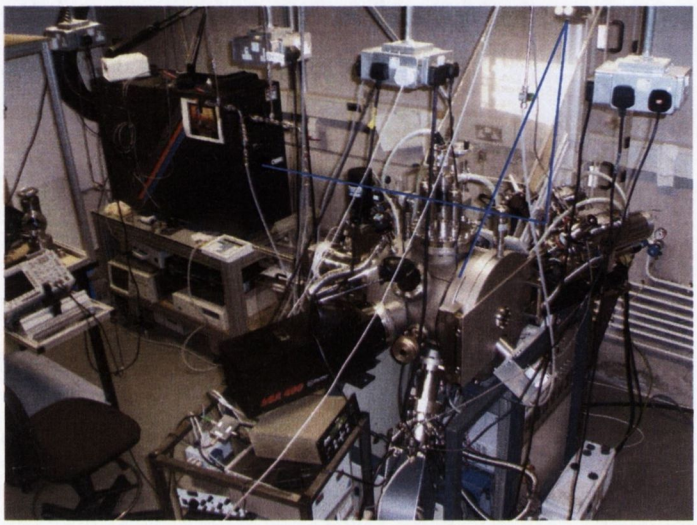

Figure B.11: Overview of the laser ablation system, the blue trace represents the laser path.

mbar in 12 h. The pressure is monitored with a compact full range gauge (Penning and Pirani gauge). The control of the background gas is done with a mass flow controller (Horiba Stec) and a baratron pressure transducer (MKS) within the range $0.1 - 120\mu$bar. If atomic oxygen or nitrogen is needed during the deposition, a R.F. plasma source has been installed and its description and operation mode can be found in Arnold (2008). The substrate heating system is composed of a linear feedthrough on which a water cooled sample heater made of Pt wire is attached allowing to vary the target-substrate distance. The target manipulator consist of a 4 target carousel which are rotated and translated with stepper motor and controlled remotely[1]. For in-situ characterisation the chamber is equipped with :

- A RHHED gun (35 kV) with differential pumping to be able to work to pressure up to 400 μbar and phosphor screen equipped with a camera.
- An optical reflectivity system using a 635 nm diode laser to monitor the thickness of the film.
- A Langmuir probe for plasma diagnostic.

[1]The software to control the stepper motor was written by J. McCauley.

The substrate is held on a stainless steel sample holder with colloidal silver paste (purchased from Agar scientific) (Fig.B.13(a)) which is heated by radiation from the Pt heater. The heater is designed to work under vacuum or mild oxidising atmosphere from room temperature up to 900 °C. The temperature is controlled with a thermocouple inserted in the middle of the sample holder. The temperature on top of the substrate has been measured by evaporating a Pt line on top of a sapphire single crystal with a resistance of approximately 100 Ω. The resistance was then measured in-situ with a resistance bridge. The calibration curve is represented on Fig.B.12 showing the effect of radiation heating at high temperature (inset of Fig.B.12). The study of

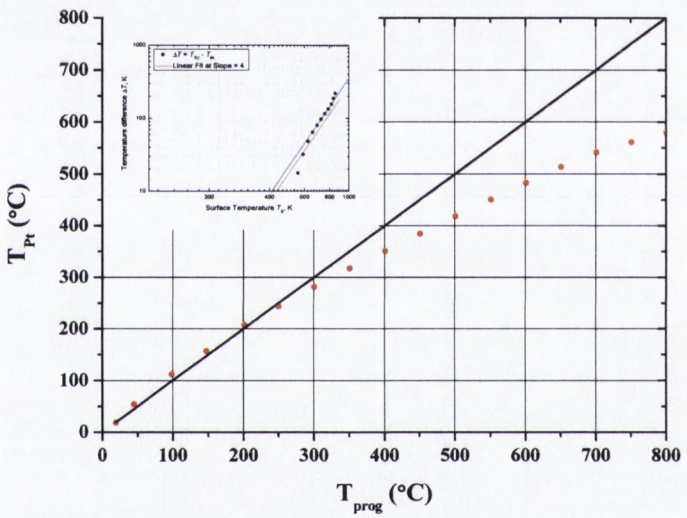

Figure B.12: Temperature measured on the surface of a sapphire substrate against the programed temperature. The inset shows that the difference is due to radiative loss.

small magnetic moment can be challenged by the contamination of external factors, and the stainless steel sample holder provided with the system is a good example of the great care that has to be taken. It can be seen on Fig.B.14 that the use of the stainless steel sample holder can introduce a large moment, therefore non-magnetic sample holder were designed and fabricated from machinable ceramic and copper (Fig.B.13(b) and (c) respectively). The magnetic moment does not come from loose stainless steel shaving that are stuck to the substrate. In fact we can observe some red spots inside the sapphire. The nature of these aggregates is still under investigation.

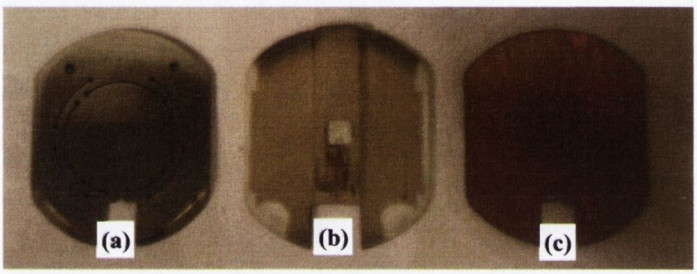

Figure B.13: Substrate sample holder made of (a) 304 stainless steel, (b) machinable ceramic, and (c) copper.

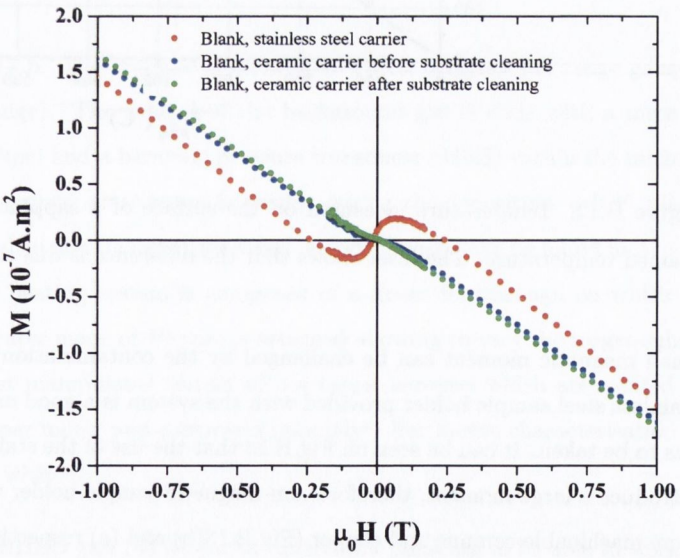

Figure B.14: Magnetic moment in function of applied field of a blank sapphire substrate after a heat treatment on the stainless steel sample holder (red dots), on the ceramic carrier before heating (green curve) and after heating (blue curve).

B.5.2 Samples preparation conditions

All the substrate used in this thesis were single crystal purchased from Crystal GmbH. and were both side polished. MgO and $MgAl_2O_4$ substrate were used without pretreatment, whereas the c-cut sapphire ($(001)Al_2O_3$) were prepared prior to deposition as described below :

1. Degreasing in hot acetone.
2. Chemical etching in a hot 3:1 H_2SO_4 : H_3PO_4 solution and rinsed in deionised water.
3. Annealing under 200 μbar of O_2 at 800 °C for 1 h. This step is performed in the deposition chamber.

B.5.2.1 Co-doped ZnO

The target was prepared by pressing and sintering (800 °C for 12 h) a pellets (3 mm × 20 mm) of $Zn_{0.95}Co_{0.05}O$ powder prepared by co-precipitation. The substrate for all the films was a c-cut sapphire. The deposition conditions for the series of Co-doped ZnO thin films is summarised in table B.3.

Sample name	Pressure (mbar)	Fluence (J/cm^2)	Rep. rate (Hz)	T °C
H2903ZCO	$\approx 10^{-6}$	3	10	500
H3003ZCO	$\approx 10^{-6}$	3	10	475
H1804ZCO	$\approx 10^{-6}$	3	10	400
H2004ZCO	$\approx 10^{-6}$	3	5	350
H2104ZCO	$\approx 10^{-6}$	3	5	300
H2304ZCO	$\approx 10^{-6}$	3	5	200
H2904ZCO	$\approx 10^{-6}$	3	5	RT
H0405ZCO	$\approx 10^{-6}$	3	5	150
H0605ZCO	$\approx 10^{-6}$	3	5	100
H1105ZCO	$\approx 10^{-6}$	3	5	125

Table B.3: Summary of the deposition condition of Co-doped ZnO by laser ablation. Rep. rate means repetition rate

B.5.2.2 $Co-O$ compounds

For these samples, we fixed several parameters : the time of deposition, the oxygen pressure ($1.0{\cdot}10^{-3}$ mbar), the fluence(2-3 J·cm^{-2}), and the repetition rate (3 Hz) and the substrate temperature was varied from 300 to 600 °C. The process to deposit the multilayer system, is represent on Fig.B.15. The $Co-O$ compounds were deposited in two different geometries the normal deposition where the target is directly facing the substrate and an off-axis geometry

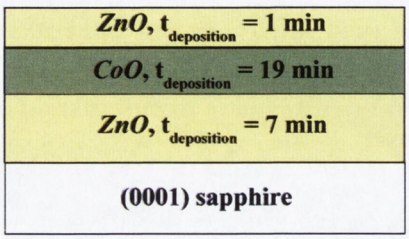

Figure B.15: Representation of the multilayer system produced in chapter 6.2.

where the substrate is shifted from the target axis, making an angle of 5° with the target. The two different geometry are represented on Fig.B.16.

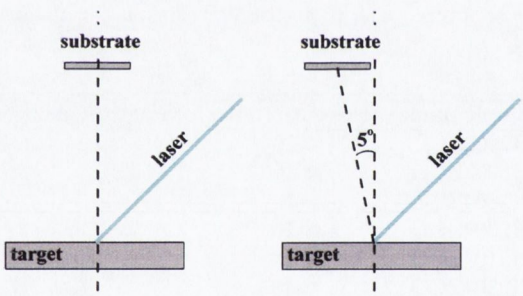

Figure B.16: Schematic representing the different geometries used in chapter 6.2. The left picture represent the normal geometry and the right the off-axis geometry.

B.5.2.3 $CuCr_2Se_4$

The preparation of chalcogenide thin films is in general a challenge due to the volatility of O, S, or Se. In the deposition of oxide material, this problem is compensated by the addition of a reactive gas containing molecular or atomic oxygen. For S and Se, the addition of $H_2S(Se)$ as a background is not use due to their toxicity and the possibility of corrosion in the system.

The films prepared by ablation laser in chapter 5.1.1.1 were deposited on $MgAl_2O_4$, MgO and c-cut sapphire. The deposition pressure for all the films was the base pressure of the chamber ($\approx 10^{-7}$ mbar). The repetition rate of the laser and the fluence were kept at 5Hz and at ≈ 0.7 J/cm^2 respectively for all depositions. The films deposited from an alloy where deposited in the same condition with the temperature kept at room temperature.

The selenisation process used in chapter 5.3 was carried out by introducing a thin film and 0.1 to 0.5 g of selenium in a fused silica ampoule which was sealed under vacuum to a final length of 8 cm. The ampoule was then inserted into a tubular furnace and heated following the temperature program presented on Fig.B.17.

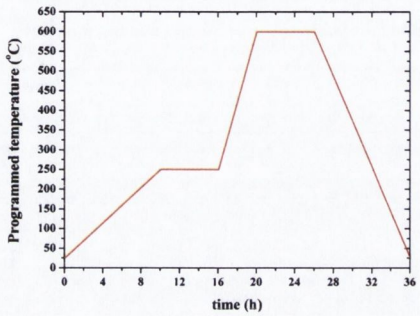

Figure B.17: Temperature program for the selenisation process described in chapter 5.3

To reduce the loss of *Se* during the deposition process, a cell made of a fused silica tube has been introduced around the target to enclose the plasma. Two length of quartz tube have been used : a short tube where the substrate is attached to a fused silica slide on top of the tube (inset of Fig.B.18) and a longer tube which is inserted between the substrate holder and the target as presented on Fig.B.18.

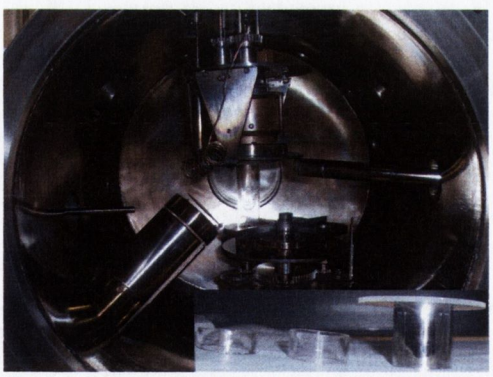

Figure B.18: Inside of the ablation chamber with a silica tube inserted between the target and the substrate holder. The inset shows the different tube sizes used for this experiment.

Appendix C

Characterisation method

In this appendix, a general introduction (or a reference) of the different techniques used during this work is given as well as the description of the experiments carried out.

C.1 Powder Neutron and x-ray diffraction

Diffraction methods are the most commonly used for the structural characterisation of compounds and can be performed with different particles. Two different particles (photons and neutrons) have been used to perform diffraction experiment during the course of this thesis. In the case of inorganic compound the interatomic spacing is of the order of the ångström, therefore the wavelength of the incident beam has to be of the same order of magnitude (x-rays for the photons). The description of x-ray and neutron powder diffraction can be found in Chatterji (2006); Pecharsky & Zavalij (2005).

C.1.1 Powder x-ray diffraction

Powder XRD is the first characterisation step of the synthesised material. A Panalytical X'pert Pro MPD (multiple purpose diffractometer) was used for all the powder synthesised in this study. It is configured in the Bragg-Bretano focusing $\theta - \theta$ geometry using a flat sample (Fig.C.1). The x-ray source is a conventional sealed tube with a Cu anode. The sample stage was chosen depending on the quantity of powder available and the quality of the data needed. Data acquired for structure refinement, were collected using the spinner sample stage, the positioning stage

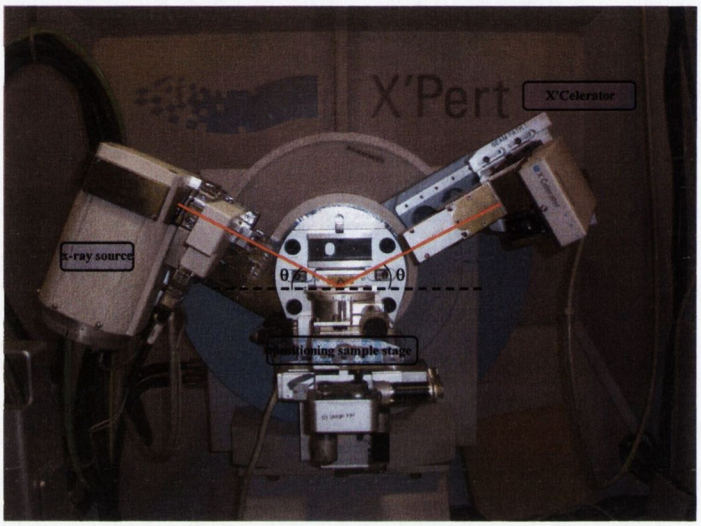

Figure C.1: X'Pert Pro diffractometer with the positioning stage installed and the X'Celerator detector.

with x, y, z tilt and ϕ movements sample stage was used otherwise. The detection was made with the X'Celerator detector which is based on real time multistrip technology. The optic of the system were kept the same for all measurements (Programmable divergence slits : 1°, beam mask : 15 mm) and the instrument resolution was determined from the NIST1976 standard. The instrument resolution function is presented on Fig.C.2.

C.1.1.1 Samples mounting

For phase analysis, samples were sprinkled on a glass slide and fixed with a drop of ethanol. The glass slide was then placed in the centre of the positioning sample stage. The height was adjusted to the required position and the mask was chosen to not overexpose the sample.

One of the most difficult condition to fulfil for structure refinement is a correct measure of the intensity. In this geometry, preferred orientation are difficult to overcome. Nevertheless several easy precautions can be taken to prevent it : to not press the powder in the sample holder, and to rotate the sample during the measurement. We therefore used the spinner sample stage to measure the sample with an appropriate mask (15 mm). Moreover, the measured powder is supposed to be cubic so the crystallite should be equiax minimising this effect. The sample

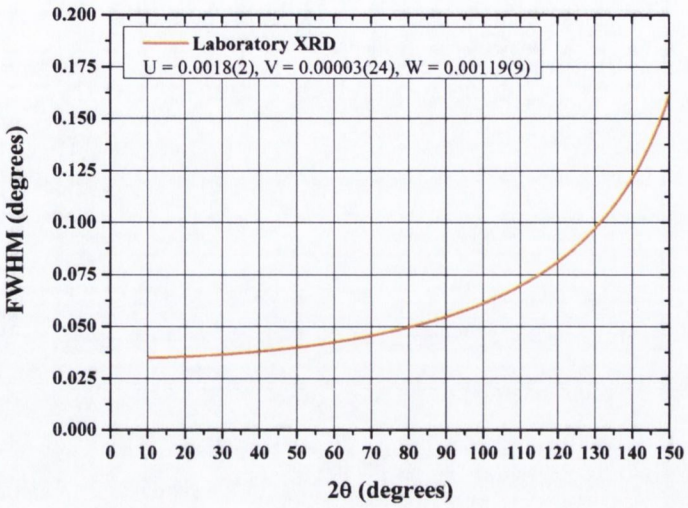

Figure C.2: Instrument resolution function of the laboratory x-ray diffractometer in the configuration used for this study.

changer option was used when a series of powder had to be measured.

C.1.1.2 Structure refinement

The structural refinements of the structures were performed using the latest (at the time of the analysis) Fullprof or FullprofSuite freeware Rodriguez-Carvajal (1993). It is based on the Rietveld method, which is a least-square fitting of the peaks profile Rietveld (1969, 1967). In the early day, this method was limited to powder neutron diffraction diagram since the peak profile of medium resolution diffractometer can be described as a simple Gaussian profile. The method rely on the good definition of the peak profile. Fit of a single low angle peak of the NIST1976 reference with a Gaussian, Lorentzian, and a Pseudo-Voigt[1] is represented on Fig.C.3. It can be seen from Fig.C.3, that the peak is better described by a Pseudo-Voigt function. The full pattern fitting is calculated using a Thompson-Cox-Hastings with axial divergence function Finger *et al.* (1994) as recommended in McCusker *et al.* (1999). The situation depicted here is the typical case, where only the $Cu\ K_{alpha_1}$ and K_{alpha_2} have to be taken into account. When the x-ray tube get older, a parasitic W wavelength is produced and a second set of diffraction

[1] A Pseudo-Voigt function is a linear combination of a Gaussian and a Lorentzian function.

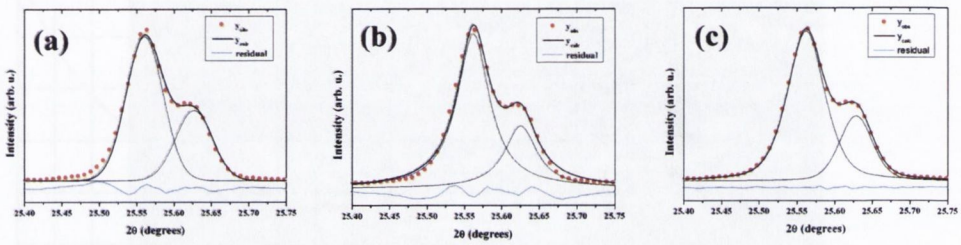

Figure C.3: Fitting of a low angle peak from the NIST1976 reference with (a) a Gaussian function, (b) a Lorentzian function, and (c) a Pseudo-Voigt function. The measured intensity is represented by a red dot, the calculated profile by a black line and the residual by a blue line.

can be observed. In this case the refinement of the structure is difficult since some of the W peaks will overlap the Cu peak as shown in Fig.C.4. In this case we generated a pattern with the W wavelengths using the parameter obtained from the refinement with the Cu wavelengths and adjusted the scale to match the intensity of the parasitic peaks.

The agreement factors reported in the main text of this thesis are calculated with the following formula :

$$R_{\text{Bragg}} = \frac{\sum_{(h,k,l)} \left| I_{obs(h,k,l)} - I_{calc(h,k,l)} \right|}{\sum_{(h,k,l)} \left| I_{obs(h,k,l)} \right|} \tag{C.1}$$

This agreement factor gives a good idea of the quality of the structural model chosen to describe the diagram, but is not sensitive to external errors such as impurity phases. To remedy this lack, the conventional profile and weighted agreement factors are given as a complement[1]

$$R_p = \frac{\sum_i |y_{i,\text{obs}} - y_{i,\text{calc}}|}{\sum_i |y_{i,\text{obs}}|} \tag{C.2}$$

$$R_{wp} = \sqrt{\frac{\sum_i w_i \cdot |y_{i,\text{obs}} - y_{i,\text{calc}}|^2}{\sum_i w_i \cdot y_{i,\text{obs}}^2}} \tag{C.3}$$

where w_i is the statistical weight. Nevertheless, it is important to judge the quality of the refinement by inspecting graphically the residual plot.

[1]The conventional profile and weighted agreement factors are not corrected for the background.

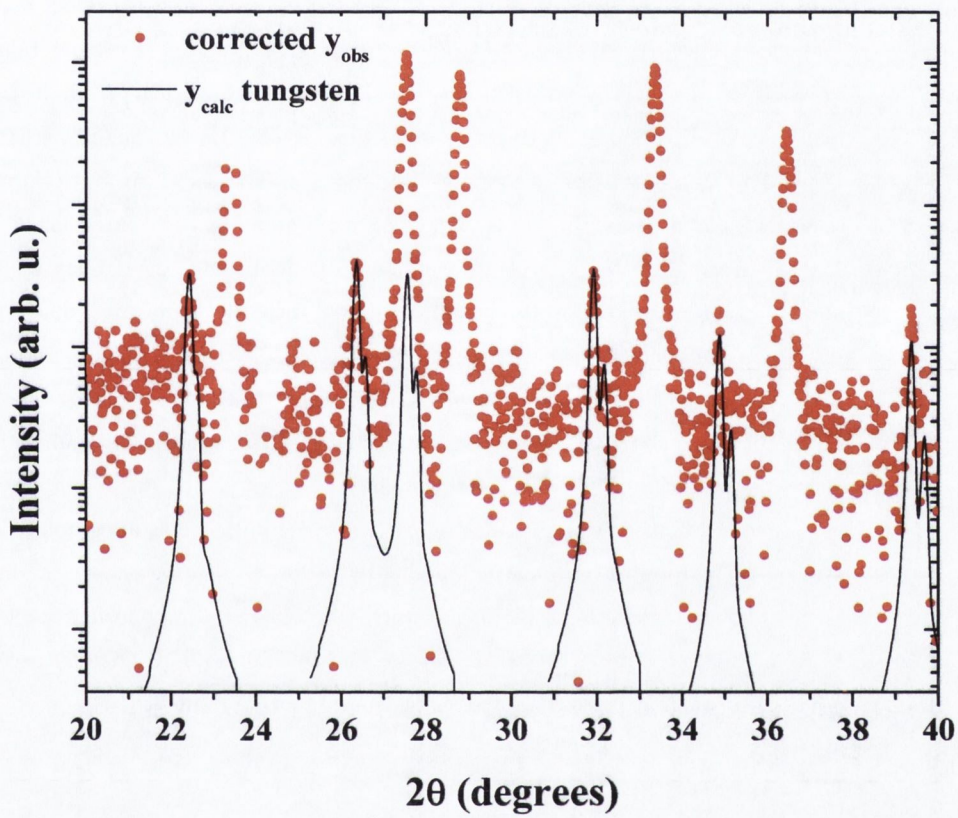

Figure C.4: Part of a $CdCr_2Se_4$ XRD pattern, the red dots correspond to the measured intensity corrected with for the background, and the black line represent the calculated pattern for the W wavelengths. Note the logarithmic intensity scale.

C.1.2 Thin films x-ray analysis

The structural characterisation of thin films was performed on the same x-ray diffractometer presented above. If in the case of powder diffraction the sample present random crystallite orientations, the thin films when prepared in optimal conditions, can present a strong orientation in particular direction. It is therefore important to align the sample in the flat configuration. Depending the information needed, several type of measurement can be performed. The phase analysis is performed with a measurement similar to a powder measurement ($\theta - 2\theta$ scan) with the XCelerator detector. In this measurement the intensity of the substrate peak are intense, and the $Cu\ K_\beta$ wavelength will contribute significantly in the diagram, therefore a Ni filter is introduced between the x-ray source and the sample. To characterise the degree of orientation of a sample a rocking curve can be performed on one of the film peak (ω scan). The FWHM of the rocking curve gives an information on the orientation of the crystallites in the film, and can be compared to the instrumental resolution[1].

When the film shows a good degree of orientation, other crystallographic direction can be studied by performing asymmetric scans ($\omega \neq 2\theta$) or in-plane measurement where the sample is tilted of an angle ψ from the flat position. In this case a pseudo four circles sample stage is used. In this geometry the texture of the sample can also be studied by performing ϕ scans where the sample is rotated around the axis normal to the sample.

C.1.2.1 X-ray reflectivity

The thickness of thin films can be measured using x-ray reflectivity. In this measurement a low angle incident x-ray beam is refracted by the thin layer producing interference fringes. Several properties can be extracted from this measurements such as :

- The layer electronic density, which is proportional to the critical angle[2] can be determined.
- The layer thickness, which is proportional to the frequency of the oscillations.
- The roughness of the sample can be estimated by the behaviour of the signal decay and the oscillations amplitude.

The reflectivity measurements presented in this thesis were simulated using IMD software Windt (1998).

[1] In the case of the diffractometer used, the instrumental resolution for the rocking curve is $\approx 0.02°$

[2] Angle below which total reflection of x-rays occurs.

C.1.3 Single crystal x-ray diffraction

Single crystal XRD was performed in Service Commun de Diffraction X CRM2 Institut Jean Barriol, Nancy Université using a Supernova Kappa diffractometer equipped with two microfocus sources (dual wavelength : Mo, Cu) (Fig.C.5) by Dr. Porcher. The high voltage was set to 35 keV in order to avoid $\lambda/2$ contamination. The full Ewald sphere was measured up to 0.6 $Å^{-1}$ with very high redundancy of 68 in order to check the space group symmetry and have a better statistical estimate of unique Bragg intensities and estimated error. The sample were cut

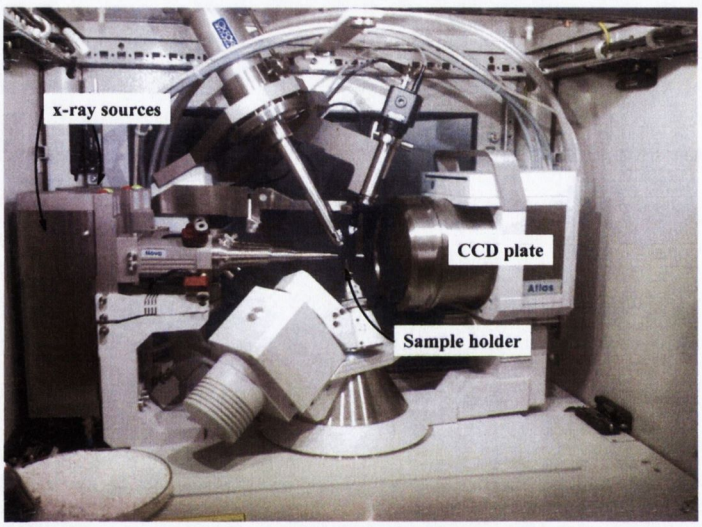

Figure C.5: Single crystal XRD equipped with two microfocus sources and a CCD.

in sphere when possible to correct the absorption analytically. One of the sample with acicular habit had to be cut in a parallepiped (Fig.C.6). In this case the absorption correction was done empirically by defining each face of the crystal. The refinement of the data was done using the software Jana2006 Petricek *et al.* (2006).

C.1.4 Powder neutron diffraction

Neutron particles are very useful for the investigation of the structure of the matter. The fact that its charge is null make their penetration depth much more important than for x-ray, moreover they carry a spin and can therefore interact with other spins. Nowadays it is commonly used to determine magnetic structure of materials. Two different powder spectrometer have

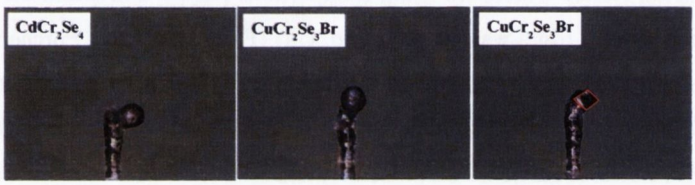

Figure C.6: Single crystal XRD equipped with two microfocus sources and a CCD.

been used in Laboratoire Léon Brillouin (CEA Saclay) to study the structural and magnetic properties of polycrystalline $CuCr_2Se_{4-x}Br_x$ and $CdCr_2Se_4$ samples. Neutrons are produced in the Orphée nuclear reactor with a nominal power of 14 MW. A high resolution powder diffractometer 3T2 and a high flux with medium resolution G4.1 have been used to characterise $CuCr_2Se_4$ and $CdCr_2Se_4$ polycrystalline powder. A description of the experimental parameters for each spectrometer is presented below with the list of the samples.

C.1.4.1 3T2

The high resolution spectrometer 3T2 is a transmission Debye-Sherrer two axis diffractometer with a $\theta - 2\theta$ capability. Thermal neutrons of a wavelength $\lambda = 1.22527$ Å are selected with a vertical focusing Ge (335) monochromator. The instrumental resolution for a collimator of 10 arcs is represented on Fig.C.7. This spectrometer is particularly well disposed to determine the crystallographic parameter such as atomic positions and the thermal parameter of the atoms. The sample environment was in the cryofurnace configuration as pictured on Fig.C.8. The detector bank constituted 50 ^3He tubes spaced 2.4° apart, the typical step size was 0.05°. The typical collection time for a diagram was 12 hr for the Cu based powders and 30 hr for the Cd based powder.

Six grams of the copper based samples were loaded in a vanadium tube, whereas 3 g of the $CdCr_2Se_4$ were used to fill a specially designed[1] annular sample holder made of two concentric vanadium tube.

[1]B. Rieu designed and constructed the annular sample holder to be compatible with both 3T2 and G4.1 sample rods.

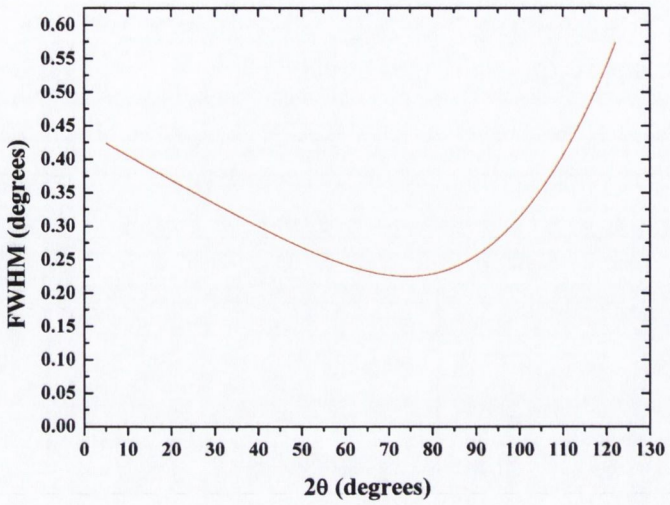

Figure C.7: FWHM as a function of 2θ for the 3T2 neutron diffractometer calculated with the Cagliotti formula Caglioti *et al.* (1958).

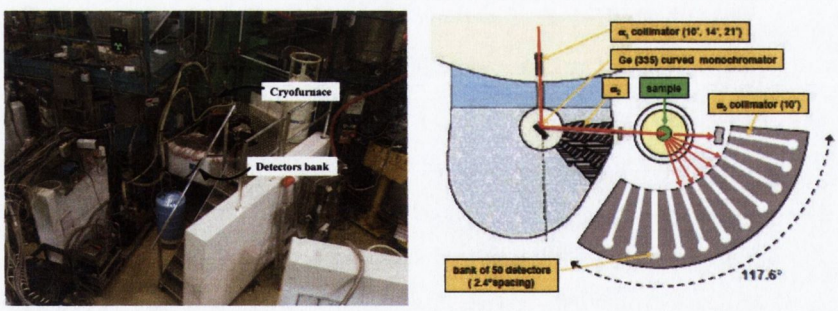

Figure C.8: 3T2 spectrometer with the cryofurnace installed (left), schematic of the setup (right).

C.1.4.2 G4.1

The G4.1 spectrometer has the same geometry as 3T2, the main difference is that cold neutron with a wavelength of 2.4226 Å are selected with a (002) pyrolytic graphite monochromator. The instrumental resolution is presented on Fig.C.9. The sample environment was in the

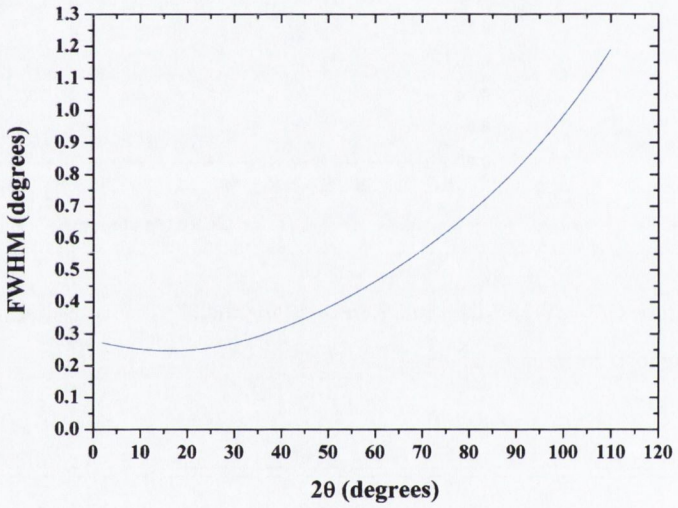

Figure C.9: FWHM as a function of 2θ for the G4.1 neutron diffractometer calculated with the Caglioti formula Caglioti *et al.* (1958).

cryostat configuration as pictured on Fig.C.10. The detectors bank constituted of a position sensitive detector with 800 BF_3 cells with 0.1 ° of separation. The acquisition time is fast and the full spectrum is obtained which is an advantage compared to 3T2. Instead of counting for a certain number of time it is possible to set a neutron counts and makes possible to compare diagram with different acquisition times. The G4.1 spectrometer has been used in this study for magnetic structure determination and to study the evolution of the lattice parameter in function of temperature. The same samples were measured on both spectrometer using the same kind of sample holder. A comparison of the resolution of the two spectrometer is presented in Fig.C.11. It can be seen that G4.1 has a better resolution in the small angle region where the magnetic intensities will be stronger and is therefore more adequate for magnetic structure determination whereas 3T2 has a better resolution at higher angle where structural parameters can be determined accurately. This two spectrometer complement each other, the

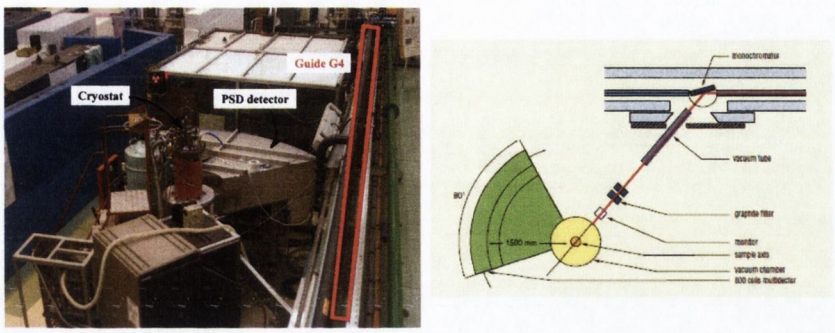

Figure C.10: G4.1 spectrometer with the cryostat installed (left), schematic of the setup (right).

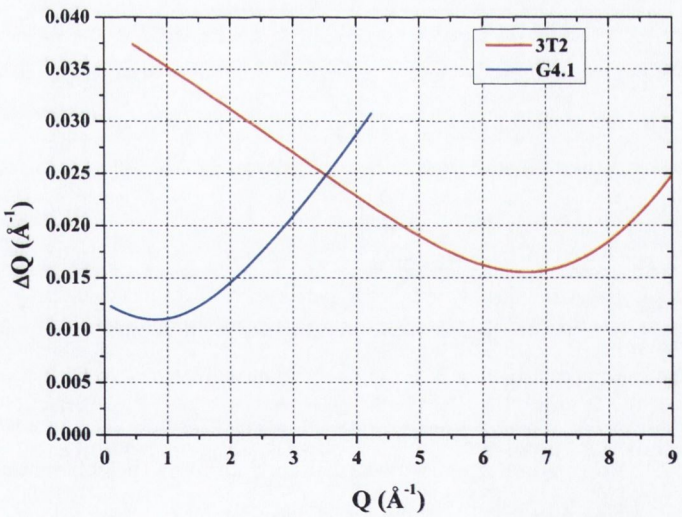

Figure C.11: Instrumental resolution of the 3T2 (red) and G4.1 (blue) spectrometers in Q space.

Composition	T (K)	
	3T2	G4.1
$CuCr_2Se_4$	2,500	2-300 (11)
$CuCr_2Se_3Br$	2,300	2-290 (13)
$CuCr_2Se_{3.5}Br_{0.5}$	2,500	2-313 (17)
$CuCr_2Se_{3.2}Br_{0.2}$	2,400	1.5-313 (19)
$CuCr_2Se_3Br$ (6 months after)	-	290
$CdCr_2Se_4$	2,300	1.5-290 (11)

Table C.1: List of measured samples on 3T2 and G4.1 spectrometer with the temperature at which they have been measured. The number indicated in brackets for G4.1 correspond to the number of steps between the two extreme temperature.

atomic positions, and atomic thermal factor determined with 3T2 data will be used to refine the magnitude of the magnetic moments calculated with G4.1 data.

The list of the samples with their composition and the temperature at which they have been measured on each spectrometer is presented in table C.1.

C.1.4.3 Structure refinement

The determination of structural parameter were done in the same fashion as for the XRD data. Only the magnetic structure determination will be described in this section.

Above the Curie point, in the paramagnetic domain, the magnetic moment on the magnetic atoms in the crystal are oriented randomly and only the coherent scattering due to the nuclear structure is observed. Below the ordering temperature, a long distance order between the magnetic moments is observed. The magnetic structure of a compound is then defined by the position of the magnetic atoms in the crystal and a magnetic propagation vector k_m. The propagation vector can be determined by symmetry analysis, or for simple case by trial and error. In the case of the study, the propagation vector is easy to determine since no purely magnetic peak appears. It means that all the magnetic order has the same symmetry as the nuclear structure, therefore the propagation vector $k_m = (0, 0, 0)$.

To calculate the magnitude of the magnetic moment, the program Fullprof was used, and

a magnetic moment was assigned to Cu and Cr on the M_z axe[1]. The atomic thermal factor determined at 2 K on the 3T2 spectrometer were used to determine the magnetic intensities measured on the G4.1 spectrometer since the low angle instrument resolution is better on the latter. The magnetic agreement factor correspond to R_{Bragg} for the magnetic peaks.

C.2 Magnetometry

The magnetic characterisation of the compound synthesised in this thesis focused on the measurement of the intrinsic magnetic parameters, such as the saturation magnetisation, Curie temperature, and the anisotropy. Different measurement method have been used depending on the property under investigation.

C.2.1 DC magnetometry

The saturation magnetisation of the sample has been obtained by applying a DC magnetic field using a SQUID magnetometer (Quantum Design Magnetic Measurement System MPMS 5 XL). The measurement on most of the polycrystalline samples (chalcogenide, oxides nanoparticles) and on the thin films have been performed with Dr. M. Venkatesan, the single crystal magnetisation were collected with Dr. P. Stamenov. The polycrystalline samples were loaded in a gelatine capsule and fixed in a plastic straw. This mounting method has the disadvantage to introduce a diamagnetic background. The single crystal were mounted, when possible[2], with zero-background by pressing the crystal between two plastic straws. Thin films were mounted in plastic straws after removal of the residual silver paste on the back of the substrate.

Absolute magnetisation measurements have been carried out on the single crystal sample by correcting the measurement magnetic moment with the appropriate terms (Stamenov (2007); Stamenov & Coey (2006)). Before the measurement an Al cylinder was measured with the two algorithms used for magnetisation in function of field (linear regression) and in function of temperature (iterative regression) (Fig.C.12). The observed difference in the measured moment is due to the fact that the two different algorithms truncate the spatial Fourier transform of the z axis magnetic moment distribution in different fashion and the DSP filtering and gain setting cannot be identical. After absolutising the data in term of an ideal dipole, the knowledge of the shape and radial offset permits to correct (in principle) any dataset produced by either

[1]This choice is arbitrary since the symmetry is cubic.

[2]For the pure $CuCr_2Se_4$ crystals, several pieces were loaded in a gelatine capsule.

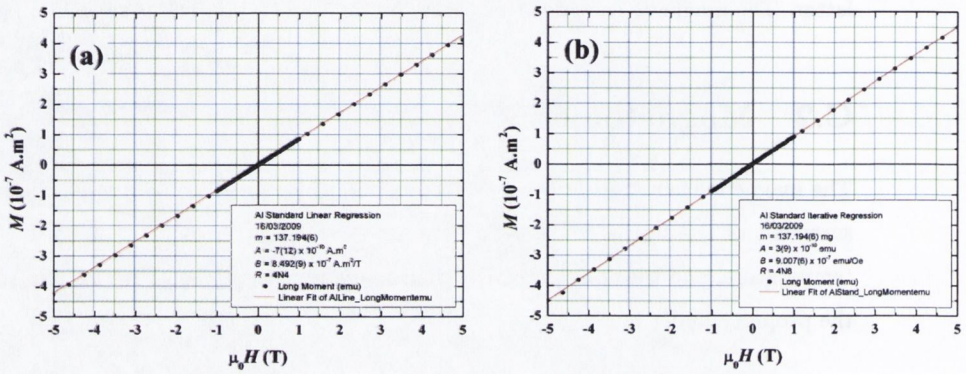

Figure C.12: Magnetisation in function of field for an *Al* cylinder standard obtained with (a) linear regression, (b) iterative regression.

algorithm. This procedure has been applied to the single crystal data for both radial offset and shape. For the sample mounted in a gelatine capsule, the absolute correction is expected to be smaller (when the masses are large) since the sample have no elongated shape and that they are centrally mounted. The moment associated with the gelatine capsule and the associated magnetisation distribution are difficult to handle and is only important for absolute sample moment $\lesssim 10^{-6}\mathrm{A}\cdot\mathrm{m}^2$.

C.2.2 AC susceptibility

The measurement were performed with the same SQUID magnetometer described above with a setup designed and realised by Dr. P. Stamenov. An AC drive field of 0.5 mT peak-peak amplitude and a frequency of 1133 Hz was applied using integrated "in-Helium" copper coils. Whenever necessary a DC bias field was applied using the usual superconducting magnet. A three point sample reciprocation algorithm was used to account primarily for mutual inductance background due to the presence of antiferromagnetic stainless steel materials in the variable temperature insert (i.e. in between the sample and the sensing coils). Residual drive field pickup is compensated with a synchronous amplitude independent oscillator driving a SQUID feedback coil located after the superconducting transformer coupling the measurement coil loops with the SQUID itself (1-5% of measured moment). Asynchronous background due to mutual inductance with surrounding main cabling was compensated using an independent system of arbitrary

waveform generator and amplifier down to a level of $\lesssim 10^{-11}\mathrm{A}\cdot\mathrm{m}^2$. The absolute sensitivity after locking detection as inferred to the sample moment is in the range $2 - 510^{-12}\mathrm{A}\cdot\mathrm{m}^2$.

C.2.3 Torque measurement

Torque magnetometry was performed with the Tq-Mag option of the PPMS together with Dr. P. Stamenov. It incorporates a torque-lever chip mounted on a rotator platform for performing angular-dependent magnetic moment measurements. It utilises a piezoresistive technique to measure the torsion of the cantilever created by the magnetic field on the sample moment : $\tau = m \times H$. The angular dependence of the torque amplitude in 14 T was measured at different temperature. A typical set of torque curve is shown on Fig.C.13. To extract the torque amplitude A at one temperature the curve is fitted with a cosine function : $T = A\cdot\cos(2\theta+\phi)$, the phase coming from the non-perfect alignment of the crystal axis with respect to the normal of the lever.

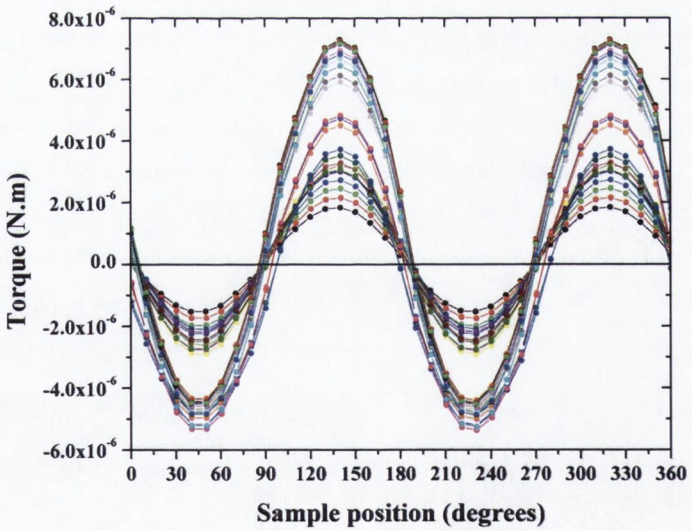

Figure C.13: Set of torque curves at different temperature of $CuCr_2Se_3Br$ single crystal.

C.3 Electrical transport measurements

All the electrical transport measurement described in the main text were carried out in the Quantum Design PPMS together with Dr. P. Stamenov.

The magnetoresistance and Hall resistance on the two metallic single crystals ($CuCr_2Se_4$, and $CuCr_2Se_3Br$) were measured using the ACT option of the PPMS by ac phase sensitive detection. Seven contacts were attached on the $CuCr_2Se_3Br$ single crystal as represented on Fig.C.14(a) with a standard Hall-bar geometry. A current excitation of 20 mA (17.5 Hz) was chosen to keep the power on the sample below 1 mW and that the second harmonic of the measured signal are small. The field was varied from -14 T to 14 T, the temperature from 5 K to 300 K, and the sample was rotated to measure AMR. In the case of the pure $CuCr_2Se_4$ sample, only four contacts were used in a van der Pauw geometry as represented on Fig.C.14(b) and an excitation current of 10 mA (17.5 Hz) was used. In this geometry only Hall resistance and magnetoresistance were measured. The magnetoresistance and the Hall resistance are obtained by calculating the symmetric part and the antisymmetric part of their respective voltage drop.

Magnetoconductance of the pure, *In*-, and *Ag*-doped $CdCr_2Se_4$ were measured with a Keithley subfemtoamp sourcemeter in two different probe. For the pure $CdCr_2Se_4$ single crystals, measurement above 50 K were done with a non-guarded probe, and 4 wires were attached to the samples in a van der Paw geometry as presented on Fig.C.14(c). For the rest of the measurements a high-impedance probe designed and constructed by Dr. P. Stamenov was used. It consists of a sample mounting assembly with a guard and two ground shields, triaxial cryogenic wiring and connectors for the pre-amplifiers. Two contacts on each side of the crystal were contacted and the current was measured at fixed voltage.

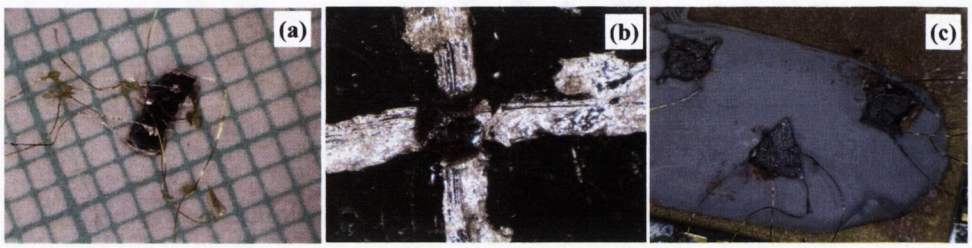

Figure C.14: (a) $CuCr_2Se_3Br$ single crystal with seven contacts, (b) pure $CuCr_2Se_4$ with four contacts, (c) three different cut of pure $CdCr_2Se_4$.

C.4 Heat capacity measurement

The heat capacity measurement were carried out on the Heat Capacity system of the PPMS together with Dr. P. Stamenov. It uses a relaxation technique with a 2-τ model which take account for bad thermal contact. The sample is mounted on an alumina sample platform suspended by 8 wires with Apiezon grease (N for T <295 and H for higher temperature). Prior to measurement the puck was measured only with the same grease used in the temperature interval to get the addenda which was automatically substracted during the measurement.

C.5 Point contact Andreev reflection

The PCAR measurements were performed in a Helium vapour flow cryostat (Oxford Instruments) using a conventional micrometre plus a piezo transducer linear translation motion (the sample is mounted on the micrometre screw translator, while the superconducting Nb tip is mounted on the piezo transducer).

Electrical measurements were performed using a two frequency AC methods, where a low frequency ($\sim$ 1 Hz) sweep the applied bias to the junction, while much higher frequency ($\sim$ 10 kHz) is used for the analogue differentiation and demodulation. Low noise filtering current pre-amplifier meters the current to the sample, while both low and high frequency voltages are produced via resistive dividers by two independent oscillators. A lock-in demodulation and detection is done at the higher of the two frequencies (in digital synchronisation with the oscillators) and the resulting in- and out-of-phase components are recorded in digital synchronisation with the low frequency oscillation into buffer digital memory for subsequent transfer to the controller PC. The resulting system permits rapid data acquisition - a full derivative spectrum is obtained approximately every second. This permits the tracking of the behaviour of the junctions on their establishing, modification, and annihilation.

C.6 Infrared spectroscopy

Infrared spectroscopy was measured on $CuCr_2Se_3Br$ and $CdCr_2Se_4$ single crystals in Pr. D. N. Basov Infrared Spectroscopy of Novel Electronic and Magnetic Materials laboratory (University of California San Diego) with the help of A. LaForge and A. Schafgans.

C. Characterisation method

The sample was mounted on a brass cone with epoxy in such a fashion that one of the face of the crystal was parallel to the base of the cone. The measurement were performed under vacuum in near-normal reflectance geometry with a broadband Fourier transform spectrometer over a frequency range of 200-16 000 cm^{-1}. Absolute reflectance was measured normalising by the reflectance of the sample coated with Au.

Appendix D

Phase diagram thermodynamic

D.1 Thermodynamic equilibrium

The existence of a phase field was defined in the main text as the range of composition for the binary system $A - B$ where the free Gibbs energy is minimum for the two phase. This definition comes from the second thermodynamic law and more precisely, at constant pressure P and temperature T, a closed system will minimise the free Gibbs energy to achieve a stable equilibrium for $dG = 0$.

$$G(T, P, n_i^{\varphi}) = \sum_{\varphi} \sum_{i} \mu_i^{\varphi} n_i^{\varphi}$$

Using the Gibbs-Duheim relation, the previous relation becomes :

$$\sum_{\varphi} \sum_{i} \mu_i^{\varphi} dn_i^{\varphi} = 0$$

Since the system is closed :

$$\sum_{\varphi}^{i} n_i^{\varphi} = n_i^0 \Rightarrow \sum_{\varphi}^{i} dn_i^{\varphi} = 0$$

Replacing this relation in the previous equation :

$$\sum_{\varphi} \sum_{i} \left(\mu_i^{\varphi} - \sum_{\varphi' \neq \varphi} \mu_i^{\varphi'} \right) dn_i^{\varphi} = 0$$

Since dn_i^{φ} are independent the minimum of free energy correspond to the equality of chemical potential : $\mu_i^{\varphi} = \mu_i^{\varphi'}$.

D.2 Geometric construction

The binary case can be interpreted geometrically. In the case of a binary system with constituent A and B having two different phases α and β, a two dimensional plot of the free Gibbs energy can be plotted (Fig.D.1).

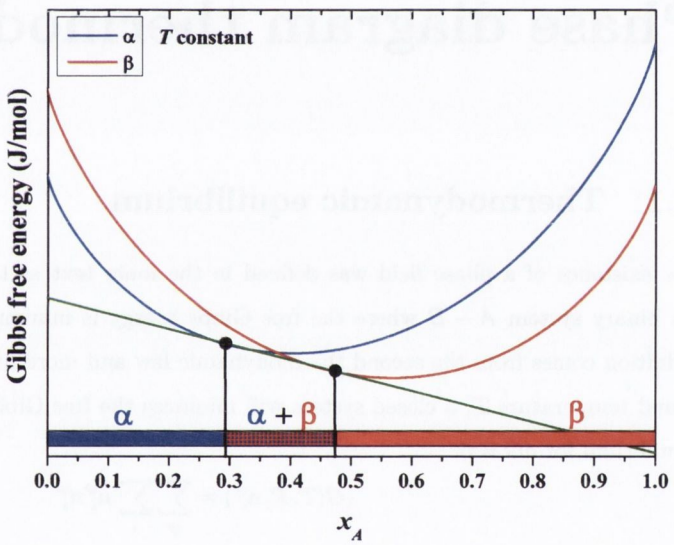

Figure D.1: Gibbs free energy at constant temperature T in function of the molar composition in A for the α phase (blue curve), the β phase (red curve). The green line represent the common tangent and the bottom rectangle the phase field with their respective phases.

The condition of energy minimisation $\mu_i^\alpha = \mu_i^\beta$ with $i = A, B$ is equivalent to find a common tangent for G^α and G^β represented by a green line in Fig.D.1. The phase fields are then defined in the corresponding concentration range.

D.3 Transformation definition

Their is a variety of transformation that can be encountered in a phase diagram, and the different reaction have different appellation depending on the state and the nature of the phases in presence. A glossary of such reaction obtained from Clark *et al.* (1994) is presented below :

Eutectic An isothermal, reversible reaction between two (or more) solid phases during the heating of a system, as a result of which a single liquid phase is produced : $L \rightleftarrows s_1 + s_2$

Eutectoid An isothermal, reversible reaction between two (or more) solid phases during the heating of a system, as a result of which a single new solid phase is produced : $s \rightleftarrows s_1 + s_2$

Monotectic The reversible transition, on cooling, of a liquid to a mixture of a second liquid and a solid $L_1 \rightleftarrows L_2 + s$

Monotectoid A reaction in a system containing two solid solution phases, α' and α'' in which α' decomposes into α'' and a new phase β : $\alpha' \rightleftarrows \alpha'' + \beta$

Peritectic An isothermal, reversible reaction between two phases, a liquid and a solid, that, on cooling of a binary, ternary, ... , n system, results in one, two, ... $(n-1)$ new solid phases. For example, in a binary system containing : $\alpha + L \rightleftarrows \beta$

Peritectoid An isothermal, reversible reaction in the solid state, that, on cooling of a binary, ternary, ... , n system, results in one, two, ... $(n-1)$ new solid phases. For example, in a binary system containing two solids α' and α'' : $\alpha' + \alpha'' \rightleftarrows \beta$

Syntectic A reversible transition that involves the conversion of two liquid phases into a solid phase on cooling : $L_1 + L_2 \rightleftarrows \alpha$

D.4 Construction of a peritectic transition

The Gibbs free energy for a three phase equilibria with a peritectic point is presented in Fig.D.2 for 4 different temperatures : $T > T_P$, $T = T_P$, $T_1 < T_P$, and $T_2 < T_1 < T_P$.

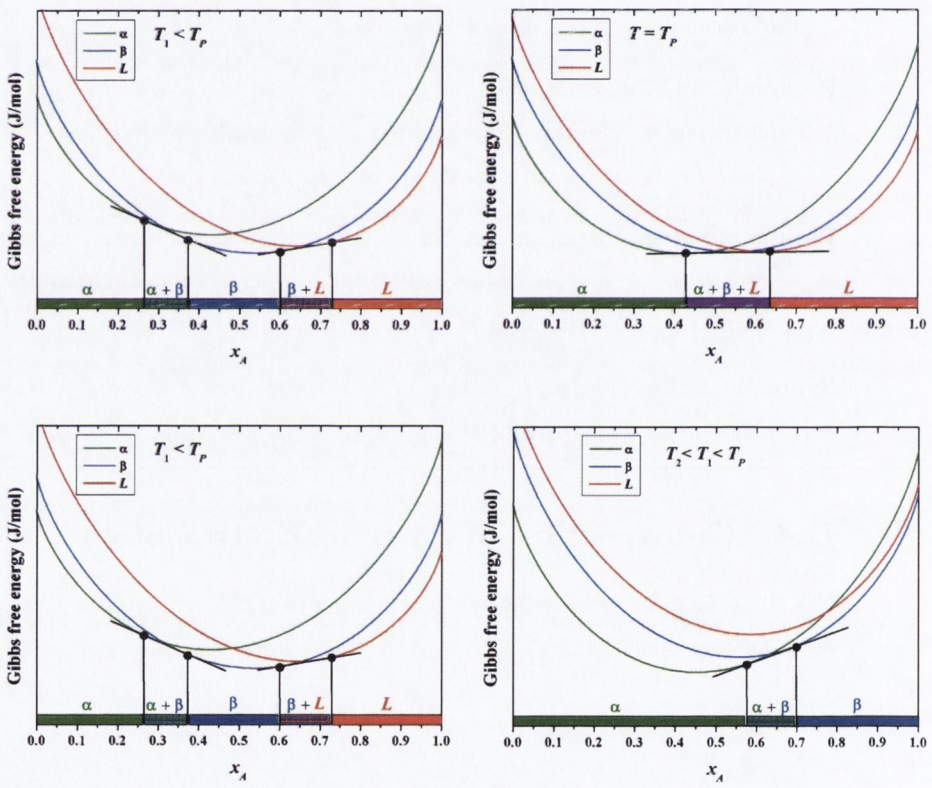

Figure D.2: Gibbs free energy at constant temperature 4 different temperature T in function of the molar composition in A for the α phase (green curve), the β phase (blue curve), and the liquid (red curve). The bottom rectangle the phase field with their respective phases.

References

Ahn, G.Y., Park, S.I. & Shim, I.B. (2004). Mossbauer studies of ferromagnetism in Fe-doped ZnO magnetic semiconductor. *J. Magn. Mag. Mat.*, **282**, 166. 173

Alaria, J., Turek, P., Bernard, M., Bouloudenine, M., Berbadj, A., Brihi, N., Schmerber, G., Colis, S. & Dinia, A. (2005). No ferromagnetism in Mn doped ZnO semiconductors. *Chem. Phys. Lett.*, **415**, 337. 168

Alaria, J., Bieber, H., Colis, S., Schmerber, G. & Dinia, A. (2006a). Absence of ferromagnetism in Al-doped $Zn_{0.9}Co_{0.10}O$ diluted magnetic semiconductors. *Appl. Phys. Lett.*, **88**, 112503. 168

Alaria, J., Bouloudenine, M., Schmerber, G., Colis, S., Dinia, A., Turek, P. & Bernard, M. (2006b). Pure paramagnetic behavior in Mn-doped ZnO semiconductors. *J. Appl. Phys.*, **99**, 08M118. 168

Almeida, N.S. & Miranda, L.C.M. (1978). Light scattering from magnons in ferromagnetic semiconductors under strong fields. *Solid State Commun.*, **27**, 11. 33

Aminov, T.G., Belov, K.P., Kalinnikov, V.T., Koroleva, L.I. & Tovmasjan, L. (1980). Low-temperature transition metal-semiconductor in $CdCr_2Se_4$ single crystals doped with indium and gallium. *J. Physique*, **41**, 155. 32, 136

Anderson, P.W. (1950). Antiferromagnetism. Theory of superexchange mechanism. *Phys. Rev.*, **79**, 350. 22

Anderson, P.W. (1959). New approach to the theory of superexchange interactions. *Phys. Rev.*, **115**, 2. 22

REFERENCES

ANDERSON, P.W. & HASEGAWA, H. (1955). Consideration on double exchange. *Phys. Rev.*, **100**, 675. 25

ANTONOV, V.N., ANTROPOV, V.P. & HARMON, B.N. (1999). Fully relativistic spin-polarized LMTO calculations of the magneto-optical Kerr effect of d and f ferromagnetic materials. I. Chromium spinel chalcogenides. *Phys. Rev. B*, **59**, 14552. 45, 47

ARNOLD, B.J. (2008). *Growth and characterisation of Al(Cr)N thin films by r.f. plasma assisted pulsed laser deposition*. Master's thesis, School of Physics, Trinity College Dublin. 214

AUSLENDER, M.I. & BEBENIN, N.G. (1989). On the band structure and anisotropy of transport properties of ferromagnetic semiconductors $CdCr_2Se_4$ and $HgCr_2Se_4$. *Solid State Commun.*, **67**, 761. 36

BABITSYNA, A.A., EMEL'YANOVA, T.A., CHERNITSYNA, M.A. & KALINNIKOV, V.T. (1978). The synthesis of single crystals of the copper selenochromate spinel $CuCr_2Se_4$. *Russ. J. Inorg. Chem.*, **23**, 151. 37

BABITSYNA, A.A., EMEL'YANOVA, T.A., KONESHOVA, T.I., CHERNITSYNA, M.A. & KALINNIKOV, V. (1980). Interaction in the Cr_2Se_3-Cu_2Se-Se system. *Russ. J. Inorg. Chem.*, **25**, 1084. 37, 39

BALAEV, A.D., GAVRICHKOV, V.A., OVCHINNIKOV, S.G., CHERNOV, V.K., AMINOV, T.G. & SHABUNINA, G.G. (1998). Quantum oscillations of resistance and magnetization in the degenerate semiconductor n-$HgCr_2Se_4$. *J. Exp. Theor. Phys.*, **86**, 1026–1029. 36

BALAL, M.M. & MANDE, C. (1976). X-ray spectroscopic study of the valency of copper in the spinels $CuCr_2X_4$ (X = O, S, Se, Te). *Solid State Commun.*, **19**, 325. 44

BALTZER, P.K., LEHMANN, H.W. & ROBBINS, M. (1965). Insulating Ferromagnetic Spinels. *Phys. Rev. Lett.*, **15**, 493–495. xiii, 6, 31, 34, 35, 98

BALTZER, P.K., WOJTOWICZ, P.J., ROBBINS, M. & LOPATIN, E. (1966). Exchange interactions in ferromagnetic chromium chalcogenide spinels. *Phys. Rev.*, **151**, 367. 28, 96

BARRACLOUGH, K.G. & MEYER, A. (1972). Vapour transport and assessment of $CdCr_2S_4$ crystals. *J. Cryst. Growth*, **16**, 265. 108

BARRACLOUGH, K.G. & MEYER, A. (1973). The CdSe-Cr_2Se_3 system and the formation of the ferromagnetic semiconducting spinel $CdCr_2Se_4$. *J. Cryst. Growth*, **20**, 212. 31

Bel'skii, N.K., Ochertyanova, L.I., Shabunina, G. & Aminov, T.G. (1985). Chemical composition of In-, Ag-, and Ga-doped $CdCr_2Se_4$ crystals. *Russ. J. Inorg. Chem.*, **21**, 496. 31

Berger, S.B. & Pinch, H.L. (1967). Ferromagnetic resonance of single crystals of $CdCr_2S_4$ and $CdCr_2Se_4$. *J. Appl. Phys.*, **38**, 949. 31

Berzhansky, V.N., Drokin, N.A., Ivanov, V.I., Kononov, V.P., Edelman, I.S., Havrichkov, S.A., Chernov, V.K., Shishkov, A.G. & Pirogova, A.M. (1989). Synthesis and physical properties of chalcogenide chromium spinel films. *Thin Solid Films*, **190**, 199. 31, 38

Bettinger, J.S., Chopdekar, R.V., Liberati, M., Neulinger, J.R., Chshiev, M., Takamura, Y., Alldredge, L.M.B., Arenholz, E., Idzerda, Y.U., Stacy, A.M., Butler, W.H. & Suzuki, Y. (2008). Magnetism and transport of $CuCr_2Se_4$ thin films. *J. Magn. Mag. Mat.*, **318**, 65–73. xxi, 38, 46, 47, 140, 165

Binnewies, M. & Milke, E. (1999). *Thermochemical data of elements and compounds*. Wiley. 196

Blonder, G.E., Tinkham, M. & Klapwijk, T.M. (1982). Transition from metallic to tunneling regimes in superconducting microconstrictions : Excess current, charge imbalance, and supercurrent conversion. *Phys. Rev. B*, **25**, 4515. 147

Bongers, P.F. & Zanmarchi, G. (1968). Infrared absperption spectrum and Faraday rotation of ferromagnetic $CdCr_2Se_4$. *Solid State Commun.*, **6**, 291. 33

Bongers, P.F., Haas, C., van Run, A.M.J.G. & Zanmarchi, G. (1969). Magnetoresistance in chalcogenide spinels. *J. Appl. Phys.*, **40**, 958. 32

Bouchard, R.J., Russo, P.A. & Wold, A. (1965). Preparation and electrical properties of some thiospinels. *Inorg. Chem.*, **4**, 685–688. 9

Brandle, H., Schoenes, J., Wachter, P. & Hulliger, F. (1990). Large room temperature magneto-optical Kerr effect in $CuCr_2Se_4$. *Appl. Phys. Lett.*, **56**, 2602. 40

Brandle, H., Schoenes, J., Wachter, P., Hulliger, F. & Reim, W. (1991). Large room-temperature magneto-optical kerr effect in $CuCr_2Se_{4-x}Br_x$ (x=0 and 0.3). *J. Magn. Mag. Mat.*, **93**, 207. 40

REFERENCES

BRIDGEMAN, P.W. (1925). *Proc. Amer. Acad. Arts Sci.*, **60**, 305. 104

BUNSEN, R. (1852). *J. Prakt. Chem.*, **56**, 53. 106

BURDETT, J., PRICE, G.D. & PRICE, S.L. (1982). Role of the crystal-field theory in determining the structure of spinels. *J. Amer. Chem. Soc.*, **104**, 92. 19

BUSCH, G., MAGYAR, B. & WACHTER, P. (1966). Optical absorption of some ferro- and antiferromagnetic spinels containing Cr^{3+} ions. *Phys. Lett.*, **23**, 438. 33

CAGLIOTI, G., PAOLETTI, A. & RICCI, F.P. (1958). Choice of collimators for a crystal spectrometer for neutron diffraction. *Nuc. Instr.*, **3**, 223. xxvi, 229, 230

CHATTERJI, T., ed. (2006). *Neutron scattering from magnetic materials*. Elsevier. 221

CHERNITSYNA, M.A., BABITSYNA, A.A. & KALINNIKOV, V.T. (1977). The Cr_2Se_3-CuSe-Se system. *Russ. J. Inorg. Chem.*, **22**, 3357. xv, 37, 56

CHERNITSYNA, M.A., KALINNIKOV, V.T., BABITSYNA, A.A. & EMEL'YANOVA, T.A. (1978). Reaction of $CuCr_2Se_4$ with various salts. *Russ. J. Inorg. Chem.*, **23**, 42. 37

CHIBA, H., ATOU, T. & SYONO, Y. (1997). Magnetic and electrical properties of $Bi_{1-x}Sr_xMnO_3$: Hole doping effect on ferromagnetic perovskite $BiMnO_3$. *J. Solid State Chem.*, **132**, 139. xiii, 6

CHO, S., CHOI, S., CHA, G.B., HONG, S., KIM, Y., FREEMAN, A., KETTERSON, J., PARK, Y. & PARK, H.M. (2004). Synthesis of new pure ferromagnetic semiconductors : $MnGeP_2$ and $MnGeAs_2$. *Solid State Commun.*, **129**, 609. xiii, 6

CLARK, J.B., HASTIE, J.W., KIHLBORG, L.H.E., METSELAAR, R. & THACKERAY, M.M. (1994). Definition of terms relating to phase transitions of the solid state. *Pure & Appl. Chem.*, **66**, 577. 240

COEY, J.M.D. (2006). Dilute Magnetic Oxide. *Current Opinion in Solid State and Materials Science*, **10**, 83. 5

COLOMINAS, C. (1967). Neutron-diffraction investigation of $CuCr_2Se_4$ and $CuCr_2Te_4$. *Phys. Rev. B*, **153**, 558. 38, 43, 67, 70, 86

CONTINENZA, A., DE PASCALE, T., MELONI, F. & SERRA, M. (1994). Electronic and magnetic properties of the spinel semiconductor $CdCr_2Se_4$. *Phys. Rev. B*, **49**, 2503. 34

Cushing, B.L., Kolesnichenko, V.L. & O'Connor, C.J. (2004). Recent advances in the liquid phase syntheses of inorganic nanoparticles. *Chem. Rev.*, **104**, 3893. 201

Czocharlski, J. (1918). *Z. Phys. Chem.*, **92**, 219. 104

Deb, A., Itou, M., Tsurkan, V. & Sakurai, Y. (2007). Effect of substitution of Cl and Br for Se in the ferromagnetic spinel $CuCr_2Se_4$: A magnetic Compton profile study. *Phys. Rev. B*, **75**, 024413. 39

DeGennes, P.G. (1960). Effects of Double Exchange in Magnetic Crystals. *Phys. Rev.*, **118**, 141. 25, 40

Deville, H.S.C. (1861). *Ann.*, **120**, 176. 106

Dietl, T., Andrearczyk, T., A. Lipinska, M.K., Tay, M., & Wu, Y. (2004). Different origins of the ferromagnetic order in (Ga,Mn)As and (Ga,Mn)N. *Phys. Rev. B*, **70**, 235209. 180

Dorneles, L.S., Venkatesan, M., Gunning, R., Stamenov, P., Alaria, J., Rooney, M., Lunney, J.G. & Coey, J.M.D. (2007). Magnetic and structural properties of Co-doped ZnO thin films. *J. Magn. Mag. Mat.*, **310**, 2087. 178

Du, M.L. & Zhao, M.G. (1988). Zero-field splitting of tetrahedral Co^{2+} in the trigonal crystal field. *J. Phys. C : Solid State Phys.*, **21**, 1561. 189

Dunitz, J.D. & Orgel, L.E. (1957). Electronic properties of transition metal oxides II. *J. Phys. Chem. Solids*, **3**, 318. 15

Dwight, K. & Menyuk, N. (1967). Magnetic interactions and spiral ground states in spinels, with application to $ZnCr_2Se_4$. *Phys. Rev.*, **163**, 435. 28

Dwight, K. & Menyuk, N. (1968). Analysis of distant-neighbor interactions in cubic spinels. *J. Appl. Phys.*, **39**, 660. 28

Eason, R., ed. (2007). *Pulsed laser deposition of thin films*. Wiley, New York. 155

Eastman, D.E. & Shafer, M.W. (1967). Magnetostriction in ferromagnetic $CdCr_2Se_4$. *J. Appl. Phys.*, **38**, 4761. 31

Emmenegger, F.P. (1972). Gaseous complexes - Their role in chemical transport. *J. Cryst. Growth*, **17**, 31. 110

FAUST, J.W., JOHN, H.F. & PRITCHARD, C. (1968). Influence of solvent and impurities on habit and morphology of semiconductor crystals. *J. Cryst. Growth*, **3-4**, 321. 114

FEDOROV, V.A., KESLER, Y.A. & ZHUKOV, E. (2003). Magnetic semiconducting spinels : preparation and physical chemistry. *Inor. Mater.*, **39**, S68–S88. 55

FIEDERLING, R., KLEIM, M., REUSHER, G., OSSAU, W., SCHMIDT, G., WAAG, A. & MOLENKAMP, L.W. (1999). Injection and detection of a spin-polarized current in a light-emitting diode. *Nature*, **402**, 787. 5

FINGER, L.W., COX, D. & JEPHCOAT, A.P. (1994). A correction for powder diffraction peak asymmetry due to axial divergence. *J. Appl. Cryst.*, **27**, 892. 223

FITZGERALD, C.B., VENKATESAN, M., LUNNEY, J.G., DORNELES, L.S. & COEY, J.M.D. (2005). Cobalt-doped ZnO - a room temperature dilute magnetic semiconductor. *Appl. Surf. Sci.*, **247**, 493. 189

FLEMING, R.M., DISALVO, F.J., CAVA, R.J. & WASZCZAK, J.V. (1981). Observation of charge-density waves in the cubic spinel structure CuV_2S_4. *Phys. Rev. B*, **24**, 2850–2853. 9

GAJ, J., GINTER, J. & GALAZKA, R. (1978). Exchange interaction of manganese $3d^5$ states with band electrons in $Cd_{1-x}Mn_xTe$. *Phys. Stat. Solidi (b)*, **89**, 655. xiii, 6

GARRETT, J., GREEDAN, J. & MACLEAN, D. (1981). Crystal growth and magnetic anisotropy of $YTiO_3$. *Mat. Res. Bull.*, **16**, 145. xiii, 6

GIBART, P. (1978). Vapor growth of $HgCr_2Se_4$. *J. Cryst. Growth*, **43**, 21. 35, 108

GLIDEWELL, C. (1976). Cation distribution in spinels. *Inorg. Chim. Acta*, **19**, L45. 18

GOLANT, K.M., TSURKAN, V.V. & VESELAGO, V.G. (1978). Effect of longitudinal magnetic field on the conductivity in magnetic semiconducting p-type spinels. *J. Exp. Theor. Phys. Lett.*, **28**, 107. 39

GOLDSTEIN, L., GIBART, P. & SELMI, A. (1978). Transport properties of the ferromagnetic semiconductor $HgCr_2Se_4$. *J. Appl. Phys.*, **49**, 1474–1476. 35

GOODENOUGH, J.B. (1955). Theory of the role of covalence in the perovskite type manganite [LaM(II)]MnO_3. *Phys. Rev.*, **100**, 564. 22, 23

GOODENOUGH, J.B. (1963). *Magnetism and the chemical bond*. John Wiley & Sons. 22, 23, 27, 189

GOODENOUGH, J.B. (1967). Tetrahedral-site copper in chalcogenide spinels. *Solid State Commun.*, **5**, 577. 41, 44

GOODENOUGH, J.B. (1969). Description of outer d electrons in Thiospinel. *J. Phys. Chem. Solids*, **30**, 261–280. xiv, 33, 41, 42

GOPAL, E.S.R. (1966). *Specific heats at low temperatures*. Heywood. 132

GRIMES, N.W. & ISAAC, E.D. (1977). A simplified interpretation of the magnetic exchange interactions for chromium chalcogenide spinels. *Phil. Mag.*, **35**, 503. 28

GRUEHN, R. & GLAUM, R. (1997). Computer program CVTrans. *Giessen University*. 111

GUNNING, R. (2006). *Magnetism in Dilute Magnetic Oxides and Related Materials*. Ph.D. thesis, School of Physics, Trinity College Dublin. 5

HAAS, C. (1968). Spin-disorder scattering and magnetoresistance of magnetic semiconductor. *Phys. Rev.*, **168**, 531. 33, 136

HAGINO, T., SEKI, Y., WADA, N., TSUJI, S., SHIRANE, T., KUMAGAI, K.I. & NAGATA, S. (1995). Superconductivity in spinel-type compounds $CuRh_2S_4$ and $CuRh_2Se_4$. *Phys. Rev. B*, **51**, 12673–12684. 10

HAHN, H., LORENT, C.D. & HARDER, B. (1956). Über die Struktur des CuV_2S_4, $CuCr_2S_4$, $CuCr_2Se_4$ und $CuCr_2Te_4$. *Z. Anorg. Allg. Chem.*, **283**, 139–142. 36

HAHN, T. (1996). *International Tables for Crystallography Volume A*, vol. A: Space-group symmetry. Kluwer Acad. Publ., 4th edn. xxvii, 10, 11, 113

HAMILTON, W.C. (1965). Significance tests on the crystallographic R factor. *Acta Cryst.*, **18**, 502. 121

HAN, M.J. & YU, J. (2006). Electronic structure and magnetic properties of wurtzite CoO. *J. Kor. Phys. Soc.*, **48**, 1496. 180

HARBEKE, G. & PINCH, H. (1966). Magnetoabsorption in single-crystal semiconducting ferromagnetic spinel. *Phys. Rev. Lett.*, **17**, 1090. 31, 33

REFERENCES

HEMBERGER, J., RUDOLF, T., NIDDA, H.A.K.V., MAYR, F., PIMENOV, A., TSURKAN, V. & LOIDL, A. (2006). Spin-driven phonon splitting in bond-frustrated $ZnCr_2S_4$. *Phys. Rev. Lett.*, **97**, 087204. 9

HOLLANDER, J.C.T., SAWATZKY, G. & HAAS, C. (1974). Monovalent copper in the chalcogenide spinel $CuCr_2Se_4$. *Solid State Commun.*, **15**, 747. 44

HORIKAWA, J.I., HAMAJIMA, T., OGATA, F., KAMBARA, T. & GONDARAI, K.I. (1982). The spin polarised electronic band structure of chromium spinel : I. $CuCr_2S_4$. *J. Phys. C : Solid State Phys.*, **15**, 2613. 44

HOSCHL, P., HLIDEK, P., KUBLA, V., MORAVEC, P., PITEL, J. & PROSSER, V. (1981). Growth and some physical properties of $CdCr_2Se_4$ crystals. *J. Cryst. Growth*, **52**, 669. 31, 32

HÉRITIER, M. (1983). n-type $CdCr_2Se_4$: a mott extrinsic semiconductor. *Phys. Rev. B*, **28**, 1136. 32

HUANG, N.L. & ORBACH, R. (1968). Systematics of the right-angle nearest-neighbor eschange interaction for d^3 ions. *J. Appl. Phys.*, **39**, 426. 28

HUBBARD, J. & MARSHALL, W. (1965). Covalency effects in neutron diffraction from ferromagnetic and antiferromagnetic salts. *Proc. Phys. Soc.*, **86**, 561. 68

ILIEV, M.N., ANASTASSAKIS, E. & ARAI, T. (1978). Raman scattering of $HgCr_2Se_4$. *Phys. Stat. Solidi (b)*, **86**, 717. 36

JOHNSTON-HALPERIN, E., LOFGREEN, D., KAWAKAMI, R.K., YOUNG, D.K., COLDREN, L., GOSSARD, A.C. & AWSCHALOM, D.D. (2002). Spin-polarized Zener tunneling in (Ga,Mn)As. *Phys. Rev. B*, **65**, 041306. 7

JONKER, B.T., PARK, Y.D., BENNETT, B.R., CHEONG, H.D., KIOSEOGLOU, G. & PETROU, A. (2000). Robust electrical spin injection into a semiconductor heterostructure. *Phys. Rev. B*, **62**, 8180. 5

JONKER, B.T., HANBICKI, A.T., PARK, Y.D., ITSKOS, G., FURIS, M., KIOSEOGLOU, G. & PETROU, A. (2001). Quantifying electrical spin injection : component-resolved electroluminescence from spin-polarized light-emitting diodes. *Appl. Phys. Lett.*, **79**, 3098. 7

JUNGWIRTH, T., SINOVA, J., MASEK, J., KUCERA, J. & MACDONALD, A.H. (2006). Theory of ferromagnetic (III,Mn)V semiconductors. *Rev. Mod. Phys.*, **78**, 809. 4

KALINNIKOV, V.T., AMINOV, T.G. & NOVOTORTSEV, V.M. (2003). Physical chemistry of the magnetic semiconductor $CdCr_2Se_4$. *Russ. J. Inorg. Chem.*, **39**, 997. xv, 31, 56

KAMBARA, T., OGUCHI, T. & GONDARAI, K.I. (1980). Electronic band structures of semiconducting ferromagnetic spinels $CdCr_2S_4$ and $CdCr_2Se_4$. *J. Phys. C : Solid State Phys.*, **13**, 1493. 33

KANAMORI, J. (1959). Superexchange interaction and symmetry properties of electron orbitals. *J. Phys. Chem. Solids*, **10**, 87. 22, 23

KANOMATA, T. & IDO, H. (1974). Exchange striction of Calcogen Spinels $CuCr_2X_4$ (X = S, Se, and Te). *J. Phys. Soc. Japan*, **36**, 1322. 62

KASUYA, T. (1956). A theory of metallic ferro- antiferromagnetism on Zener's model. *Prog. Theoret. Phys.*, **16**, 45. 26

KIM, D., GEDANKEN, A., TVER'YANOVICH, Y.S., LEE, D.W. & KIM, B.K. (2006). Synthesis and characterization of nanocrystalline $CuCr_2Se_4$ particles. *Materials Letters*, **60**, 2807. 38

KIM, D.S., RUSNAK, A.N., TVER'YANOVICH, Y.S., VOLOBUEVA, O., KIM, M. & KWON, S. (2008). Preparation of $CuCr_2Se_4$/ZnSe layered films on glass substrates by laser ablation. *Glass Phys. Chem.*, **34**, 146–149. 38, 165

KIM, J.H., KIM, H., KIM, D., IHM, Y.E. & CHOO, W.K. (2004). The origin of room temperature ferromagnetism in cobalt-doped zinc oxide thin films fabricated by PLD. *J. Eur. Cer. Soc.*, **24**, 1847. 178

KIMURA, A., MATSUNO, J., OKABAYASHI, J., FUJIMORI, A., SHISHIDOU, T., KULATOV, E. & KANOMATA, T. (2001a). Soft x-ray magnetic circular dichroism study of the ferromagnetic spinel-type Cr chalcogenide. *J. Electron Spectroscopy and Related Phenomena*, **114-116**, 789. 44, 45

KIMURA, A., MATSUNO, J., OKABAYASHI, J., FUJIMORI, A., SHISHIDOU, T., KULATOV, E. & KANOMATA, T. (2001b). Soft x-ray magnetic circular dichroism study of the ferromagnetic spinel-type Cr chalcogenide. *Phys. Rev. B*, **63**, 224420. 44, 45, 47

REFERENCES

KIOSEOGLOU, G., HANBICKI, A.T., SULLIVAN, J.M., VAN'T ERVE, O.M.J., LI, C.H., ERWIN, S.C., MALLORY, R., YASAR, M., PETROU, A. & JONKER, B.T. (2004). Electrical spin injection from an n-type ferromagnetic semiconductor into a III-V device heterostructure. *Nat. Mat.*, **3**, 799–803. 34

KITTEL, C. (2005). *Introduction to solid state physics*. Wiley. 62

KIYOSAWA, T. & MASUMOTO, K. (1977). P-T phase diagram for ferromagnetic semiconductor $CdCr_2Se_4$. *J. Phys. Chem. Solids*, **38**, 609. 31

KOGAN, E.M. & AUSLANDER, M.I. (1988). Anderson localization in ferromagnetic semiconductors due to spin disorder. *Phys. Stat. (a)*, **147**, 613. 32

KOHN, K., INOUE, K., HORIE, O. & AKIMOTO, S.I. (1976). Crystal chemistry of $MSeO_3$ and $MTeO_3$ (M=Mg,Mn,Co,Ni,Cu, and Zn). *J. Solid State Chem.*, **18**, 27. xiii, 6

KOIDL, P. (1977). Optical absorption of Co^{2+} in ZnO. *Phys. Rev. B*, **15**, 2493. 176

KOLOWOS, I., KNOBLOCH, A. & SIELER, J. (1974). Darstellung von $CdCr_2Se_4/CrCl_3/Se$. *Krist. Tech.*, **9**, 157. 31

KOMAROV, A., RYABCHENKO, S. & TERLETSKII, O. (1980). Giant spin splitting of exciton states in ZnSe with Mn and Fe impurities. *Phys. Stat. Solidi (b)*, **102**, 603. xiii, 6

KOSHIZUKA, N., YOKOYAMA, Y. & TSUSHIMA, T. (1977). Spin-dependent phonon Raman scattering in $CdCr_2Se_4$. *Solid State Commun.*, **23**, 967. 33

KOSTYLEVB, V.A., GIZHEVSKAII, B.A., SAMOKHVALMOV, A.A., AUSLENDER, M.I. & BEBENIN, N.G. (1990). Anisotropy of the magnetoristance of the p-type ferromagnetic semiconductor $HgCr_2Se_4$. *Phys. Stat. Solidi (b)*, **158**, 307. 35

KOVTUN, N.M., KALINNIKOV, V.T. & SCHEMYAKOV, A.A. (1977). Concerning on emechanism of the phase transition from ferromagnetic into the ferrimagnetic state. *J. Exp. Theor. Phys. Lett.*, **25**, 148. 43, 44

KOVTUN, N.M., PROKOPENKO, V.K. & SCHEMYAKOV, A.A. (1978). Electroconductivity and electron exchange in spinel structures. *Solid State Commun.*, **26**, 877. 43

KOVTUN, N.M., NEIDEN, N.P., PROKOPENKO, V.K. & SCHEMYAKOV, A.A. (1979). Neutron diffraction investigations of the magnetic structure of the copper-chromium chalcogenide spinel $CuCr_2S_4$. *J. Exp. Theor. Phys.*, **50**, 207. 43

KOZLOWSKA, I.O., MALICKA, E., WASKOWSKA, A., HEIMANN, J. & MYDLARZ, T. (2001). Distribution of Metal Ions and Magnetic Properties in Spinel System $CdCr_{2-x}Ga_xSe_4$. *J. Solid State Chem.*, **158**, 34. 32

KRAMERS, H. (1934). L'interaction entre les atomes magnétogènes dans un cristal paramagnétique. *Physica*, **1**, 182. 22

KROK-KOWALSKI, J., WARCZEWSKI, J. & NIKIFOROV, K. (2001). Correlation of the magnetic and electrical properties with the ionic radii of cations and anions for the series of ternary and quaternary spinel-type chromium compounds. *J. Alloys Comp.*, **315**, 62. xiv, 29, 30

KUZ'MIN, M.D. (2005). Shape of temperature dependance of spontaneous magnetization of ferromagnets : Quantitative analysis. *Phys. Rev. Lett.*, **94**, 107204. xix, 100, 101

LANDAU, L.D. & LIFSHITZ, E.M. (1980). *Course on theroretical physics Volume 5 Statistical physics (Part 1)*. Robert Maxwell. 133

LARSON, G.H. & SLEIGHT, A.W. (1968). FMR study of Ag-doped $CdCr_2Se_4$. *Phys. Lett. A*, **28**, 203. 31

LEE, W.L., WATAUCHI, S., MILLER, V.L., CAVA, R.J. & ONG, N.P. (2004). Dissipationless Anomalous Hall Current in the Ferromagnetic Spinel $CuCr_2Se_{4-x}Br_x$. *Science*, **303**, 1647–1649. 40, 45

LEHMANN, H.W. (1967). Semiconducting Properties of Ferromagnetic $CdCr_2Se_4$. *Phys. Rev.*, **163**, 488–496. 32, 93, 136

LEHMANN, H.W. & EMMENEGGER, F.P. (1969). Crystal growth, semiconducting and optical properties of ferromagnetic $HgCr_2Se_4$. *Solid State Commun.*, **7**, 965. 35

LEHMANN, H.W. & ROBBINS, M. (1966). Electrical transport properties of the insulating ferromagnetic spinels $CdCr_2S_4$ and $CdCr_2Se_4$. *J. Appl. Phys.*, **37**, 1389. 9, 31

LEMS, W., RIJNIERSE, P.J. & BONGERS, P.F. (1968). Photomagnetic effect in a chalcogenide spinel. *Phys. Rev. Lett.*, **21**, 1643. 33

LI, J., CHEN, Z., WANG, R.J. & PROSERPIO, D.M. (1999). Low temperature route to new materials : solvothermal synthesis of metal chalcogenides in ethylenediamine. *Coord. Chem. Rev.*, **190-192**, 707. 204

LIBERATI, M., NEULINGER, J.R., CHOPDEKAR, R.V., BETTINGER, J.S., ARENHOLZ, E., BUTLER, W.H., STACY, A.M., IDZERDA, Y.I. & SUZUKI, Y. (2008). Electronic structure of halogen doped $CuCr_2Se_4$. *J. Appl. Phys.*, **103**, 07D711. 44

LIU, B. & ZENG, H.C. (2003). Hydrothermal synthesis of ZnO nanorods in the diameter regime of 50 nm. *J. Amer. Chem. Soc.*, **125**, 4430. 203

LIVAGE, J. (1997). The sol-gel processes (Les procédés sol-gels : De l'art du feu à la chimie douce). *Actualite Chimique*, **10**, 4. 201

LOCHER, P.R. (1967). Cu-NMR in paramagnetic and ferromagnetic $CuCr_2Se_4$. *Solid State Commun.*, **5**, 185. 44

LOCHER, P.R. & VAN STAPELE, R.P. (1970). Supertransferred hyperfine fields on tetrahedral sites in some chromium sulfo- and seleno spinels. *J. Phys. Chem. Solids*, **31**, 2643. 44

LOTGERING, F. (1964a). Ferromagnetic interactions in sulphides, selenides and tellurides with the spinel structure. In Nottingham, ed., *Proceedings of the International conference on Magnetism*, 533–537, Institute of Physics and the Physical Society. 36, 37, 38, 40, 108, 114, 209

LOTGERING, F.K. (1964b). Ferromagnetism in Spinels : $CuCr_2S_4$ and $CuCr_2Se_4$. *Solid State Commun.*, **2**, 55–56. 40, 63, 64

LOTGERING, F.K. (1971). Exchange interactions in semiconducting chalcogenides with normal spinel structure from an experimental point of view. *J. Physique*, **32**, 34. 28

LOTGERING, F.K. & STAPELE, R.P.V. (1968). Magnetic properties and electrical conduction of copper-containing Sulfo- and Selenospinels. *J. Appl. Phys.*, **39**, 417–423. xiv, 41, 42

LOTGERING, F.K. & VAN STAPELE, R.P. (1967). Magnetic properties and electrical conduction of copper containing sulphides and selenides with spinel structure. *Solid State Commun.*, **5**, 143–146. 9, 43, 44

LOTGERING, F.K. & VAN STAPELE, R.P. (1968). Cation-anion distances in chalcogenide spinels. *Mat. Res. Bull.*, **3**, 507. 37, 39

LUBECKA, M., MAKSYMOWICZ, L.J., ZUBEREK, R. & POWROZNIK, W. (1989). X-band microwave study of $CdCr_2Se_4$ doped with in and $Cd_{1-x}In_xCr_2Se_4$ thin films. *Phys. Rev. B*, **40**, 2090. 31

LUBECKA, M., MAKSYMOWICZ, J. & ZUBEREK, R. (1990). Exchange-interaction constant of polycristalline $CdCr_2Se_4$ thin films doped with In. *Phys. Rev. B*, **42**, 3926. 32

LUTZ, H.D., PARTIK, M. & M.SASSMANNSHAUSEN (2000). True space group of spinel-type chromium oxides and sulfides, and ternary lithium chloride - band structure calculations. *Z. Kristallogr.*, **215**, 523. 117

LUZHNAYA, N.P., SHABUNINA, G.G., KALINNIKOV, V.T. & AMINOV, T.G. (1981). Ternary Reciprocal System 3 CdSe +2 $CrCl_3$ = Cr_2Se_3 + 3 $CdCl_2$. *Russ. J. Inorg. Chem.*, **26**, 1075. 112

MASUMOTO, K., KOGUCHI, N. & TAKAHASHI, S. (1983). Preparation of ferromagnetic semiconducting $HgCr_2Se_4$ thin films by molecular-beam deposition. *Il Nuovo Cimento D*, **2**, 1798. 35

MATSUMOTO, K. & NAKATANI, I. (1976). Magnetic properties of $CuCr_2Se_4$ single crystals. *Trans. JIM*, **17**, 519. 37

MATSUMOTO, Y., MURAKAMI, M., SHONO, T., HASEGAWA, T., FUKUMURA, T., KAWASAKI, M., AHMET, P., CHIKYOW, T., KOSHIHARA, S. & KOINUMA, H. (2001). Room-Temperature Ferromagnetism in Transparent Transition Metal-Doped Titanium Dioxide. *Science*, **291**, 854. xiii, 5, 6, 167

MATTHIAS, B., BOZORTH, R. & VAN VLECK, J. (1961). Ferromagnetic interaction in EuO. *Phys. Rev. Lett.*, **7**, 160. xiii, 6

MAURER, A. & COLLIN, G. (1980). Structural and physical properties of $Cr_{3\pm\delta}Se_4$ ($x \leq 0.20$). *J. Solid State Chem.*, **34**, 23. 157

MAZURAK, Z., CIWOSKI, J., HEIMANN, J., NATEPROV, A. & CZAJA, M. (2000). Magnetic susceptibility and luminescence of α-$ZnAl_2S_4$ thiospinel doped with chromium. *Chem. Phys.*, **254**, 25–30. 9

MCCUSKER, L.B., DREELE, R.B.V., COX, D.E., LOUER, D. & SCARDI, P. (1999). Rietveld refinement guideline. *J. Appl. Cryst.*, **32**, 36. 223

REFERENCES

MERKULOV, A.I., RADAUTSAN, S.I. & TEZLEVAN, V.E. (1982). Growth and physical properties of $CdCr_2Se_4$ defect single crystals. *J. Cryst. Growth*, **57**, 563. 31, 32

MINISCALCO, W.J., MCCOLLUM, B.C., STOFFEL, N. & MARGARITONDO, G. (1982). Photoemission determination of the occupied d-band position for $CdCr_2S_4$ and $CdCr_2Se_4$. *Phys. Rev. B*, **25**, 2947. 34

MITCHELL, P.W.D. & MORGAN, P.E.D. (1974). Direct Precipitation Method for Complex Crystalline Chalcogenides. *J. Amer. Ceram. Soc.*, **57**, 278. 38

MIYATANI, K., WADA, Y. & OKAMOTO, F. (1968). Magnetic properties of single crystal chalcogenide spinels; $CuCr_2X_3Y$ (X=S, Se and Te, Y=Cl, Br and I) system. *J. Phys. Soc. Japan*, **25**, 369. 37, 39, 108, 123, 209

MIYATANI, K., MINEMATSU, K., WADA, Y., OKAMOTO, F., KATO, K. & BALTZER, P.K. (1971). Magnetic and electrical properties of $CuCr_2Se_{4-x}Br_x$ and $CuCr_2Se_{4-x}Cl_x$. *J. Phys. Chem. Solids*, **32**, 1429. 37, 39, 81, 82, 136

MUNEKATA, H., OHNO, H., VON MOLNAR, S., SEGMULLER, A., CHANG, L. & ESAKI, L. (1989). Diluted magnetic III-V semiconductors. *Phys. Rev. Lett.*, **63**, 1849. xiii, 6

MURAKAMI, M., MATSUMOTO, Y., HASEGAWA, T., AHMET, P., NAKAJIMA, K., CHIKYOW, T., OFUCHI, H., NAKAI, I. & KOINUMA, H. (2004). Cobalt valence states and origins of ferromagnetism in Co doped TiO_2 rutile thin films. *J. Appl. Phys.*, **95**, 5330. 5

NAGAEV, E.L. (1983). *Physics of magnetic semiconductors*. Mir publishers. 7, 26, 32, 33

NAGAOSA, N., SINOVA, J., ONODA, S., MACDONALD, A.H. & ONG, N.P. (2009). Anomalous Hall Effect. *http://arxiv.org/abs/0904.4154?context=cond-mat*. 137

NAGATA, S., HAGINO, T., SEKI, Y. & BITOH, T. (1994). Metal-insulator transition in thiospinel $CuIr_2S_4$. *Physica B*, **194-196**, 1077–1078. 9

NAKATANI, I., NOSE, H. & MASUMOTO, K. (1977). Magnetic properties of $CuCr_2Se_4$ single crystals. *J. Phys. Chem. Solids*, **39**, 743. 37, 38, 43, 108, 123, 209

NAVROTSKY, A. & KLEPPA, O. (1967). The thermodynamics of cation distribution in simple spinels. *J. Inorg. Nucl. Chem.*, **29**, 2701. 14

NEIDA, A.R.V. & SHICK, L. (1969). Single-crystal growth of some chalcogenide spinels. *J. Appl. Phys.*, **40**, 1013. 31

NÉEL, L. (1948). Propriétées magnétiques des ferrites; ferrimagnétisme et antiferromagnétisme. *Ann. Phys. Paris*, **3**, 147. 26

NEULINGER, J.R. (2006). *Synthesis, structure and magnetism in copper chalcochromite spinels*. Ph.D. thesis, University of California, Berkeley. 37, 38, 39, 108, 121, 123

NITSCHE, R. (1960). The growth of single crystals of binary and ternary chalcogenides by chemical transport reactions. *J. Phys. Chem. Solids*, **17**, 163. 108, 123

NOH, H.J., KANG, J.S., LEE, S.S., KIM, G., HAN, S.W., OH, S.J., KIM, J.Y., LEE, H.G., YEO, S., GUHA, S. & CHEONG, S.W. (2007). Valence values of the cations in selenospinels $Cu(Cr,Ti)_2Se_4$. *Europhys. Lett.*, **78**, 27004. 44

NOVOTORTSEV, V.M., KALINNIKOV, V.T. & AMINOV, T.G. (2005). Spin Glass State in Multinary Chromium Compounds. *Russ. J. Inorg. Chem.*, **50**, S54–S80. 10

OGATA, F., HAMAJIMA, T., KAMBARA, T. & GONDARAI, K.I. (1982). The spin-polarised electronic band structure of chromium spinels : II. $CuCr_2Se_4$ and $CuCr_2Te_4$. *J. Phys. C : Solid State Phys.*, **15**, 3483. 44, 47

OGUCHI, T., KAMBARA, T. & GONDARAI, K.I. (1980). Self-consistent electronic structures of magnetic semiconductors by a discrete variational X_α calculation. I. Ferromagnetic spinels, $CdCr_2S_4$ and $CdCr_2Se_4$. *Phys. Rev. B*, **22**, 872. 34

OGUCHI, T., KAMBARA, T. & GONDARAI, K.I. (1981). Self-consistent electronic structures of magnetic semiconductors by a discrete variational X calculation. II. $HgCr_2Se_4$. *Phys. Rev. B*, **24**, 3341. 36

OHGUSHI, K., OKIMOTO, Y., OGASAWARA, T., MIYASAKA, S. & TOKURA, Y. (2008). Magnetic, optical, and magnetooptical properties of spinel-type ACr_2X_4 (A=Mn, Fe, Co, Cu, Zn, Cd; X= O, S, Se). *J. Phys. Soc. Japan*, **3**, 1. 123

OHNO, H., SHEN, A., MATSUKURA, F., OIWA, A., END, A., KATSUMOTO, S. & IYE, Y. (1996). (Ga,Mn)As : A new diluted magnetic semiconductor based on GaAs. *Appl. Phys. Lett.*, **69**, 363. xiii, 6

REFERENCES

Ohno, Y., Young, D.K., Beschoten, B., Matsukura, F., Ohno, H. & Awschalom, D.D. (1999). Electrical spin injection in a ferromagnetic semiconductor heterostructure. *Nature*, **402**, 790. 7

Okada, H., Koyama, K. & Watanabe, K. (2005). Transport, magnetic, thermal and structural properties of the spinel compound $CuTi_2S_4$. *J. Alloys Comp.*, **403**, 34–37. 10

Okuda, T., Tsushima, T. & Masuda, T. (1980). Crystal growth of $CdCr_2Se_4$ from high temperature solution. *Jpn. J. Appl. Phys.*, **Sup 19-3**, 209. 31

Osipov, V.V., Viglin, N.A. & Samokhvalov, A.A. (1998). Investigation of heterostructure "ferromagnetic semiconductor-semiconductor" in the millimeter and submillimeter microwave range. *Phys. Lett. A*, **247**, 353. 36

Pan, F., Song, C., Liu, X.J., Yang, Y.C. & Zeng, F. (2008). Ferromagnetism and possible application in spintronics of transition-metal- doped ZnO films. *Mat. Sci. Eng. Reports*, **62**, 1. 167

Park, Y.D., Hanbicki, A.T., Mattson, J.E. & Jonker, B.T. (2002). Epitaxial growth of an n-type ferromagnetic semiconductor $CdCr_2Se_4$ on GaAs (001) and GaP (001). *Appl. Phys. Lett.*, **81**, 1471. 31

Payer, A., Schmalz, M., Paulus, W., Schollhorn, R., Schlogl, R. & Ritter, C. (1992). Formation of Cu_3^{2+} clusters : structure, bonding and topotactic reactivity of chalcogen spinels $Cu_{1+y}Cr_2Se_3Br$. *J. Solid State Chem.*, **98**, 71. 39

Payer, A., Schollhorn, R., Ritter, C. & W.Paulus (1993). Neutron diffraction study of the structure of chalcogen spinels $Cu_{1+y}Cr_2X_4$ (X≡Se,Te). *J. Alloys Comp.*, **191**, 37. 39

Pecharsky, V.K. & Zavalij, P.Y. (2005). *Fundamentals of powder diffraction and structural characterization of materials*. Springer. 221

Pechini, M.P. (1967). Method of preparing lead and alkaline earth titanates and niobates and coating method using the same to form a capacitor. *US Patent*, 3,330,697. 202

Petricek, V., Dusek, M. & Palatinus (2006). Jana2006. The crystallographic computing system. Institute of Physics, Praha, Czech Republic. 227

Philisborn, H.V. (1967). Growth of single crystals of cadmium chromium selenide by liquid transport with platinum catalyst. *J. Appl. Phys.*, **38**, 955. 31

PHILISBORN, H.V. (1969). Crystal growth by topochemical reaction ; $CdCr_2Se_4$ in the system CdSe-$CrCl_3$-Pt. *J. Cryst. Growth*, **5**, 135. 31

PIERSON, H.O. (1999). *Handbook of chemical vapor deposition (CVD) Principles, technology, and Applications*. Noyes Publication/William Andrew Publishing. 108

PINCH, H.L. & BERGER, S.B. (1968). The effects of non-stoichiometry on the magnetic properties of cadmium chromium chalcogenide spinels. *J. Phys. Chem. Solids*, **29**, 2091. 32, 92

PINK, H., SCHAFFER, H., GOBEL, H. & UNGER, W.K. (1974a). Stability of Br-substituted $CuCr_2Se_4$ spinels. *IEEE Trans. Mag.*, **10**, 623–625. 37, 55, 72, 73, 77

PINK, H., UNGER, W.H., SCHAFFER, H. & GOBEL, H. (1974b). Preparation, stoichiometry and magnetic properties of $Cu_yCr_2Se_{4-z}Br_x$ with $0.5 \lesssim x \lesssim 2$. *Appl. Phys. A*, **4**, 147. 55, 72

RADAUTSAN, S.I. (1983). Preparation and characterization of ternary magnetic semiconductors. *Il Nuovo Cimento D*, **2D**, 1782. 37, 209

RADAUTSAN, S.I., TSURKAN, V.V. & TEZLEVAN, V.E. (1983). Transport phenomena and magnetic-ion exchange in ferromagnetic $Cu_yCr_2Se_{4-x}Br_x$ spinel single crystals. *Il Nuovo Cimento D*, **2D**, 1823. 39

RAJAMATHI, M. & SESHADRI, R. (2002). Oxide and chalcogenide nanoparticles from hydrothermal/solvothermal reactions. *Current Opinion in Solid State and Materials Science*, **6**, 337. 203

RAMDAS, A. & ALAWADHI, H. (1998). Magneto-optics of II-VI diluted magnetic semiconductors. *Current Science*, **75**, 1216. 4

RAMESHA, K. & SESHADRI, R. (2004). Solvothermal preparation of ferromagnetic sub-micron spinel $CuCr_2Se_4$ particles. *Solid State Sci.*, **6**, 841. 38, 45, 47, 204

RAO, C.N.R. & RAO, G.V.S. (1974). *Transition Metal Oxide: Crystal Chemistry Phase transitions and Related Aspects*. National Bureau of Standards Washington DC. 178, 189

RIEDEL, E. & HORVARTH, E. (1973). Kationen-anionen-abstande in kupfer- und chromthiospinellen. *Mat. Res. Bull.*, **8**, 973. 44

RIETVELD, H. (1969). A profile refinement for nuclear and magnetic structure. *J. Appl. Cryst.*, **2**, 65. 59, 223

RIETVELD, H.M. (1967). Line profiles of neutron powder-diffraction peaks for structure refinement. *Acta Cryst.*, **22**, 151. 223

RISBUD, A., SESHADRI, R., ENSLING, J. & FELSER, C. (2005a). Dilute ferrimagnetic semiconductors in Fe-substituted spinel $ZnGa_2O_4$. *J. Phys. : Condens. Matter.*, **17**, 1003. xiii, 6

RISBUD, A.S., SNEDEKER, L.P., ELCOMBE, M.M., CHEETHAM, A.K. & SESHARDI, R. (2005b). Wurtzite CoO. *Chem. Mater.*, **17**, 834. 178, 180, 185, 188

ROBBINS, M., LEHMANN, H.W. & WHITE, J.G. (1967). Neutron diffraction and electrical transport properties of $CuCr_2Se_4$. *J. Phys. Chem. Solids*, **28**, 897. 38, 39, 43, 67, 70

ROBBINS, M., BALTZER, P.K. & LOPATIN, E. (1968). Ferromagnetic Halo-Chalcogenide Spinels ($CuCr_2X_3Y$) and Some Properties of the System $CuCr_2Se_3Br$-$CuCr_2Se_4$ and $CuCr_2Te_3I$-$CuCr_2Te_4$. *J. Appl. Phys.*, **39**, 662–664. xiii, 6, 37, 38, 39, 81, 82

RODE, K., MATTANA, R., ANANE, A., CROS, V., JACQUET, E., CONTOUR, J.P., PETROFF, F., FERT, A., ARRIO, M.A., SAINCTAVIT, P., BENCOK, P., WILHELM, F., BROOKES, N.B. & ROGALEV, A. (2008). Magnetism of (Zn,Co)O thin films probed by x-ray absorption spectroscopies. *Appl. Phys. Lett.*, **92**, 012509. 178

RODIC, D., ANTIC, B., TELLGREN, R., RUNDOLF, H. & BLANUSA, J. (1998). A change in magnetic moment of cr ion with the magnetic phase transition in $CuCr_2Se_4$. *J. Magn. Mag. Mat.*, **187**, 88. 38, 43, 44, 60, 62, 67, 68, 70

RODRIGUEZ-CARVAJAL, J. (1993). Recent Advances in Magnetic Structure Determination by Neutron Powder Diffraction. *Physica B*, **192**, 55. 223

RUDERMAN, M.A. & KITTEL, C. (1954). Indirect exchange coupling of nuclear magnetic moments by conduction electrons. *Phys. Rev.*, **96**, 99. 26

RUSNAK, A.N., KIM, D., PARAMESWARAN, S., PATRA, C.R., TROFIMOV, V.B., HARPNESS, R., GEDANKEN, A. & TVERŠYANOVICH, Y.S. (2006). Syntheses and magnetic properties of nanocrystalline $CuCr_2Se_4$. *J. Non Cryst. Sol.*, **352**, 2885. 38

SAGREDO, V. & DE CHALBAUD, L.M. (2004). Crystal growth of the $CdGa_{2(1-x)}Cr_{2x}Se_4$ compounds by chemical transport method. *Cryst. Res. Tech.*, **39**, 877. 32

SAHA-DASGUPTA, T., RAYCHAUDHURY, M.D. & SARMA, D.D. (2007). Ferromagnetism in metallic chalcospinels $CuCr_2S_4$ and $CuCr_2Se_4$. *Phys. Rev. B*, **76**, 054441. 28

SAITO, H., ZAYETS, V., YAMAGATA, S. & ANDO, K. (2003). Room temperature ferromagnetism in a II-VI diluted magnetic semiconductor $Zn_{1-x}Cr_xTe$. *Phys. Rev. Lett.*, **90**, 207202. xiii, 6

SATOH, T., TSUSHIMA, T. & KUDO, K. (1974). A classification of normal spinel type compounds by "ionic packing factor". *Mat. Res. Bull.*, **9**, 1297. 29

SCHAFFER, H. (1964). *Chemical transport reactions*. Academic Press. 106, 107, 108

SCHOLLHORN, R. & PAYER, A. (1986). Isothermal magnetic phase transitions controlled by reversible electron/ion transfer reaction. *Angw. Chem. Int. Ed. Engl.*, **25**, 905. 37, 39

SELMI, A., MAUGER, A. & HÉRITIER, M. (1985). Anomalous transport properties of n-type $HgCr_2Se_4$. *J. Appl. Phys.*, **57**, 3216. 35

SELMI, A., HERITIER, M. & GIBART, P. (1986). Spinel magnetic semiconductor $HgCr_2Se_4$. *Progress In Crystal Growth And Characterization*, **13**, 121–143. 9, 35, 36

SEO, W.S., SHIM, J.H., OH, S.J., LEE, E.U.K., HUR, N.H. & PARK, J.T. (2005). Phase- and size-controlled synthesis of hexagonal and cubic CoO nanocrystals. *J. Amer. Chem. Soc.*, **127**, 6188. 178, 185, 188

SHABUNINA, G.G., VINOGRADOVA, N.P. & AMINOV, T.G. (1981). Growth of $CdCr_2Se_4$ single crystals from high temperature solutions in different salts. *Russ. J. Inorg. Chem.*, **17**, 1727. 31

SHABUNINA, G.G., SADYKOV, R.A. & AMINOV, T.G. (2003). Magnetic properties and spin-glass state of $CdCr_{2-x}In_xSe_4$ and $Cd_{1-x}In_xCr_2Se_4$ solid solutions. *Russ. J. Inorg. Chem.*, **36**, 1208. 32

SHANTHI, N., MAHADEVAN, P. & SARMA, D.D. (2000). Electronic band structure of cadmium chromium chalcogenide spinels : $CdCr_2S_4$ and $CdCr_2Se_4$. *J. Solid State Chem.*, **155**, 198. 34

SHON, Y., LEE, W., PARK, Y., KWON, Y., S.J.LEE, CHUNG, K., KIM, H., FU, D., KANG, T., FAN, X., PARK, Y. & OH, H. (2004). Mn-implanted dilute magnetic semiconductor InP:Mn. *Appl. Phys. Lett.*, **84**, 2310. xiii, 6

SIKORA, M., KAPUSTA, C., MAKSYMOWICZ, L., LUBECKA, M., CIECIWA, B., SZYMCZAK, R., WELTER, E., BOROWIEC, M. & ZAJAC, D. (2004). EXAFS study of indium doped magnetic semiconductor $CdCr_2Se_4$. *J. Alloys Comp.*, **362**, 151. 31

SLEIGHT, A.W. (1967). Cu^{+2} or Cu^{+1} in chalcogenide spinels ? *Mat. Res. Bull.*, **2**, 1107. 44

SLEIGHT, A.W. & JARRETT, H.S. (1967). Preparation and properties of some copper chromium halochalcogenide with the spinel structure. *J. Phys. Chem. Solids*, **29**, 868. 37, 39

SLUITER, M.H.F., KAWAZOE, Y., SHARMA, P., INOUE, A., RAJU, A.R., ROUT, C. & WAGHMARE, U.V. (2005). First Principles Based Design and Experimental Evidence for a ZnO-Based Ferromagnet at Room Temperature. *Phys. Rev. Lett.*, **94**, 187204. 168, 169, 202

SOLIN, N.I., USTINOV, V.V. & NAUMOV, S.V. (2008). Colossal magnetoresistance of the inhomogeneous ferromagnetic semiconductor $HgCr_2Se_4$. *Phys. Solid State*, **50**, 901. 35

SOULEN, R.J., BYERS, J.M., OSOFSKY, M.S., NADGORNY, B., AMBROSE, T., CHENG, S.F., BROUSSARD, P.R., TANAKA, C.T., NOWAK, J., MOODERA, J.S., BARRY, A. & COEY., J.M.D. (1998). Measuring teh spin polarization of a metal with a superconducting point contact. *Science*, **282**, 85. 147

STAMENOV, P. (2007). *Metals, semimetals, and semiconductors for spinelectronics*. Ph.D. thesis, School of Physics, Trinity College Dublin. 5, 233

STAMENOV, P. & COEY, J.M.D. (2006). Sample size, position, and structure effect on magnetization measurements using a second order gradiometer pickup coils. *Rev. Sci. Instr.*, **77**, 015106. 233

STOCKBARGER, D.C. (1938). The production of large single crystals of Lithium Fluoride. *Rev. Sci. Instr.*, **7**, 133. 104

SUGITA, H., WADA, S., MIYATANI, K., TANAKA, T. & ISHIKAWA, M. (2000). s-wave superconductivity of an itinerant weak antiferromagnet $CuCo_2S_4$. *Physica B*, **284**, 473–474. 9

SUNDARESAN, A. & RAO, C.N.R. (2009a). Ferromagnetism as universal feature of inorganic nanoparticles. *Nano Today*, **4**, 96. 168

SUNDARESAN, A. & RAO, C.N.R. (2009b). Implications and consequences of ferromagnetism universally exhibited by inorganic nanoparticles. *Solid State Commun.*, **149**, 1197. 168

SUNDARESAN, A., BHARGAVI, R., RANGARAJAN, N., SIDDESH, U. & RAO, C.N.R. (2006). Ferromagnetism as a universal feature of nanoparticles of the otherwise nonmagnetic oxides. *Phys. Rev. B*, **74**, 161306. 168

SZYMCZAK, R., SZEWCZYK, A., BARAN, M. & TSURKAN, V.V. (1990). Domain structure in $CuCr_2Se_4$ single crystals. *J. Magn. Mag. Mat.*, **83**, 481. 39

TAKAHASHI, T. (1969). Growth of $HgCr_2Se_4$ single crystals by chemical transport. *J. Cryst. Growth*, **6**, 319. 35

TAKAHASHI, T., MINEMATSU, K. & MIYATANI, K. (1971). Single crystal growth and some properties of $HgCr_{2-x}In_xSe_4$ solid solutions. *J. Phys. Chem. Solids*, **32**, 1007. 35

TANIGUCHI, M., FUJIMORI, A. & SUGA, S. (1989). Electronic structure of magnetic semiconductor $CdCr_2Se_4$: Cr 3d partial density of states and p-d hybridization. *Solid State Commun.*, **70**, 191. 34

TAY, S.W., HONG, L. & LIU, Z. (2006). Generation of high spin state in the spinel Co_3O_4 nano-domains through interfacial induction. *Mat. Chem. Phys.*, **100**, 60. 189

THEURER, H.C. (1952). *US Patent*, 3,060,123. 104

THOMPSON, P. & GRIMES, N.W. (1977). Madelung calculations for the spinel structure. *Phil. Mag.*, **36**, 501. 18

THOMSON, W. (1857). *Proc. R. Soc. London*, **8**, 546. 138

TINKHAM, M. (1996). *Introduction to Superconductivity: Second Edition*. McGraw-Hill. 147

TRET'YAKOV, Y.D., GORDEEV, I.V., ALFEROV, V.A. & SAKSONOV, Y.G. (1972). Deviation from stoichiometry in chalcogenide chromites with spinel structure. *Russ. J. Inorg. Chem.*, **8**, 2215. 31

TRET'YAKOV, Y.D., GORDEEV, I.V. & KESSLER, Y.A. (1977). Investigation of some chalcogenides with spinel structure. *J. Solid State Chem.*, **20**, 345. 196

TSUBOKAWA, I. (1960). On the Magnetic Properties of a $CrBr_3$ Single Crystal. *J. Phys. Soc. Japan*, **15**, 1664. xiii, 3, 6

REFERENCES

TSURKAN, V.V., RATSEEV, S.A., TEZLEVAN, V.E. & RADAUTSAN, S.I. (1984). Hall effect and conductivity of ferromagnetic $CuCr_2Se_4$ single crystals. *Prog. Cryst. Res. Tech.*, **10**, 385. 39, 136, 209

TVER'YANOVICH, Y.S., KIM, D.S., RUSNAK, A.N., TURKINA, E.Y. & KORZININ, A.A. (2005). Formation of $CuCr_2Se_4$ ferromagnetic spinel mycrocrystals in a chalcogenide glass matrix. *Glass Phys. Chem.*, **31**, 168. 37

UPADHYAY, S.K., PALANISAMI, A., LOUIE, R.N. & BUHRMAN, R.A. (1998). Probing ferromagnets with Andreev reflection. *Phys. Rev. Lett.*, **81**, 3247. 147

VAN STAPELE, R.P. & LOTGERING, F.K. (1970). Trivalent and tetravalent chromium in the seleno-spinel series $CuCr_{0.3}Rh_{1.7-x}Sn_xSe_4$. *J. Phys. Chem. Solids*, **31**, 1547. 43

VENKATESAN, M., FITZGERALD, C.B. & COEY, J.M.D. (2004). Unexpected magnetism in a dielectric oxide. *Nature*, **430**, 630. 169

VERNEUIL, A. (1902). *C. R. Acad. Sci. Paris*, **135**, 791. 104

VERNEUIL, A. (1904). *Ann. Chem. Phys.*, **3**, 20. 104

VIGLIN, N.A., OSIPOV, V.V. & SAMOKHVALOV, A.A. (1999). The Ferromagnetic Semiconductor - Semiconductor Heterostructures p-$HgCr_2Se_4$ - n-InSb and n-EuO - n-InSb : Emission in the Millimeter and Sub millimeter Microwave Range. *Physics of Low-Dimensional Structures*, **1-2**, 129. 36

VINOGRADOVA, G.I., ANZINA, L.V., VESELAGO, V.G., GLUSHKOV, M.V., MENSHCHIKOVA, T.N. & ZHUKOV, E.G. (2007). Effect of charge carriers on magnetic properties of $CdCr_2Se_4$ ferromagnetic semiconductor. *Phys. Solid State*, **49**, 865. xxv, 112, 211, 212

VISPUTE, R.D., TALYANSKY, V., TRAJANOVIC, Z., CHOOPUN, S., DOWNES, M., SHARMA, R.P., VENKATESAN, T., WOODS, M.C., LAREAU, R.T., JONES, K.A. & ILIADIS, A.A. (1997). High quality crystalline ZnO buffer layers on sapphire (001) by pulsed laser deposition for III-V nitrides. *Appl. Phys. Lett.*, **70**, 2735. 183

VON PHILISBORN, H. (1971). Crystal growth and characterization of chromium sulfo- and seleno-spinels. *J. Cryst. Growth*, **9**, 296–304. 107

WAGNER, V., MITLEHNER, H. & GEICK, R. (1971). Infrared active phonon in $CdCr_2Se_4$. *Optics Comm.*, **2**, 429. 151

WANG, X., XU, J.B., KE, N., YU, J., WANG, J., LI, Q., ONG, H.C. & ZHANG, R. (2006). Imperfect oriented attachment: Direct activation of high-temperature ferromagnetism in diluted magnetic semiconductor nanocrystals. *Appl. Phys. Lett.*, **88**, 223108. 171, 173, 204

WANG, Y.H., GUPTA, A., CHSHIEV, M. & BUTLER, W.H. (2008). Half-metallic electronic structures of quaternary ferromagnetic chalcospinels : $Cd_xCu_{1-x}Cr_2S_4$ and $Cd_xCu_{1-x}Cr_2Se_4$. *Appl. Phys. Lett.*, **92**, 062507. 46, 47

WANG, Y.H., GUPTA, A., CHSHIEV, M. & BUTLER, W.H. (2009). Induced half-metallicity in Cr-based ferromagnetic chalcospinels with anion substitutions : $CuCr_2S(Se)_{4-x}E_x$ (E=F, Cl, Br), $Cu(Cd)Cr_2S(Se)_{4-x}$, and $CdCr_2S(Se)_{4-x}D_x$ (D=N, P, As). *Appl. Phys. Lett.*, **94**, 062515. 46, 47

WANG, Y.H.A., BAO, N., SHEN, L., PADHAN, P. & GUPTA, A. (2007). Size controlled synthesis of magnetic $CuCr_2Se_4$ nanocrystals. *J. Amer. Chem. Soc.*, **129**, 12408. 38

WARCZEWSKI, J., KROK-KOWALSKI, J., GUSIN, P. & LISZKOWSKI, P. (2002). On the relation of the r_o/r_a versus r_t/r_a plot with direct and RKKY exchanges in the compounds containing chromium. *Phys. Stat. Solidi (a)*, **189**, 965. 28

WEBER, S., LUNKENHEIMER, P., FICHTL, R., HEMBERGER, J., TSURKAN, V. & LOIDL, A. (2006). Colossal magnetocapacitance and colossal magnetoresistance in $HgCr_2S_4$. *Phys. Rev. Lett.*, **96**, 157202. 9

WEHMEIER, F.H. (1969). The growth of cadmium chromium selenide by chemical transport ith cadmium chloride and the behavior of cadmium chromium selenide at elevated temperature. *J. Cryst. Growth*, **5**, 26. 31

WEN, C.P., HERSHENOV, B., VON PHILISBORN, H. & PINCH, H.L. (1968). Device application feasibility of single-crystal $CdCr_2Se_4$, a ferromagnetic semiconductor spinel. *IEEE Trans. Mag.*, **4**, 702. 7, 34

WINDT, D.L. (1998). IMD-software for modeling the optical properties of multilayer films. *Computer in Physics*, **12**, 1. 226

WOJTOWICZ, P.J. (1969). Semiconducting ferromagnetic spinels. *IEEE Trans. Mag.*, **5**, 840. 34

REFERENCES

WOLD, A. & RULFF, J.K., eds. (1973). *Inorganic Syntheses vol. VIX*. McGraw-Hill. 31, 112, 210

YAMAGUSHI, Y., OHISHI, Y., OHASHI, M., YAMASHITA, O. & WATANABE, H. (1980). Electric conductivity and 3d-electron distribution in $CuCr_2Se_{4-x}Br_x$. *Jpn. J. Appl. Phys.*, **Sup. 19-2**, 291. 39

YAMANAKA, S., KOBAYASHI, S., NAKAI, S. & NAOE, M. (1971). $CuCr_2Se_4$ Films by Simultaneous Vacuum deposition from Separate Sources. *Jpn. J. Appl. Phys.*, **10**, 668–669. 38

YAMASHITA, O., YAMAGUSHI, Y., NAKATANI, I., WATANABE, H. & MASUMOTO, K. (1979a). Polarized neutron diffraction study of a $CuCr_2Se_4$ single crystal. *J. Phys. Soc. Japan*, **46**, 1145. 38, 43, 68

YAMASHITA, O., YAMAUCHI, H., YAMAGUSHI, Y. & WATANABE, H. (1979b). Magnetic properties of the system $CuCr_2Se_{4-x}Y_x$ (y=Cl, Br). *J. Phys. Soc. Japan*, **47**, 450. 39

YANG, Z. (2004). Magnetic anisotropy in colossal magnetoresistive $FeCr_2S_4$ single crystals. *Solid State Commun.*, **130**, 511–515. 9

YAO, S.S., PELLEGRINO, F., ALFANO, R.R., MINISCALCO, W.J. & LEMPICKI, A. (1981). Photoluminescent Determination of the Fundamental Gap for the Ferromagnetic Semiconductor $CdCr_2Se_4$. *Phys. Rev. Lett.*, **46**, 558. 34

YAO, Y., LIANG, Y., XIAO, D., NIU, Q., SHEN, S.Q., DAI, X. & FANG, Z. (2007). Theoretical evidence of Berry-phase mechanism in anomalous Hall transport : First-principles studies of $CuCr_2Ss_{4-x}Br_x$. *Phys. Rev. B*, **75**, 020401. 45, 47

YARESKO, A. & ANTONOV, V. (2007). Magnetic interactions in Cr spinels. *J. Magn. Mag. Mat.*, **310**, 1672. 28

YARESKO, A.N. (2007). Electronic band structure and exchange coupling constants in ACr_2S_4 spinels (A = Zn, Cd, Hg ; X = O, S, Se). *Phys. Rev. B*, **77**, 115106. 28

YOKOYAMA, H., WATANABE, R. & SHIBA, S. (1967). Nuclear magnetic resonance studies of $CuCr_2Se_4$ and $CuCr_2Te_4$. *J. Phys. Soc. Japan*, **23**, 450. 43, 44

YOSIDA, K. (1957). Magnetic properties of Cu-Mn Alloys. *Phys. Rev.*, **106**, 893. 26

ZENER, C. (1951). Interaction between the d-shells in transition metals; Part II-Ferromagnetic compounds of manganese with erowskite structure. *Phys. Rev.*, **82**, 403–405. 3, 25

ZHANG, H., YANG, D., JI, Y., MA, X., XU, J. & QUE, D. (2004). Low temperature synthesis of flowerlike ZnO nanostructures by Cetylmethylammonium bromide- assisted hydrothermal process. *J. Phys. Chem. B*, **108**, 3955. 203

ZHUKOV, E.G., MENSHCHIKOVA, T.K., OCHERTYANOVA, L.I. & FEDOROV, V.A. (2006). Phase relation in the $HgCr_2Se_4$-$CdCl_2$ system. *Russ. J. Inorg. Chem.*, **42**, 951. 35

ZUNGER, A. (1980). Systematization of the stable crystal structure of all AB-type binary compounds : A pseudopotential orbital radii approach. *Phys. Rev. B*, **22**, 5839. 19

ZUTIC, I., FABIAN, J. & SARMA, S.D. (2004). Spintronics : fundamentals and application. *Rev. Mod. Phys.*, **76**, 323. 5